University of Reading

On the Structural and Physical Properties of Earth-abundant Sulphides for Thermoelectric Applications

A thesis submitted for the degree of Doctor of Philosophy

School of Chemistry, Food & Pharmacy

Gabin P. L. Guélou

September 2016

Declaration

I confirm that this is my own work and the use of all material from other sources has been properly and fully acknowledged.

(Gabin P. L. Guélou)

To my family.

Abstract

The work presented in this thesis focuses on improving the thermoelectric performance of cost-efficient, widely available, non-toxic transition-metal sulphides. Three families of materials, titanium-disulphide derivatives, tetrahedrites and bornites, were investigated owing to their promising electrical and/or thermal properties. Alongside thermoelectric property measurements, structural characterisation and measurements of various physical properties were carried out in order to explain the relationship between structural and physical features.

A series of composition Co_xTiS_2 ($0 \leq x \leq 0.75$) was synthesised and structural characterisation was carried out using a combination of powder X-ray diffraction and neutron diffraction analysis. Electrical and thermal transport property measurements, thermal analysis, magnetic susceptibility measurements and muon spectroscopy analysis were carried out to complete the investigation. The intercalation of cobalt within the van der Waals' gap of TiS_2 leads to the formation of three superstructure types, monoclinic M_5S_8 ($x = 0.25$), trigonal M_2S_3 ($x = 1/3$) and monoclinic M_3S_4 ($x = 0.5$). At intercalation levels $x \leq 0.20$ and $x \geq 2/3$, Co atoms randomly occupy octahedral sites. In the case of $x \geq 2/3$, Co atoms also occupy tetrahedral sites. The thermoelectric properties of Co_xTiS_2 ($0 \leq x \leq 2/3$) have been systematically investigated. A figure of merit of 0.3 is obtained for Co_xTiS_2 ($0.04 \leq x \leq 0.08$) at 573 K, a 25 % improvement over pristine TiS_2 and one of the highest figures of merit reported for a *n*-type sulphide at such a low temperature. A series with composition $Mo_xTi_{1-x}S_2$ ($0 \leq x \leq 0.09$) was synthesised and consolidated by hot-pressing and spark plasma sintering. The ball milling conditions used and the SPS processing lead to a power factor of $S^2\rho^{-1} \approx 2.1$ mW m^{-1} K^{-2} at 323 K, which is the highest reported for TiS_2. The reproducibility of the electrical properties of TiS_2 for application at temperatures that do not exceed 473 K was confirmed by a heat-soak experiment. Nanoparticles of TiS_2 with controlled morphologies were synthesised using a scalable solution-based route. Measurements of the Seebeck coefficient were carried out on TiS_2 nanoflakes and a stoichiometry of $Ti_{1+x}S_2$ where x lies within the range $0.02 \leq x \leq 0.03$ was determined. The thermoelectric properties of TiS_2 nanocomposites with TiO_2 nanoparticles and carbon

nanotubes (CNTs) were investigated. A 12 % increase in the figure of merit over that of pristine TiS_2 at 573 K, ZT = 0.28, is observed for the nanocomposite with 0.5 vol% of nano-TiO_2.

Two families of copper sulphides were investigated for their promising *p*-type thermoelectric properties, tetrahedrites, including $Cu_{12-x}Mn_xSb_4S_{13}$ (x = 0; 1) and $Cu_{12+y}Sb_4S_{13}$ (x = 0; 0.3; 1; 1.5 and 2), and manganese-doped bornite, $Cu_5Fe_{1-x}Mn_xS_4$ ($0 \leq x \leq 0.10$).

A combination of powder X-ray and neutron diffraction analysis of $Cu_{12-x}Mn_xSb_4S_{13}$ (x = 0; 1) located the Mn atoms on the Cu(1) site in tetrahedral position. Manganese substitution leads to a substantial reduction in thermal conductivity and the figure of merit is improved with ZT = 0.56 at 573 K. Structural analysis using powder X-ray diffraction and measurements of the thermoelectric properties of a series of copper-enriched tetrahedrite $Cu_{12+y}Sb_4S_{13}$ (y = 0.3; 1; 1.5; 2) were carried out. At room temperature, $Cu_{12+y}Sb_4S_{13}$ exists as a mixture of a Cu-poor and a Cu-rich phase and a change of behaviour in the electrical and thermal properties are observed over the temperature range $380 \leq T / K \leq 410$. An increase in the Seebeck coefficient and a simultaneous decrease in the thermal conductivity are responsible for a large improvement in the figure of merit with ZT = 0.62 at 573 K for $Cu_{12+y}Sb_4S_{13}$ (y = 1.5 and 2).

A manganese-doped bornite series of composition $Cu_5Fe_{1-x}Mn_xS_4$ ($0 \leq x \leq 0.10$) was successfully synthesised using mechanical alloying. This synthetic method offers a simplified route to large scale production as well as better thermoelectric performance (ZT = 0.55 at 543 K) compared with samples prepared by solid-state reaction ($ZT \approx 0.4$ at 573 K). Structural investigation was carried out using a combination of powder X-ray diffraction and SEM/EDX analysis and the solubility limit of $Cu_5Fe_{1-x}Mn_xS_4$ was determined to be x = 0.1. Repeated electrical measurements and thermogravimetric analysis were carried out in order to investigate the stability of the samples and the reproducibility of the electrical properties as a function of time and temperature.

Acknowledgements

I would like to express my sincere gratitude to the countless people that have contributed, directly and indirectly, to the completion of the work presented in this thesis.

First and foremost, I am forever grateful to my supervisors, ***Dr Paz Vaqueiro*** and ***Prof Anthony V. Powell*** for their selfless time, encouragements, good humour, support and guidance throughout the past seven years; from my year 2 project in 2009 to my MChem project and Ph. D. thesis.

Financial support from the European Commission and the University of Reading is gratefully acknowledged.

Special thanks go to:

The materials groups from Heriot-Watt University and the University of Reading, especially ***Ruth***, ***Sarah 1.0***, ***Sarah 2.0***, ***Jack***, ***Jesus***, ***John***, ***Panos***, ***Seb***, ***Son*** and ***Srinivas*** for their help and friendship.

Dr Emmanuel Guilmeau for the thermal conductivity measurements on square samples but above all for his excellent counsel, friendship, good wine and good food.

Dr Fiona Coomer for the considerable amount of time she spent helping me with muon spectroscopy. I am very grateful for her patience and guidance.

Dr Ron Smith and ***Dr Winfried Kockelmann*** for their assistance with neutron diffraction experiments on POLARIS and GEM.

The Chemical Analysis Facility (CAF) for letting me use thermal analysis equipment.

Dr Sylvie Hébert for performing SQUID measurements at CRISMAT laboratory.

Dr Gavin Stenning and ***Dr Jesus Prado-Gonjal*** for performing SQUID measurements at the ISIS facility.

Dr Rob Haigh for his help on solution synthesis and for being a reasonably annoying health and safety officer.

Dr Tristan Barbier and the materials group at CRISMAT for their assistance and friendship.

Mr Nick Spencer for the many hours we spent fixing the X-ray diffractometers after an undergrad's hit-and-run.

Ms Judy Butler for the countless times she has saved me from administrative hassle, for her friendship, cakes, good humour, cakes, kindness, cakes and good counsel. Did I mention she makes amazing cakes?

Mr Mark McClemont for his friendship and the innumerable silica tubes he has prepared. His contribution to the materials group's research cannot be overstated.

Mr Andy Whittam and ***Mr Gary Yeo*** for their expertise and assistance. Without their help, keeping the laboratories in working condition would have been impossible.

Prof Mike Reece, ***Dr H. Ning*** and ***Dr B. Du*** for their assistance with SPS at Queen Mary College, University of London.

Ben for proofreading this thesis.

KaiYe, for her constant support throughout the years, never failing to believe in me. She is a true source of inspiration. **我**爱你**宝**贝.

Ma famille, pour leur soutient et encouragements et pour avoir supporté mon caractère pendant la rédaction de cette thèse (et avant d'ailleurs). Je remercie en particulier mes grands-parents et ma mère pour m'avoir gardé en pension complète le temps de la rédaction!

Last but not least, I cannot begin to fully acknowledge the support of my friends, ***Steph***, ***Alex***, ***FX***, ***JeanPin***, ***Lenny***, ***Loli***, ***Max***, ***Toto***, ***The Longstone team***, and many others, without whom I would have finished writing much earlier. Thanks guys… Thanks for keeping me sane too.

Table of Contents

Chapter 1 - Introduction 12

1.1 Sustainable energy 14
1.1.1 Promising technologies 14
1.1.2 Thermoelectricity 16
1.1.2.1 Thermoelectric devices 16
1.1.2.2 Thermoelectric performance 17
1.2 Structures and superstructures 20
1.2.1 Low-dimensional structures 21
1.2.2 Layered transition-metal dichalcogenides 22
1.2.3 Superstructures 23
1.3 Magnetism 24
1.3.1 Diamagnetism and paramagnetism 25
1.3.2 Cooperative magnetic phenomena 26
1.3.3 Muons in magnetism 27
1.4 Structure-property relationships 29
1.4.1 Band theory and density-of-states 29
1.4.2 Conduction mechanisms in thermoelectric materials 31
1.4.3 Phonon scattering 32
1.5 Current advances and strategies 34
1.5.1 Improving ZT 35
1.5.2 State-of-the-art thermoelectric materials 37
1.5.3 Thermoelectric sulphides 39
1.6 Materials investigated 44
1.6.1 Copper-containing sulphide minerals 44
1.6.1.1 Tetrahedrite 44
1.6.1.2 Bornite 45
1.6.2 Titanium disulphide 46
1.7 Aims of the present work 47

Chapter 2 - Experimental techniques 48

2.1 Synthesis 48
2.1.1 High temperature solid-state reaction 48
2.1.2 Mechanical alloying/milling 48

2.1.3 Solution synthesis 50
2.2 Powder X-ray diffraction 51
2.3 Powder neutron diffraction 53
2.3.1 The GEM diffractometer 55
2.3.2 The POLARIS diffractometer 56
2.4 Analysis of powder diffraction data 57
2.4.1 The Rietveld method 57
2.4.2 The Le Bail method 59
2.5 SQUID magnetometry 59
2.6 Muon spectroscopy and the EMU spectrometer 60
2.7 Physical property measurements 62
2.7.1 Sample fabrication 62
2.7.2 Electrical transport property measurements 64
2.7.2.1 Electrical resistivity 64
2.7.2.2 Seebeck coefficient 65
2.7.3 Thermal conductivity 66
2.7.3.1 Flash method 67
2.7.3.2 Specific heat 68
2.8 Electron microscopy 68
2.8.1 Scanning electron microscope 69
2.8.2 EDX analysis 70
2.9 Thermal analysis 71

Chapter 3 - Substitution and intercalation in titanium disulphide 72

3.1 Introduction 72
3.2 Co_xTiS_2 74
3.2.1 Synthesis 74
3.2.2 Structural investigations 74
3.2.2.1 Powder X-ray diffraction 74
3.2.2.2 Powder neutron diffraction 80
3.2.3 Magnetic properties 92
3.2.3.1 Low temperature neutron diffraction 92
3.2.3.2 Magnetic susceptibility 93
3.2.3.3 Muon spectroscopy 96
3.2.4 Thermogravimetric analysis 103
3.2.5 Thermoelectric performance 104
3.2.5.1 Density and anisotropy 104

3.2.5.2 Electrical properties 108
3.2.5.3 Thermal transport properties and figure of merit 113
3.3 $Mo_xTi_{1-x}S_2$ 118
3.3.1 Synthesis 119
3.3.2 Structural investigations 120
3.3.3 Thermoelectric performance 124
3.3.3.1 Electrical properties 124
3.3.3.2 Thermal transport properties 128
3.3.4 Heat soak experiment 129
3.4 Conclusions 130

Chapter 4 - TiS_2 nanoparticles and nanocompositing 133

4.1 Introduction 133
4.2 TiS_2 nanoflakes and nanoflowers 134
4.2.1 Synthesis 135
4.2.2 SEM/EDX analysis 136
4.2.3 TiS_2 nanoflakes as thermoelectric materials 138
4.3 TiS_2/nano-TiO_2 nanocomposites 140
4.3.1 Sample preparation 140
4.3.2 Powder X-ray diffraction 141
4.3.3 Thermoelectric performance 144
4.3.3.1 Electrical properties 144
4.3.3.2 Thermal transport properties and figure of merit 147
4.4 TiS_2/CNTs nanocomposites 151
4.4.1 Sample preparation 152
4.4.2 Powder X-ray diffraction 152
4.4.3 Thermoelectric performance 155
4.4.3.1 Electrical Properties 155
4.4.3.2 Thermal transport properties and figure of merit 157
4.5 Conclusion 159

Chapter 5 - Copper-containing sulphide minerals as thermoelectric materials 162

5.1 Introduction 162
5.2 Tetrahedrite phases $Cu_{12}Sb_4S_{13}$ and $Cu_{11}MnSb_4S_{13}$ 163
5.2.1 Synthesis 164
5.2.2 Structural investigations 164

5.2.2.1 Powder X-ray diffraction 164
5.2.2.2 Powder neutron diffraction 167
5.2.3 Thermoelectric performance of $Cu_{12}Sb_4S_{13}$ and $Cu_{11}MnSb_4S_{13}$ 178
5.2.3.1 Electrical properties 178
5.2.3.2 Thermal transport properties and figure of merit 181
5.3 Tetrahedrite phases $Cu_{12+y}Sb_4S_{13}$ 184
5.3.1 Synthesis and structure confirmation 184
5.3.2 Thermoelectric performance of $Cu_{12+y}Sb_4S_{13}$ 186
5.3.2.1 Electrical properties 186
5.3.2.2 Thermal transport properties and figure of merit 188
5.4 Bornite phase $Cu_5Fe_{1-x}Mn_xS_4$ 191
5.4.1 Synthesis 191
5.4.2 Structural investigations 192
5.4.2.1 Powder X-ray diffraction 192
5.4.2.1 SEM/EDX analysis 195
5.4.3 Thermoelectric performance 196
5.4.3.1 Electrical properties 196
5.4.3.2 Thermal transport properties 200
5.4.3.3 Figure of merit 202
5.4.4 Stability of $Cu_5Fe_{1-x}Mn_xS_4$ 203
5.4.4.1 Thermogravimetric analysis 203
5.4.4.2 Repeatability and $Cu_{2-x}S$ exsolution 205
5.5 Conclusions 206

Chapter 6 - Conclusions 208

6.1 Titanium disulphide derivatives 208
6.1.1 Cobalt intercalation in titanium disulphide 208
6.1.2 Molybdenum substitution in titanium disulphide 209
6.1.3 TiS_2 nanoparticles and nanocomposites 209
6.1.4 Further work 210
6.2 Copper-containing ternary sulphides 211
6.2.1 Manganese substitution in tetrahedrite 211
6.2.2 Copper-enriched tetrahedrite 211
6.2.3 Manganese substitution in bornite 212
6.2.4 Performance comparison and further work 212
6.3 Final comments 213

Chapter 1 - Introduction

The energy crisis poses one of the major threats of the 21st century. There is now extremely little doubt, if any, that the rapid climate change of the past century, and the consequences associated with it, is caused by human activity. The consensus in the scientific community, as cited through the publications in peer-reviewed scientific journals, is overwhelmingly in favour of an anthropogenic global warming (AGW) hypothesis with 97.1 % of the articles matching the topics of "global climate change" or "global warming" in support of AGW.[1] In order to slow down, and ultimately reverse the trend of the earth's temperature curve, Figure 1.1 and Figure 1.2, many governments have started taking actions towards a reduction in the use of fossil fuels by encouraging research on renewable energies, such as the European Union's Renewable Energy Directive.[2] The motivations are both ecological and economical, with the aim of reducing the greenhouse gas emission as well as our dependence on the limited fossil fuel reserves.

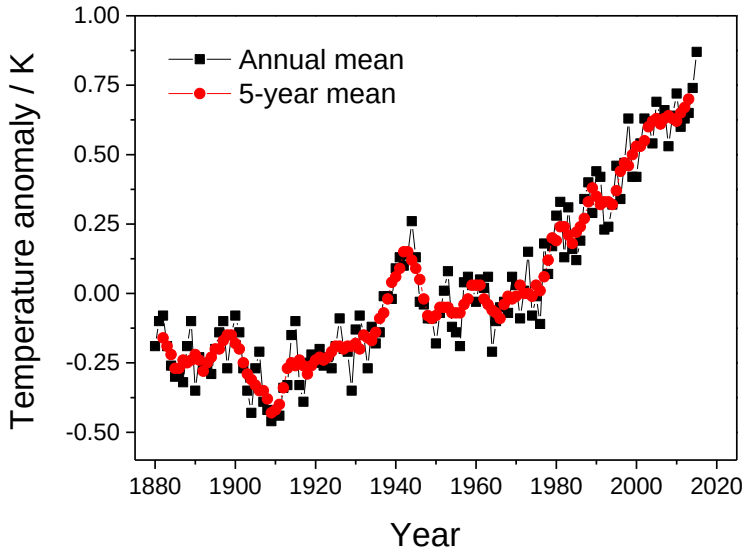

Figure 1.1 Annual mean and 5-year mean of the global land-ocean temperature relative to 1951-1980 average temperatures. These measurements, from NASA's Goddard Institute for Space Studies (GISS),[3] are very consistent with those of the NOAA National Climatic Data Center, the Met Office Hadley Centre/Climatic Research Unit and the Japanese Meteorological Agency.

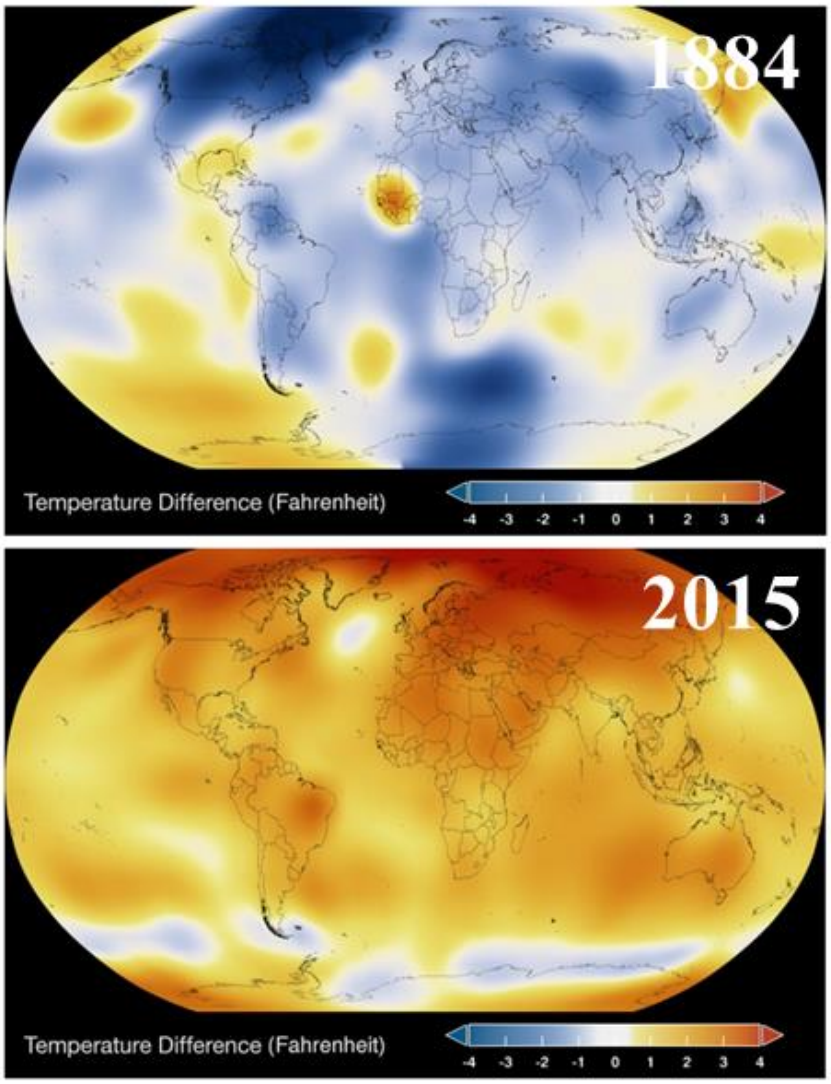

Figure 1.2 5-year average variation of global surface temperatures in 1884 and 2015 from NASA/GISS measurements. Credit to NASA/Goddard Space Flight Center Scientific Visualization Studio.[4]

The work in this thesis was partially financed by the European Commission programme (FP7-SME, project reference: 315019) funding research for the benefit of small and medium-sized enterprises (SMEs). The InnovTEG project, "An innovative very low-cost thermoelectric technology for large-scale renewable solar energy applications" was coordinated in the UK and research was carried out in Sweden, the UK, France, Netherlands and Estonia. Transition-metal sulphides, which are based on low cost and earth-abundant elements, are ideal candidates.

1.1 Sustainable energy

As the amount of greenhouse gas released into the atmosphere increases, threatening the earth's ecosystem as a whole, the need for "clean" energy has never been more crucial. Sustainable energy can be obtained in many ways, from replacing combustion-based electricity generation by environmentally-friendly renewable energy sources to implementing energy-harvesting devices in existing industrial processes. Combustion engines and industrial processes produce waste-heat as a by-product of useful energy generation. A considerable amount of energy is then lost through heat dissipation, cooling water, lubricant and exhaust gas.[5] Thermoelectric devices, operating in the appropriate temperature range, can either be used to harvest this industrial waste-heat or to harvest natural energy such as heat from sunlight.[6, 7] Ultimately, reducing our reliance on fossil fuels is likely to involve a combination of existing technologies such as photovoltaics, wind turbines, heat pumps, etc.

1.1.1 Promising technologies

Energy is considered renewable when its source replenishes naturally on a human timescale. Some examples include solar, wind, geothermal and hydroelectric power as well less common resources such as vibrational energy from human or industrial movements. Thermoelectricity is one of many technologies that can produce electrical energy without the need for harmful chemical combustion.

Today, hydroelectricity is the first source of renewable energy with 16 % of the world's global electricity production in 2015.[8] There are many reasons why hydroelectricity has become increasingly important: electricity production costs are relatively low; the level of greenhouse gases released is dramatically reduced compared to fossil fuels; the production is flexible and does not release any by-product waste. However, the major downside to conventional hydroelectricity is the impact on local ecosystems through the use of dams that interrupt the normal course of a river. The second largest source of renewable energy is wind power and contributes to almost 5 % of the world global electricity production.[9] Wind turbines can be implanted both in land, where their installation and maintenance cost is cheaper than new coal-based generation and other renewable energies, and offshore, where the energy production is

larger and steadier but the cost of generation is more than doubled.[10] Wind power generation is extremely clean, and, unlike hydroelectricity, the impact on local ecosystems is negligible with only the aesthetic aspect to consider. However, the power generation depends on the weather forecast and varies significantly on short timescales.

Solar power, whether it is as light or heat, can be converted into useful energy in many ways including water heating, process heat, artificial photosynthesis or thermoelectricity. Using solar photovoltaics (PV) is the most successful method to directly convert solar energy into an electrical source. PV cells consist of semiconductors that exhibit the photovoltaic effect, a phenomenon that corresponds to the excitation of electrons by photons of light from the sun and the subsequent generation of charge carriers. Solar PV is now the third most important renewable power generation in the world and counts for *ca*. 1 % of the world's global electricity production in 2015.[11]

There are many other promising technologies that keep improving and can be combined with wind and solar power in order to outperform fossil fuels. Fuel cells convert chemical energy into electricity using hydrogen ions (protons) and an oxidising agent, often simply oxygen or air. The main advantage over a classic battery is the continuous power generation for as long as the hydrogen and oxidising agent are supplied to the battery.[12] The by-products of the electrical power generation are mainly water and heat with traces of some pollutants. While the production costs are still high, fuel cells can find applications in many specific field such as replacement for electrical car batteries.[13] Geothermal energy, although restricted in its accessibility, has the potential to supply colossal amounts of power, and the price for power generator is constantly decreasing.[14] Piezoelectric generators are another promising technology that convert mechanical stress into a useful electrical current using the intrinsic properties of some materials.[15] Potential large scale applications include harvesting the energy from vibrations caused by human activity and industry.

1.1.2 Thermoelectricity

1.1.2.1 Thermoelectric devices

The concept of thermoelectricity dates back to the early 1820's when Thomas Johann Seebeck, an Estonian physicist, discovered that some metals respond differently to an applied temperature difference.[16] He pointed out that an electrical potential appeared when a temperature difference was applied between two ends of a circuit made of dissimilar metals. This discovery marked the beginning of the field of thermoelectricity and of a new potential renewable source of electricity as well as heating and cooling devices. Thermoelectric power generation consists of converting heat into electricity using the intrinsic properties of thermoelectric materials. Thermoelectric devices are reliable and relatively easy to make, but their use is still limited by the efficiency and relatively high production cost of current thermoelectric materials.[5, 17] Typically, such materials have an efficiency below 10 % of energy conversion, limiting their application to very specific fields where high reliability is more important than production cost and efficiency. This includes applications such as electrical generators on NASA's deep space probes, gas pipelines or cooling devices on laboratory equipment. Despite the currently low efficiency, it is believed that thermoelectric devices have a future as a renewable energy source, harvesting waste-heat from fuel combustion, exothermic reactions and even directly from sunlight.[7, 18] A thermoelectric device, Figure 1.3, is composed

Figure 1.3 Picture of a thermoelectric module. (Taken at Crismat laboratories, Caen)

of multiple thermocouples, Figure 1.4, connected electrically in series and thermally in parallel. A thermocouple is composed of two legs, made of two different materials, *n*-type and *p*-type, with opposite electrical flow directions. The difference between *n*-type and *p*-type lies in the type of charge carriers moving away from the junction. If the dominant charge carriers in a material are negative (electrons), it is an *n*-type material, while if the absence of an electron (hole) is the dominant type of charge carriers, the material is *p*-type. In power generation mode, a temperature gradient is created between a heat source at the junction and a heat sink on the other side of the device. Because of the Seebeck effect, the presence of a temperature gradient induces a voltage gradient. As the *n*-type and *p*-type legs are connected in series, an electrical current flows through the junction from the *n*-type to the *p*-type leg, Figure 1.4. In cooling mode, the effect is reversed, a current is applied and a temperature gradient is generated, cooling the junction.

1.1.2.2 Thermoelectric performance

Thermoelectric material performance directly depends on the temperature gradient, ΔT, and on three parameters: the electrical conductivity, σ, thermal conductivity, κ, and the Seebeck

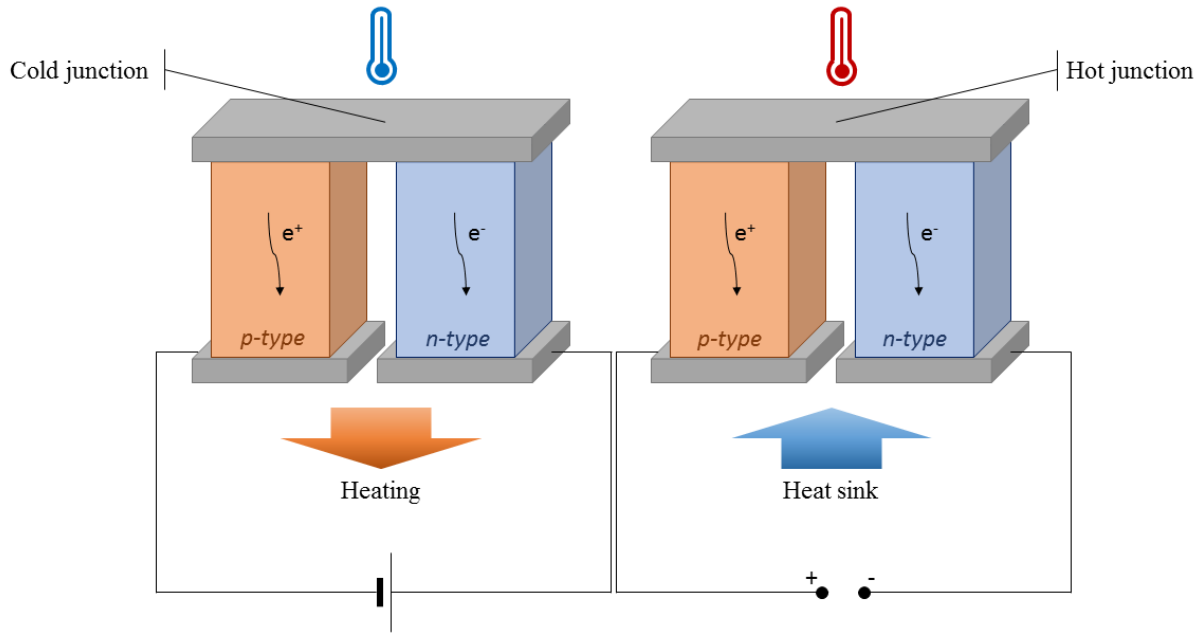

Figure 1.4 A typical thermocouple in cooling mode (left) and power generation mode (right).

coefficient, *S*. The figure of merit, ZT, is a dimensionless coefficient that quantifies the thermoelectric response of a material. It is defined according to Equation 1.1:

$$ZT = \frac{S^2\sigma}{\kappa}T \tag{1.1}$$

The maximum efficiency of a thermoelectric device in power generation mode, η_{max}, composed of *n*-type and *p*-type materials and ignoring contact resistance, is expressed in Equation 1.2:[19]

$$\eta_{max} = \frac{\Delta T}{T_{hot}} \frac{\sqrt{1 + ZT_{avg}} - 1}{\sqrt{1 + ZT_{avg}} + \frac{T_{cold}}{T_{hot}}} \tag{1.2}$$

where $\Delta T/T_{hot}$ is the Carnot efficiency and ZT_{avg} is the averaged ZT between the *n*-type and *p*-type materials. In power generation mode, the physical meaning of the efficiency is the quantity of electrical energy delivered to the circuit divided by the energy consumed from the heat source. Currently, the best commercially-viable thermoelectric materials have an efficiency of less than 10 % achieved when the figure of merit is around 1.[17, 19-21] Materials with ZT values higher than 1 have been reported, but in many cases these materials cannot be adapted to large scale production.[22, 23] Common issues include the scarcity, cost or toxicity of the elements of which the materials are composed (bismuth, lead, tellurium, selenium, etc.),[24-28] or complicated synthesis processes (metalorganic chemical vapour deposition, molecular beam epitaxy, etc.).[29-32] Impressive performance, with ZT > 1, has been reported for cheap copper-based materials but have either never been reproduced ($CuCrS_2$, ZT = 2 at 300 K)[33] or involve materials with substantial copper-ion mobility; "liquid-like" copper ions in $Cu_{1.97}S$ result in a ZT of *ca*. 1.7 at 1000 K.[34] However, ion mobility is highly destructive in thermoelectric devices (Section 1.4.2).[35]

A good thermoelectric material must combine three important characteristics: a high electrical conductivity, a high Seebeck coefficient and a low thermal conductivity. This combination will increase the figure of merit, according to Equation 1.1. However, these electrical and thermal parameters are interdependent and improving one is often done to the detriment of at least one of the other two. For instance, an increase in the electrical conductivity usually accompanies a

reduction in the absolute value of the Seebeck coefficient and an increase in the electronic component of the thermal conductivity. Therefore, tuning the thermoelectric properties often consists in finding the best trade-off between these properties, limiting the potential improvements in ZT (Section 1.5.1). Although, S, σ and κ_{tot} are the parameters that directly define ZT, they are themselves dependent on other fundamental parameters, particularly on the charge carrier concentration, n, and the charge carrier mobility, μ. The electrical conductivity, σ, is related to these parameters via the Equation 1.3:

$$\sigma = ne\mu \tag{1.3}$$

where e is the electronic charge (*ca*. 1.602×10^{-19} C). Logically, an increase in the charge carrier concentration corresponds to an increase in the electrical conductivity, if no substantial changes are made to carrier mobility. However, increasing n has a detrimental effect on the Seebeck coefficient. Equation 1.4 below, based on the free electron model[34, 35] and approximated for metals or degenerated semiconductors,[22] illustrates the dependence of the Seebeck coefficient, S, on the charge carrier concentration, n, and effective mass, m^*,

$$S = \frac{8\pi^2 k_B^2}{3eh^2} m^* T \left(\frac{\pi}{3n}\right)^{2/3} \tag{1.4}$$

where k_B is the Boltzmann constant, h, the Planck constant, e, the electronic charge and T, the temperature. Ideally, there should be only one type of charge carrier, electrons or holes, in order to optimise the Seebeck coefficient. In a mixed conduction mechanism, both holes and electrons thermally excited and the Seebeck coefficient corresponds to the conductivity weighted sum of electron, σ_n, and hole contributions, σ_p, Equation 1.5:[36]

$$S = \frac{\sigma_p S_p - |\sigma_n S_n|}{\sigma_p + \sigma_n} \tag{1.5}$$

where S_n and S_p are the partial Seebeck coefficient of electrons and holes, respectively. The overall Seebeck coefficient of a material, whose sign is determined by the type of dominant charge carrier, will be reduced by the presence of minority carriers of opposite sign. As the temperature increases, the concentration of thermally excited minority carriers increases, resulting in a peak in the temperature dependence of the overall Seebeck coefficient.[36, 37]

In 1959, Chasmar and Stratton[38] expressed ZT as being proportional to the Fermi energy and a factor, β, containing these parameters. The Chasmar and Stratton's factor's overall trend is estimated from Equation 1.6:

$$\beta \propto \frac{\mu}{\kappa_{latt}} \left(\frac{m_{eff}}{m}\right)^{3/2} T^{5/2} \tag{1.6}$$

where μ is the charge carrier mobility, m and m_{eff} are respectively the mass and effective mass of the density of states (DOS), T is the temperature and κ_{latt} is the lattice vibrational contribution to the thermal conductivity, κ. The dependence on the DOS of the Seebeck coefficient will be discussed again in Section 1.4.2. The thermal conductivity can be expressed as Equation 1.7:

$$\kappa = \kappa_{latt} + \kappa_{el} \tag{1.7}$$

where κ_{el} is the charge carrier contribution to the thermal conductivity. It is related to the electrical conductivity and can be estimated using the Wiedemann-Franz law, Equation 1.8:

$$\kappa_{el} = L\sigma T \tag{1.8}$$

where L is the Lorenz number, generally constant for metal and semi-metal behaviours, σ is the electrical conductivity and T is the temperature. Decreasing the lattice component to the thermal conductivity has been one of the best strategies to increase the figure of merit,[39] and the concept of "phonon glass-electron crystal" (PGEC) was introduced by Slack.[40] This proposes that the ideal thermoelectric material should have a minimum phonon transport, as in glasses, and a high electron mean free path like in a crystal.[40] Promising families of PGEC materials include superlattices, low-dimensional structures, lattices with a large amounts of atoms or presence of "rattlers" (Section 1.5).

Beside the aforementioned thermoelectric properties, the materials are subject to constraints relative to the stability, cost, toxicity, availability, and other mechanical requirements relative to the making of devices, such as tensile strength, hardness and density.

1.2 Structures and superstructures

The bonds between atoms can be ionic, covalent, metallic, hydrogen, or van der Waals'. A covalent bond can be polar if it has a significant ionic character. A pattern of atoms, that is

repeated along the three spatial directions to form a crystal, is a unit cell of the structure. The investigation of a material requires a good understanding of its structure, as the spatial arrangement and electronic configuration of atoms are responsible for the physical properties of the material. The term “superstructure” refers to an additional arrangement derived from a smaller crystal structure.

1.2.1 Low-dimensional structures

In a crystal structure, the anisotropy in the chemical bonding can reduce the dimensionality of the structure. A two-dimensional structure has strong interatomic bonds in only two directions, and weaker interactions, such as van der Waals’ or hydrogen bonds, in the third crystallographic direction. As a result, the crystal can have different properties depending on the orientation. Typically, because of the weaker interactions in one or two crystallographic directions, the crystals can also have specific morphologies such as flakes, ribbons, tubes, etc. The two-dimensional structure of TiS_2, studied in Chapters 3 and 4, has led to the formation of flake-like and flower-like crystallites, (Section 4.2), and a substantial anisotropy in the electrical and thermal properties of consolidated samples.

Another excellent example of low-dimensionality is the quasi-one-dimensional structure of TiS_3, Figure 1.5. The Ti-Ti distance along the *b*-axis, shorter than along the *a*- and *c*- axis, forms one-dimensional chains, while van der Waals’ gaps are formed between the two

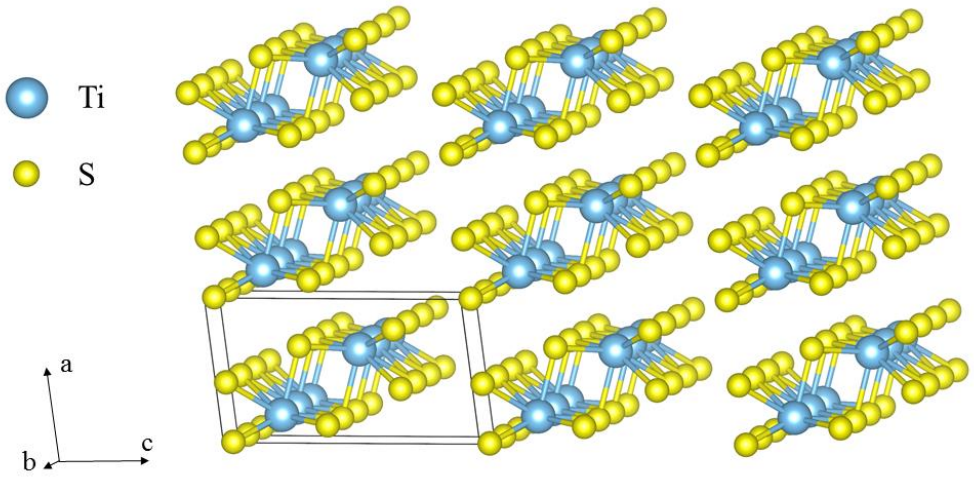

Figure 1.5 Quasi-one-dimensional structure of TiS_3 (space group $P2_1m$).

successive layers of sulphur along the *c*-axis, giving a strong two-dimensional character.[41-44] As a result of the low-dimensional structure of TiS_3, whiskers and ribbons can be obtained. During the synthesis of a large batch of TiS_2, some TiS_3 impurities were accidently produced, possibly because of the large sulphur pressure built up in the silica tube, and whiskers and ribbons were observed, Figure 1.6.

Materials with reduced dimensionality, in which a van der Waals' gap is present, are of particular interest because of the possibility to intercalate a wide range of guest species into these gaps. Layered structures of this type are extensively used as cathode materials in lithium ion batteries because of the high mobility of Li^+ in the van der Waals' gap.[45] The intercalation of a guest species in two-dimensional structures can lead to the formation of a vacancy-ordered superstructure.

1.2.2 Layered transition-metal dichalcogenides

There exist many materials having layered structures, including graphite, transition-metal phosphates, transition-metal oxy-halides and transition-metal dichalcogenides (TMDs). In these structures, which may serve as host for the intercalation of a guest species, layers of strongly bonded elements alternate with van der Waals' gaps. The structure of layered TMDs arises from two types of MX_2 (M = Transition metal, X = S, Se, Te) building blocks in a

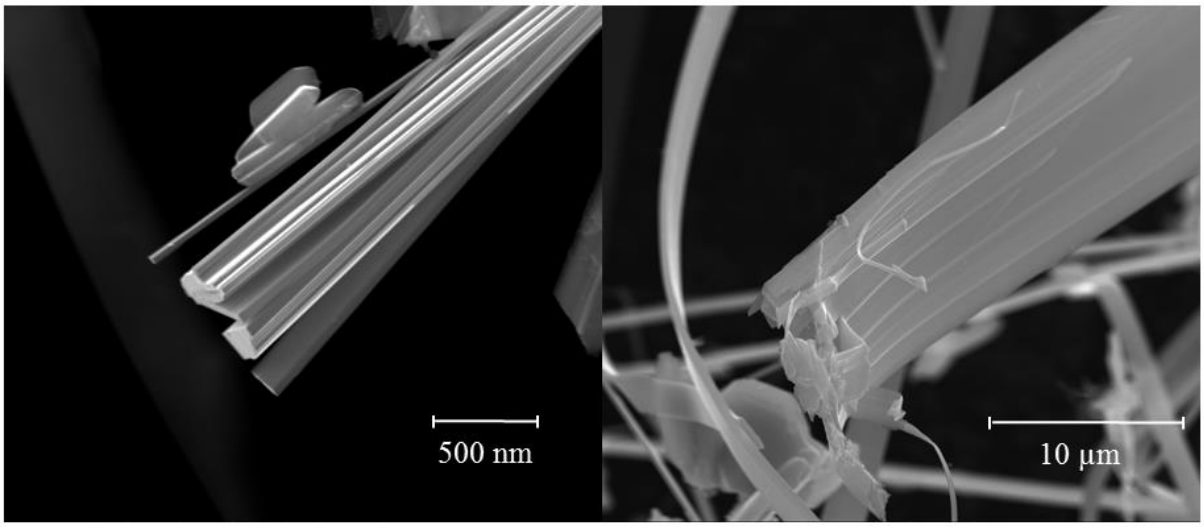

Figure 1.6 Scanning electron micrograph of TiS_3 whiskers and ribbons.

XMXXMX stacking sequence. The MX_2 slabs are formed by either edge-sharing octahedra or edge-sharing trigonal prisms, depending on the transition metal.[46] Transition-metal sulphides, MS_2, of group IV (M = Ti, Zr, Hf) crystallise in the CdI_2-type structure that arises from the stacking of MS_2 building blocks of edge-sharing MS_6 octahedra (Section 1.6.2).[47] The van der Waals' gap between consecutive layers can accommodate a guest species in octahedral (or tetrahedral) position up to a fully occupied distorted NiAs-type structure, Figure 1.7.

1.2.3 Superstructures

A superstructure is formed when an additional arrangement is superimposed on a crystal structure, thus forming a larger unit cell. For instance, the magnetic ordering of some atoms below a magnetic transition temperature can form an array with a larger unit cell compared to that of the nuclear structure. The formation of superstructures can also arise from a rearrangement of the atoms with temperature where the atom positions remain the same and the occupancy is changed. In many cases this rearrangement is allowed by the presence of vacancies and is energetically favoured over a statistical repartition of atoms over a vacancy array.[48] Bornite is a good example of a material with different superstructures that depends on the temperature. These are detailed in Section 1.6.1.2.

In a MS_2 system with a CdI_2-type structure, a series of superstructures can be obtained from the vacancy ordering in the van der Waals' gap.[49] In this case, the superstructure at room

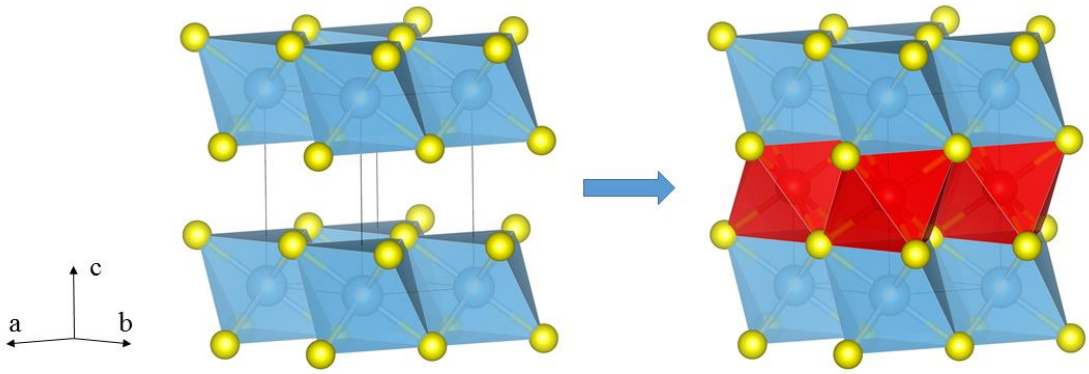

Figure 1.7 Filling of octahedral vacancies in an A_xMS_2-type structure, from CdI_2 on the left for x = 0 to NiAs on the right for x = 1.

temperature is a function of the level of intercalation. The intercalation and ordering of a guest species in the host MS_2 structure is made possible by the ready interlayer expansion and the electronic band structure of the host. The highly oxidised transition metal has empty low-lying electronic states that can accommodate charge transfer from the guest. Vacancy ordering can then be energetically favoured over a fully disordered guest/vacancy layer for some level of intercalation.[48] Figure 1.8 represents the ideal arrangement of vacancies and guest species in the van der Waals' gap of MS_2 at specific intercalation levels,[50] although in many cases the superstructures can exist over a range of compositions.

1.3 Magnetism

The presence of unpaired electrons on the valence shell of atoms, usually metal cations in an inorganic solid, generates a magnetic moment.[51] This moment arises from both spin and orbital motion of the electrons. Because the movement of charges induces a magnetic field, the atomic nuclei also possess a magnetic moment that arises from the spin of the protons and neutrons

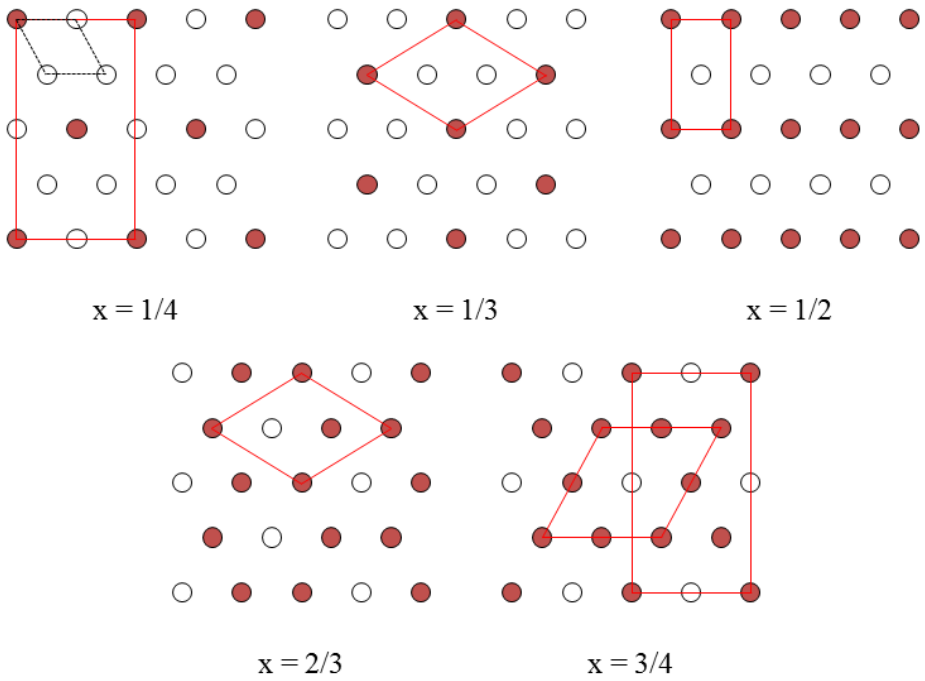

Figure 1.8 Possible ordering of a guest species, A, for partial occupation of octahedral sites in the van der Waals' gap in A_xMS_2 ($0 \leq x \leq 1$). The dashed black line shows the primitive hexagonal cell of the pristine (x = 0) phase, whilst the red lines outline the possible supercells.

and is substantially smaller than that of the electron. The magnetic response of a material is defined by its magnetic susceptibility, χ, a parameter that indicates the degree of magnetisation of a material in an applied magnetic field. The applications for magnetic materials are vast, ranging from magnetic compasses to microphones, guitar pickups, information storage, magnetic resonance imaging (MRI) or nuclear magnetic resonance (NMR).

1.3.1 Diamagnetism and paramagnetism

In vacuum, an induced field, *B*, is directly proportional to the applied magnetic field, *H*, and the vacuum permeability, μ_o, Equation 1.9:

$$B = \mu_o H \tag{1.9}$$

in the SI unit system where $\mu_o = 4\pi \times 10^{-7}$ J s^2 C^{-2} m^{-1}. In the more commonly used cgs unit system, the proportionality between the induced field and the applied field in vacuum is one, and $B = H$. When a substance is introduced in the field, the induced field within the substance is different from that in vacuum, Equation 1.10:

$$B = H + \Delta H \tag{1.10}$$

Diamagnetism is a property of all materials that defines the magnetic field induced in the opposite direction to an applied magnetic field, therefore ΔH is negative. Materials with no inherent magnetic dipoles are diamagnetic and have a small negative susceptibility. Perfect diamagnets are materials where no other form of magnetism is observed and external magnetic fields are repelled. In superconductors, the magnetic flux density is expelled completely from a material, this is called the Meissner effect.[52]

In contrast with diamagnetism, paramagnetic materials are attracted by external magnetic fields and an internal field is induced in the same direction as the applied field. The induced magnetisation in a paramagnetic substance is greater than that vacuum, thus ΔH (Equation 1.10) is positive. The magnetic susceptibility of an ideal paramagnet, with no interaction between neighbouring magnetic dipoles, follow the simple Curie law, Equation 1.11:

$$\chi = {}^{C}/_{T} \tag{1.11}$$

where C is the Curie constant. The effective moment, μ_{eff}, of a substance can then be determined using Equation 1.12:

$$\mu_{eff} = \sqrt{8C} \tag{1.12}$$

However, in many materials with magnetic dipoles a temperature may be reached where the energy of interactions between magnetic dipoles is comparable with thermal energy. As a result, the paramagnetic region of such materials does not obey the simple Curie law and a modification accounting for the spontaneous interaction between neighbouring spins is found in the Curie-Weiss law, Equation 1.13:

$$\chi = {}^{C}/_{(T-\theta)} \tag{1.13}$$

where θ is the Weiss constant. Information on the nature of the interaction between magnetic dipoles is contained in the Weiss constant, positive and negative values indicate ferromagnetic and antiferromagnetic interactions respectively (Section 1.3.2). Therefore, the inverse susceptibility, χ^{-1}, has a linear dependence on temperature with a slope of C^{-1} and a χ^{-1} vs T curve does not extrapolate to 0 K.

1.3.2 Cooperative magnetic phenomena

In paramagnetic materials where interactions between magnetic dipoles occur, ordered magnetic structures can form spontaneously below a transition temperature at which the thermal energy is lower than that of the interatomic exchange interactions. Depending on the type of arrangements this transition temperature is called the Curie point, T_C, for ferro- and ferrimagnetic materials or the Néel point, T_N, for antiferromagnetic materials.

In a solid, the magnetic moments on individual atoms or ions can align in parallel, resulting in a crystal with an overall magnetic moment, in which case the material is ferromagnetic, Figure 1.9(a). Conversely, a material exhibits antiferromagnetic behaviour when the atomic moments align antiparallel, Figure 1.9(b), and the overall magnetic moment of the materials is zero. Ferrimagnetism is a form of antiferromagnetism where a net magnetic moment is observed either because the number of magnetic moments in the two orientations is unequal, Figure

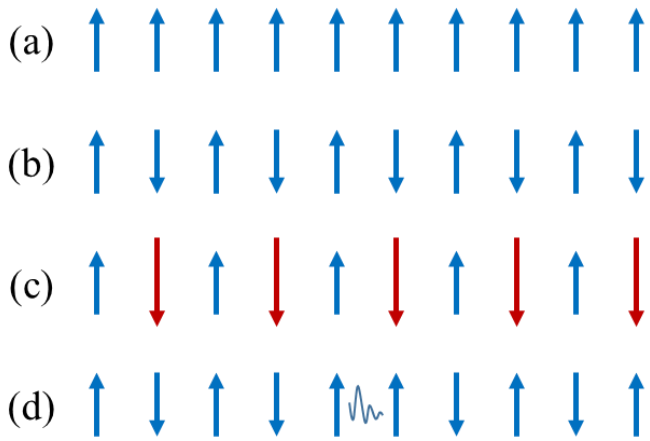

Figure 1.9 Schematic cooperative magnetic phenomena in a unidimensional crystal in (a) ferromagnetic, (b) antiferromagnetic and (c) ferrimagnetic ordering. (d) Example of a frustrated antiferromagnetic array.

1.9(c), or because the magnitude of the opposing moments is different. Other cooperative magnetic phenomena are found in frustrated systems such as spin-glasses, canted systems and incommensurate magnetic systems such as helimagnetic ordering. Figure 1.9(d) shows an example of a frustrated system where the antiferromagnetic ordering is disrupted by a ferromagnetic coupling. This type of behaviour can be found in spin glasses where the dipole exchange interactions are stronger than thermal motion but no long range ordering is observed.

1.3.3 Muons in magnetism

Muons are spin-½ particles identified as the main component of cosmic rays by S. Neddermeyer and C. Anderson in 1936. Positive muons, as produced at ISIS, are short-lived particles (average lifetime of 2.19 μs in vacuum) that interact with magnetic fields in condensed matter to form the basis of muon spectroscopy. They are particularly well adapted to study weak magnetic fields.[53, 54] Muons have a mass, a magnetic moment and a gyromagnetic ratio

Table 1.1 Some fundamental properties of electrons, muons and protons.

Particle	Mass / m_e	Magnetic moment / μ_P	Gyromagnetic ratio / kHz G^{-1}	Lifetime / μs
Electron	1	657	2800	∞
Muon	207	3.18	13.5	2.19
Proton	1836	1	4.26	∞

between those of electrons and protons, Table 1.1. Although muons are found in nature, hitting the earth every minute, they need to be produced in spin-polarised beams to be used in condensed matter physics. Production of a muon beam usually involves firing a high energy proton beam into a graphite target, producing a pion, a proton and a neutron from the collision of two protons. The pion then decays into a muon and a muon-neutrino in a simple two-body decay that, because of the conservation of momentum, produces a 100 % spin-polarised muon beam. The muons are then implanted in the sample under investigation. They decay, emitting a positron preferentially in the direction parallel to its spin, Figure 1.10. Before the muon dies and emits a positron, it precesses with an angular frequency directly proportional to the magnetic field it experiences. In the presence of a magnetic field, *B*, the muon will precess about this field with the Larmor frequency, ω_μ, Equation 1.14:

$$\omega_\mu = \gamma_\mu B \tag{1.14}$$

where γ_μ is the gyromagnetic ratio of the muon. Therefore, the angular dependence of the emitted positron is in turn dependent on the internal field experienced by the muon. Because the incoming muon beam is 100 % spin-polarised, information on the material's internal field

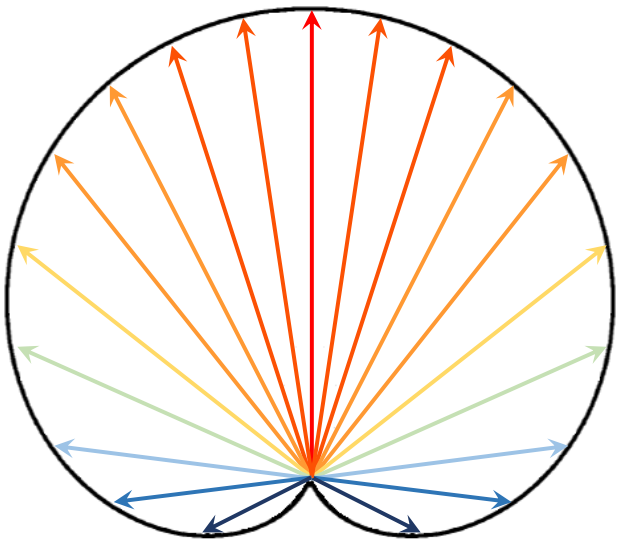

Figure 1.10 The angular distribution of the most energetically emitted positrons where the central red arrow is parallel to and in the same direction than to the muon spin.

can be obtained by measuring the position of the emitted positron. This constitutes the basis of muon spectroscopy, outlined in Section 2.6.

1.4 Structure-property relationships

In a condensed phase, the electronic structure of the material is directly related to the crystal structure and the chemical bonding within the solid. It is therefore necessary to describe this electronic structure in order to understand the physical properties of a material and hence to establish a suitable strategy to improve the thermoelectric performance. Determining the electronic structure of a material is within the scope of quantum physics; however, the band theory and the density-of-states, DOS, are frequently used in solid-state chemistry. They are powerful tools to describe the electrical behaviour, which may be metallic (when the electrical conductivity decreases with temperature) or semiconducting (when the electrical conductivity increases with temperature), and how electronic doping affects the thermoelectric properties of a material.[55]

1.4.1 Band theory and density-of-states

Band theory relies on the linear combination of atomic orbitals approach, LCAO.[56] In a crystal, the combination of orbital energies of an infinite chain of atoms forms a large number of molecular orbitals and, ultimately, the range of energies covered by molecular orbitals increases up to a point where it can be thought of as a continuous band, Figure 1.11. This band

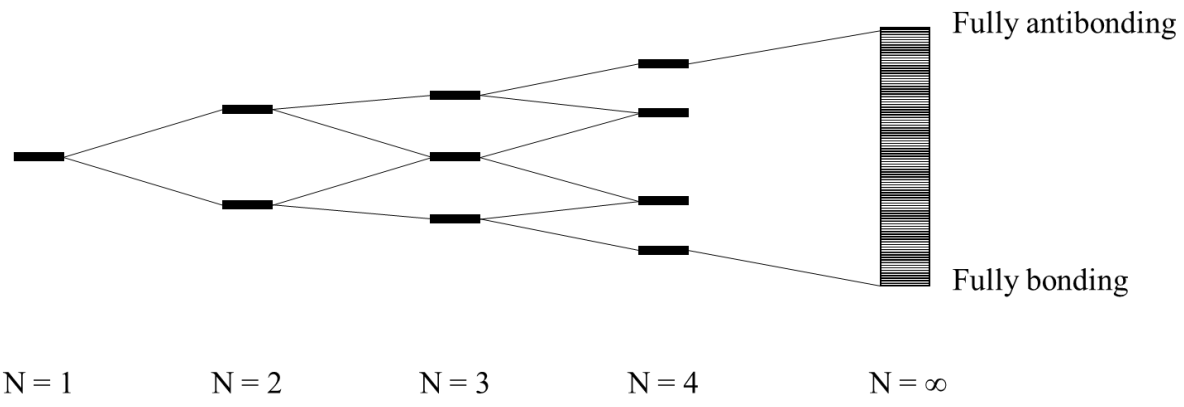

Figure 1.11 Formation of a band from the linear combination of N atomic orbitals in a hypothetical one-dimensional line of atoms.

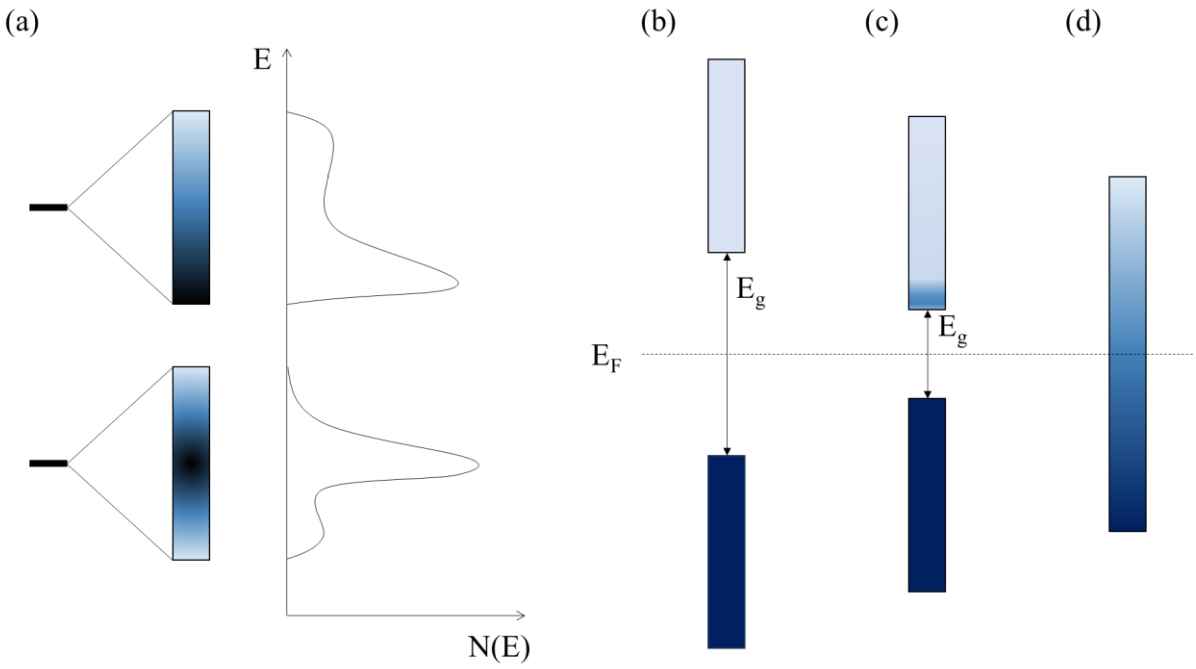

Figure 1.12 (a) Schematic of two bands and the corresponding density-of-states; regions with a high concentration of molecular orbitals are represented as a darker areas and correspond to a peak in the DOS. Valence and conduction bands in (b) a semiconductor with insulating electrical behaviour, (c) a semiconductor and (d) a metal. The Fermi level, E_F, and the band gap, are shown.

has a finite width that can be quantified for a chain and the energy separation between individual levels can be determined using the Hückel method.[56] The density-of-states, DOS, corresponds to the numbers of molecular orbitals available over a small energy range (E + δe), Figure 1.12(a). The conduction mechanism in a solid depends on the filling of these bands and the eventual energy gaps between consecutive bands. The presence of such gap, termed the band gap, E_g, between the filled valence band and the conduction band leads to a semiconducting electrical behaviour, where only thermally, or optically, excited electrons can be promoted to the conduction band, Figure 1.12(c). Therefore, a semiconductor is insulating at 0 K in the absence of light and the highest occupied orbital at this temperature is called the Fermi level, E_F. Similarly, an insulating material is a semiconductor with a band gap that is too large for a significant number of electrons to be promoted, Figure 1.12(b). In a metal, there is no band gap and a substantial amount of electrons can move freely within the electronic

structure and are thought of as fully delocalised, Figure 1.12(d). The consequence is a high electrical conductivity which, unlike semiconductors, decreases with temperature. Interactions between delocalised electrons and heat carrying phonons are responsible for the residual resistivity (this is not the case for superconductors).

1.4.2 Conduction mechanisms in thermoelectric materials

Electrons, and holes, are not the only charge carriers responsible for conduction mechanisms in solids. In ionic conductors, ions with substantial mobility such as small monovalent cations (*e.g.* Li^+ or Cu^+) can move within the crystal structure, via van der Waals' gaps or suitable neighbouring vacancies.[57] While this feature is highly desirable in some materials for applications such as batteries,[45] it has a particularly destructive impact on thermoelectric devices as mobile ions accumulate on one end of the thermoelectric leg.[35]

The key thermoelectric parameters, Seebeck coefficient, electrical conductivity and thermal conductivity, are closely related to the electronic structure of a material. All three depend directly on the charge carrier concentration (Section 1.1.2.2). Following band theory, the charge carrier concentration can be optimised by adjusting the Fermi level of a semiconductor.

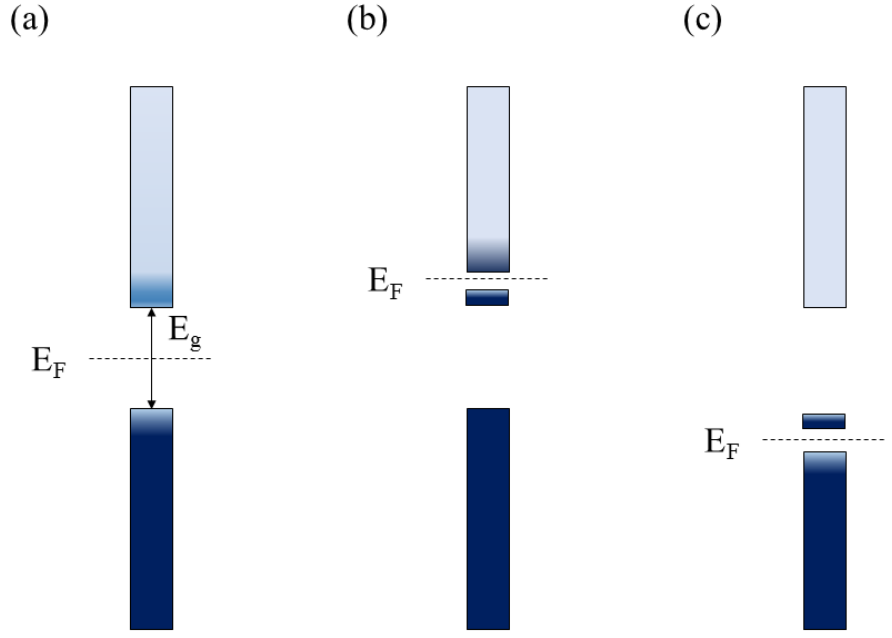

Figure 1.13 Valence and conduction bands of (a) an intrinsic semiconductor, (b) an *n*-type semiconductor and (c) a *p*-type semiconductor.

In an intrinsic semiconductor (i.e. a pure semiconductor), the Fermi level lies between the valence band and the conduction band; the electrical conduction is a result of thermally (or optically) promoted electrons, leaving an equal concentration of holes in the valence band, Figure 1.13(a). This mixed system gives a high electrical conductivity but the Seebeck coefficient is reduced (Equation 1.5). Extrinsic semiconductors are doped semiconductors where the number of electrons in the electronic structure is changed by chemical methods. When electrons are added to the materials, via substitution or intercalation, the Fermi level is increased and lies within the conduction band, Figure 1.13(b). In this case, donor levels are created below the conduction band and a high concentration of electrons can be promoted from these new levels to the conduction band and the material is *n*-type. Conversely, adding a dopant with the ability to capture electrons lowers the Fermi level that lies within the valence band. The main charge carriers are holes in the valence band from the promotion of electrons into acceptor levels, the material is then described as being *p*-type, Figure 1.13(c).

While the sign of the Seebeck coefficient depends on the identity of the dominant charge carriers, its absolute value depends on the electronic structure around the Fermi level. By extrapolating from the Boltzmann transport theory, Mott and Jones established the following relationship, Equation 1.15:

$$S = \left(\frac{\pi^2}{3}\right)\left(\frac{k^2 T}{e}\right)\left(\frac{dln\sigma(E)}{dE}\right)_{E=E_F} \tag{1.15}$$

where $\sigma(E)$ is the electrical conductivity as a function of energy, k is the Boltzmann constant, T is the temperature, e is the electronic charge and E_F is the Fermi level. The Seebeck coefficient depends on $d \ln \sigma(E)/d(E)$, where $\sigma(E)$ is proportional to the density of states at a given energy. Therefore, the magnitude of the Seebeck coefficient is proportional to the slope of the density of states at the Fermi level, Figure 1.14. Overall, it is desirable for a good thermoelectric material to have a wide band gap with large band extrema degeneracy.

1.4.3 Phonon scattering

The thermal conductivity of a thermoelectric material is a key parameter that describes its ability to conduct heat and needs to be kept as low as possible. Unfortunately, part of the

thermal conductivity is caused by the movement of the charge carriers (Section 1.1.2.2) and cannot be reduced without altering the material's ability to conduct electricity. The second contribution to the thermal conductivity arises from vibrations of the lattice and is conveyed by phonons (a quantum of lattice vibration). A material with a low lattice thermal conductivity has a high scattering rate of phonons, impeding the lattice's ability to transfer heat.

Different types of phonon scattering contribute to lower the lattice thermal conductivity.[39] Disorder or distortion in the unit cell introduces point defects such as vacancies, substituted or interstitial atoms. The differences in mass, size and interatomic forces have been found to be efficient at scattering phonons.[58] Materials with cage-like structures such as skutterudites, can accommodate an atom or molecule in an oversized vacancy.[59] The "guest" species is weakly bound to the structure and the phonon's energy is diffused by the localised rattling. Rattlers behave as Einstein oscillators with different resonance frequencies for different atoms.[60, 61] Consequently, a broader range of vibrational frequencies are available in multiple-filled caged structures, such as skutterudites, maximising the phonon resonant scattering. Phonon scattering also occurs at the interfaces within the lattice, such as van der Waals' gaps in layered structures, or at the grain boundaries between crystallites of the same or different phase. In a

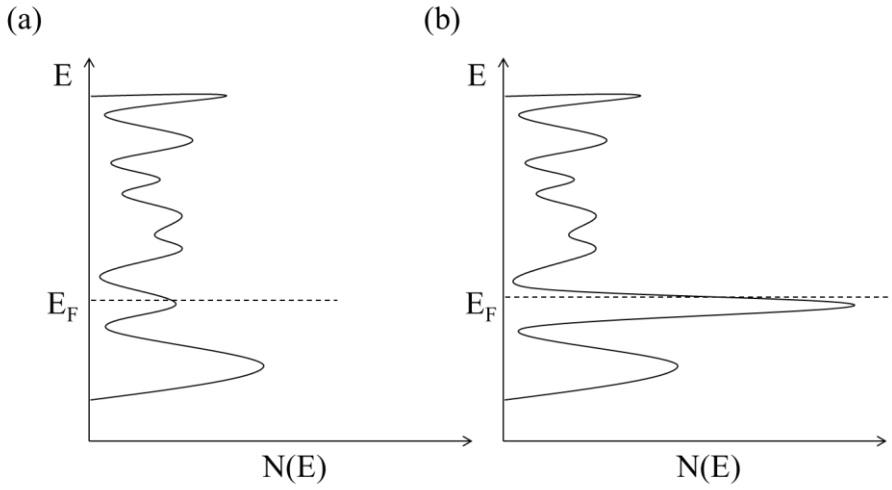

Figure 1.14 Density of states of hypothetical materials with small (a) and large (b) $d \ln \sigma(E)/d(E)$ slope.

polycrystalline sample, the number of grain boundaries increases as the particle size get smaller, enhancing the interface scattering rate.

Finally, the last two mechanisms are phonon-electron and phonon-phonon scattering. While the contribution to reductions in the thermal conductivity of phonon-electron interactions is negligible,[62] phonon-phonon is the dominant scattering mechanism for reducing the thermal conductivity of low defect concentration crystals at high temperature. This type of scattering is an Umklapp scattering process where the momentum of the phonon is not conserved.

1.5 Current advances and strategies

From the structure-property relationship, detailed in Section 1.4, it is possible to identify the desirable features of a material and formulate different strategies to increase the power factor and/or decrease the thermal conductivity. These strategies have led to tremendous improvements in the figure of merit of thermoelectric materials. Some of the most successful strategies and the state-of-the-art thermoelectrics and promising families of materials that emerge are presented here.

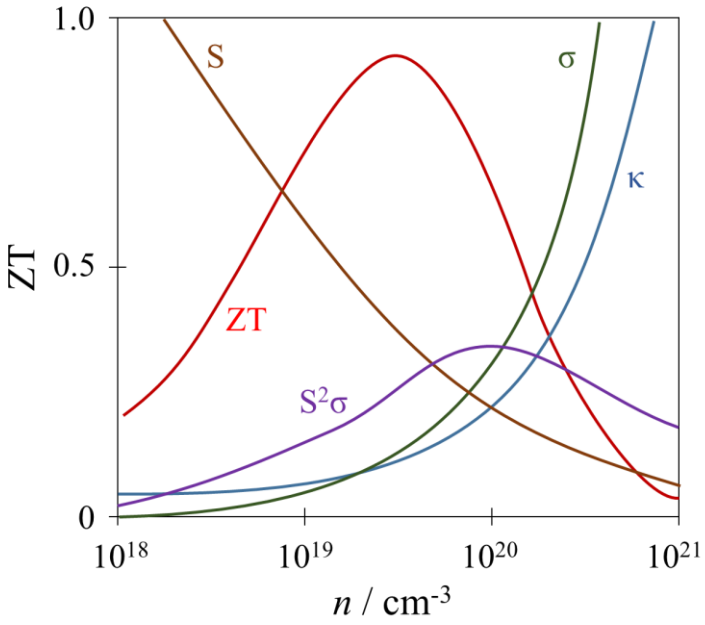

Figure 1.15 Interdependence of the key thermoelectric parameters, Seebeck coefficient, S, electrical conductivity, σ, thermal conductivity, κ, power factor, $S^2\sigma$, and the figure of merit, ZT, as a function of the charge carrier concentration, n. Adapted from Snyder and Toberer.[22]

1.5.1 Improving ZT

Improving the thermoelectric performance of a TE device is achieved, in part, by increasing the ZT value of both *n*- and *p*-type materials. As highlighted in Section 1.1.2.2, there is a conflict between Seebeck coefficient, electrical conductivity, and electronic component to the thermal conductivity. This means that improving the figure of merit of a material solely by varying the charge carrier concentration is limited by the interdependency of these parameters. It is possible to determine the ideal charge carrier concentration, Figure 1.15. The charge carrier contribution to the figure of merit is maximised when the charge carrier concentration, *n*, lies in the range $10^{19} \leq n / \text{cm}^{-3} \leq 10^{20}$. Ideally, one type of charge carrier should dominate the conduction mechanism (Section 1.4.2). The most promising thermoelectrics are therefore heavily doped semiconductors with a large band gap. The Seebeck coefficient also depends on the shape of the density of states around the Fermi level, with sharp changes in the DOS near E_F expected to lead to high Seebeck coefficient.[19] Reducing the dimensionality has a dramatic effect on the form of the density of states, Figure 1.16, with sharper features appearing for low-dimensional materials.[21] Such materials are expected to have a higher absolute value of the Seebeck coefficient, providing the Fermi level can be adjusted to a region with a large $d \ln \sigma(E)/d(E)$, while no substantial changes are made to the electrical conductivity.

The effect of low dimensionality on the Seebeck coefficient has been exploited to the nanoscale level where the increased interface scattering of phonons, both within the structure and because of the higher number of grain boundaries, also contributes to decrease the thermal conductivity. Under certain conditions, such nanomaterials may also exhibit energy filtering. This mechanism contributes to increase the Seebeck coefficient by filtering out the charge carriers with low kinetic energies while high-energy electrons are allowed to pass through. This is made possible by the energy barrier formed at grain boundaries between nanoparticles.[63] A combination of low-dimensionality and quantum size effects has led to dramatic improvements in the field of thermoelectrics. For instance, bulk silicon is a very poor thermoelectric material with $ZT \approx 10^{-2}$; however, one-dimensional silicon nanowires have a ZT value 100 times higher, with $ZT \approx 1$ at 200 K and $ZT \approx 0.6$ at room temperature.[64, 65]

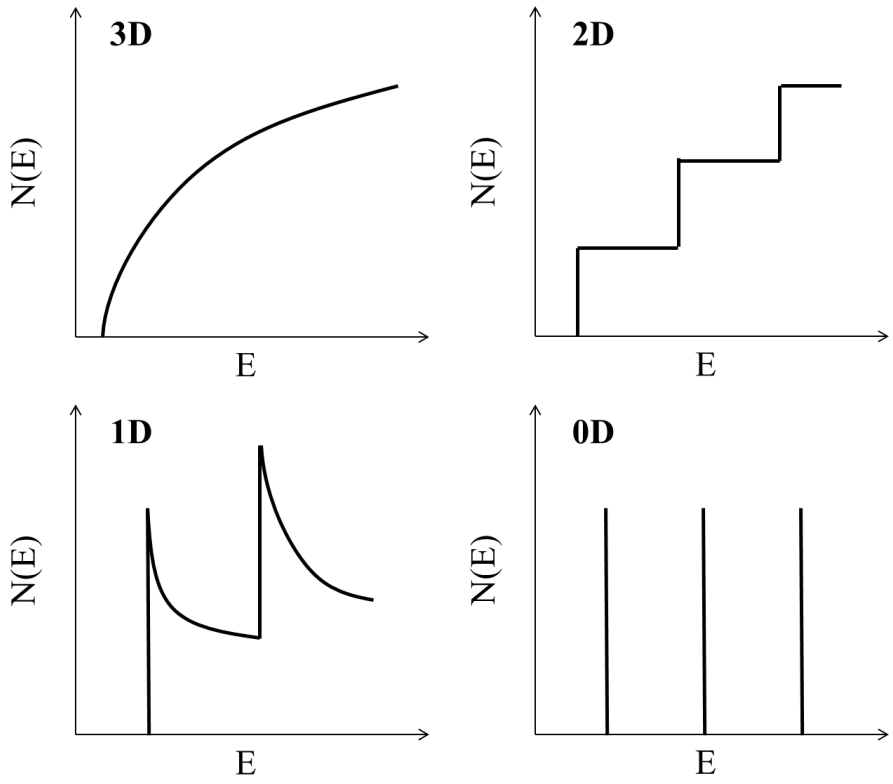

Figure 1.16 Schematic of the density-of-states with decreasing dimensionality: bulk 3D crystalline semiconductor, 2D quantum well, 1D quantum wire and 0D quantum dot. Adapted from Dresselhaus *et al.*[21]

To summarise, many strategies exist either in order to increase the power factor, by increasing the electrical conductivity or increasing the Seebeck coefficient, or by decreasing the lattice thermal conductivity. Forming solid solutions remains a widely used strategy as it involves electronic doping as well as inducing point defects in the structure that increases phonon scattering. Many thermoelectric materials take advantage of low-dimensionality, like Bi_2Te_3, Sb_2Te_3 or TiS_2 layered structures, or rattling mechanisms in cage-like structures, e.g. skutterudites or clathrates, in order to lower the thermal conductivity.

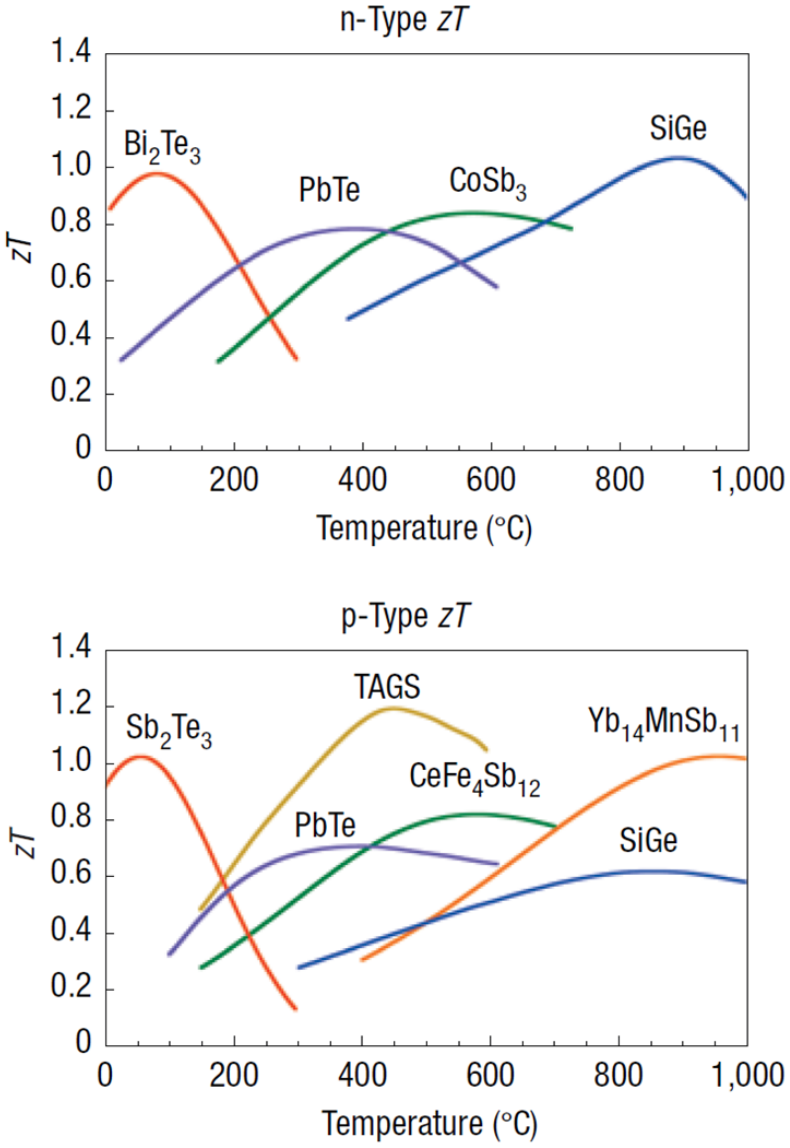

Figure 1.17 Temperature dependence of the figure of merit of commercial thermoelectrics. Compositions are approximate as most materials are doped derivatives. TAGS = $(AgSbTe_2)_{0.15}(GeTe)_{0.85}$.[22]

1.5.2 State-of-the-art thermoelectric materials

There is a wide range of thermoelectric materials that is currently being commercialised and an even wider range of potential thermoelectrics. Different applications will require different operating temperatures and therefore different materials. However, there are some families of materials that stand out. At relatively low temperature, below 200 °C, the market is still

dominated by derivatives of bismuth and antimony tellurides, Figure 1.17, while intermediate and high-temperature materials, above 700°C, are dominated by lead tellurides and silicon germanium alloys, respectively.[22] Bismuth and lead tellurides have been extensively studied and nanostructuring of these materials began after the work of Hicks and Dresselhaus,[66, 67] leading to a new generation of thermoelectrics with high ZT, Figure 1.18, reaching values above 2 for hierarchical PbTe.[68] The development of thin-film superlattice thermoelectrics and their ability to scatter phonons without altering the electron conduction mechanism has led to a ZT above 2.5 at *ca*. 300 K for Bi_2Te_3/Sb_2Te_3 superlattices.[32] However, hierarchical nanostructures or thin-film superlattices are limited to niche applications and the use of heavy and toxic elements such as tellurium or lead is not desirable for large scale production.

Beside the bismuth or lead selenides and tellurides, a number of other families have shown promising performance with ZT reaching values above unity. These include skutterudites, clathrates, silicides, Zintl phases and half-Heusler alloys.[69]

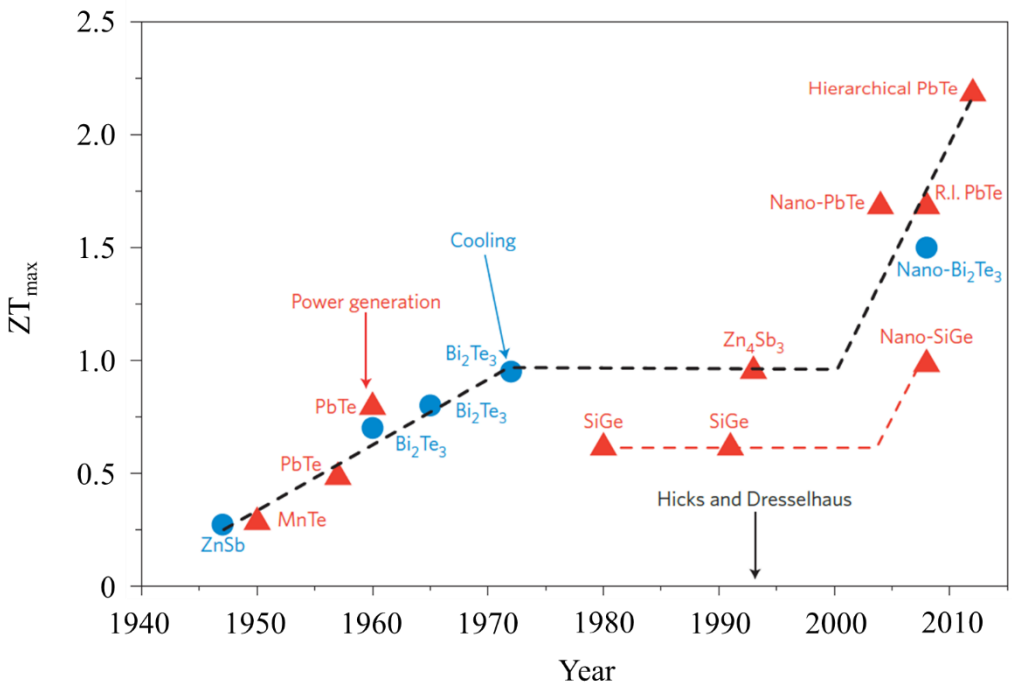

Figure 1.18 Evolution of the maximum ZT with time showing the impact of nanostructuring on some typical thermoelectric materials with approximate compositions.[67]

Materials that are easily prepared and rely on earth-abundant, environmentally benign, elements are more desirable for large-scale thermoelectric power generation. Unfortunately, their efficiency is still much lower than current selenides or tellurides. For the past twenty years, oxides have been actively studied as potential thermoelectric materials, in particular layered cobalt oxides, perovskite-type oxides ($SrTiO_3$) and doped zinc oxides (ZnO).[70, 71] However, because of the ionic character of the atomic bonding in oxides and their high electrical resistivity, the best ZT values are observed at high temperature and remain below unity.[71] Consequently, thermoelectric sulphides appear as an alternative between oxides and toxic selenides and tellurides.

1.5.3 Thermoelectric sulphides

Bismuth sulphide, Bi_2S_3, is the sulphide analogue of the commercial Bi_2Te_3. However, Bi_2S_3 has a one-dimensional structure formed by edge-sharing BiS_5 square based pyramids and corner-sharing BiS_3 pyramids, Figure 1.19(a), as opposed to the layered, two-dimensional structure of Bi_2Te_3, Figure 1.19(b). Bismuth sulphide was identified as a potential thermoelectric material because of its high absolute value of Seebeck coefficient, $S \approx -325$ μV K^{-1} at room temperature, and a thermal conductivity 25 % lower than that of Bi_2Te_3 at around 300 K. [72, 73] Optimising the sulphur content, combined with hot-forging, has been found to be a successful strategy in order to reduce the electrical resistivity of bismuth sulphide, principal

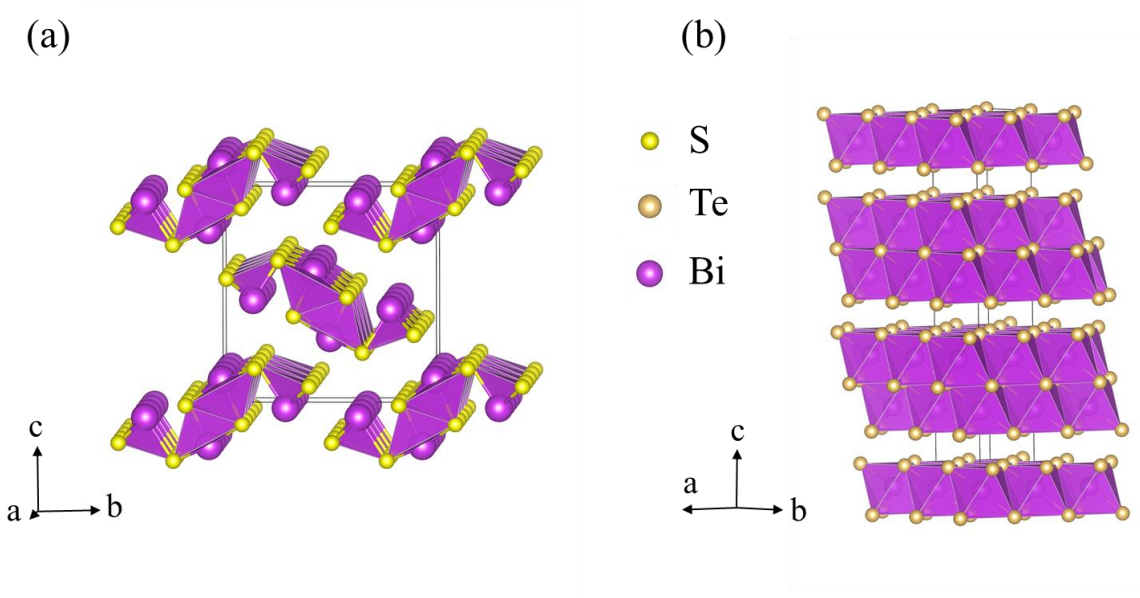

Figure 1.19 Structure of (a) bismuth sulphide, Bi_2S_3, and (b) bismuth telluride, Bi_2Te_3.

issue to its competitiveness. The electrical resistivity was reduced by two orders of magnitude, from 10^{-2} Ω m in Bi_2S_3 to 10^{-4} Ω m in $Bi_2S_{2.90}$, increasing ZT from 0.05 to 0.11 at 523 K.[74] The best reported thermoelectric performance for *n*-type bulk Bi_2S_3 was reported for mechanically-alloyed polycrystalline samples consolidated by SPS, reaching a ZT value of 0.22 at 573 K.[75] Copper substitution on the bismuth site was carried out on mechanically-alloyed samples consolidated by SPS, causing reduction in the thermal conductivity and electrical resistivity, subsequently improving ZT that reaches 0.34 at 573 K.[76] Dramatic improvements were obtained by doping Bi_2S_3 with 0.5 mol% $BiCl_3$, increasing the power factor by one order of magnitude and reaching a ZT value around 0.6 at 760 K.[77]

Similarly, lead sulphide, PbS, was studied as an alternative to its telluride analogue PbTe. Both having a NaCl-type cubic structure with Pb and S/Te occupying the cation and anion sites respectively, Figure 1.20. Bulk, *n*-type, PbS samples, mechanically milled down to 53 μm[3] and consolidated by SPS, reached a ZT value of 0.31 at 723 K.[78, 79] Sodium-doped PbS samples, prepared in the same conditions, are *p*-type semiconductors that reached a maximum ZT value of 0.54 at 723 K for $Pb_{0.975}Na_{0.025}S$. This performance is increased further by adding 3.0 % of SrS or CaS second phase, reaching a ZT value of 0.73 and 0.72, respectively at 723 K and 1.22 and 1.12, respectively at 923 K. This performance is attributed to the phonon scattering induced by the point defects in the solid solution and the nanostructuring with a second phase.[78] Slightly better results were obtained in a similar study using ZnS and CdS nanophase precipitates, with ZT reaching 1.3 at 923 K for $Pb_{0.975}Na_{0.025}S$ with 3.0 % CdS.[80]

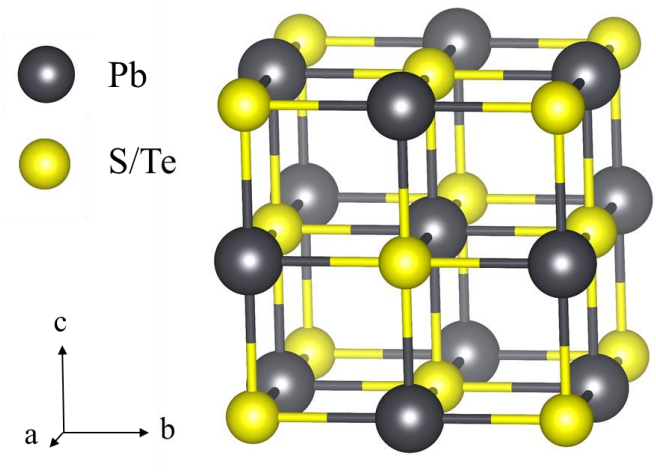

Figure 1.20 Structure of PbCh, Ch = S, Te.

Ternary molybdenum sulphides $M_xMo_6S_8$ ($1 \leq x \leq 4$), known as Chevrel phases, have been studied as potential, high temperature, thermoelectric materials.[81] Their particular structure allows for a wide range of elements, *M*, to be intercalated within a three-dimensional array of Mo_6S_8 building blocks that forms channels of vacancies, Figure 1.21(b).[82] The Mo_6S_8 cluster is composed of a Mo_6 octahedron with each of the 8 faces capped by a sulphur atom, forming a quasi-regular cubic S_8 cage with a Mo atom at the centre of each face, Figure 1.21(a). The structure is completed by another S_8 cubic cage containing the Mo_6S_8 cluster. The thermoelectric properties of MMo_6S_8 (*M* = Fe, Ni, Ag, Zn, Sn, Pb, Cu) were measured on cold-pressed and sintered samples prepared by solid-state reaction. All samples contained some level of MoS_2 impurities and the best ZT was obtained for *p*-type $SnMo_6S_8$ with a ZT value of *ca*. 0.08 at 1073 K.[83] More recently, thermoelectric properties of $M_xMo_6S_8$ (*M* = Cr, Mn, Fe, Ni and x = 1.3, 2.0) prepared by solid-state reaction and consolidated by SPS have been reported. The highest figure of merit, ZT = 0.17 at 973 K, was obtained for *p*-type $Cr_{1.3}Mo_6S_8$.[84] The best performance to date for a sulphide Chevrel phase was obtained for Cu_4MoS_8, with a ZT value reaching a maximum of 0.4 at 950 K.[85]

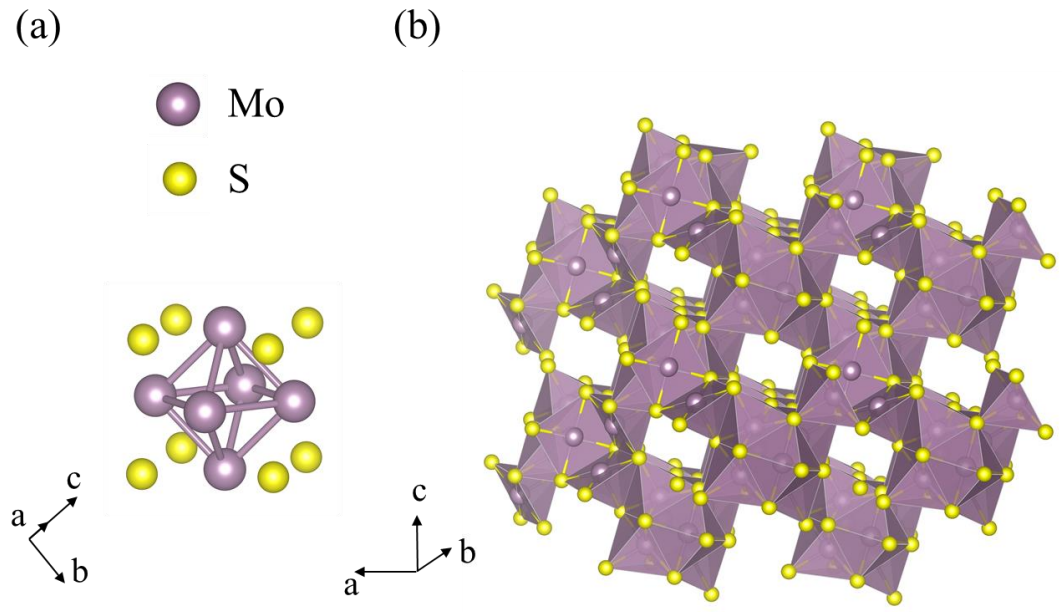

Figure 1.21 (a) A single M_6S_4 cluster. (b) The structure of $M_xMo_6S_8$ ($1 \leq x \leq 4$) Chevrel phase, showing the three-dimensional arrangement of M_6S_8 clusters. The intercalated elements *M* have been omitted for clarity.

Binary rare-earth sulphides, LnS_x ($1.33 \leq x \leq 1.5$),[86, 87] and ternary rare-earth sulphides, $LnGd_{1+x}S_3$ (*Ln* = Nd, La and Sm) [88, 89] have been found to be good high-temperature thermoelectric materials. They crystallise in the γ-phase, a cubic defect Th_3P_4-type structure. Because of a very low lattice thermal conductivity, ZT values of 0.64 and 0.75 at 1273 K were determined respectively for *n*-type $LaS_{1.48}$,[86] and $LaS_{1.42}$ prepared by pressure-assisted reaction sintering.[87] Ternary sulphides, prepared by CS_2 sulphurisation and consolidated by SPS, gave high ZT values of 0.3, 0.4 and 0.51 at 953 K for $SmGd_{1.02}S_3$, $LaGd_{1.02}S_3$ and $NdGd_{1.02}S_3$ respectively.[88, 89]

Copper-containing sulphides are ones of the current most promising cost-efficient materials because of the low cost of copper (5.95 \$ kg^{-1}) and sulphur (0.1 \$ kg^{-1})[90] and the good performance achieved for binary and ternary copper sulphides. Chalcopyrite, $CuFeS_2$, is a *n*-type semiconductor with a band gap of 0.53 eV,[91] that crystallises in the tetragonal system where CuS_4 and FeS_4 tetrahedra form a double-sphalerite structure, Figure 1.22.[92] Carrier doping from the substitution of Cu by Fe and Zn has simultaneously increased the power factor and decreased the thermal conductivity of bulk chalcopyrite prepared by solid-state reaction, rising the figure of merit by an order of magnitude up to ZT = 0.07 at 400 K for $Cu_{0.97}Zn_{0.03}S_2$.[93, 94] A maximum ZT value of 0.22 at 675 K was reported for cobalt-substituted bulk chalcopyrite, $Cu_{0.96}Co_{0.04}FeS_2$, prepared in similar conditions.[95] Mechanically alloyed sulphur-deficient

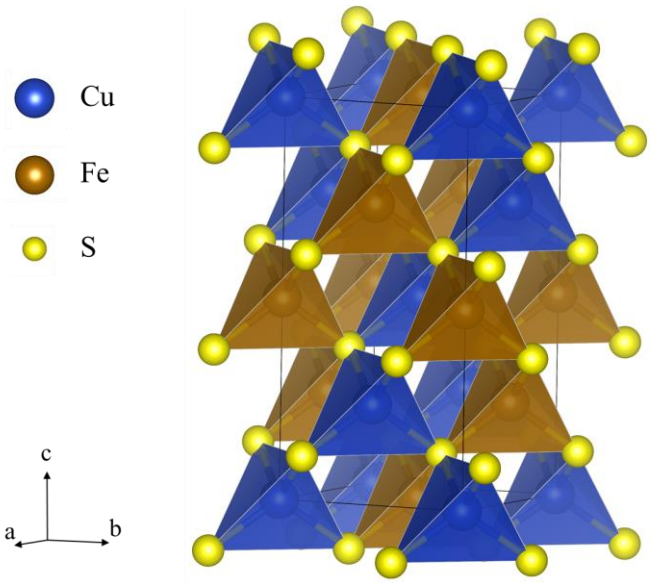

Figure 1.22 Structure of chalcopyrite, $CuFeS_2$.

chalcopyrite, consolidated by SPS, reached a similar ZT value of 0.21 but at the lower temperature of 500 K. Such an increase in ZT over bulk chalcopyrite is attributed to a combination of increased charge carrier concentration and increased interface phonon scattering.[96] *p*-type chalcopyrite nanocrystals were produced via a solution route and a maximum ZT value of 0.264 was measured at 500 K, attributed to the energy filtering at the grain-grain interfaces, considerably increasing the Seebeck coefficient up to 816.3 μV K^{-1} at 500 K and decreasing the thermal conductivity by an order of magnitude over the whole temperature range investigated ($300 \leq T / K \leq 500$).[97] Other promising ternary copper sulphides include Cu_3SbS_4, that reached ZT = 0.095 at 323 K when 3 % of the Cu site was substituted for Ag and 6 % of the Sb site was substituted for Ge,[98] and bulk shandite materials of composition $Co_3Sn_{2-x}In_xS_2$ ($0 \leq x \leq 2$), that reached a ZT of 0.32 at 673 K for x = 0.4.[99, 100]

Tetrahedrite and bornite minerals are extremely promising as a result of their availability as natural minerals and their exceptional thermoelectric performance. Structural information on these two families can be found in Section 1.6.1 and the thermoelectric properties of tetrahedrite and bornite derivatives are reviewed in Chapter 5 and investigated further as part of the present work. Similarly, structural information on titanium disulphide can be found in Section 1.6.2 and the current progress on the thermoelectric performance of titanium disulphide derivatives is summarised in Chapter 3.

The highest reported ZT for cost-efficient earth-abundant materials have been attributed to binary copper sulphide phases $Cu_{2-x}S$, that have been investigated for more than 190 years.[35] Recent studies, have reported a ZT value of *ca*. 0.8 at 650 K and 1.7 at 1000 K for bulk *p*-type $Cu_{1.97}S$.[34] However, the major intrinsic issues related to the mobility of copper ions in binary sulphides have prevented any commercialisation of Cu_2S-based thermoelectric devices since a thermoelectric "battery" was made by A. E. Becquerel in 1866, containing legs of Cu_2S and Cu-Ni-Zn alloy.[101]

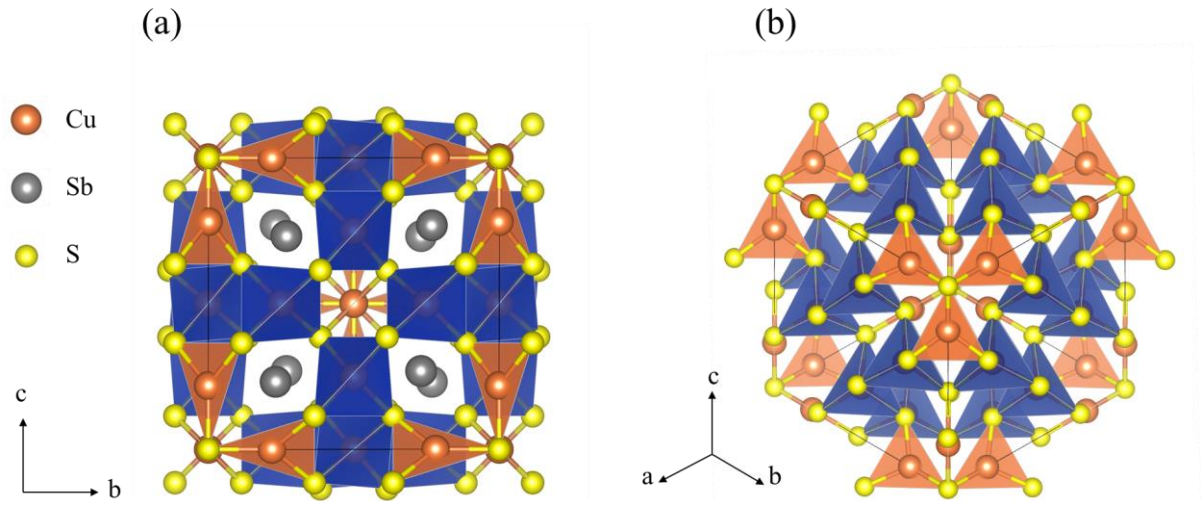

Figure 1.23 Crystal structure of tetrahedrite, $Cu_{12}Sb_4S_{13}$, (a) Viewed along [100], (b) Viewed along [111] with Sb atoms omitted for clarity. The CuS_4 tetrahedra are shown in blue and the CuS_3 trigonal planar polyhedra are shown in orange.

1.6 Materials investigated

All materials investigated in this thesis are transition-metal sulphides that have been selected for two principal reasons. (1) The elements that constitute the materials are cheap, readily available and non-toxic and (2) they have promising thermoelectric properties with a potential for further improvement. Titanium disulphide has a two-dimensional structure that allows for doping strategies to target a reduction in both electrical and thermal conductivity. Copper-containing sulphides have been studied only very recently for their thermoelectric properties and much work is left to be done on electrical doping and optimisation of synthesis routes.

1.6.1 Copper-containing sulphide minerals

1.6.1.1 Tetrahedrite

Tetrahedrites form a large family of naturally-occurring minerals of composition $A_{10}B_2C_4Q_{13}$ (A = Cu, Ag; B = Mn, Fe, Co, Ni, Zn, Cu, Hg, Cd; C = As, Sb, Bi; Q = S, Se).[102] Tetrahedrite was re-named in 1845 by Austrian mineralogist Wilhelm Karl Ritter von Haidinger after the tetrahedral form of the crystals.[103] The complex crystal structure of $A_{10}B_2C_4Q_{13}$, space group $I\bar{4}3m$ ($a \approx 10.3$ Å), can be described as a defect derivative of the sphalerite structure in which

six of the twelve transition metals occupy 12*d* tetrahedral sites, the other six occupy 12*e* trigonal planar sites and the pnictogen atoms occupy trigonal pyramidal sites, Figure 1.23. Out of the twelve transition metals, two are divalent, A, while the remaining ones, B, are monovalent cations. Previous work has determined that only monovalent cations occupy the trigonal planar sites, with the tetrahedral sites being shared between four monovalent and two divalent cations.[104]

1.6.1.2 Bornite

Like tetrahedrite, bornite is a naturally-occurring copper-containing sulphide mineral. The material adopts an antifluorite-related structure with a general formula is $Cu_5Fe\square_2S_4$, where $\square$ represents a vacancy in the Cu/Fe layer. Its chemical composition was disputed at the beginning of the 20th century and in 1915, Austin F. Rogers from Stanford University suggested that Cu_5FeS_4 is indeed the composition of bornite, although he advanced the hypothesis that it might be a solid solution of Cu_2S in Cu_3FeS_3. Based on previous observations that bornite was often found with intergrowth of chalcocite and chalcopyrite, Frueh concluded in 1951 that there must be at least two different phases, below 443 K and above 493 K, related by an order-disorder rearrangement of the metal atoms and vacancies.[105] The polymorphism in bornite has been studied since, using X-ray diffraction,[106-108] thermal analysis[109, 110] and neutron diffraction.[111]

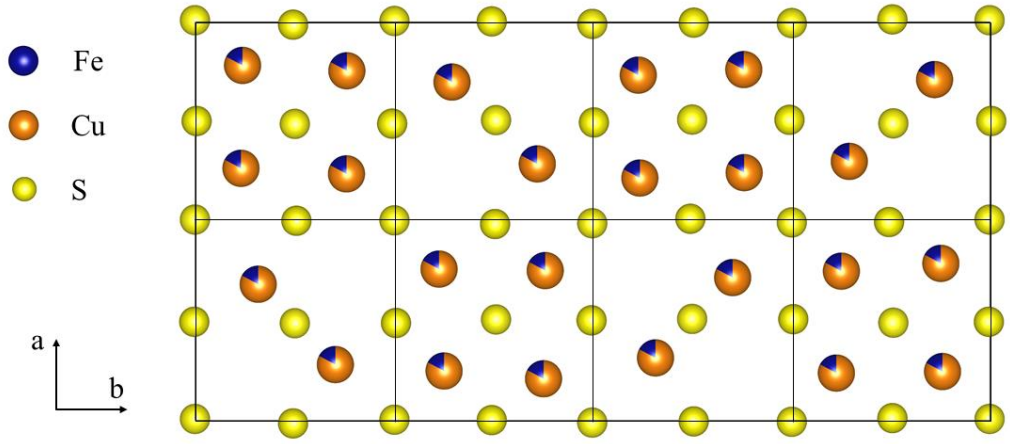

Figure 1.24 Crystal structure of the low-temperature phase of bornite, Cu_5FeS_4, viewed along the *c* axis, showing the alternating sphalerite and antifluorite subcells.

These studies showed that bornite undergoes complex cation order–disorder phase transitions over the temperature range 473 ≤ T / K ≤ 543. Above 543 K, vacancies are completely disordered, and the material adopts an antifluorite-type structure, denoted as *1a*, (space group $Fm\bar{3}m$, $a \approx 5.5$ Å).[107] At room temperature, long-range ordering and clustering of vacancies results in an orthorhombic (pseudo-tetragonal) structure with a *2a*×*4a*×*2a* supercell (space group *Pbca*) consisting of antifluorite and sphalerite subcells, Figure 1.24,[106] although a HRTEM study suggests that at room temperature, *1a*, *2a*, *4a* and *6a* superstructure domains coexist.[112] At intermediate temperatures, 473 ≤ T / K ≤ 543, a cubic structure with a *2a*×*2a*×*2a* supercell, denoted as *2a*, is found.[108, 113] This intermediate superstructure alternates Fe-containing and Fe-free subcells while in the *1a* phase unit cell, Cu and Fe are statistically distributed over the available tetrahedral sites. Changes in the temperatures at which these two phase transitions occur have been related to the iron content and the Cu: Fe ratio.[109]

1.6.2 Titanium disulphide

Titanium disulphide, TiS_2, has been receiving considerable attention over the past 50 years owing to the two-dimensional character and the countless possibilities that this feature offers in a wide range of applications.[45, 114, 115] TiS_2 crystallises in a CdI_2-type structure (space group

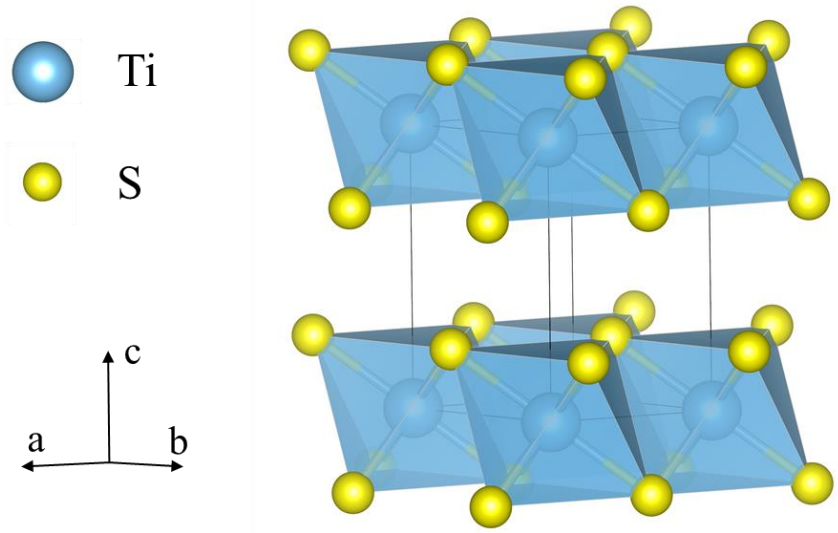

Figure 1.25 Crystal structure of TiS_2

$P\bar{3}m1$) where two-dimensional slabs of edge-sharing TiS_6 octahedra are stacked along the c axis and separated by a van der Waals' gap, Figure 1.25. The layered structure and the presence of an array of vacant octahedral and tetrahedral sites permits the ready intercalation of a wide range of guest species, including monatomic cations,[114] molecular ions[116, 117] and organic molecules,[118] that may form superstructures that may be stable over a particular range of *x*.

1.7 Aims of the present work

The aims of the present work are to improve the thermoelectric properties of cost-efficient widely available transition-metal sulphides, to improve the scalability and to reduce the energy cost of synthesis processes. The effect of chemical intercalation and substitution on the structural and physical properties of the selected materials are investigated. Through this chemical doping, the intention is to optimise the thermoelectric response via a careful tuning of the electrical and thermal properties. Additionally, nanocomposites of titanium disulphide are investigated for the potential reduction in thermal conductivity via interface phonon scattering. As well as optimising the thermoelectric properties, this work seeks to improve the scalability of materials and aims to meet industrial requirements for large scale applications. This includes the establishment of energy-efficient synthesis routes such as mechanical alloying or solution-based synthesis and a study of the stability of the materials.

Chapter 2 - Experimental techniques

2.1 Synthesis

2.1.1 High temperature solid-state reaction

High-temperature reaction in absence of oxygen is a well-established route that offers great control over the stoichiometry of the products and was used for the synthesis of titanium disulphide and tetrahedrite samples and their doped derivatives. Solid-state reaction is carried out between carefully weighed amounts of starting materials in evacuated fused silica tubes placed in a furnace for one or more firing at elevated temperatures. Because all synthesised samples in this work contain sulphur, a slow heating rate had to be applied to prevent the rapid build-up of pressure and minimise the risk of explosion while a slow cooling rate enables sulphur to reintegrate into the powder without condensing on the inside wall of the tube. The sulphur flakes were dried in vacuum for a period of time exceeding 4 h with frequent warming of the vessel to remove traces of moisture. Flakes were preferred to powder for their much lower surface to volume ratio, limiting the adsorption of moisture. Unless otherwise stated, starting materials were ground together using an agate pestle and mortar to produce a fine powder. It is necessary for the mixture to be homogeneous to ensure complete reaction as the slow diffusion rate of the solid reagents can lead to partial reaction and variations in stoichiometry in the product. However, sulphur has a low melting point (115.2 °C), meaning that most high-temperature reactions here are best described as solid-liquid-gas phase reactions where the homogeneity is good and the reaction time lower than the usual few days or weeks often necessary.

2.1.2 Mechanical alloying/milling

Mechanical alloying (MA) consists of using high-velocity ball milling in order to supply enough energy to a powdered mixture of reagents for it to chemically react. Grinding solids together in order to form a product with properties that are different from the starting materials is an old concept. One famous example is the discovery of gunpowder in China well before the

14th century.[119] However, it has been applied to synthetic chemistry in the late 1960's with the mechanical alloying of oxide-dispersion strengthened superalloys.[120, 121] It has since been improved and increasing interest has been given to mechanically-alloyed materials; not only because of the attractiveness of working without need for energy-demanding high-temperature furnaces but also for the control over the powders' microstructure. Indeed, the constant fracturing and welding-rewelding process of powder particles greatly impacts on its morphology, size and induces defects in the structure of the material such as stacking faults, points defects or local non-stoichiometry that can be controlled to alter the physical properties of a material.[122, 123] Mechanochemical synthesis can also be used as an alternative to solution chemistry in the production of nanomaterials.[124] In a dry mechanochemical synthesis, powder reagents are mixed together and placed in a jar with balls of variable sizes. The material used for the jar and balls is often stainless steel but other costlier but harder and more chemically unreactive materials such as yttrium-doped zirconia or tungsten carbide can be preferred depending on the nature of the starting materials. The jar is then sealed in air or inert atmosphere and placed in a mill.

There are different types of mills that differ by their capacity, speed, design and overall efficiency to reduce the particle size. However, the planetary ball mill stands out in research laboratories by its small size and high efficiency. While most industrial mills use one rotation axis, a planetary ball mill adds one degree of rotation with the introduction of a sun wheel, an extra rotating disc on which the jar is eccentrically placed and rotating in the opposite direction. The resulting combination of centrifugal, tangential and impacts forces contributes to transfer enough energy to the powder to greatly reduce the average particle size and eventually to induce a chemical reaction.[125] The forces applied to the jar and transferred to the balls and powder are extremely complicated and current mathematical understanding is insufficient to add an element of prediction to the forces involved in MA.[125-127] It is possible, however, to simplify the planetary ball milling system, represented in Figure 2.1. Because the jar is spinning (r_2) in the opposite direction to the sun wheel (r_1), the centrifugal force (F_1) caused by the latter is in turn added and subtracted to the forces applied on the balls by the spinning of the jar (r_2),

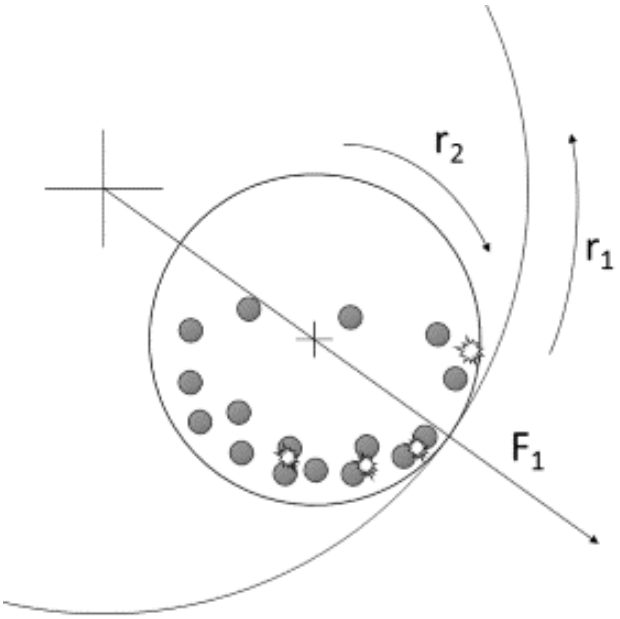

Figure 2.1 Simplified schematic representation of a planetary ball mill.

causing violent changes of direction in the momentum of the balls and high energy impacts occur against the wall of the jar.

In this work, ball milling was carried out on a Retsch PM100 planetary ball mill using a 25 ml stainless steel jar with 6 mm stainless steel balls. The powder and the balls were weighed separately and sealed in the jar in either air or argon atmosphere. The ball milling conditions such as weight-to-powder ratio and milling time are specified in the appropriate sections.

2.1.3 Solution synthesis

The concept of liquid-based reaction is probably the most common synthesis technique across a vast range of different chemistry fields. Chemical manufacturers are very familiar with this synthesis route and its application to large scale production of materials can be reasonably straightforward. The temperatures required for solution syntheses are kept much lower than conventional solid-state reactions and the absence of fine and flammable powders represents a net advantage over mechanical alloying. Nanoscale samples of TiS_2 have been synthesised from the reaction of titanium tetrachloride with sulphur using a simple reflux under inert atmosphere. Details of the procedure are given in the appropriate Section 4.2.1.

2.2 Powder X-ray diffraction

X-ray radiations were discovered in 1895 by Wilhelm Röntgen, a German physicist, for which he was awarded the Nobel Prize in Physics six years later. It has now become an essential tool in many fields of research especially in materials chemistry where X-ray diffraction (XRD) is used routinely to identify crystalline (and to a certain extent, amorphous) solids. X-rays are part of the electromagnetic spectrum between ultraviolet and Gamma radiations with a wavelength ranging between 1 nm (soft X-rays, *ca.* 1 keV) and 0.1 Å (hard X-rays, *ca.* 100 keV). While hard X-rays require a synchrotron to be produced, soft X-rays are produced on lab-scale instruments when a metal target (generally Cu or Mo) is hit with high energy electrons from an electrically heated filament, knocking electrons out of the metal. Various electrons from orbitals higher in energy then decay to fill the voids left by the core electrons, emitting a continuous X-radiation over a range of energies. However, sharp intensity peaks are produced at wavelengths corresponding to quantised electron transitions, K_α and K_β,[128] both being close doublets ($K_{\alpha1}/K_{\alpha2}$ and $K_{\beta1}/K_{\beta2}$). Usually, $K_{\alpha1}$ is kept by filtering out in turn K_β with a metal filter and $K_{\alpha2}$ with a monochromator. Because the K_α wavelength ($\lambda \approx 1.54$ Å) is of the same order of magnitude as the inter-atomic distances in crystalline solids, the incoming X-ray beam can be scattered by planes of atoms, as illustrated in Figure 2.2. While most diffracted beams suffer destructive interferences, the ones diffracted by parallel planes of atoms (separated by a distance noted d_{hkl}) undergo constructive interferences that enables the signal to be detected at a specific angle, θ_{hkl}. Two waves produce a constructive interference when out of phase by a factor n where n is an integer, this can be put into an equation where the extra distance, AB + BC, travelled by the second beam equals to $n\lambda$. Simple mathematics gives the relationship between this distance and the distance d_{hkl}, known as Bragg's law, Equation 2.1:

$$AB + BC = 2d_{hkl}\sin(\theta_{hkl}) = n\lambda \qquad (2.1)$$

The unit cell of crystalline solids is directly related to the inter-plane distances, d-spacings or d_{hkl}, via a series of equations that depends on the geometry of the crystal structure and can therefore be determined. However, in powder X-ray diffraction, there is a loss of information from the 1D compression of the 3D diffraction pattern of a crystal. When some information

such as structure type, unit cell and atom positions are approximately known, they can then be refined with powder X-ray diffraction using a refinement method, detailed in Section 2.4. To identify an unknown structure, however, the need for three-dimensional information is usually fulfilled by single-crystal X-ray diffraction.

X-ray diffraction data for powders and pellets were collected using a Bruker D8 Advance Powder X-ray diffractometer, operating with Ge monochromated $CuK_{\alpha 1}$ radiation (λ = 1.54046 Å) and fitted with a LynxEye detector. Samples were ground using an agate mortar and pestle and placed in an X-ray transparent sample holder. The range of 2θ used was varied with the need of the different sample series and are specified in the appropriate sections but routine scans for phase identification purposes were typically made over 1h over the range $5 \leq 2\theta / ° \leq 85$ with a step size of 0.02762 ° and a counting time of 1.2 s per step. X-ray diffraction data of samples for which only a few mg were available have been collected on a Bruker D8 Discover over the range $5 \leq 2\theta /° \leq 50$ with a step size of 0.02019 ° and a counting time of 0.75 s per step. This instrument, operating in transmission geometry, uses an X-ray focussing mirror for K_α radiation (λ = 1.5418 Å) and a LynxEye detector. Samples were ground using an agate mortar and pestle and placed on a copper multi-sample holder. The powder diffraction patterns were compared against the ICDD-PDF database using the EVA software[129] package to confirm the identity of the phases. The refinement of structural parameters was done using the General Structure Analysis System (GSAS) software package described in Section 2.4.[130, 131]

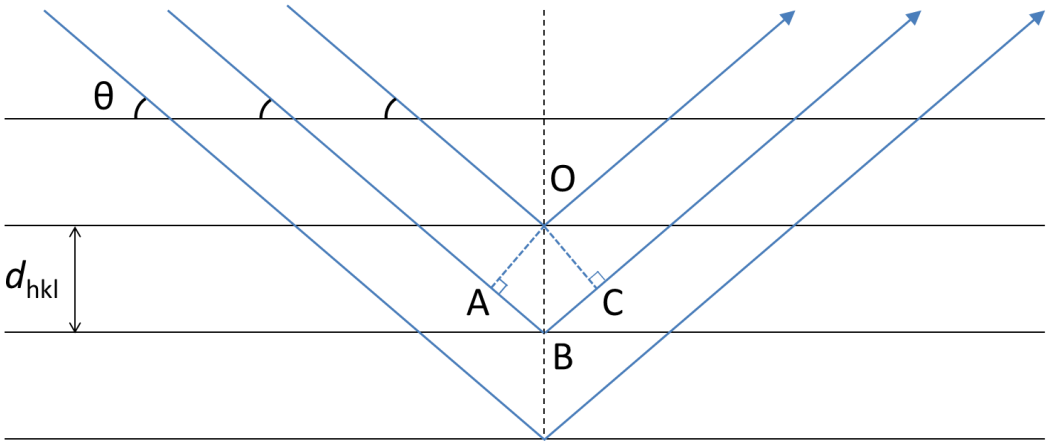

Figure 2.2 Diagram of the diffraction process in a crystalline solid.

2.3 Powder neutron diffraction

Despite the undisputable capabilities of X-ray diffraction, the technique is limited when it comes to differentiating atoms close to one another in the periodic table or simply observing atoms with low atomic number. This occurs because the X-ray beam is diffracted by the electronic clouds of atoms and the information obtained is a reflection of the electron density in a solid. Conversely, neutrons are uncharged particles that are diffracted by the atomic nuclei and a much clearer contrast can then be obtained. The neutron scattering length depends strongly on the nuclear structure of the atom and can vary greatly from one atom to the next in the periodic table, including both positive and a negative value.[132, 133]

Because neutrons are subatomic particles with a non-zero magnetic moment they are also affected by the magnetic moments present in the materials and can couple with magnetic atoms or ions in the structure. Neutron diffraction can therefore be used to characterise materials with magnetic moments, whether they are ordered (magnetically ordered lattice) or disordered (diffuse magnetic scattering).

Powder neutron diffraction experiments were conducted on two instruments, GEM and POLARIS, at the ISIS facility, (Rutherford Appleton Laboratory, Didcot, Oxfordshire) a spallation source that produces pulsed neutron beams from the collision of high energy protons with 2 tungsten targets, in target station 1 and 2 (TS1 and TS2), supporting respectively 22 and 13 instruments, Figure 2.3. Both GEM and POLARIS are part of the facility's TS1. The production of the high energy protons beam necessary to produce the neutrons can be summarised in two steps. In the first part, negatively charged hydrogen ions, H^-, are accelerated in a 70 MeV linear accelerator to reach 37 % of the speed of light using a radio-frequency quadrupole accelerator and copper drift tube electrodes. In the second part, the H^- ions are deprived of their electrons by an alumina foil and accelerated continuously in a large 800 MeV synchrotron (163 m of circumference) to reach 84 % of the speed of light before hitting the targets. The neutrons are produced in very intense pulses that need to be slowed down by passing through a moderator before travelling towards the different instruments.

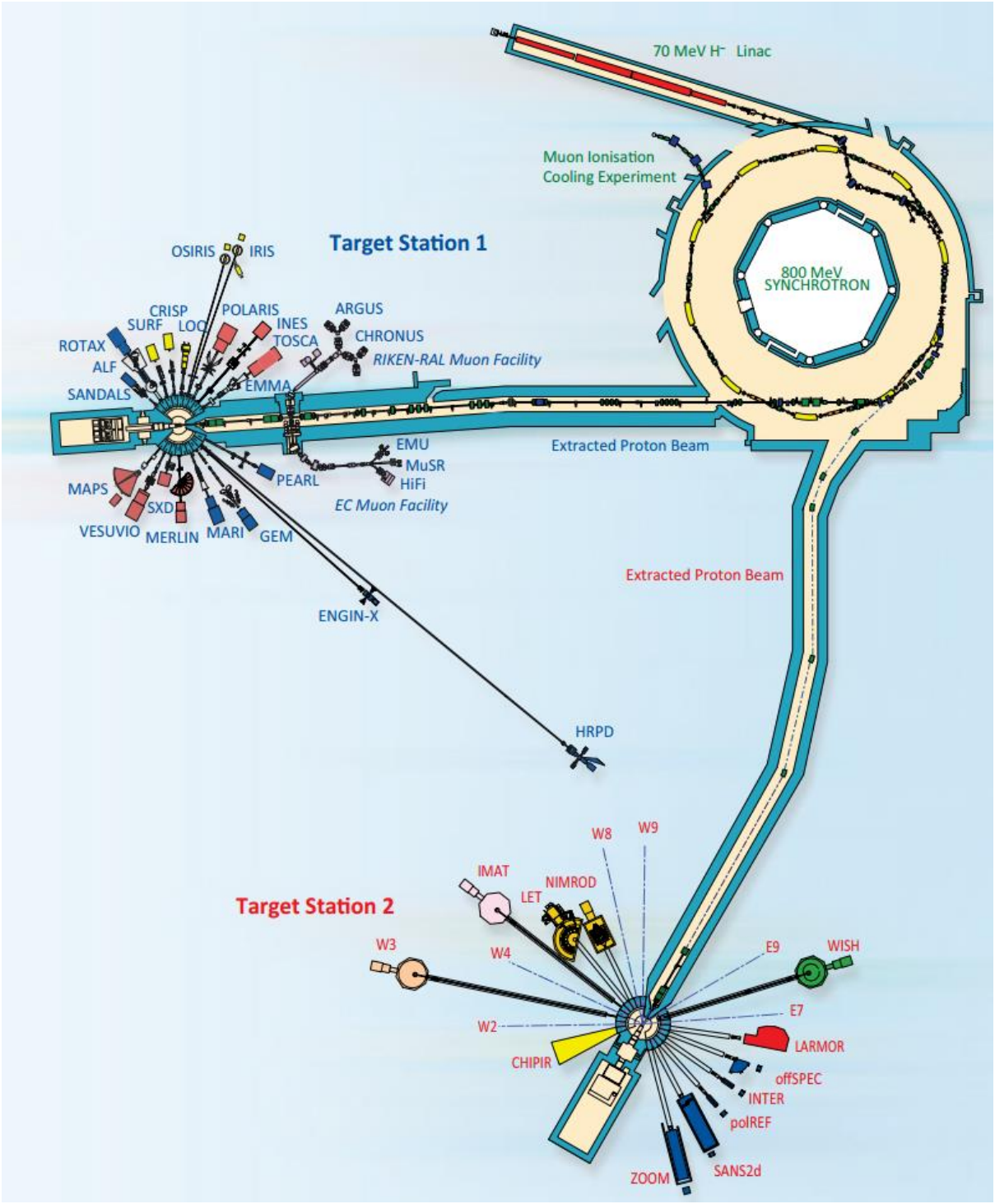

Figure 2.3 The ISIS facility.[134]

2.3.1 The GEM diffractometer

The General Materials diffractometer (GEM) receives cool neutrons of narrow pulse width from a liquid methane moderator at a temperature ranging between 100 and 110 K. It possesses a large set of 9 ZnS/^{6}Li scintillator detectors banks, Figure 2.4, that cover a wide range of d-spacings with high resolution, stability and count rate. Time-of-flight powder neutron diffraction data for selected samples of Co_xTiS_2 (x = 0.2; 0.25; 1/3; 0.5 and 2/3) were collected using the GEM diffractometer.

Powdered samples (*ca*. 3 g) were placed in 8 mm wide thin-walled vanadium cans and placed directly on the beam path for room temperature measurements and inside a vanadium-tailed helium cryostat for measurements down to 2 K. Data from bank 3 to bank 7, Table 2.1,[135] were used for the structural characterisation of the investigated phases. Initial data manipulation and reduction, including the subtraction of the empty cryostat signal for low-temperature measurements was carried out using the Mantid software package.[136, 137]

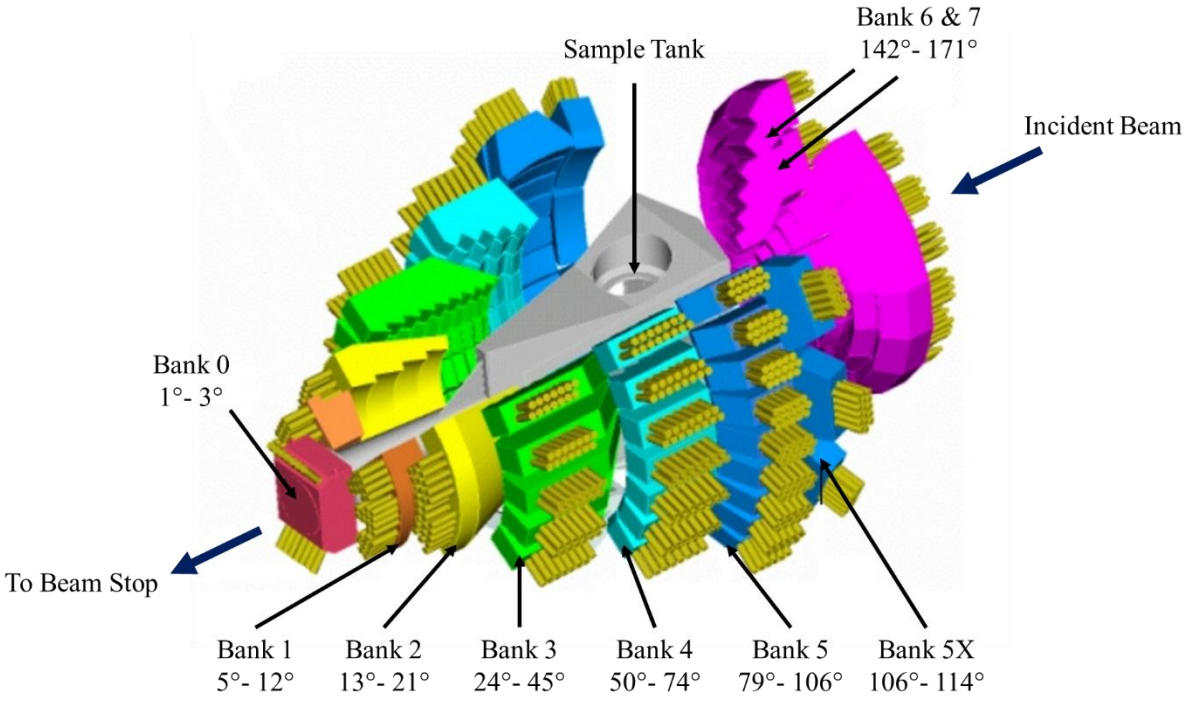

Figure 2.4 A schematic layout of the GEM detector banks.[135]

Table 2.1 Parameters of the GEM detector banks.

Bank	1	2	3	4	5	5X	6	7
Scattering angle 2θ / °	5.32-12.67	13.44-21.59	24.67-45.61	50.07-74.71	79.07-106.60	106.02-114.19	142.50-149.72	149.98-171.40
Resolution Δd/d / %	4.7	2.4	1.7	0.79	0.51	0.5	0.34	0.35
d_{max}/ Å	30	14	7	4	2.5[a]		1.7[a]	

[a] Data from banks 5 and 5X and from banks 6 and 7 are combined in single data sets.

2.3.2 The POLARIS diffractometer

POLARIS is a high intensity, medium resolution diffractometer that was upgraded in 2012. The instrument is now composed of 6 banks of detectors over the range $6 \leq 2\theta\ /^{o} \leq 168$, Figure 2.5, with a similar resolution to the GEM diffractometer, Table 2.2. The instrument views an ambient temperature water moderator that supplies a high flux of thermal neutrons. The high incident flux enables rapid characterisation of samples, even very small quantities, in a short period and in a large range of different sample environments. POLARIS was used to monitor the unit cell variation and study the evolution of copper mobility of tetrahedrite samples, $Cu_{12}Sb_4S_{13}$ and $Cu_{11}MnSb_4S_{13}$, over the temperature range $50 \leq T\ /\ °C \leq 500$. The powdered samples (*ca.* 3 g) were sealed in high purity suprasil® quartz tubes evacuated to 10^{-4} Torr and placed inside 8 mm wide thin-walled vanadium cans. Samples were mounted in an evacuated aluminium furnace (Rutherford-Appleton Laboratory design, up to 1000°C) fitted with a vanadium window. Initial data manipulation and subtraction of the signal from quartz tubes at temperature measurements were carried out using the Mantid software package.[136, 137]

Table 2.2 Parameters of the POLARIS detector banks.

Bank	1	2	3	4	5	6
Scattering angle 2θ / °	6 - 14	19 - 34	40 - 67	75 - 113	135 - 143	146 - 168
Resolution Δd/d / %	> 2.7	1.2-1.9	0.85	0.51	0.30[a]	
d_{max} / Å	19.6	8.7	7.0	3.2	2.7 [a]	

[a] Data from banks 5 and 6 are combined in single data sets.

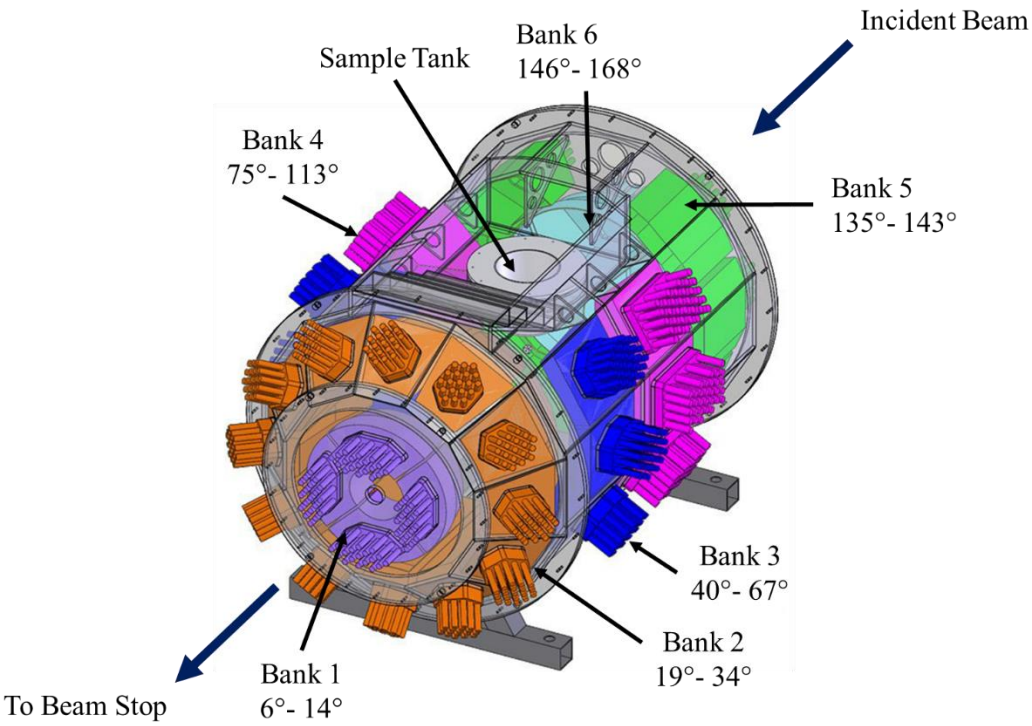

Figure 2.5 A schematic layout of the POLARIS detector banks.[138]

2.4 Analysis of powder diffraction data

Both powder X-ray diffraction and powder neutron diffraction data were analysed using the GSAS package[130] through the EXPGUI user interface.[131] Two different refinements methods, Rietveld and Le Bail, were used. For both technique, the instrument parameter file and the space group and approximate unit-cell parameters of the investigated material are required. The unit cell is determined by indexing of the peaks, either manually or with a refinement software such as Topas3,[139] FullProf[140, 141] or even GSAS.

2.4.1 The Rietveld method

The Rietveld method for characterising structures that was originally developed for neutron diffraction by the Dutch crystallographer Hugo M. Rietveld in 1969.[142, 143] The method[144, 145] uses a least-squares approach to refine a model structure in order to fit the collected diffraction pattern. The aim of the analysis process is to minimise the residual (S_y) given in Equation 2.2:

$$S_y = \sum_i \frac{(y_i - y_{ci})^2}{y_i} \quad (2.2)$$

where y_i and y_{ci} are the observed and calculated intensities at the *i*-th point. The goodness-of-fit between the model line profile and the collected data is improved by refining various parameters. While peak positions are dependent on the lattice parameters, the peaks' intensity contains information on the atom positions, thermal parameters and site occupancy. These parameters are refined in order to minimise S_y. Parameters that describes the specific conditions of the experiment, including the sample and instrumental contributions, are also refined. These experimental parameters include the background, that can also be fitted manually, absorption correction, that depends on the sample symmetry, the scale factors and the peak profile coefficients. The peak shape depends on instrument contributions, such as axial divergence or misalignment, and sample contributions, such as crystallite size effects or strain broadening. The peak shape used in the present work, for both X-ray and neutron diffraction experiments, was modelled using a pseudo-Voigt function[146, 147] that mixes Gaussian and Lorentzian functions.

The quality of the fit is illustrated by the weighted-profile *R* value, R_{wp}, representing the level of agreement between calculated and observed data. It is given by Equation 2.3:

$$R_{wp} = \left[\frac{\sum_i w_i(y_i - y_{ci})^2}{\sum_i w_i(y_i)^2}\right]^{1/2} \quad (2.3)$$

Although it is intuitive to think that R_{wp} needs to be close to zero, it should actually approach the statistically expected *R* value, R_{exp}, that includes the number of observations, *N*, and the number of parameters refined, *P*. R_{exp} is given by Equation 2.4:

$$R_{exp} = \left[\frac{(N-P)}{\sum_i^N w_i {y_i}^2}\right]^{1/2} \quad (2.4)$$

A second important coefficient, χ^2, can be calculated by simply calculating the goodness-of-fit between R_{wp} and R_{exp}, that should, ideally, approach 1, Equation 2.5:

$$\chi^2 = (R_{wp}/R_{exp})^2 \quad (2.5)$$

2.4.2 The Le Bail method

The Le Bail method was first described by French researcher Armel Le Bail in 1988 when he successfully fitted the powder pattern of $LiSbWO_6$ by adapting the Rietveld method.[148, 149] In this simplified refinement technique, it is not necessary to know the atoms' positions and as the refinement algorithm does not refine the peak intensity from structural parameters but extracts them directly from powder diffraction data. Only the background, instrument geometry related parameters, peak profile parameters and positions (i.e. unit cell parameters) are refined in a Le Bail fit. This information can then be used for a full Rietveld refinements or to monitor the evolution of the unit-cell expansion with temperature or doping.

2.5 SQUID magnetometry

A Superconducting Quantum Interference Device (SQUID) is a highly sensitive probe to investigate the magnetic properties of materials down to low temperatures, typically of a few Kelvin. The magnetic susceptibility (χ) of a material is determined by applying a known magnetic field (H) and measuring the magnetisation (M). A SQUID magnetometer exploits the electron tunnelling effect in two Josephson junctions (a thin insulating layer separating two superconductors) fitted in parallel in a superconducting loop, Figure 2.6.[150] The junctions act as a high-sensitivity probe to observe quantum electrodynamic phenomena. The presence of an external field in a sample moving through a superconducting coil induces a current in the wires and the SQUID sensor. It is the interference between the two junctions, with only one of them altered by the sample's magnetic field, that enables the determination of the magnetisation from the

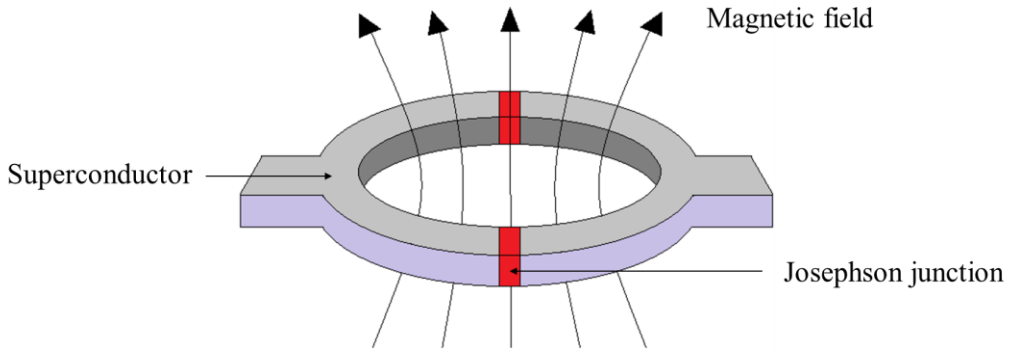

Figure 2.6 Diagram of a DC SQUID device.

relationship between sample position and measured output voltage. A superconducting magnet applies an external magnetic field to the sample.

The magnetisation was measured and the magnetic susceptibility (χ) determined on *ca.* 40 mg samples in gelatine capsules for Co_xTiS_2 (x = 0.2; 0.25; 1/3; 0.5; 2/3 and 0.75). The capsules were fixed in a plastic straw and mounted in the instrument. Measurements were performed on two Quantum Design MPMS XL magnetometers at CRISMAT laboratory in Caen and at the ISIS facility at Rutherford Appleton Laboratories, Didcot. Data were collected over the temperature range $2.5 \leq T/K \leq 298$ both after zero-field cooling (ZFC) and after cooling in the measuring field of 0.01 T (FC).

2.6 Muon spectroscopy and the EMU spectrometer

When a muon is implanted in the sample, its polarisation and its momentum are antiparallel. As a radioactive particle, the muon decays shortly after being implanted with a lifetime of 2.2 μs. As it decays, the muon emits a positron predominantly in the direction parallel to its spin, giving a non-random statistical distribution of emitted positrons. These positrons are then detected by the two banks of detectors, backwards and forwards, and it is the asymmetry between the signals of the two detector banks that constitutes the measured data, Figure 2.7. As it precesses, the spin-direction of a muon changes, ending up pointing either backward or forward, subsequently perturbing the asymmetry. Because of the radioactive nature of the decay, the signal from the backward and forward sets of detectors sum up to an exponential

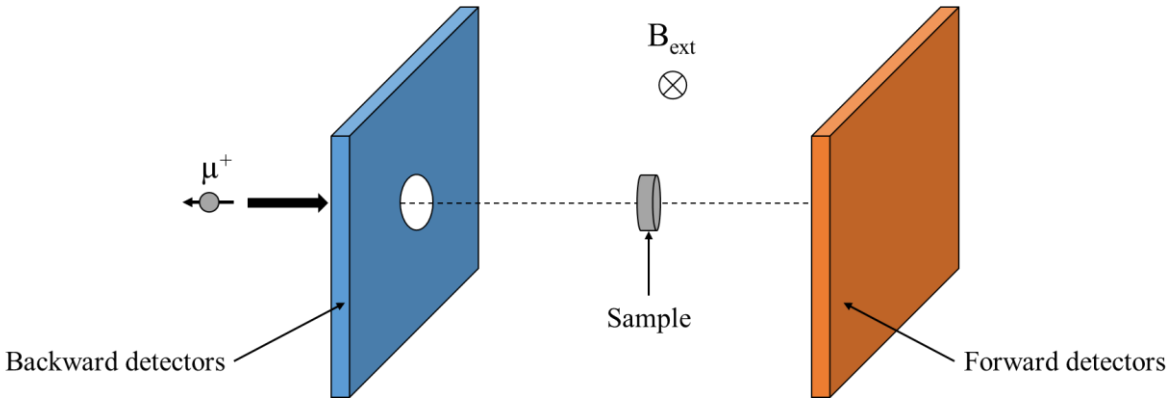

Figure 2.7 Diagram of the detector set of a muon spectrometer. An external field, B_{ext}, can be applied in longitudinal (along the muon incident path) or transversal direction.

decay, Figure 2.8(a). The time evolution of the muon decay, Figure 2.8(b), is given by the normalised difference of the two functions $N_B(t)$ and $N_F(t)$, respectively the time evolution of detected positrons in the backward and forward banks, Equation 2.6:

$$A(t) = \frac{N_B(t) - N_F(t)}{N_B(t) + N_F(t)} \tag{2.6}$$

This relaxation asymmetry is interpreted to extract information on localised fields.

The pulsed muon source at the ISIS Facility, Rutherford Appleton Laboratory, UK, is the most intense in the world, allowing 7 instruments to run simultaneously. The EMU spectrometer has 96 detectors (each composed of a scintillator, a light guide and a photomultiplier tube) split in two detector rings placed before and after the sample along the beamline, Figure 2.9. Magnetic fields up to 5000 G can be applied to the sample in either longitudinal or transverse mode.

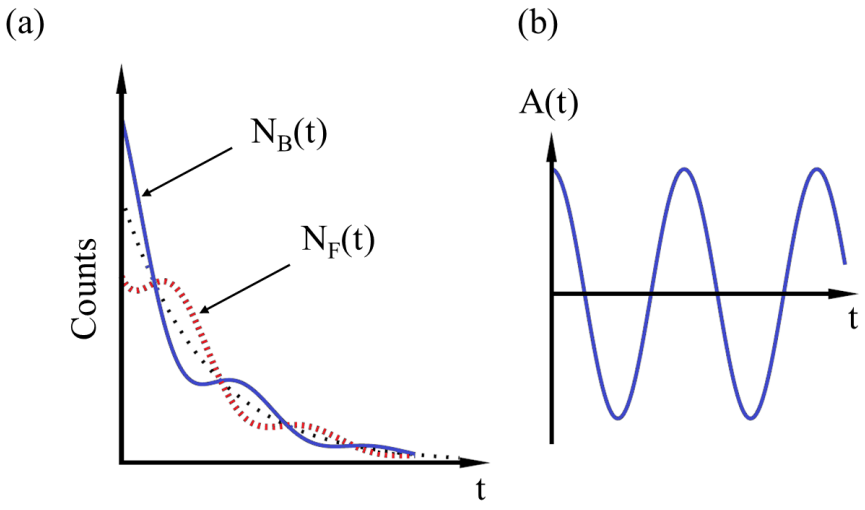

Figure 2.8 (a) Positrons counts from backward, $N_B(t)$, and forward, $N_F(t)$, detector banks. (b) A muon asymmetry function.[53]

The μSR experiments of powdered samples of Co_xTiS_2 (x = 0.2; 0.25; 1/3; 0.5 and 2/3) were carried out on EMU. The powdered samples were loaded into a silver plate with a circular recess (dia. 30 mm, depth 2 mm), covered with Kapton film. All samples were initially mounted on the closed cycle refrigerator, temperature range $8 \leq T / K \leq 350$, and evacuated to a pressure below 10^{-4} Torr. The initial calibration run was performed in a transverse field of 100 G at

room temperature. The samples were cooled down in zero applied field and measurements taken on cooling and heating and at base temperature (*ca.* 8 K). Field sweeps, with longitudinal field ($5 \leq LF / G \leq 20$), were performed at temperatures above 250 K and at base temperature. For sample of composition Co_xTiS_2 (x = 0.25 and 0.5), additional measurements were carried out in an Oxford Instruments sorption cryostat, temperature range $0.350 \leq T / K \leq 50$. The procedure followed for measurements carried out in cryostat was similar to CCR experiments.

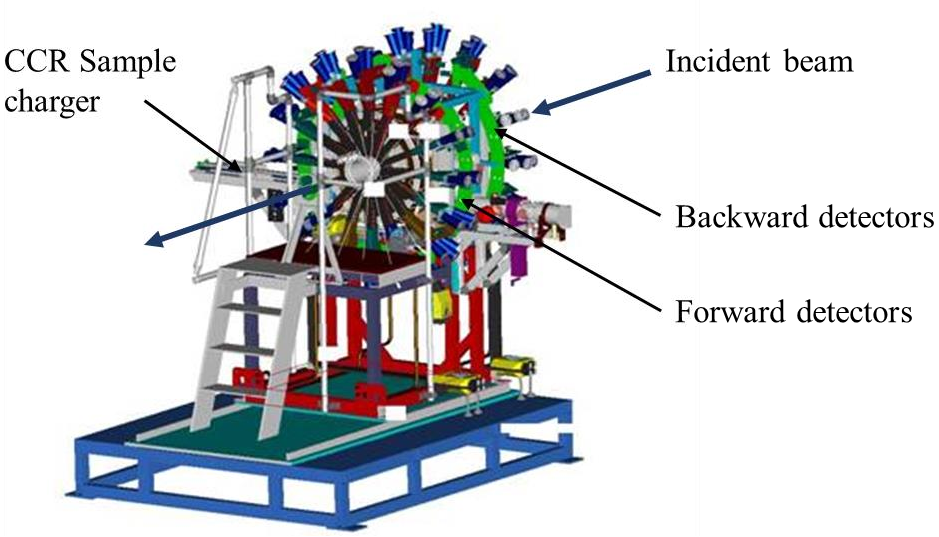

Figure 2.9 A schematic layout of the EMU spectrometer.[151]

2.7 Physical property measurements

2.7.1 Sample fabrication

The electrical and thermal transport properties of all materials investigated in this work were measured on consolidated pellets, polished and cut appropriately to adapt to the characterisation instruments. Circular pellets were obtained by compacting the powder while annealing on a hot-press constructed in-house, Figure 2.10. This step is crucial due to the large impact of porosity on the electrical and thermal conductivity. The heating process is carried out in an inert atmosphere using moulds and dies that can withstand high temperatures and pressures without deforming.

The pellets have been hot-pressed under constant nitrogen flow in graphite moulds, using graphite dies initially (P_{max} = 55 MPa), later upgraded to tungsten carbide in order to reach

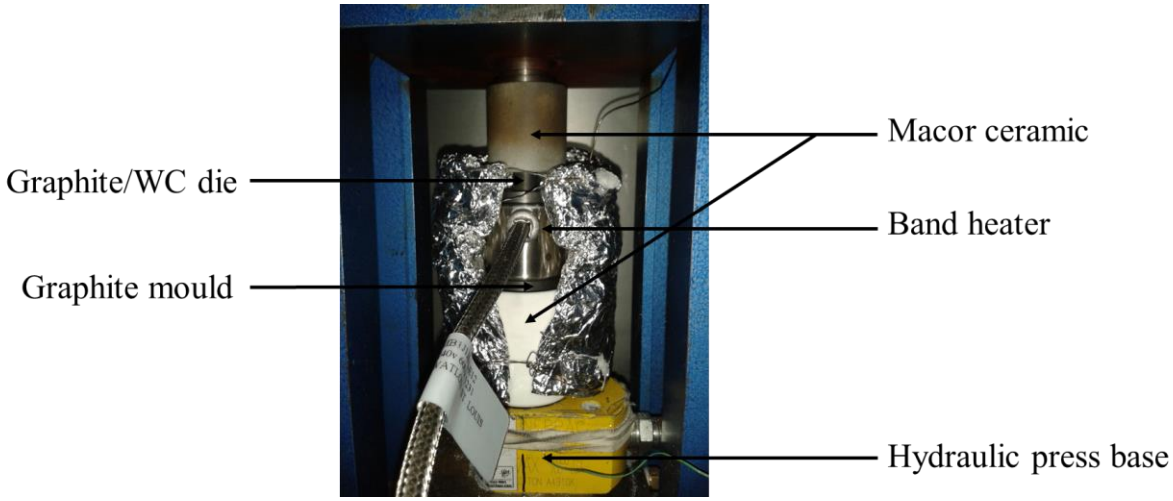

Figure 2.10 The in-house hot-press set-up, placed in a closed steel and wired glass chamber.

higher pressures. Graphite foils were placed above and below the powder to avoid contact with the dies and facilitate the removal of the pellet. The mould and dies are heated using a band heater wrapped around the mould. Heating was kept on for variable periods of time ($15 \leq t$ / min ≤ 30) under a constant pressure between 55 MPa and 109 MPa applied using a hydraulic press. The hot-pressed discs have a diameter of *ca.* 12.7 mm and a thickness of ca. 2 mm or 10 mm with less than 0.05 mm variation across the whole surface. Details of the pressing conditions for a given material are given in the appropriate chapters.

Spark Plasma Sintering (SPS) was carried out by the author at Queen Mary University, London, using an FCT Systeme GmbH SPS furnace. SPS is a highly efficient technique that exploits a pulsed DC current that passes through an electrically conductive die. Unlike hot-pressing where the heat is provided by external heating, the current is here supplied directly to the sample. Besides reducing energy cost of the consolidation, this enables a very accurate and fast cooling rate, up to 1000 K min^{-1} as well as being computer monitored.

Samples of composition $Mo_xTi_{1-x}S_2$ (x = 0; 0.015 and 0.035) have been consolidated by SPS using graphite mould and dies with a 16 mm diameter. The mould was then placed in the instrument, between two graphite pistons. The pressure and temperature profiles for a pressing are given in Appendix A.

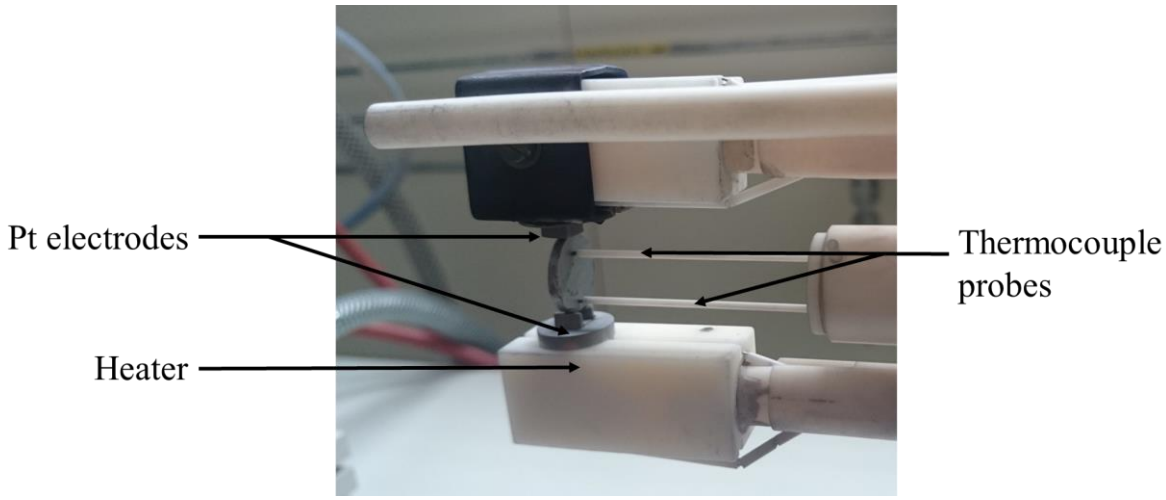

Figure 2.11 The Linseis LSR-3 sample mount.

The density of all consolidated pellets was measured using an ADAM PW184 Archimedes balance. Prior to physical property measurements, the consolidated pellets were polished using a MTI EQ-Unipol-300 grinder/polisher. The consolidated pellets were then cut into the appropriate shape using a MTI SYJ-150 digital diamond saw.

2.7.2 Electrical transport property measurements

The temperature dependences of the electrical resistivity (ρ) and Seebeck coefficient (S) were measured simultaneously on the polished samples using a Linseis LSR-3 instrument, under a partial pressure of He, and over the temperature range $300 \leq T\ /K \leq 600$, Figure 2.11. The measurements were mostly conducted on ingots of dimension *ca.* 2 × 2 × 8-10 mm; however, hard and brittle (and therefore difficult to cut) samples such as the bornite series were measured directly on discs using a shape correction.

2.7.2.1 Electrical resistivity

In a semiconductor, the electrical resistivity can be related to the charge carrier concentration and mobility via Equation 2.7:

$$\rho = \frac{1}{N_n\, e\, \mu_n + N_p\, e\, \mu_p} \tag{2.7}$$

where N_n and N_p are respectively the electron and hole concentration, e is the elementary charge, and μ_n and μ_p the charge carrier mobility of electrons and holes respectively. In a semiconductor, N increases with temperature as more charge carriers are thermally activated, decreasing the resistivity. The electrical resistivity was measured with the four-point DC method using a current of 15 mA to 100 mA between the terminal Pt electrodes and with the axial thermocouple probes separated by a distance of 5.7 mm or 8.0 mm.

2.7.2.2 Seebeck coefficient

The Seebeck coefficient, sometime called thermopower, is a direct measure of the voltage generated by a temperature gradient applied across the sample. The value of S can be negative or positive; it is the nature of the dominant charge carriers in a material defines the sign. The Seebeck coefficient was measured with a constant applied temperature gradient controlled by a heater situated below the bottom Pt electrode. A 30 K gradient was applied for ingots while discs require a 50 K gradient because of reduced contacts with the bottom Pt electrode.

A second instrument, constructed in-house, was used to measure S, at low-temperature, using two electrode blocks acting as a sample holder, Figure 2.12, placed in a Closed Cycle Refrigerator (CCR). The two copper blocks are connected through a thermally and electrically insulating bridge and connected to separate temperature controllers TC1 and TC2 (both Lakeshore LS-331). The CCR is evacuated and cooled by an Advance Research System Inc. ARS-2HW compressor. A temperature gradient is applied by use of a heater placed on one of the copper blocks and monitored by TC1 and TC2 while the voltage difference is measured by a nanovoltmeter (Keithley 2182A). The whole setup is computer controlled through a LabVIEW program and is able to measure the Seebeck coefficient over the temperature range $100 \leq T / K \leq 350$.

In this work, the instrument was adapted to measure the Seebeck coefficient of a 5 mm cold-press and sintered pellet of TiS_2 nanoflakes, Section 4.2.3. Copper wires were attached to each end of the pellet using silver paint and connected to the temperature controllers. The pellet was then fixed to the two copper blocks using silver paste. Measurements were done in air from room temperature to 350 K.

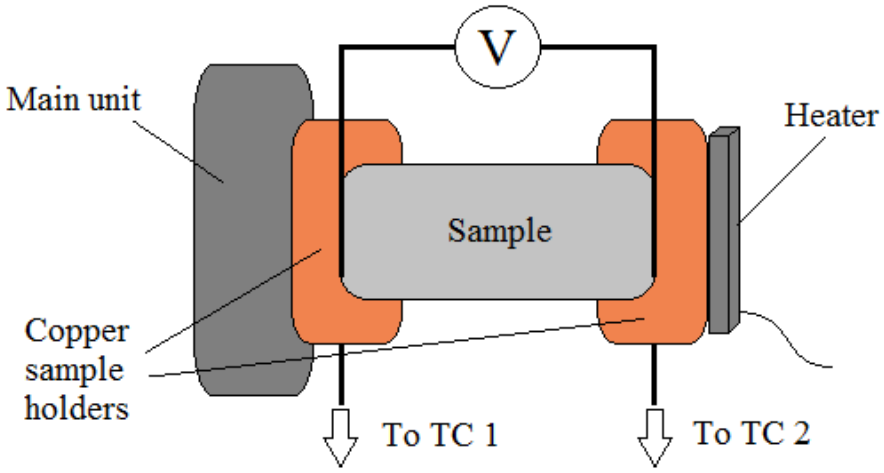

Figure 2.12 Schematic representation of the CCR sample setup.

2.7.3 Thermal conductivity

Thermal conductivity, κ, defines the ability of a material to transport heat and depends on the thermal diffusivity, α, the specific heat, C_p, and the sample's density, d, via Equation 2.8:

$$\kappa = \alpha \times d \times C_P \tag{2.8}$$

Because the diffusion of heat through a material is the consequence of the propagation of phonons as well as electrical charge carriers, the thermal conductivity can hence be split into two components, κ_l and κ_{el}.

The lattice contribution, κ_l, from the phonon propagation rate, depends on structural features. The size and mass of the atoms, bond distances or structural defects are as many parameters that will have an impact on the phonon propagation. These mechanisms include, for instance, phonon-phonon or phonon-electron scattering, point defects or mass fluctuation. Another mechanism comes from the boundary scattering at the grains interfaces, that depends on the particles' size and shape and can be varied in order to lower κ_L.

The second contribution, κ_{el}, to the thermal conductivity originates from the movement of electrons in the structure and can be estimated from the electrical conductivity using the Wiedemann-Franz law, Equation 2.9:

$$\kappa_{el} = \sigma \times L \times T \quad (2.9)$$

where σ is the electrical conductivity, L the Lorenz number and T the temperature. The Lorentz number commonly used for small band gap semiconductors is 2.44×10^{-8} W Ω K^{-2}.

2.7.3.1 Flash method

The flash method to measure the thermal diffusivity, and determine the thermal conductivity, that consists in firing a short intense light or laser pulse on a pellet. When the light or laser illuminates one surface, the energy in the form of heat traverses the pellet and causes the opposite face to experiences a rise in temperature. This temperature rise is recorded by an infrared detector.[152]

The temperature at the back of the pellet reaches a limiting value after a certain time, t_{max}. At a time, t_x, between the pulse and t_{max}, the diffusivity can be calculated using the distance, L, travelled by the heat (the thickness of the pellet), using Equation 2.10:

$$\alpha = \frac{k_x \times L^2}{t_x} \quad (2.10)$$

where k_x is a constant depending on x, x is usually seen as the percentage of the maximum temperature. This is calculated using the Proteus® software supplied with the instrument. The unit of the thermal diffusivity, α, is expressed in m^2 s^{-1}. Cowan's model with a pulse correction was applied by the software to account for energy loss at the surfaces.[153]

Thermal diffusivity measurements were carried out using the flash method on a Netzsch LFA 447 NanoFlash instrument for polished discs of ca. 2 mm width *ca.* 12.7 mm diameter. Measurements on square samples of *ca.* 6 × 6 × 2 mm^3 were performed using a Netzsch LFA 457 MicroFlash instrument at CRISMAT laboratory, Caen, France by Dr E. Guilmeau. The LFA 447 NanoFlash instrument uses a pulsed light source with a InSb IR-detector while the LFA 457 MicroFlash uses a pulsed laser and a MCT (Mercury Cadmium Telluride) IR-detector. A graphite coating was deposited with a graphite spray on both sides of the sample to ensure uniformity and improve the energy absorption from the short intense pulse on one side

and the emissivity of the heat detected on the rear surface. Thermal diffusivity was measured over the temperature range $303 \leq T / K \leq 573$ and each point was averaged over three shots.

2.7.3.2 Specific heat

The specific heat, C_p (in J K^{-1} g^{-1}), represents the amount of energy needed to raise 1 g of material by 1 K. It can be calculated from the density, ρ (in g cm^{-3}), and volume, V (in cm^3), of the pellet, and Q (in J), representing the heat transferred to the sample, using Equation 2.11:

$$C_P = \frac{Q}{\rho \times V \times \Delta T} \tag{2.11}$$

where ΔT is the temperature rise on the back face of the pellet under test. Q can be determined by side-by side measurement of a suitable reference material and the specific heat of the sample is given by Equation 2.12:

$$C_{p_{Sample}} = \frac{(m \times C_p \times \Delta T)_{Reference}}{(m \times \Delta T)_{Sample}} \tag{2.12}$$

where m is the mass of sample (in g). However, the determination of Cp using a second measurement on a reference sample increases the error margin and an estimated specific heat is often preferred. The most commonly used approximation is the Dulong-Petit specific heat[154] which relies on the fact that most solid elements have a molar heat capacity of $3R$, where R is the universal gas constant. The specific heat of a compound is estimated using Equation 2.13:

$$C_P = \frac{3R}{M/n} \tag{2.13}$$

where M is the molar weight of a compound containing n atoms per unit formula. The specific heat can also be measured independently using differential scanning calorimetry. In this work, the specific heat was determined using the Dulong-Petit law.

2.8 Electron microscopy

Electron microscopy is a powerful characterisation tool that enables the morphology, topography and even the chemical composition of a sample to be investigated. In any electron microscope, an electron beam is focused on the surface of a sample, acting like light in a

conventional microscope with a much shorter wavelength that enables much higher magnification. The beam is produced by an electron gun, accelerated and focused by magnetic lenses. There are two main types of electron microscope that are widely used, Transmission Electron Microscopes (TEM) achieve a resolution of just a few Angstroms by detecting electrons transmitted through a thin sample, while Scanning Electron Microscopes (SEM) have a lower resolution of typically a few nanometres but require very little or no sample preparation, Figure 2.13.

In this work SEM combined with Energy-Dispersive X-ray spectroscopy (EDX) has been used for looking at the particles size and morphology and the elemental composition of TiS_2 nanoparticles and bornite derivatives.

2.8.1 Scanning electron microscope

All measurements were made on a FEI Quanta FEG 600 Environmental Scanning Electron Microscope fitted with an EDX detector that enables the detection of the three main types of signals: Back-Scattered Electrons (BSE), secondary electrons and characteristic X-rays. The electron beam interacts with the sample over an area shaped like a tear drop from the impact point called the interaction volume. The secondary electrons originate from the top of the interaction volume (*ca.* 100 nm from the surface) then BSE (*ca.* 1 µm) and characteristic X-rays (*ca.* 10 µm).

Back-scattered electrons are reflected from the initial beam via elastic scattering and provide information on the composition of the sample. Because electrons are scattered differently depending on the atomic number (Section 2.2), with heavier elements having a stronger signal, good contrast can be seen in the micrograph between regions of different composition. Conversely, inelastic scattering of the primary electrons causes the ejection of secondary electrons from the inner shell of the atoms. Because they originate from the surface of the sample, and the intensity of the beam depends on the angle of incidence of the primary electrons, three-dimensional topographic information is collected. In this work, secondary electron detection mode was used for all the micrographs.

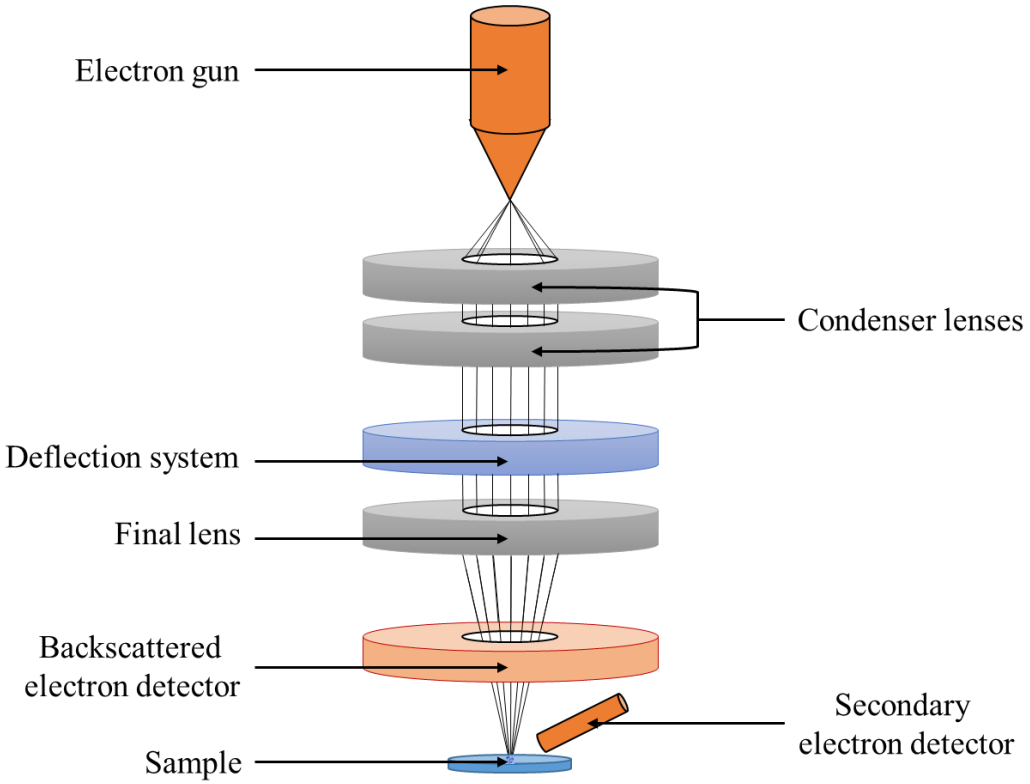

Figure 2.13 Diagram of a SEM instrument.

Samples were fixed on an aluminium sample holder fitted with a carbon tab and placed in the chamber without the need for coating the samples (no electrically insulating samples). The chamber was then evacuated to a pressure below 10^{-4} Torr and a 20 kV accelerating voltage was used. The image was focused by adjusting the contrasts and lens alignment and correcting the astigmatism.

2.8.2 EDX analysis

Energy-Dispersive X-ray spectroscopy (EDX) is a qualitative and quantitative elemental analysis technique that can produce a compositional map of a small portion of a sample. EDX uses the characteristic X-rays emitted when the voids left by inner shell electrons, knocked out by the electron beam, are filled by electrons initially higher in energy. It is the same mechanism that is used in the production of monochromated X-rays in XRD, explained in Section 2.2. When these electrons decay, energy is emitted in the form of X-rays peaking at energies corresponding to quantised transitions in the emission spectrum. Because every element has a

different atomic structure, these quantised transitions form a unique set that becomes the atom signature in the X-ray emission spectrum. This spectrum is then measured by the EDX detector of the FEI Quanta FEG 600 Environmental Scanning Electron Microscope and matched with a database to determine the composition.

2.9 Thermal analysis

Thermogravimetric Analysis (TGA) monitors the thermal dependence of the sample's weight and is used to determine a material's thermal stability in a chosen atmosphere. Differential Thermal Analysis (DTA) is very similar to Differential Scanning Calorimetry (DSC), both giving information on the thermal events. DTA measures the temperature difference between the sample and a reference for the same amount of energy supplied as heat, whereas DSC monitors the energy required to keep them at the same temperature. Thus, DSC instruments can quantify the heat flow, into and from the sample, and the specific heat can be determined.

In this work, thermogravimetric analysis and differential thermal analysis were measured simultaneously on a TA Instruments SDT Q600 with powdered samples of *ca.* 20 mg. The samples were heated at a constant rate (usually 5 ºC min^{-1}) in a nitrogen flow of 100 ml min^{-1} or in air, up to 1000 ºC in ceramic sample holders. An additional isotherm step has been added when required for the analysis.

Chapter 3 - Substitution and intercalation in titanium disulphide

3.1 Introduction

In 2001, Imai et al. reported[155] that the value of the thermoelectric power factor ($S^2\sigma$) of TiS_2 single crystals is 3.71 mW cm^{-1} K^{-2} at 300 K within the *ab* plane; a comparable value with that of commercial Bi_2Te_3, Table 3.1. While the thermal conductivity is significantly higher, thereby reducing the figure of merit, the low dimensionality of layered disulphide TiS_2 coupled with the capacity to tune transport properties by intercalation or substitution (Section 1.6.2) have sparked interest in TiS_2 as a candidate thermoelectric material.[118, 156-161]

Table 3.1 Thermoelectric properties of TiS_2 and $Bi_{1.65}Te_3$, measured along the *ab* plane of single crystals at 300 K.[155]

	TiS_2	$Bi_{1.65}Te_3$
S / μV K^{-1}	-250	-240
ρ / mΩ cm	1.7	1
$S^2\rho^{-1}$ / mW cm^{-1} K^{-2}	3.71	5.76
κ / mW cm^{-1}K^{-1}	67.8	20.2
ZT	0.16	0.86

The thermoelectric properties of bulk $Ti_{1+x}S_2$ samples ($0 \leq x \leq 0.05$), synthesised by solid-state reaction and consolidated by SPS, have been investigated.[157] The self-intercalation of titanium, accompanied by a charge carrier transfer to the Ti 3*d* band, enabled the optimisation of the charge carrier concentration. ZT reached a value of 0.48 at 700 K for $Ti_{1.025}S_2$. Similarly, bulk $Ti_{1.008}S_2$ prepared by sulphurisation of TiO_2 and consolidated by SPS reached ZT = 0.34 at 663 K.[162] Intercalating copper and silver has been a successful approach to improve the thermoelectric figure of merit by decreasing the thermal conductivity and the electrical resistivity simultaneously. A ZT value of 0.45 was observed for $Cu_{0.1}TiS_2$ and $Ag_{0.1}TiS_2$ at 800 K and 700 K respectively. [156, 160, 163] Substitution of sulphur by selenium has substantially improved the thermoelectric performance of $TiS_{2-x}Se_x$ ($0 \leq x \leq 2$) mainly because of a 25 % reduction in the thermal conductivity, reaching a ZT just above 0.4 at 673 K.[71, 163] Full block layers can be intercalated between consecutive TiS_2 layers, forming superlattices with general formula $(MX)_{1+x}(TiS_2)_n$, (M = Pb, Bi, Sn, Sb, rare-earth elements; n = 1, 2, 3).[164] The lattice

contribution to the thermal conductivity is substantially reduced by stacking faults while the electron mobility is conserved,[165] increasing ZT to 0.35 at 670 K for $(SnS)_{1.2}(TiS_2)_2$.[166]

According to the mineral commodity summary published by the US government in 2016 and based on the 2015 prices,[90] the prices of elemental titanium and sulphur are very competitive (respectively 9.93 \$ kg^{-1} and 0.1 \$ kg^{-1}) compared with bismuth and tellurium (respectively 16.54 \$ kg^{-1} and 89 \$ kg^{-1}) and these materials can be purchased and stored in large quantities. The raw materials cost of TiS_2 can be estimated to be around 4.3 \$ kg^{-1} (£ 2.9 kg^{-1}). Comparatively and with the same approach, the raw materials cost of Bi_2Te_3 is estimated to be 51.2 \$ kg^{-1} (*ca.* £ 35 kg^{-1}). While these numbers might not reflect the reality of large scale production and do not take processing costs into account, it is important to note that TiS_2 is an order of magnitude cheaper than the current commercialised materials.

The electrical properties of TiS_2 have been a subject of dispute, caused by discrepancies between the physical properties reported by different groups. This has led to uncertainty over whether 1T-TiS_2 is a semi-metal[167, 168] or a semiconductor, with different values of direct or indirect band gap. However, it is now well understood that the origin of the variations in physical properties are caused by non-stoichiometry as a result of sulphur volatilisation at high temperatures. This deviation from the nominal composition may be formulated as $Ti_{1+\gamma}S_2$, in which the excess titanium self-intercalates into the van der Waals' gap. The physical properties of $Ti_{1+\gamma}S_2$ phases are therefore sensitively dependent on the level of non-stoichiometry.[157, 158, 169] To ensure a systematic investigation of the compositional evolution of transport properties of doped titanium disulphide, the synthetic and pressing conditions were kept identical across all the members of the same series. This means that pristine TiS_2 was synthesised and consolidated for each investigated series. This accounts for the small variations in the transport properties of TiS_2 between the different sections of this chapter. Part of the following results have been published in the Journal of Materials Chemistry C.[170]

In this chapter, the effects of cobalt intercalation and molybdenum substitution on the electronic and thermal properties of TiS_2 are investigated. The structural changes and magnetic properties of Co_xTiS_2 ($0 \leq x \leq 0.75$) are also described.

3.2 Co_xTiS_2

A series of cobalt intercalated titanium disulphide, Co_xTiS_2 ($0 \leq x \leq 0.75$) has been prepared and characterised by powder X-ray and neutron diffraction, electrical and thermal transport property measurements, thermal analysis, SQUID magnetometry and muon spectroscopy. Intercalation has been used as a strategy to improve the thermoelectric performance of TiS_2 by attempting to control the charge carrier concentration using the charge transfer from Co^{2+} to the TiS_2 host electronic structure. A large range of cobalt doping level, $0 \leq x \leq 0.75$, was investigated to study the evolution of the transport and structural properties from a two-dimensional to a three-dimensional structure.

3.2.1 Synthesis

TiS_2 samples were synthesised, Section 2.1.1, from the elements Ti (Alfa Aesar, dehydrided, 99.99 %) and S (Sigma Aldrich, flakes, 99.99 %). Sealed silica tubes containing stoichiometric amounts of dried elements were evacuated down to a pressure of 10^{-4} Torr and placed in a furnace and heated at 350 °C for 4 h and 650 °C for 12 h, using a heating and cooling rate of 1 °C min^{-1}. Samples of composition Co_xTiS_2 (x = 0.02; 0.04; 0.06; 0.08; 0.1; 0.15; 0.2; 0.25; 0.3; 1/3; 0.4; 0.5; 2/3; 0.75) were synthesised from TiS_2 and elemental cobalt, Co (Alfa Aesar, 99.99 %). Appropriate quantities of the binary sulphide and Co were ground together, evacuated and sealed at 10^{-4} Torr in silica tubes. The heat treatment consisted in 2 successive periods of 48 h at 650 °C (heating/cooling rate 1 °C min^{-1}) with an intermediate regrinding.

3.2.2 Structural investigations

3.2.2.1 Powder X-ray diffraction

All investigated compositions of Co_xTiS_2 ($0 \leq x \leq 0.75$) were confirmed to be single phases by powder X-ray diffraction. However, due to the high fluorescence of cobalt with Cu radiation, the signal-to-noise ratio decreases abruptly with the incorporation of cobalt. This results in a loss of quality in the X-ray diffraction patterns and their structural refinement, in particular for samples that exhibit superstructure peaks at low 2θ where the background is the highest. At low intercalation levels (Co_xTiS_2 samples with $x \leq 0.15$), the powder X-ray diffraction data,

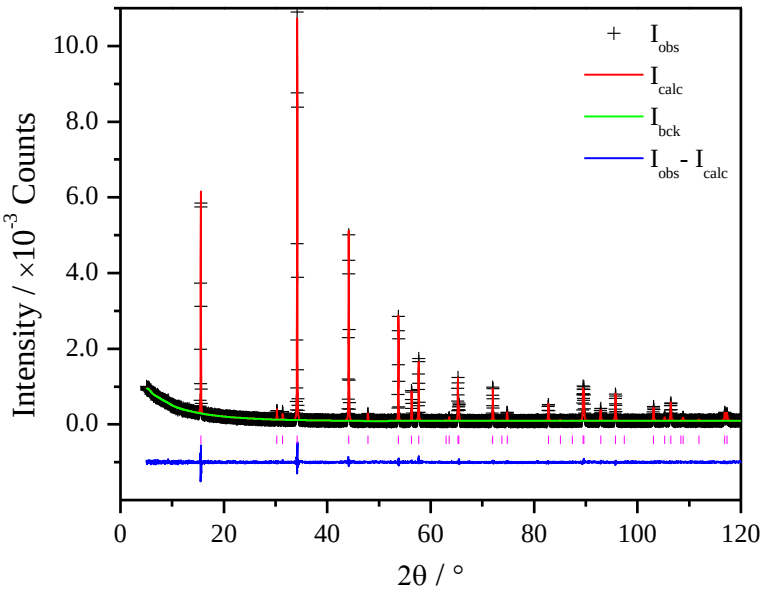

Figure 3.1 Observed (crosses), calculated (full line) and difference (lower full line) profiles for TiS_2 from Rietveld refinement of XRD data (R_{wp} = 8.35 %, χ^2 = 1.32). Bragg reflection positions are signalled by tick marks.

collected over the angular range $5 \leq 2\theta / ° \leq 120$ with a step size of 0.027646 ° for a period of 6 hours (Section 2.2) produced data suitable for reliable Rietveld refinement, Figure 3.1 and Figure 3.2. The structure of Co_xTiS_2 ($0 \leq x \leq 0.15$) was refined using the Rietveld method based on the CdI_2-type structure (space group: $P\bar{3}m1$) of TiS_2 single crystal data[171] using the GSAS software package.[130] The determined unit-cell parameters for TiS_2 are $a = b$ = 3.40676(5) Å and c = 5.69716(8) Å. Co_xTiS_2 phases are well described by a structural model in which cobalt atoms occupy the octahedral interstitial sites in a completely disordered fashion. The statistical distribution of Co in the van der Waals' gap of TiS_2 is represented in Figure 3.3 by the example of x = 0.15, for which Co occupies 15 % of the 1(b) octahedral site. The structural parameters determined for Co_xTiS_2 ($0 \leq x \leq 0.15$) are presented in Table 3.2.

The background parameters were refined first using the reciprocal interpolation function available in GSAS, followed by the scale factor, zero shift, unit cell parameters, atomic coordinates and isotropic thermal parameters. The peak shape was described using a pseudo-Voigt function (Section 2.4.1). All coefficients were refined individually until the refinement was stable enough for all non-zero coefficients to be refined simultaneously.

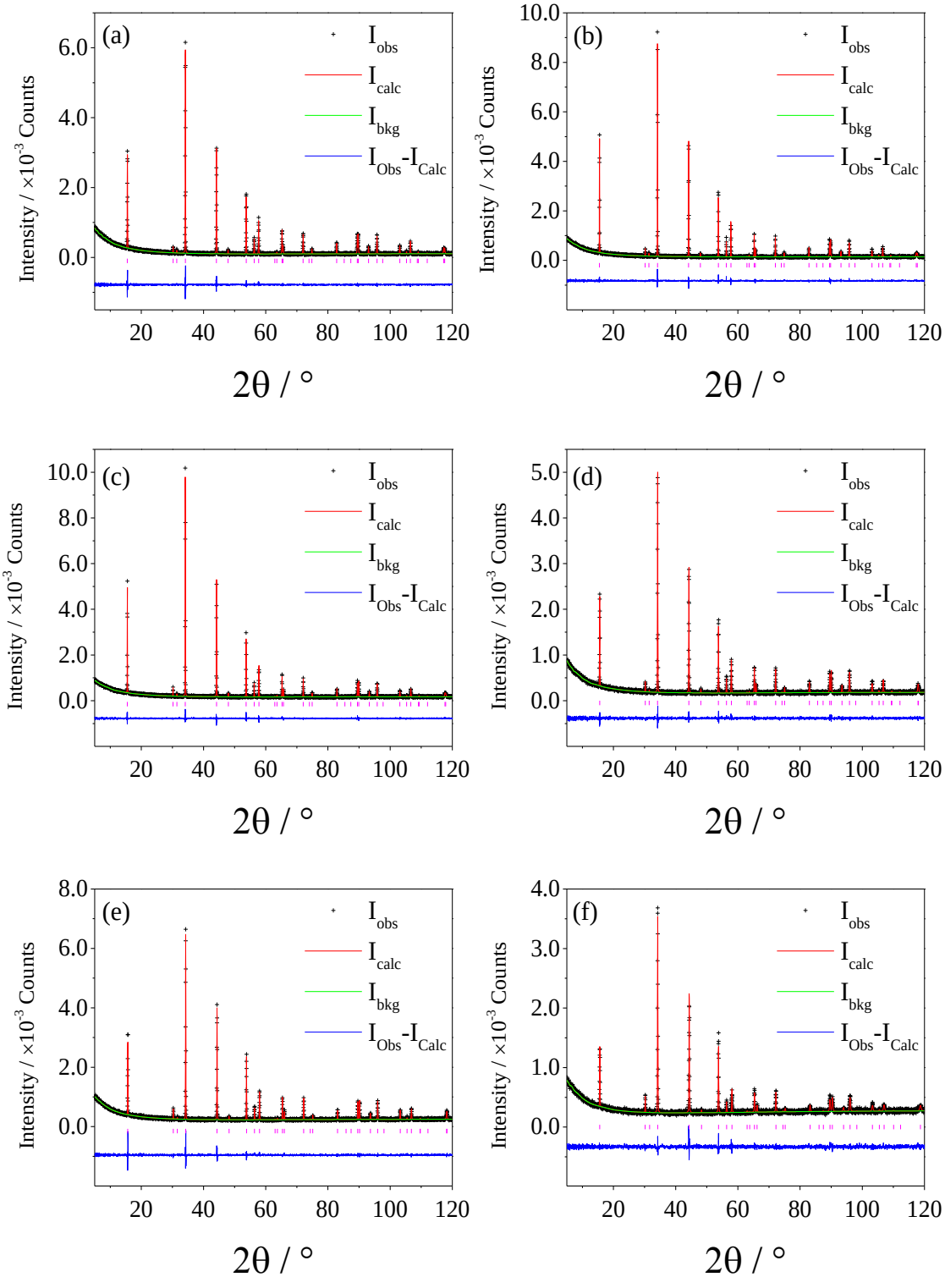

Figure 3.2 Observed (crosses), calculated (full line) and difference (lower full line) profiles for Co_xTiS_2 from Rietveld refinement of XRD data: (a) x = 0.02, (b) x = 0.04, (c) x = 0.06, (d) x = 0.08, (e) x = 0.10 and (f) x = 0.15. Reflection positions are signalled by tick marks.

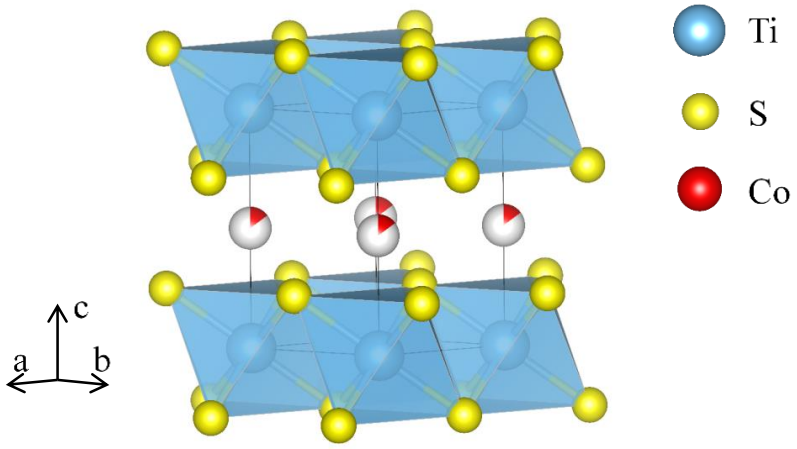

Figure 3.3 Structure of $Co_{0.15}TiS_2$ determined by powder X-ray diffraction. The white spheres correspond to octahedral vacancies, statistically occupied by Co atoms.

Table 3.2 Refined parameters from Rietveld analysis of powder X-ray diffraction data for Co_xTiS_2 with $x \leq 0.15$. (Space group $P\bar{3}m1$)[a]

		x in Co_xTiS_2			
		0	0.02	0.04	0.06
	a / Å	3.40676(5)	3.40527(6)	3.40442(5)	3.40321(5)
	c / Å	5.69716(8)	5.6841(1)	5.67862(9)	5.6687(1)
Ti	*B* / Å^2	0.44(5)	0.45(6)	0.71(6)	0.74(6)
S	*z*	0.2487(4)	0.2501(4)	0.2481(4)	0.2497(4)
	B / Å^2	0.31(4)	0.27(5)	0.50(4)	0.42(5)
Co	*B* / Å^2	-	0.45(6)	0.71(6)	0.74(6)
	d/ g cm^{-3}	3.25	3.29	3.33	3.38
	R_{wp} / %	8.4	8.5	7.5	7.2
	χ^2	1.33	1.33	1.28	1.31

		0.08	0.10	0.15
	a / Å	3.40311(8)	3.40302(4)	3.3997(2)
	c / Å	5.6616(2)	5.6550(1)	5.6341(3)
Ti	*B* / Å^2	0.34(7)	0.36(8)	0.12(12)
S	*z*	0.2514(5)	0.2526(5)	0.2521(9)
	B / Å^2	0.19(5)	0.07(5)	0.33(9)
Co	*B* / Å^2	0.34(7)	0.36(8)	0.12(12)
	d/ g cm^{-3}	3.41	3.46	3.56
	R_{wp} / %	6.9	6.7	6.8
	χ^2	1.17	1.45	1.42

[a] Ti on 1(a), (0, 0, 0); S on 2(d), (1/3, 2/3, z); Co on 1(b) (0, 0, 1/2). constrained at nominal composition.

A correction factor for low-angle asymmetry was also refined. The site occupancy factor (SOF) of Ti, Co and S were fixed to their nominal values and no significant improvement in the quality of fit was observed when allowing them to refine. Because Co is only occupying a small fraction of the interstitial octahedral position the thermal parameters for Ti and Co were constrained to be equivalent.

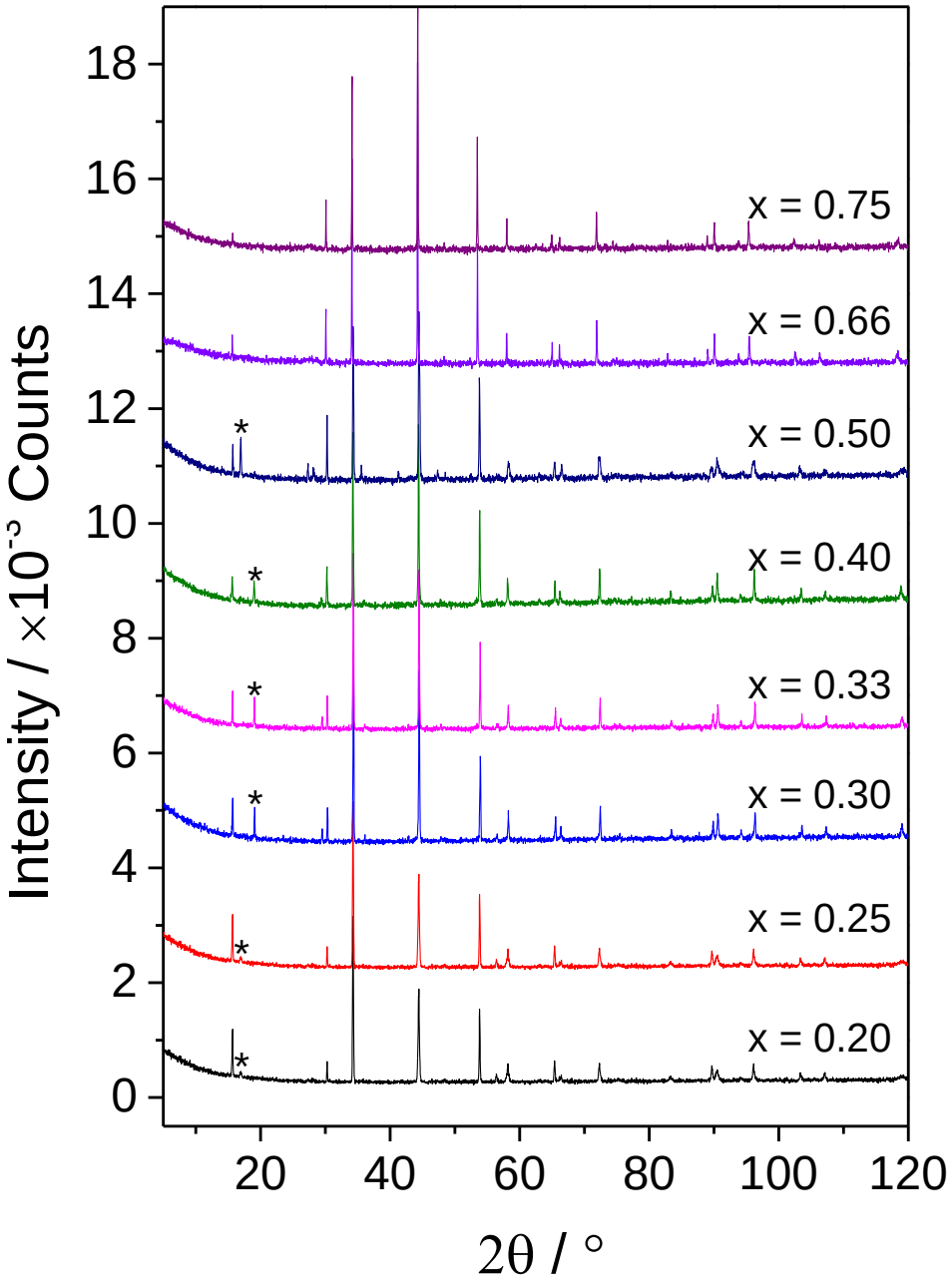

Figure 3.4 Powder X-ray diffraction data of Co_xTiS_2 samples ($0.20 \leq x \leq 0.75$) over the range $5 \leq 2\theta / ^{o} \leq 120$. Additional reflections arising from the formation of superstructures are signalled by an asterisk.

Powder X-ray diffraction patterns for Co_xTiS_2 ($x \geq 0.20$), Figure 3.4, show that additional reflections can be observed at low angle ($2\theta < 40^o$) for higher intercalation levels, $x \geq 0.25$. The presence of additional reflections, at high d-spacing, provides evidence for the formation of superstructures arising from cobalt-vacancy ordering. Due to the increased background and the relatively weak intensity of the superstructure peaks, the complete structural characterisation of these materials was performed using powder neutron diffraction, detailed in Section 3.2.2.2. The unit-cell parameters of the MS_2 phase, excluding the reflections corresponding to the existence of a superstructure, were refined based on the $P\bar{3}m1$ model. The compositional evolution of the primitive unit-cell parameters (a_p, c_p) of Co_xTiS_2, Figure 3.5, shows that, up to an intercalation level of 0.50, the introduction of inter-layer cobalt cations causes a marked contraction along the *c*-axis and to a lesser extent, changes in the in-plane (a_p) lattice parameter. The initial decrease in c_p and the presence of a minimum has been attributed to the covalency of the Co-S bond.[172, 173] This behaviour differs from most guest-TiS_2 systems such as Cu_xTiS_2,[160] Ag_xTiS_2[156] and misfit phases, $(SnS)_{1.2}(TiS_2)_2$,[166] where an increase in the *c* lattice parameter with increasing intercalation levels of the guest species is observed. For intercalation levels higher than 0.50, c_p increases again. Semi-empirical calculations accounting for ionic

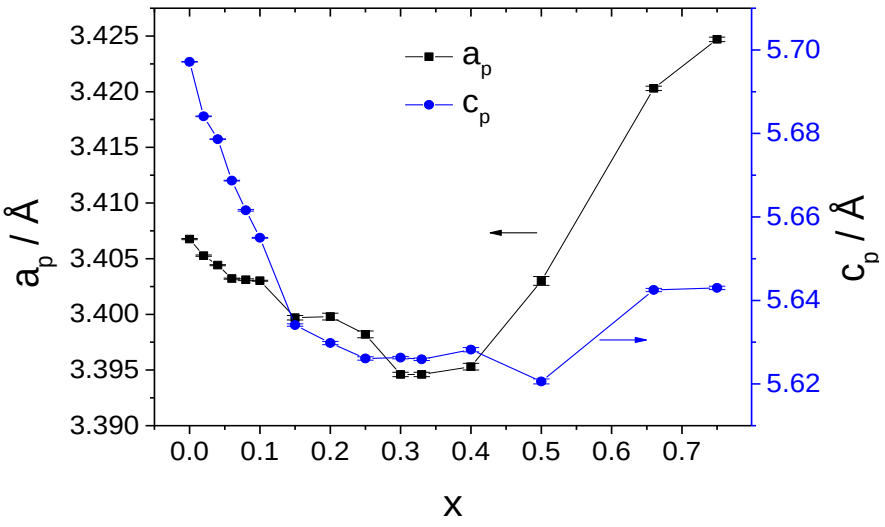

Figure 3.5 Primitive lattice parameters of Co_xTiS_2 as a function of x determined by powder X-ray diffraction.

radii, bond lengths, force constants and bond ionicity are in good agreement with the observations from powder X-ray diffraction reported here.[173] Detailed investigation of the compositional dependence of the structures of Co_xTiS_2 was carried out by powder neutron diffraction.

3.2.2.2 Powder neutron diffraction

Powder neutron diffraction data for Co_xTiS_2 (x = 0.2; 0.25; 1/3; 0.40; 0.5 and 2/3) were collected at the ISIS facilities on the GEM diffractometer described in Section 0. Rietveld refinement of the structural parameters was performed using the GSAS software package[130] in a multibank refinements using data from the banks 3 (high d-spacing, 2θ = 34.96 º) to 6 (back scattering, high resolution, 2θ = 154.4 º). The initial model was based on the primitive lattice parameters obtained from X-ray diffraction experiments and previously reported atom parameters. The refinement was initiated using the highest resolution bank (bank 6, 2θ = 154.4 º) before including data from other detector banks. By doing so, the multibank refinement benefits from the resolution of the backscattering detector bank while extending the range of d-spacing investigated on banks with lower resolution. The diffractometer constants were kept fixed and the background, histogram scale and absorption coefficient were refined until convergence. Structural parameters were then refined in turn until convergence, including the lattice parameters, atom coordinates and isotropic thermal displacement. The site occupancy factor (SOF) was also introduced as a variable, although in cases where no discernible

Table 3.3 Space group, unit cell parameters and goodness of fit of Rietveld refinements of neutron diffraction data for Co_xTiS_2.

	$Co_{0.20}TiS_2$	$Co_{0.25}TiS_2$	$Co_{1/3}TiS_2$	$Co_{0.40}TiS_2$	$Co_{0.50}TiS_2$	$Co_{2/3}TiS_2$
Space Group	$P\bar{3}m1$	$F2/m$	$P\bar{3}1c$	$P\bar{3}1c$	$I2/m$	$P\bar{3}m1$
a / Å	3.40037(3)	11.7708(4)	5.88111(4)	5.88235(4)	5.8943(2)	3.42065(3)
b / Å	-	6.8038(2)	-	-	3.40429(9)	-
c / Å	5.63223(7)	11.2444(2)	11.2573(2)	11.2563(2)	11.2350(2)	5.64181(8)
α / °	90	90	90	90	90	90
β / °	90	90.31(2)	90	90	90.278(2)	90
γ / °	120	90	120	120	90	120
R_{wp} / %	2.9	3.1	2.7	2.7	2.6	2.7
d / g cm^{-3}	3.65	3.74	3.86	4.01	4.17	4.31
χ^2	1.70	2.13	1.56	1.76	2.05	1.95

improvement in the quality of fit was observed, they were constrained to their nominal values. The peak shape was described by a pseudo-Voigt function and the profile parameters were refined last. Once convergence was achieved with all the aforementioned parameters refined, data from bank 5 (2θ = 91.30 º) were added. All refined parameters were fixed and the background, histogram scale and absorption correction of the added bank was refined to convergence. The diffractometer constants DIFA and DIFC were then refined to adjust with the high resolution detector bank. The instrument dependent ZERO, accounting for the timing differences between accelerator and acquisition and response times in the detector electronics was kept fixed to the calibrated value. When convergence was achieved, the diffractometer constants were fixed and the refinement of the Co_xTiS_2 phase was repeated for both detector banks, following the same procedure described above. This was repeated another two times with bank 4 (2θ = 63.62 º) and 3 (2θ = 34.96 º). The space group, unit cell parameters and goodness of fit, illustrated by the R_{wp} and χ^2, of Co_xTiS_2 (x = 0.2; 0.25; 1/3; 0.40; 0.5 and 2/3) are shown in Table 3.3.

All multibank refinements, Figure 3.6 to Figure 3.11 were stable with all aforementioned parameters refined simultaneously and values of R_{wp} and χ^2 that confirms the validity of the different models used. The converted primitive unit cell parameters, Table 3.4, are well in agreement with those obtained by X-ray diffraction analysis. The neutron diffraction investigation has led to the identification of three superstructure types that include monoclinic (x = 0.25 and 0.50) and trigonal (x = 1/3 and 0.40) crystal systems.

Table 3.4 Primitive unit cell parameters for Co_xTiS_2 determined by neutron diffraction and symmetry relationship to the superstructure cell.

x	a_p / Å	b_p / Å	c_p / Å	Symmetry
0.2	3.40037(3)	-	5.63223(7)	$a = a_p$, $c = c_p$
0.25	3.3979(4)	3.4019(4)	5.6222(2)	$a \approx 2\sqrt{3}\, a_p$, $b \approx 2\, a_p \approx 2\, b_p$, $c \approx 2\, c_p$
1/3	3.39546(4)	-	5.62865(2)	$a \approx \sqrt{3}\, a_p$, $b \approx \sqrt{3}\, a_p$, $c \approx 2\, c_p$
0.4	3.39618(4)	-	5.62815(2)	$a \approx \sqrt{3}\, a_p$, $b \approx \sqrt{3}\, a_p$, $c \approx 2\, c_p$
0.5	3.4031(2)	3.40429(2)	5.6175(2)	$a \approx \sqrt{3}\, a_p$, $b \approx a_p \approx b_p$, $c \approx 2\, c_p$
2/3	3.42065(3)	-	5.64181(5)	$a = a_p$, $c = c_p$

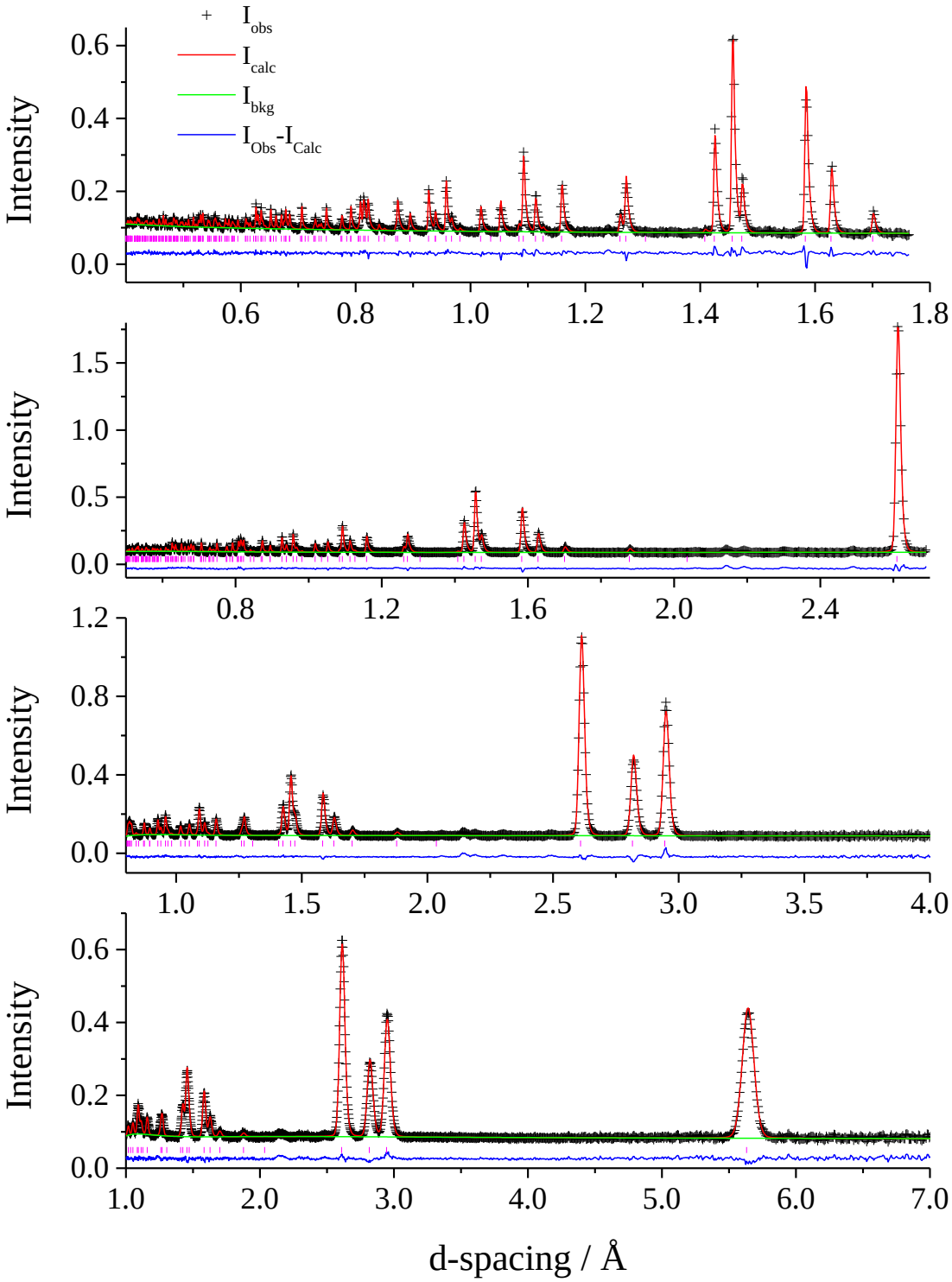

Figure 3.6 Observed (crosses), calculated (full line) and difference (lower full line) profiles for multibank Rietveld refinements of $Co_{0.20}TiS_2$ from powder neutron diffraction data simultaneously refined using 4 banks of the GEM diffractometer. From top to bottom, bank 6 (2θ = 154.4 º), bank 5 (2θ = 91.30 º), bank 4 (2θ = 63.62 º), bank 3 (2θ = 34.96 º). Bragg reflection positions are signalled by tick marks.

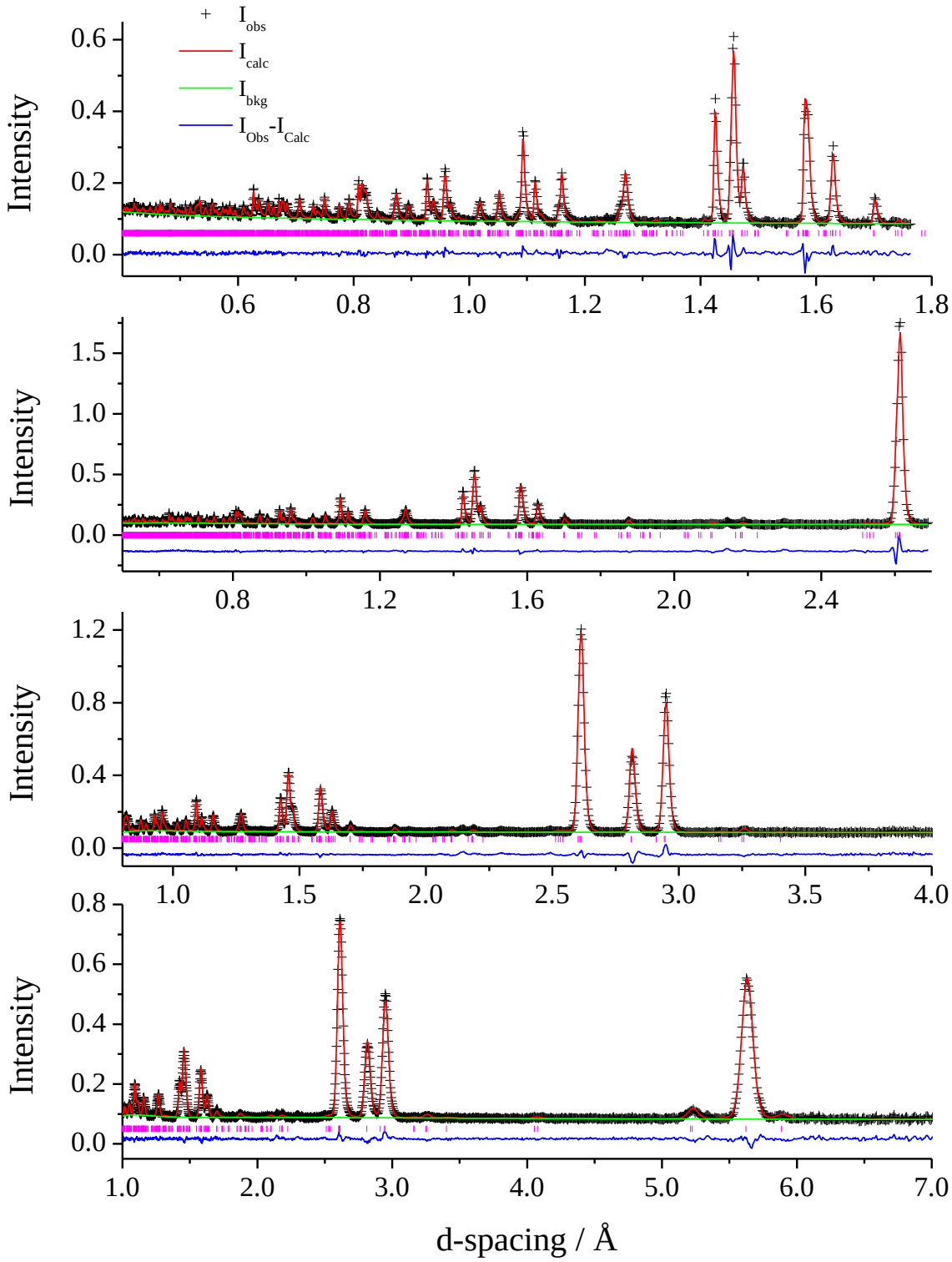

Figure 3.7 Observed (crosses), calculated (full line) and difference (lower full line) profiles for multibank Rietveld refinements of $Co_{0.25}TiS_2$ from powder neutron diffraction data simultaneously refined using 4 banks of the GEM diffractometer. From top to bottom, bank 6 (2θ = 154.4 º), bank 5 (2θ = 91.30 º), bank 4 (2θ = 63.62 º), bank 3 (2θ = 34.96 º). Bragg reflection positions are signalled by tick marks.

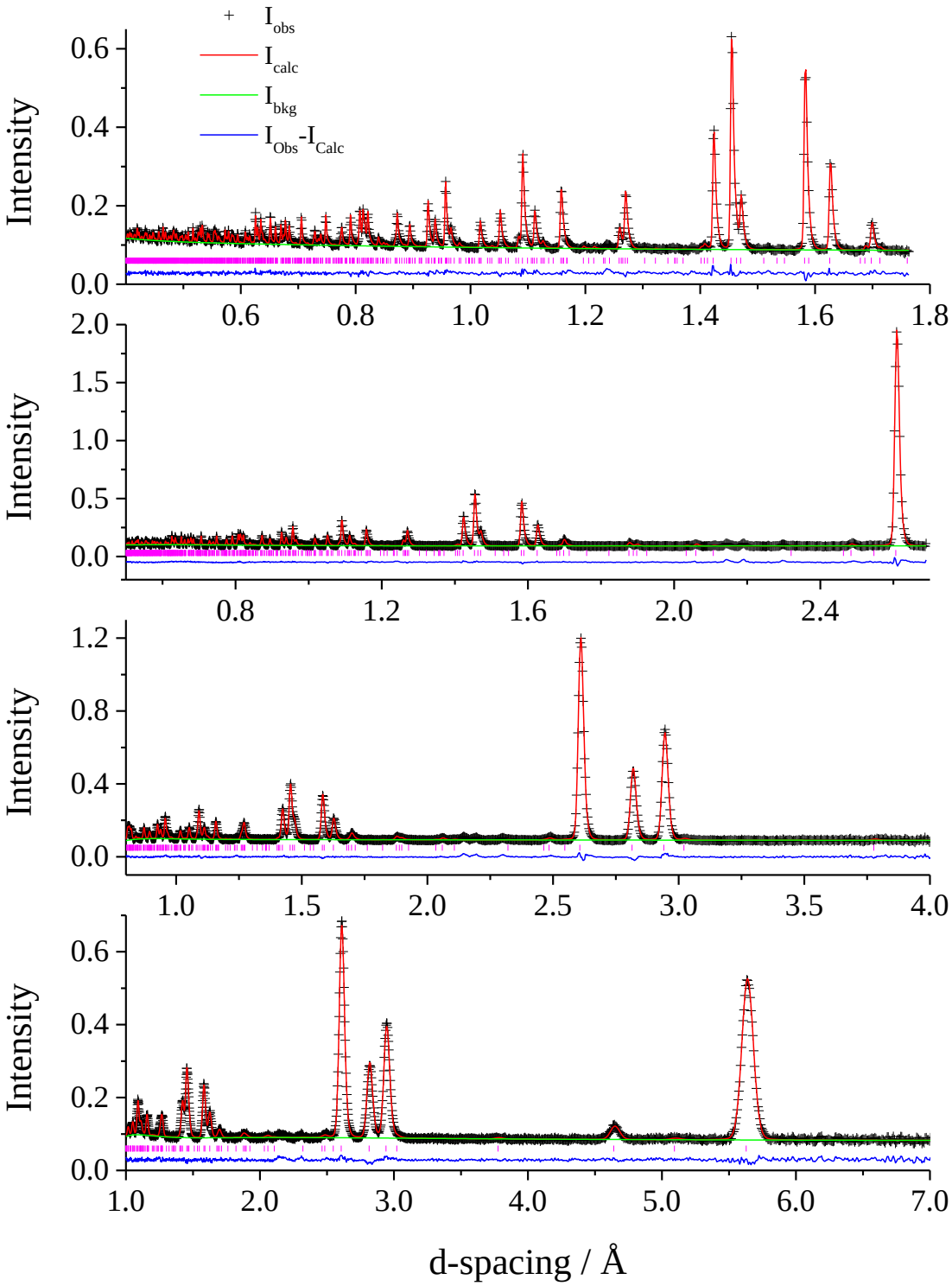

Figure 3.8 Observed (crosses), calculated (full line) and difference (lower full line) profiles for multibank Rietveld refinements of $Co_{1/3}TiS_2$ from powder neutron diffraction data simultaneously refined using 4 banks of the GEM diffractometer. From top to bottom, bank 6 (2θ = 154.4 º), bank 5 (2θ = 91.30 º), bank 4 (2θ = 63.62 º), bank 3 (2θ = 34.96 º). Bragg reflection positions are signalled by tick marks.

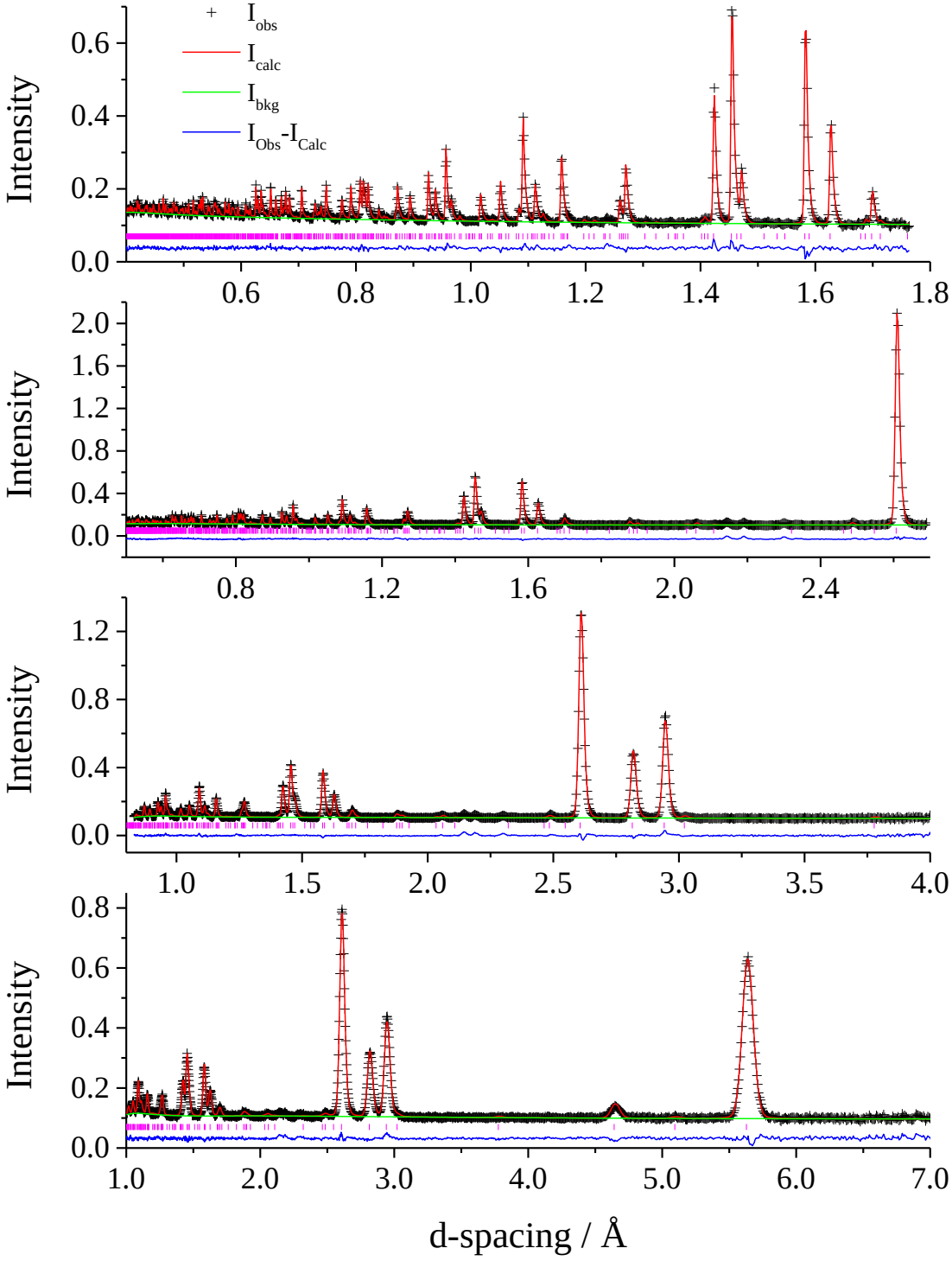

Figure 3.9 Observed (crosses), calculated (full line) and difference (lower full line) profiles for multibank Rietveld refinements of $Co_{0.40}TiS_2$ from powder neutron diffraction data simultaneously refined using 4 banks of the GEM diffractometer. From top to bottom, bank 6 (2θ = 154.4 º), bank 5 (2θ = 91.30 º), bank 4 (2θ = 63.62 º), bank 3 (2θ = 34.96 º). Bragg reflection positions are signalled by tick marks.

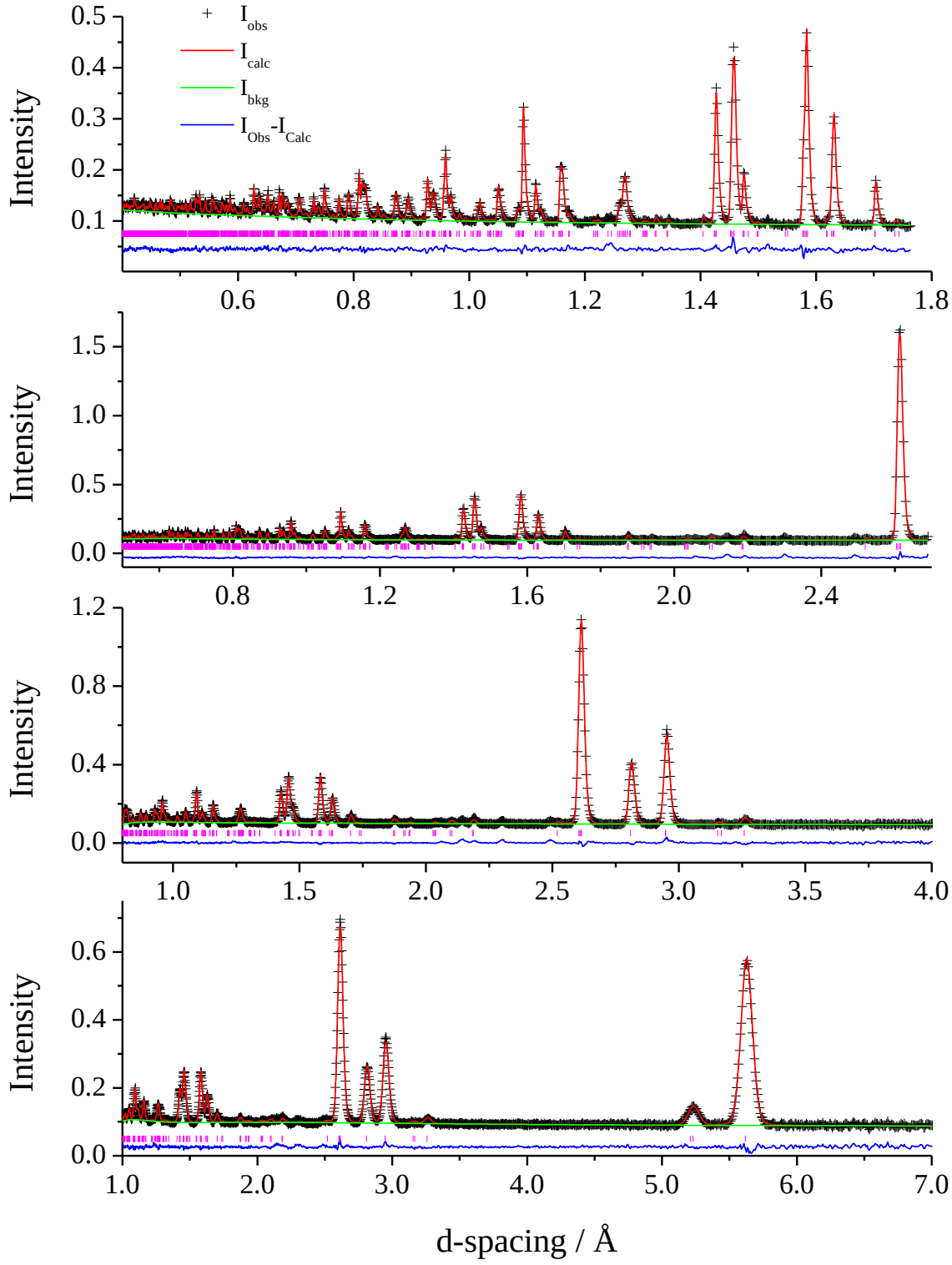

Figure 3.10 Observed (crosses), calculated (full line) and difference (lower full line) profiles for multibank Rietveld refinements of $Co_{0.50}TiS_2$ from powder neutron diffraction data simultaneously refined using 4 banks of the GEM diffractometer. From top to bottom, bank 6 (2θ = 154.4 º), bank 5 (2θ = 91.30 º), bank 4 (2θ = 63.62 º), bank 3 (2θ = 34.96 º). Bragg reflection positions are signalled by tick marks.

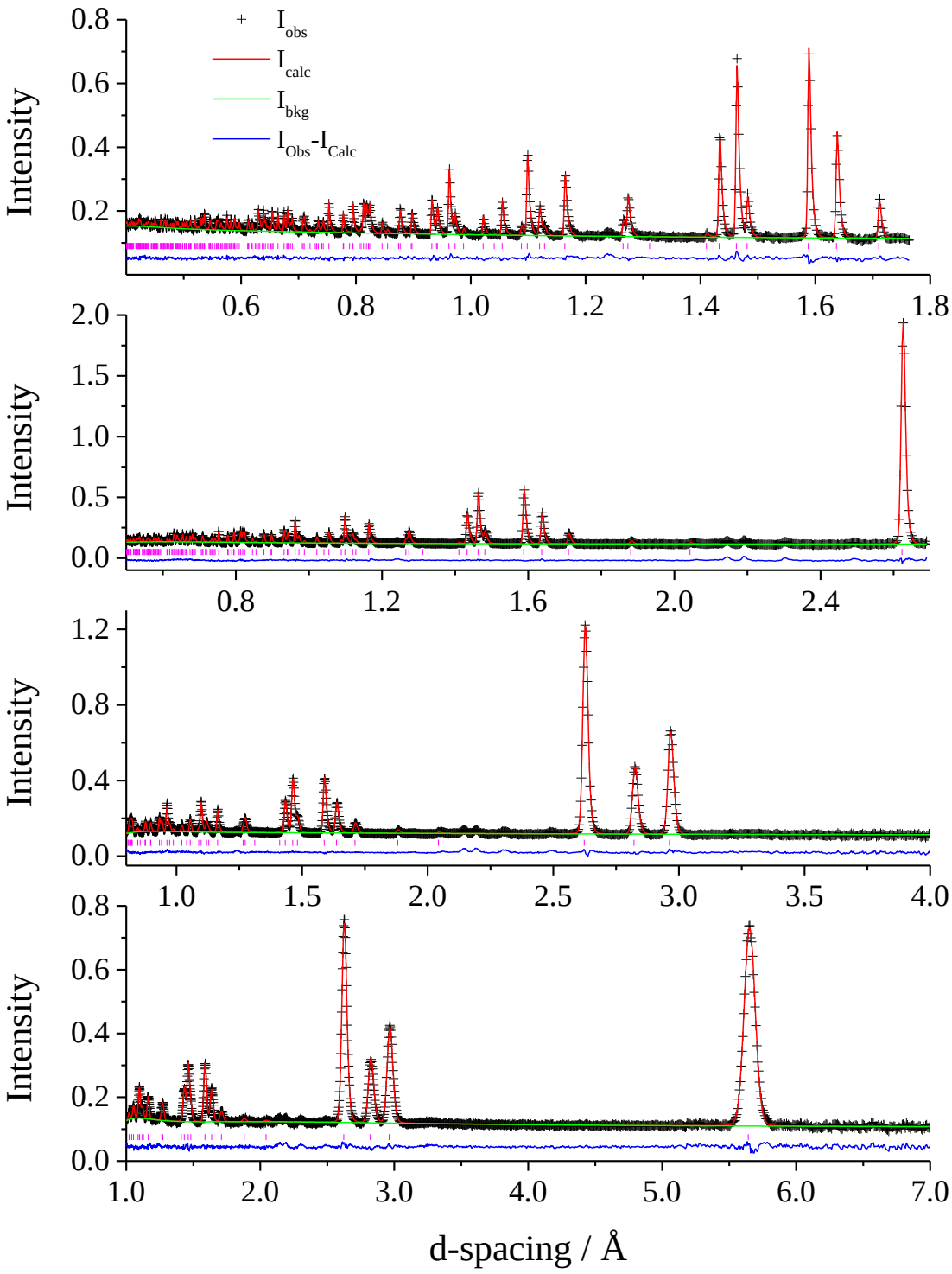

Figure 3.11 Observed (crosses), calculated (full line) and difference (lower full line) profiles for multibank Rietveld refinements of $Co_{2/3}TiS_2$ from powder neutron diffraction data simultaneously refined using 4 banks of the GEM diffractometer. From top to bottom, bank 6 (2θ = 154.4 º), bank 5 (2θ = 91.30 º), bank 4 (2θ = 63.62 º), bank 3 (2θ = 34.96 º). Bragg reflection positions are signalled by tick marks.

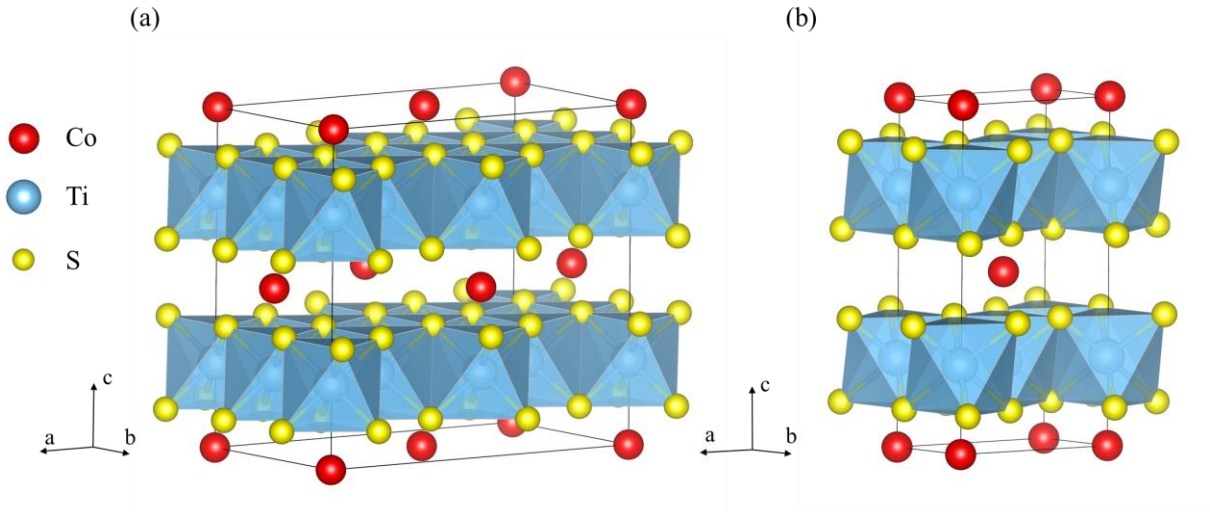

Figure 3.12 Superstructure of (a) $Co_{0.25}TiS_2$ and (b) $Co_{0.5}TiS_2$.

The structural model for $Co_{0.25}TiS_2$, Figure 3.12(a), is based on the M_5S_8 structure (space group $F2/m$)[174-176] in which cobalt in the 4(a) position occupies one in four octahedral sites within the van der Waals' gap following the arrangement for x = 0.25 presented in Section 1.2.3. This produces a super-cell related to that of TiS_2 by $a \approx 2\sqrt{3}\ a_p$, $b \approx 2\ a_p$, $c \approx 2\ c_p$. The model for $Co_{0.50}TiS_2$, Figure 3.12(b), is based on the M_3S_4 structure (space group $I2/m$)[50, 175, 177, 178] where the intercalated cobalt atoms occupy half of the available octahedral positions, forming chains of CoS_6 octahedra within the van der Waals' gap of TiS_2. In this case, the cobalt ordering

Table 3.5 Refined atomic parameters of $Co_{0.25}TiS_2$ (Space group $F2/m$) and $Co_{0.50}TiS_2$ (Space group $I2/m$).

$Co_{0.25}TiS_2$

Atom	Wyckoff Site	x	y	z	SOF	B / Å^2
Co(1)	4(a)	0	0	0	1	1.11(7)
Ti(1)	8(i)	0.5004(8)	0	0.2445(4)	1	0.47(2)
Ti(2)	8(h)	1/4	0.251(2)	1/4	1	0.47(2)
S(1)	8(i)	0.1674(8)	0	0.1248(5)	1	0.34(2)
S(2)	8(i)	0.1640(7)	1/2	0.1157(4)	1	0.34(2)
S(3)	16(j)	0.4173(4)	0.2491(9)	0.1245(3)	1	0.34(2)

$Co_{0.50}TiS_2$

Atom	Wyckoff Site	x	y	z	SOF	B / Å^2
Co(1)	2(a)	0	0	0	1	0.74(3)
Ti(1)	4(i)	-0.0100(5)	0	0.2555(2)	1	0.37(2)
S(1)	4(i)	0.3301(5)	0	0.3762(2)	1	0.22(2)
S(2)	4(i)	0.3344(5)	0	0.8822(2)	1	0.22(2)

Table 3.6 Refined atomic parameters of $Co_{1/3}TiS_2$ and $Co_{0.40}TiS_2$ (Space group $P\bar{3}1c$).

$Co_{1/3}TiS_2$

Atom	Wyckoff Site	x	y	z	SOF	B / Å^2
Ti(1)	2(b)	0	0	0	1	0.40(2)
Ti(2)	4(f)	1/3	2/3	-0.0047(2)	1	0.40(2)
S(1)	12(i)	0.333(1)	-0.0006(4)	0.37192(6)	1	0.33(2)
Co(1)	2(c)	1/3	2/3	1/4	0.852(9)	0.41(5)
Co(2)	2(a)	0	0	1/4	0.09(1)	0.41(5)

$Co_{0.40}TiS_2$

Atom	Wyckoff Site	x	y	z	SOF	B / Å^2
Ti(1)	2(b)	0	0	0	1	0.41(2)
Ti(2)	4(f)	1/3	2/3	-0.0048(3)	1	0.41(2)
S(1)	12(i)	0.333(1)	0.0001(4)	0.37142(6)	1	0.29(2)
Co(1)	2(c)	1/3	2/3	1/4	1	0.82(4)
Co(2)	2(a)	0	0	1/4	0.151(9)	0.82(4)
Co(3)	2(d)	2/3	1/3	1/4	0.049(9)	0.82(4)

produces lattice parameters related to the underlying hexagonal sub-cell through $a \approx \sqrt{3}\, a_p$, $b \approx a_p$, $c \approx 2\, c_p$. The refined atomic parameters determined from powder neutron diffraction data for the two monoclinic systems, $Co_{0.25}TiS_2$ and $Co_{0.50}TiS_2$, are given in Table 3.5.

Recently, Kawasaki *et al.*[179] have used single-crystal X-ray diffraction data to solve the structures of $Co_{0.26}TiS_2$ and $Co_{0.57}TiS_2$ in the trigonal space groups $P\bar{3}m1$ with a unit cell corresponding to $2a_p \times 2a_p \times 2c_p$ where a_p and c_p are the unit cell parameters of TiS_2. However, these models describe two successive cobalt/vacancy layers differently with one nearly fully ordered and the next one almost fully disordered; such an arrangement is energetically unlikely.[48] Support for the monoclinic distortions in Co_xTiS_2 with x = 0.25 and 0.50 have been found in the work of Danot *et al*. on $Co_{0.25}TiS_2$[180] and M_xTiS_2 (M = Fe, Co and Ni).[181, 182]

Both $Co_{1/3}TiS_2$ and $Co_{0.40}TiS_2$ adopt the trigonal M_2S_3-type structure (space group $P\bar{3}1c$),[50, 183] with a unit cell related to that of TiS_2 by $a \approx \sqrt{3}a_p$, $b \approx \sqrt{3}a_p$, $c \approx 2c_p$. The atomic parameters for both compositions are given in Table 3.6. The ideal superstructure, presented in Section 1.2.3, corresponds to complete site occupancy of the Co(1) position; however, to obtain satisfactory fits, refinement of cobalt site occupancy factors was extended the other two possible positions, Co(2) and Co(3), Figure 3.13. For $Co_{1/3}TiS_2$, only the Co(2) position produced a non-zero SOF, and 85 % occupancy of the expected Co(1) position was observed, leading to a

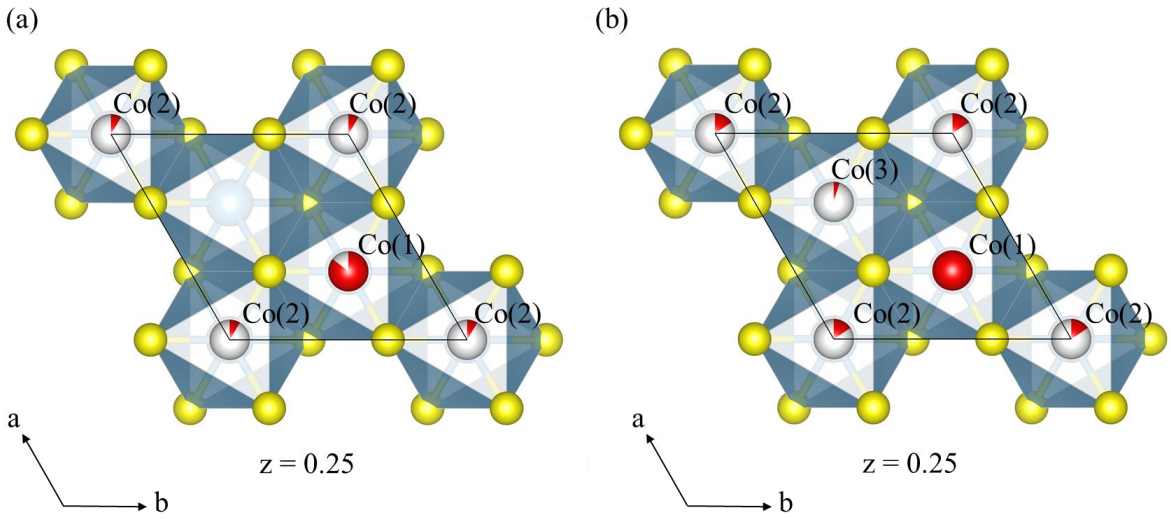

Figure 3.13 Cobalt ordering in (a) $Co_{1/3}TiS_2$ and $Co_{0.40}TiS_2$,

crystallographically-determined composition $Co_{0.31(2)}TiS_2$. The structure of $Co_{0.40}TiS_2$ was refined allowing the excess cobalt to be distributed over the two additional octahedral positions. The SOF of Co(1) was fixed to 1 while the SOF of Co(2) and Co(3) were allowed to refine. The sum of the SOF of Co(2) and Co(3) was constrained to 0.2 in order to keep the total stoichiometry of $Co_{0.40}TiS_2$. Removing the stoichiometry constraints during refinement does not lead to significant deviations from their constrained values, nor does it produce any apparent improvement in the quality of refinement. In the recent work of Kawasaki *et al.*[179], the structure of $Co_{0.43}TiS_2$ was solved by single crystal methods in the same trigonal structure (space group $P\bar{3}1c$) with a higher degree of disorder in the cation distribution: SOF(Co(1)) = 0.72, SOF(Co(2)) = 0.47 and SOF(Co(3)) = 0.09.

The remaining two compositions, $Co_{0.2}TiS_2$ and $Co_{2/3}TiS_2$, at the extremes of the investigated series, show no evidence for the formation of superstructures due to cobalt ordering. No additional reflections appear at high d-spacing (bank 3, 2θ = 34.96 º), Figure 3.6 and Figure 3.11 for $Co_{0.2}TiS_2$ and $Co_{2/3}TiS_2$, respectively. The atomic parameters for $Co_{0.2}TiS_2$ and $Co_{2/3}TiS_2$ are given in Table 3.7. Both structures consist of randomly distributed cobalt in the van der Waals' gap of the TiS_2 host (space group $P\bar{3}m1$) similarly to the X-ray diffraction studies presented in Section 3.2.2.1 for Co_xTiS_2 ($0.02 \leq x \leq 0.15$). While the distribution of cobalt in $Co_{0.2}TiS_2$ is well described by this model (refinement of the SOF does not

Table 3.7 Refined atomic parameters of $Co_{0.20}TiS_2$ and $Co_{2/3}TiS_2$ (Space group $P\bar{3}m1$).

$Co_{0.20}TiS_2$

Atom	Wyckoff Site	x	y	z	SOF	B / Å^2
Ti(1)	1(a)	0	0	0	1	0.56(2)
S(1)	2(d)	1/3	2/3	0.2539(2)	1	0.43(2)
Co(1)	1(b)	0	0	1/2	0.2	0.81(8)

$Co_{2/3}TiS_2$

Atom	Wyckoff Site	x	y	z	SOF	B / Å^2
Ti(1)	1(a)	0	0	0	1	0.73(2)
S(1)	2(d)	1/3	2/3	0.2591(2)	1	0.53(2)
Co(1)	1(b)	0	0	1/2	0.484(4)	0.69(5)
Co(2)	2(d)	2/3	1/3	0.354(3)	0.070(2)	0.69(5)

substantially change the quality of the fit nor does the SOF deviate significantly from 0.2), the case of $Co_{2/3}TiS_2$ is different. The disordered distribution of cobalt in octahedral sites of the van der Waals' gap does not adequately describe the powder neutron diffraction data with higher than expected values of the weighted residual (R_{wp} = 3.2 %, χ^2 = 2.76) being observed. Moreover, there is a significant discrepancy between the refined composition ($Co_{0.43(1)}TiS_2$) and the nominal stoichiometry ($Co_{2/3}TiS_2$).

To investigate the origin of this discrepancy, the difference Fourier map ($|F_{obs}-F_{calc}|$) was computed using DRAWxtl.[184] The 3D map of $Co_{2/3}TiS_2$ from Rietveld refinement with statistical distribution of cobalt ions in octahedral sites, Figure 3.15 (a), indicates some residual nuclear density within the van der Waals' gap, at the tetrahedral site, and on the sulphur site. Introduction of cobalt into the tetrahedral site, Co(2) in 2(d), substantially improves the quality of the refinement, Figure 3.15 (b). The refined composition of $Co_{0.624(8)}TiS_2$ is also much closer to the nominal stoichiometry with only a slight remaining Co deficiency. The conclusion drawn here is supported by similar findings from Kawasaki *et al.*[179], where 11 % of Co in $Co_{0.57}TiS_2$ is present in tetrahedral positions. The simultaneous presence of cobalt in octahedral and tetrahedral sites is also expected to play a role in the observed increase in the c_p and a_p lattice parameter observed for Co_xTiS_2 ($x \geq 0.50$) in Figure 3.5. The semi-empirical calculations by Inoue and Negishi,[173] referred to in Section 3.2.2.1, did not take the occupancy of tetrahedral sites into account and the calculated c parameter is lower than expected with $c_p \approx$ 5.60-5.61 Å against $c = c_p \approx$ 5.64 Å from X-ray and neutron diffraction analysis.

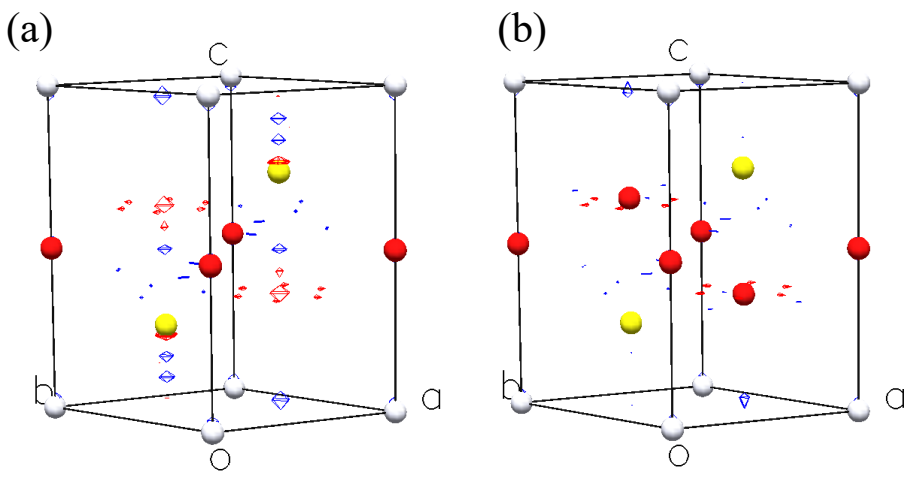

Figure 3.15 Difference Fourier maps of $Co_{2/3}TiS_2$, (a) with cobalt only in octahedral sites and (b) with cobalt in octahedral and tetrahedral positions. Red and blue contours correspond to positive and negative regions with identical amplitudes.

3.2.3 Magnetic properties

3.2.3.1 Low temperature neutron diffraction

Powder neutron diffraction data of samples of composition Co_xTiS_2 (x = 0.2; 0.25; 1/3; 0.40; 0.5 and 2/3) were collected at a temperature of *ca.* 2 K, Figure 3.14 and Appendix B. Comparison with room temperature data shows no evidence for magnetic scattering.

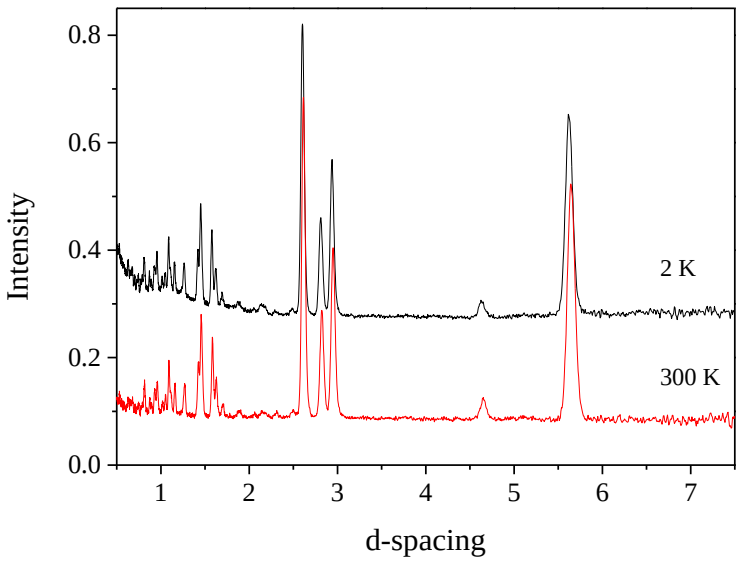

Figure 3.14 Powder neutron diffraction data (bank 3, 2θ = 34.96º) of $Co_{1/3}TiS_2$ at 2 K (black line) and at 300 K (red line).

3.2.3.2 Magnetic susceptibility

Magnetic susceptibility data for Co_xTiS_2 (x = 0.25; 1/3 and 2/3) were collected by Dr S. Hébert at the CRISMAT laboratories in Caen, France. Data for Co_xTiS_2 (x = 0.20; 0.5 and 3/4) were collected by Dr J. Prado-Gonjal with the help of Dr G. Stenning at the ISIS facility, Didcot, UK.

Magnetic susceptibility data for $Co_{0.20}TiS_2$, Figure 3.16(a), clearly reveal a ferromagnetic transition at T_C = 130 K. A similar transition in AC susceptibility data for single crystals of Co_xTiS_2 ($0.075 \leq x \leq 1/3$) has been reported by Inoue *et al.*[185], but in the present studies, no magnetic ordering transitions were observed for x = 0.25 and x = 1/3, which may be attributable to differences in the homogeneity of the single crystal and powder samples. It is also possible that the samples in the previous studies and in the present $Co_{0.20}TiS_2$ sample contain trace amounts of CoS_2, which is a ferromagnet with a Curie temperature reported to be between 110 K and 130 K.[186-188] For Co_xTiS_2 with $0.25 \leq x \leq 2/3$, Figure 3.16, the magnetic susceptibility decreases with cobalt intercalation, consistent with the work of Danot *et al.*[182] Data in the paramagnetic regions are well described by a modified Curie-Weiss law ($\chi = \chi_0 + C/T-\theta$) incorporating a temperature independent term (χ_0). At low cobalt contents, the effective magnetic moments (Table 3.8) are in reasonable agreement with the spin-only values for low-spin octahedral Co^{2+} (μ_{eff} = 1.73). However, as the cobalt content increases above x = 1/3, the effective moment falls and begins to deviate significantly from spin-only behaviour. This may be attributed to an increasing degree of electron delocalisation as the concentration of cobalt in the vacancy layer increases. This observation supports the conclusion previously drawn by Inoue *et al.*[114, 185] on the formation of a $(t_{2g})^6(e_g)^1$ low-spin cobalt-based band near the Ti 3*d* band for $x \geq 0.175$. The negative Weiss constant indicates that in all phases for $x \leq 2/3$, the dominant magnetic exchange interactions are antiferromagnetic in origin, with a weak ferromagnetic component observed in the $\chi(T)$ behaviour for $Co_{0.25}TiS_2$ and $Co_{2/3}TiS_2$. Antiferromagnetic correlations may also serve to reduce the effective magnetic moment as evidenced by the decrease in the quantity $(8\chi T/n)^{1/2}$ with decreasing temperature, Figure 3.17.

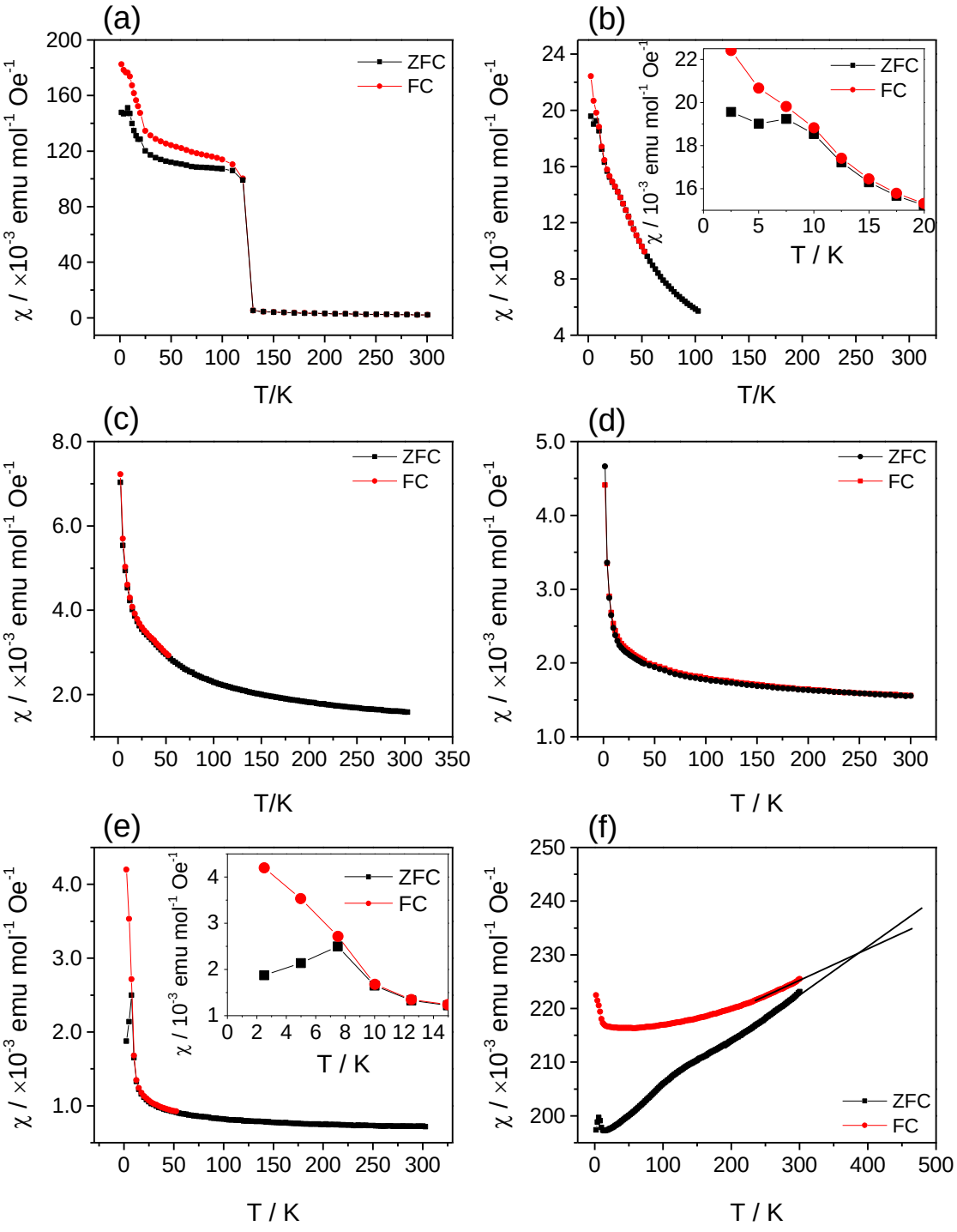

Figure 3.16 Zero-field cooled and Field-cooled molar magnetic susceptibility of Co_xTiS_2, (a) x = 0.20; (b) x = 0.25; (c) x = 1/3; (d) x = 0.50; (e) x = 2/3 and (f) x = 0.75.

Table 3.8 Derived magnetic parameters from the fit of a modified Curie-Weiss law to magnetic susceptibility data over the temperature range specified.

x	Temp. range (K)	χ_0 (emu mol^{-1})	θ (K)	μ_{exp} per Co
0.2	150-300	-	-26(3)	2.36(7)
0.25	40-100	$3.91(8)\times10^{-4}$	-13.5(5)	2.24(3)
1/3	40-300	$1.100(7)\times10^{-3}$	-36(1)	1.15(4)
0.5	55-215	$1.430(6)\times10^{-3}$	-45(2)	0.63(1)
2/3	25-220	$6.70(2)\times10^{-4}$	-17(2)	0.37(3)

The magnetic susceptibility data observed for $Co_{0.75}TiS_2$, Figure 3.16(f), have a very different behaviour. The data appear to indicate a magnetic ordering transition that occurs above 300 K, extrapolation of the data, corresponding to the solid lines, was used to estimate the transition temperature in the range 350 K to 400 K. This may be associated with the presence of trace amounts of CoS (T_N = 358 K),[187] suggesting that the limit of the single-phase region of Co_xTiS_2 lies in the range $2/3 \leq x \leq 0.75$. These results compare very well with the recent study by Hébert et al., published almost simultaneously with the present work, in which the solubility limit of Co_xTiS_2 is established to be x = 0.6 by combining magnetic susceptibility data, electron diffraction and EDX analysis.[71]

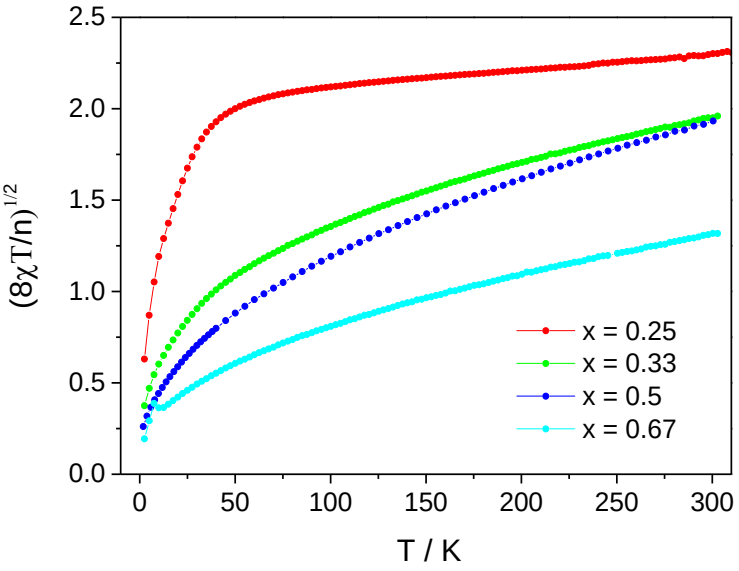

Figure 3.17 Temperature dependence of the effective magnetic moments, expressed as $(8\chi T/n)^{1/2}$ in Co_xTiS_2.

3.2.3.3 Muon spectroscopy

In order to continue the investigations on the magnetic properties of Co_xTiS_2, muon spin relaxation experiments, μSR, were carried out with Dr F. Coomer on the EMU spectrometer at the ISIS facility, Didcot, UK. The time dependence of the muon spin relaxation of Co_xTiS_2 (x = 0.20; 1/3 and 2/3), Figure 3.18, and Co_xTiS_2 (x = 0.25 and 0.5), Figure 3.19, are shown from high temperature (T = 200 K) down to the CCR or cryostat base-temperatures, *ca*. 9 K and 1.7 K respectively.

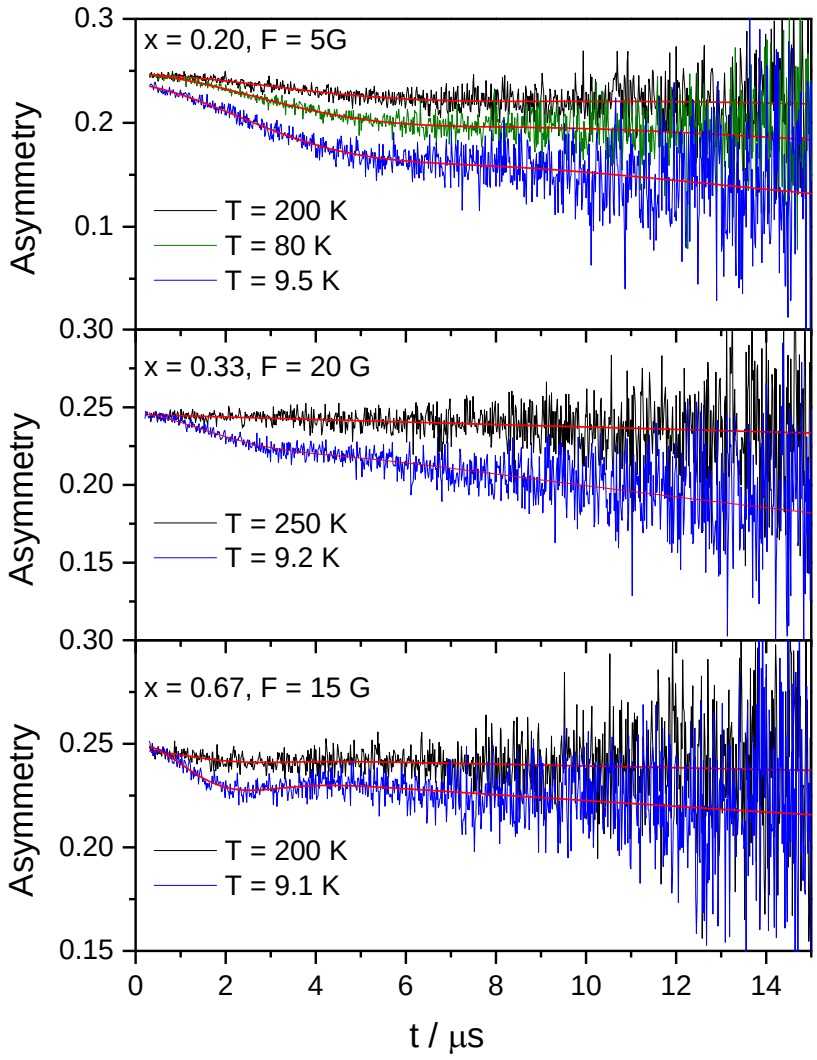

Figure 3.18 Time dependence of the spin relaxation in specified longitudinal field at selected temperatures for Co_xTiS_2 (x = 0.20; 1/3 and 2/3). The red lines correspond to fits described in the text.

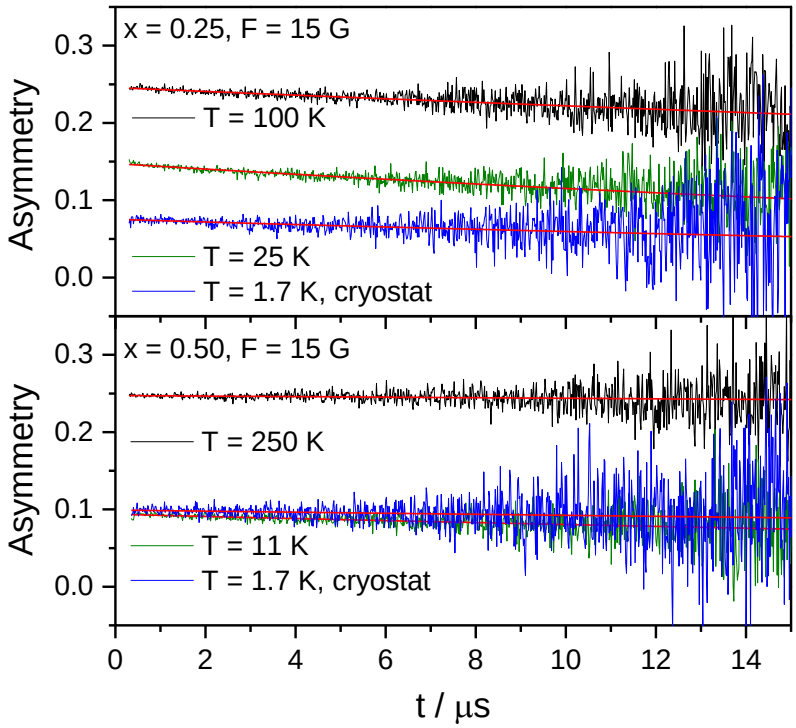

Figure 3.19 Time dependence of the spin relaxation in a longitudinal field at selected T for Co_xTiS_2 (x = 0.25 and 0.5). The red lines correspond to fits described in the text.

A small longitudinal field ($5 \leq LF / G \leq 20$) was applied to decouple the muon spin from the nuclear moment of Co in order to observe the muon relaxation asymmetry due to the electronic spins alone. For Co_xTiS_2 (x = 0.20; 1/3 and 2/3), the applied fields were too weak to fully decouple the nuclear moments and a small Kubo-Toyabe component to account for this contribution was implemented to the fit. The muon spin relaxation was therefore modelled using an exponential decay, to account for fluctuating electronic moments, and a small static Kubo-Toyabe contribution. The LF-μSR data of Co_xTiS_2 (x = 0.20; 1/3 and 2/3) were well-described by the following function, Equation 3.1:

$$A(t) = A_1 \exp(-\lambda_1 t) + A_2 \times \left[{}^1/_3 + {}^2/_3 \left(1 - {\Delta_2}^2 t^2\right) \exp\left(- {}^1/_2 {\Delta_2}^2 t^2\right) \right] \quad (3.1)$$

Where A_1 and A_2 are the scale factors of the exponential and Kubo-Toyabe function respectively, λ_1 is the depolarisation rate and Δ_2 is the Gaussian field distribution experienced at the muon site. The temperature dependences of the initial asymmetry ($A_0 = A_1 + A_2$) and the

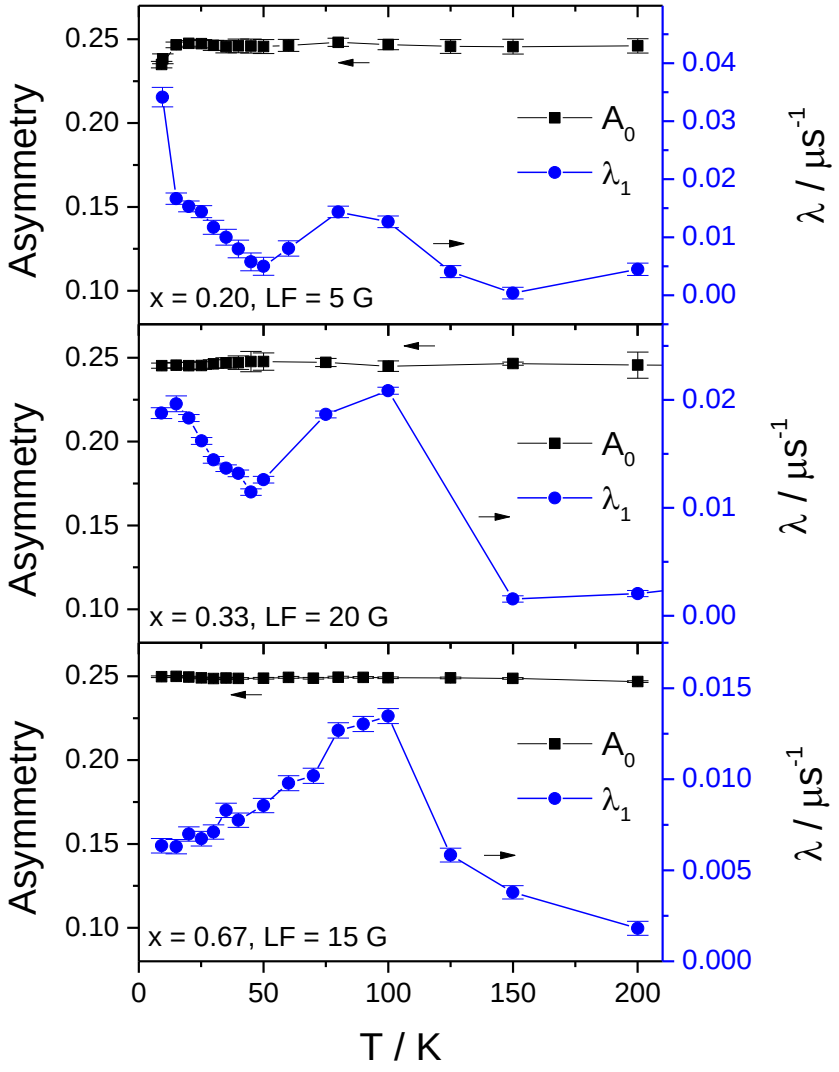

Figure 3.20 Time dependence of the initial asymmetry, A_0, and the depolarisation rate, λ_1, from μSR measurements on Co_xTiS_2 (x = 0.20; 1/3 and 2/3).

depolarisation rate are given in Figure 3.20. As expected, the scale factors and the field distribution for Co_xTiS_2 (x = 0.20; 1/3 and 2/3), Appendix C, remain largely temperature independent with $A_2 \ll A_1$. The initial asymmetry, A_0, Figure 3.20, remains constant across the investigated temperature range, indicating that the relaxation occurs within the observable time window. In the case of x = 0.20, a small decrease appears at the two lowest investigated temperatures indicating that some depolarisation occurs outside the time window measurable at the ISIS source, due to the finite width of the ISIS muon pulse. All three samples exhibit an increase in the depolarisation rate below 150 K, peaking at 100 K. This may be indicative of a

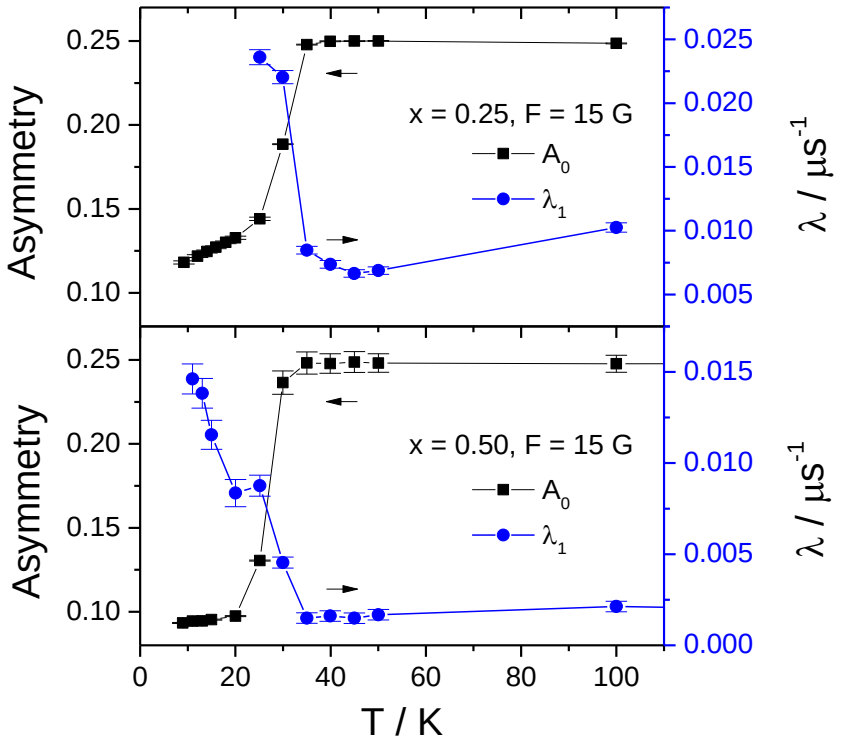

Figure 3.21 Time dependence of the initial asymmetry, A_0, and the depolarisation rate, λ_1, from μSR measurements on Co_xTiS_2 (x = 0.25 and 0.5).

transition between paramagnetic and ordered states in CoS_2 traces observed in the magnetic susceptibility of $Co_{0.20}TiS_2$. As the temperature decreases further, the depolarisation rate increases again for samples of composition Co_xTiS_2 (x = 0.20 and 1/3), indicating a slowing down of the electronic spin fluctuations. In the case of x = 2/3, this slowing down does not occur at the temperatures investigated. No evidence of magnetic ordering was found in these samples.

Conversely, the muon spin relaxation, Figure 3.19, for samples of composition Co_xTiS_2 (x = 0.25 and 0.50) shows a large fall of the initial asymmetry below *ca*. 35 K. This is indicative of a strong internal field causing the muon to depolarise before the detection limit set by the muon pulse duration. This constitutes strong evidence for the presence of magnetic moments that are static or quasi-static within the observable time window. For both samples, the longitudinal

field of 15 G was sufficiently strong to fully decouple the nuclear moments and the parameters given in Figure 3.21 are the result of the fit to a simple exponential decay, Equation 3.2:

$$A(t) = A_1 \exp(-\lambda_1 t) \tag{3.2}$$

where A_1 is the scale factor and λ_1 is the depolarisation rate. At time t = 0, the initial asymmetry of $Co_{0.50}TiS_2$ has lost 2/3 of its high temperature value, corresponding to a transition to a magnetically ordered state. Because no magnetic ordering was observed using neutron diffraction, this ordered state appears to be short-range in character. The initial asymmetry of $Co_{0.25}TiS_2$ shows two successive falls below 35 K. The first one at 35 K, similar to that observed for $Co_{0.50}TiS_2$, is a sharp decrease accompanied by an increase in the depolarisation rate. The second one, below 25 K, is a gradual decrease. The muon spin relaxation below this

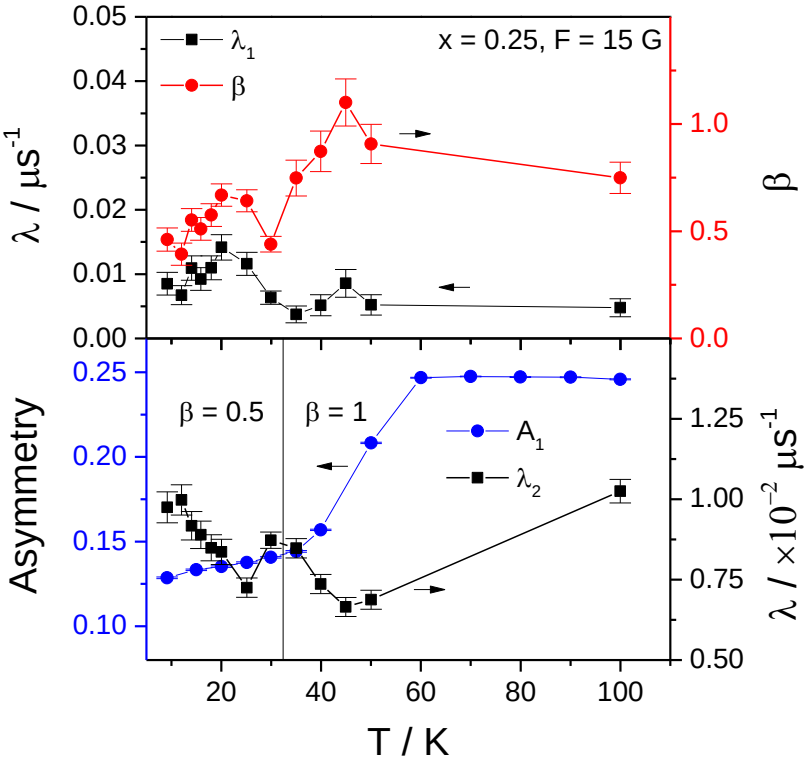

Figure 3.22 Temperature dependence of the relaxation rate, λ_1, and β coefficient of the stretched exponential fit of $Co_{0.25}TiS_2$ μSR data (top). Initial asymmetry and relaxation rate of the stretched exponential, λ_2, with fixed β coefficients (bottom).

temperature can no longer be fitted using a simple exponential function and the data were most successfully described using a stretched exponential, Equation 3.3:

$$A(t) = A_1 \exp\left(-(\lambda_1 t)^{\beta}\right) \tag{3.3}$$

where β is the stretching exponent, the value of which deviates from unity as the distribution of relaxation times broadens. The stretching exponent, β, is first allowed to vary and falls from a value around unity to around 0.5 below 40 K, Figure 3.22. A value of β around 0.5 could be indicative of a spin glass behaviour and a second set of fits were successful by fixing β as 1 at $T \geq 35$ K and as 0.5 at $T \leq 30$ K. However, there is no evidence in the magnetic susceptibility data that supports such a transition at this temperature. The deviation from 1 of the stretching exponent is more likely to be indicative of a wider local field distribution. In order to investigate the low-temperature behaviour of Co_xTiS_2 (x = 0.25 and 0.50), additional experiments in a cryostat sample environment were carried out to investigate the muon spin relaxation down to *ca*. 1.7 K. A field sweep, giving the longitudinal field dependence of the initial asymmetry at *ca*. 1.7 K, was measured for both samples, Figure 3.23. Both dependences are nearly identical with 0.4 T needed to decouple the muon spin from the electronic moments, indicating that the internal field experienced at the muon site is around 0.4 T. Zero-field μSR data from

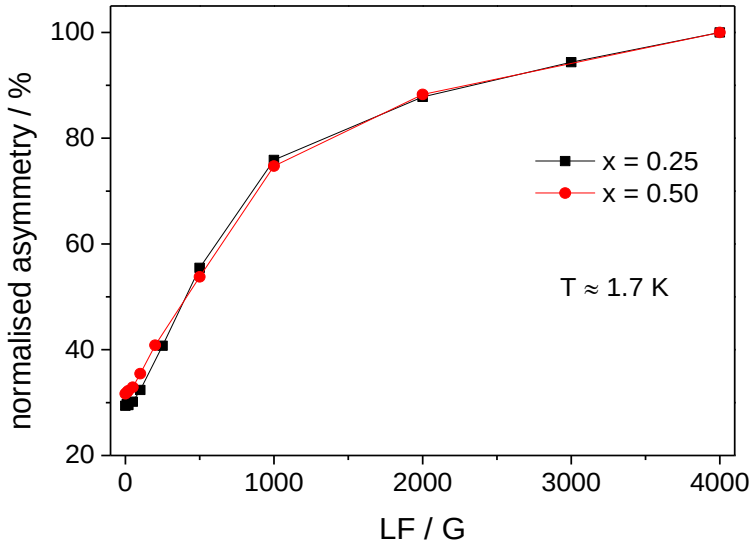

Figure 3.23 Field dependence (longitudinal) of the normalised initial asymmetry of Co_xTiS_2 (x = 0.25 and 0.50) at base temperature.

measurements in the cryostat were fitted using Equation 3.1. The temperature dependence of the relaxation rate, determined from measurements in the CCR and the cryostat, are given in Figure 3.24. For $Co_{0.50}TiS_2$, the depolarisation rates from the CCR and cryostat measurements are consistent with each other and λ peaks around 10 K. Data for $Co_{0.25}TiS_2$ seem consistent as well, although the need for a stretched exponential at $T \leq 20$ K in the CCR experiment is not repeated for the cryostat experiment at the highest temperature investigated, T = 10 K. This could correspond to a temperature range at which the local field distribution is large.

Overall, samples of composition Co_xTiS_2 (x = 0.20; 1/3 and 2/3) show no evidence for magnetic ordering for temperatures above 10 K but an increase in the muon depolarisation rate below 150 K could indicate a transition between paramagnetic and ordered states in CoS_2 impurities. A slowing down of the electronic spin fluctuations below 50 K occurs for samples of composition Co_xTiS_2 (x = 0.20 and 1/3). For samples of composition Co_xTiS_2 (x = 0.25 and 0.50), a large fall of the initial asymmetry below *ca*. 35 K indicates the presence of a strong internal field and static or quasi-static magnetic moments. For $Co_{0.25}TiS_2$ and $Co_{0.50}TiS_2$, strong evidences for short-range magnetic ordering have been found and the internal field experienced at the muon site is around 0.4 T.

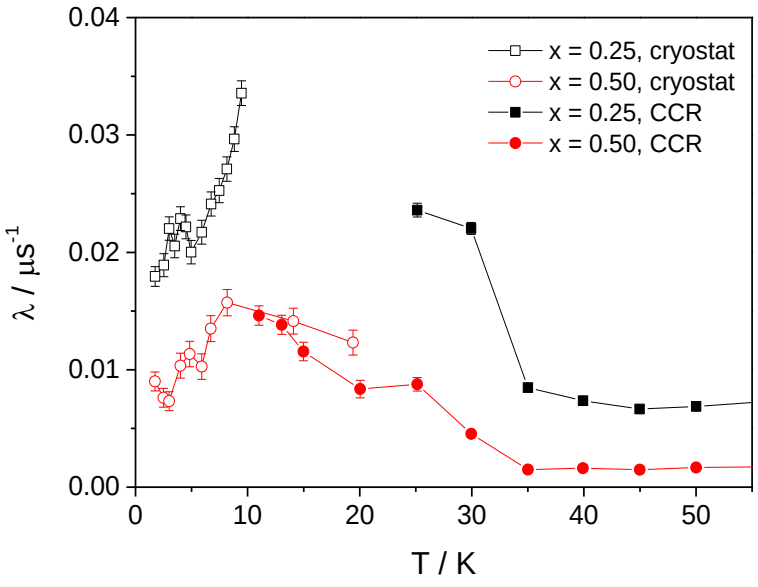

Figure 3.24 Temperature dependence of the relaxation rate in Co_xTiS_2 (x = 0.25 and 0.50).

3.2.4 Thermogravimetric analysis

A combined TGA/DSC analysis of selected samples of Co_xTiS_2 (x = 0; 0.08; 0.25 and 1/3) was carried out to investigate the effect of cobalt intercalation and superstructure formation on the thermal stability of the material. The analysis was performed under inert (N_2) and oxidising (air) atmospheres over the temperature range 290 ≤ T / K ≤ 1070, Figure 3.25. Powder X-ray diffraction data of the residues are supplied in Appendix D.

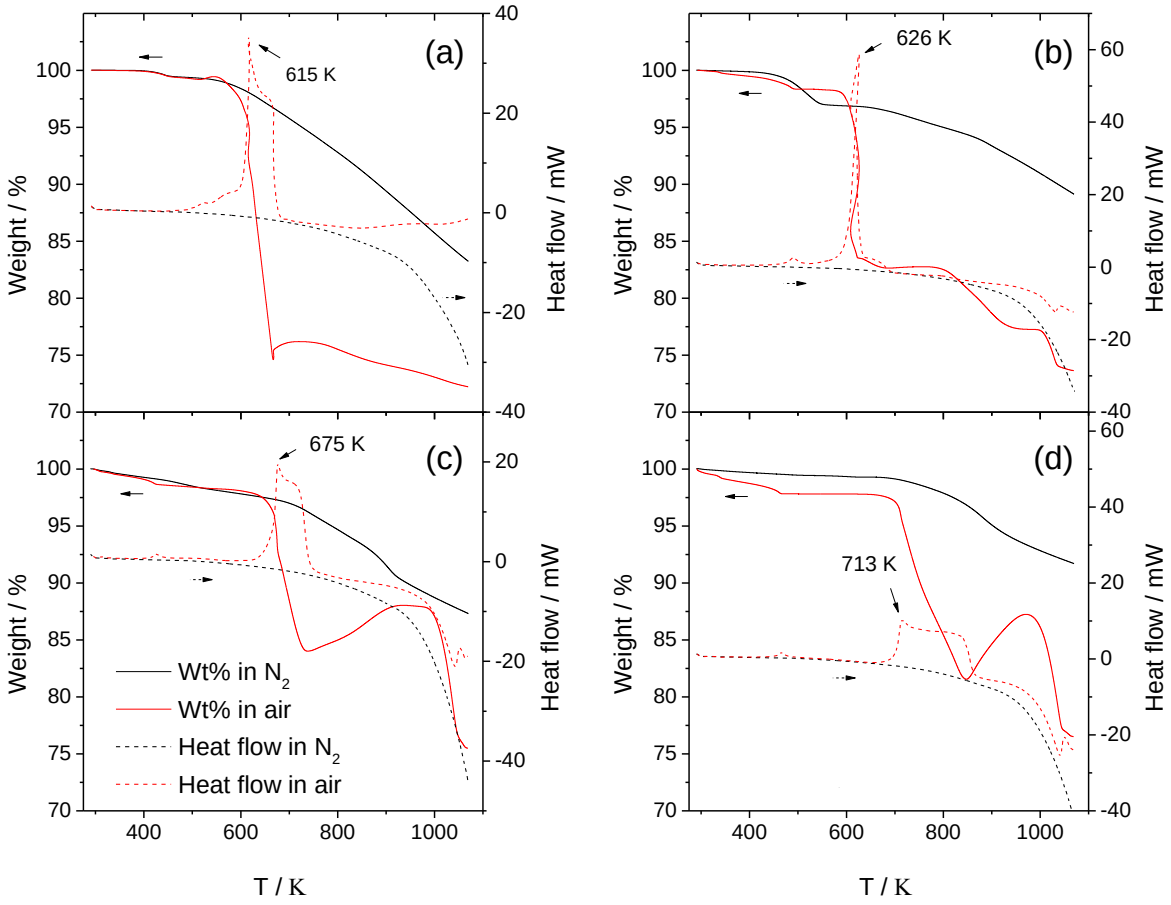

Figure 3.25 TGA/DSC data for (a) TiS_2, (b) $Co_{0.08}TiS_2$, (c) $Co_{0.25}TiS_2$ and (d) $Co_{1/3}TiS_2$, full lines correspond the weight loss and dashed lines to the heat flow. Black lines correspond to the analysis in N_2, red lines to analysis in air.

An exothermic peak is observed in all four samples heated in air, corresponding to a rapid oxidation. This peak is shifted to higher temperature upon cobalt intercalation; from 615 K for TiS_2 to 713 K for $Co_{1/3}TiS_2$. The oxidation products have been identified by powder X-ray

diffraction, Figure D.1, as being anatase TiO_2 for x = 0; anatase with evidence for the rutile form at x = 0.08; and a mixture of rutile and $CoTiO_3$ for higher cobalt content. In inert atmosphere, no exothermic peaks are observed; however, a slow oxidation due to the presence of trace amounts of oxygen in the gas stream occurs over the 160 min of the thermal analysis run, leading to formation of rutile and anatase TiO_2. For TiS_2 and $Co_{0.08}TiS_2$, weight loss associated with sulphur volatilisation occurs with an onset in the range $473 \leq T\ /K \leq 573$, suggesting that a protective coating would be required for applications at temperatures above 573 K. In the present work, physical property measurements were carried out below 573 K.

3.2.5 Thermoelectric performance

3.2.5.1 Density and anisotropy

An initial series, series A, of compositions Co_xTiS_2 (x = 0, 0.02, 0.04, 0.06, 0.08, 0.10, 0.20, 0.30 and 0.40) was hot-pressed (Section 2.7.1) from powder, previously ground using a pestle and mortar. A pressure of 110 MPa was applied and a temperature of 650ºC was kept for 30 min. While the density at low levels of intercalation ($x \leq 0.10$) is in the range of 90 % to 93 % of the crystallographic value, at higher cobalt contents a marked decrease in the density was observed, reaching 72 % for $Co_{0.40}TiS_2$. A second series, series B, of compositions Co_xTiS_2 (x = 0, 0.02, 0.04, 0.06, 0.08, 0.10, 0.25, 1/3 and 0.50) was hot-pressed from powder that had been ball milled, with homogenised and reduced particle size. Ball milling (1 h, 350 rpm, 5min intervals with change of direction) was carried out under argon atmosphere in a 25 mL

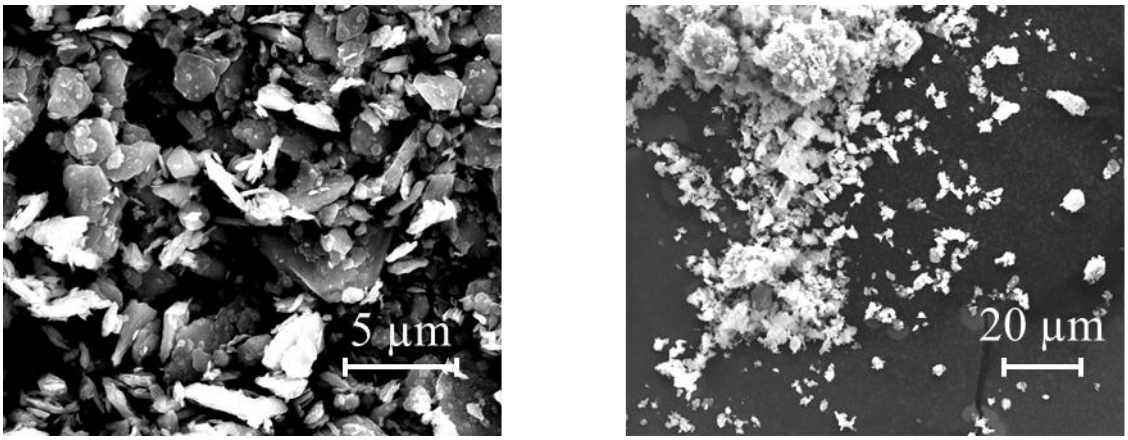

Figure 3.26 Scanning electron micrograph of ball milled powder of TiS_2.

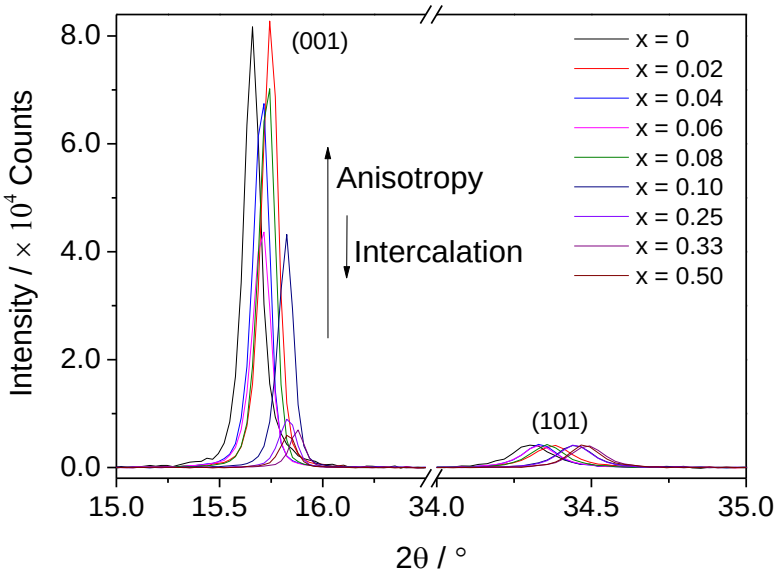

Figure 3.27 Superimposed XRD plots of the surface of Co_xTiS_2 pellets highlighting the ratio between the (001) and (101) reflections.

stainless-steel jar with 6 mm stainless-steel balls and a powder-to-ball ratio of 3:10 (Section 2.1.2). Ball milled samples were confirmed to have a homogenous particle size repartition using SEM, Figure 3.26. The particles have a flake-like morphology with dimension about 1-10 microns in length and *ca.* 1 µm in width. Hot-pressing (110 MPa, 650 ºC, 30 min) of the so-prepared powders, Series B, resulted in higher densities than for Series A. The measured

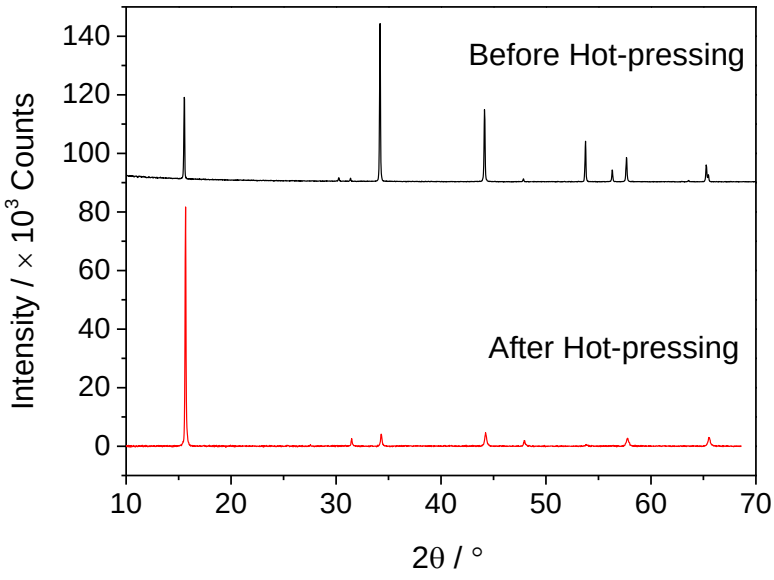

Figure 3.28 Powder X-ray diffraction patterns of TiS_2 before and after hot-pressing.

density of low cobalt content samples ($x \leq 0.08$) was ≥ 95 % of the crystallographic value. Higher cobalt content samples were, again, found to have a high porosity with densities of 92 % for $x = 0.10$ and *ca.* 80 % for $x \geq 0.25$.

Powder X-ray diffraction data collected on consolidated pellets, show strong evidence of significant preferred orientation, Figure 3.28, consistent with the flake-like particle shape observed in Figure 3.26. The intensity of the (001) reflection is considerably increased after hot-pressing. The degree of preferred orientation in consolidated materials (Series B) becomes less marked with increasing values of x, Figure 3.27. This observation can be illustrated by ratio of the intensities, *R*, of the (001) against the strongest reflection (101). *R* is reduced from *ca.* 30 for TiS_2 to *ca.* 4 for $Co_{0.5}TiS_2$ where simulations of the powder X-ray diffraction pattern in the absence of preferred orientation give ratios of 0.57 and 0.37 for TiS_2 and $Co_{0.5}TiS_2$ respectively.

Because of the high level of preferred orientation in the pellets, evidenced by the X-ray diffraction data, the electrical and thermal properties were measured in two directions to account for the anisotropic nature of the samples. Measurements conducted in the direction of pressing are referred to as cross-plane while measurements done in the perpendicular direction are referred to as in-plane.

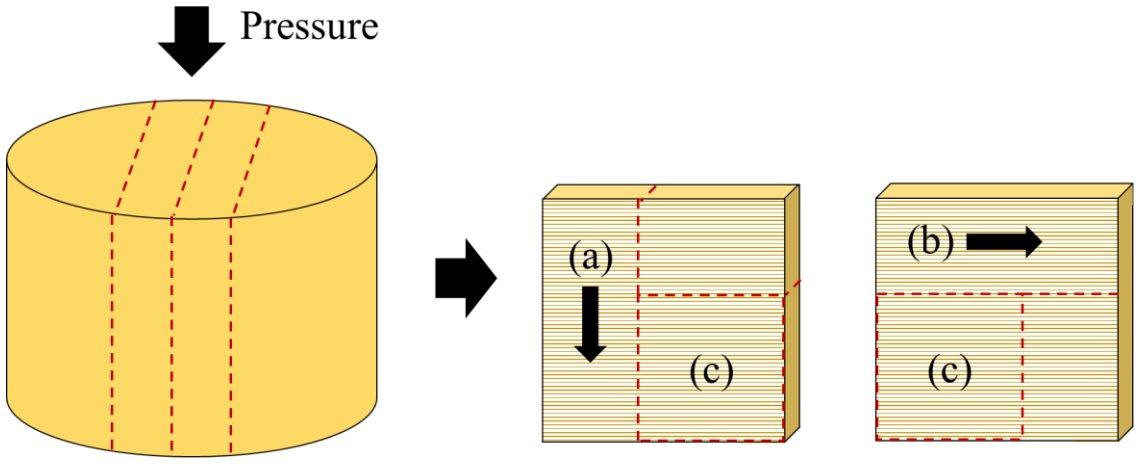

Figure 3.29 Cutting diagram for 10 mm pellets to measure (a) cross-plane electrical properties, (b) in-plane electrical properties and (c) the in-plane thermal diffusivity.

The different sections for physical property measurement were cut with a diamond saw from a hot-pressed pellet of *ca.* 10 mm in height and 12.7 mm in diameter, Figure 3.29. Electrical measurements were carried out on bars of *ca.* 2 × 2 × 8-10 mm^3 and in-plane thermal diffusivity was measured on 6 × 6 × 2 mm^3 squares. Cross-plane thermal diffusivity was measured on polished discs of ca. 2 mm width and *ca.* 12.7 mm diameter. Details of instrumentation are given in Section 2.7.

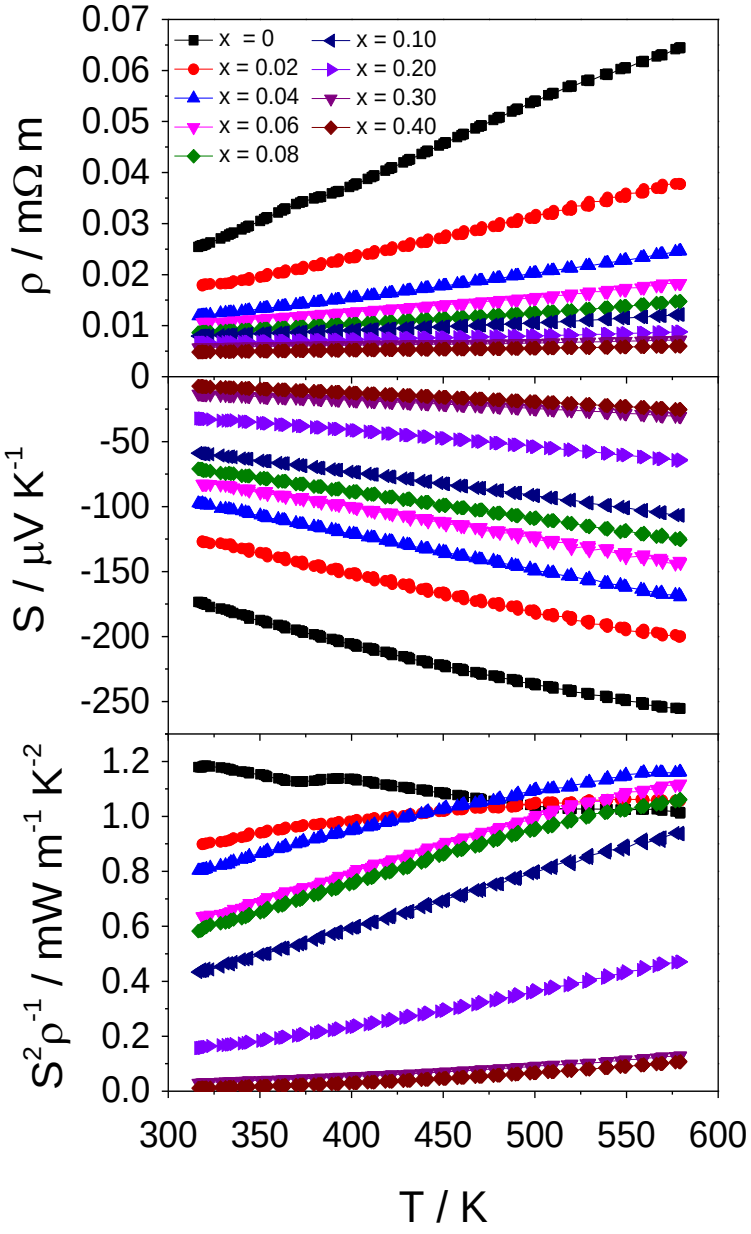

Figure 3.30 Measurements of the in-plane temperature dependence of the electrical resistivity (ρ), Seebeck coefficient (S) and power factor ($S^2\rho^{-1}$) of Co_xTiS_2 ($0 \leq x \leq 0.40$), Series A, as a function of x.

3.2.5.2 Electrical properties

The in-plane electrical properties of the series A of composition Co_xTiS_2 (x = 0, 0.02, 0.04, 0.06, 0.08, 0.10, 0.20, 0.30 and 0.40) are shown in Figure 3.30. Incorporation of cobalt in the van der Waals' gap of TiS_2 has a beneficial impact on the properties with a clear reduction in electrical resistivity with increasing x despite the slightly increased porosity of the consolidated samples for x > 0.10. The negative Seebeck coefficient confirms that the dominant charge carriers are electrons and that upon intercalation the materials remain *n*-type. However, the absolute value of S for Co_xTiS_2 decreases markedly with increasing cobalt content. The reduction in |S| and the electrical resistivity can be attributed to the donation of electrons from the cobalt cation to the empty t_{2g}-derived conduction band of TiS_2, thereby increasing the charge carrier density at E_F. Figure 3.31 represents the density of states in 1T-TiS_2, determined from *Ab initio* band-structure calculations (localised spherical wave method).[168] This calculated band structure has been reproduced by many groups[167, 189-193] and is widely accepted as being representative of the system. The conduction band is mainly composed of the Ti 3*d* orbitals with a small overlap between the Ti 3*d* and the S 3*p* states.

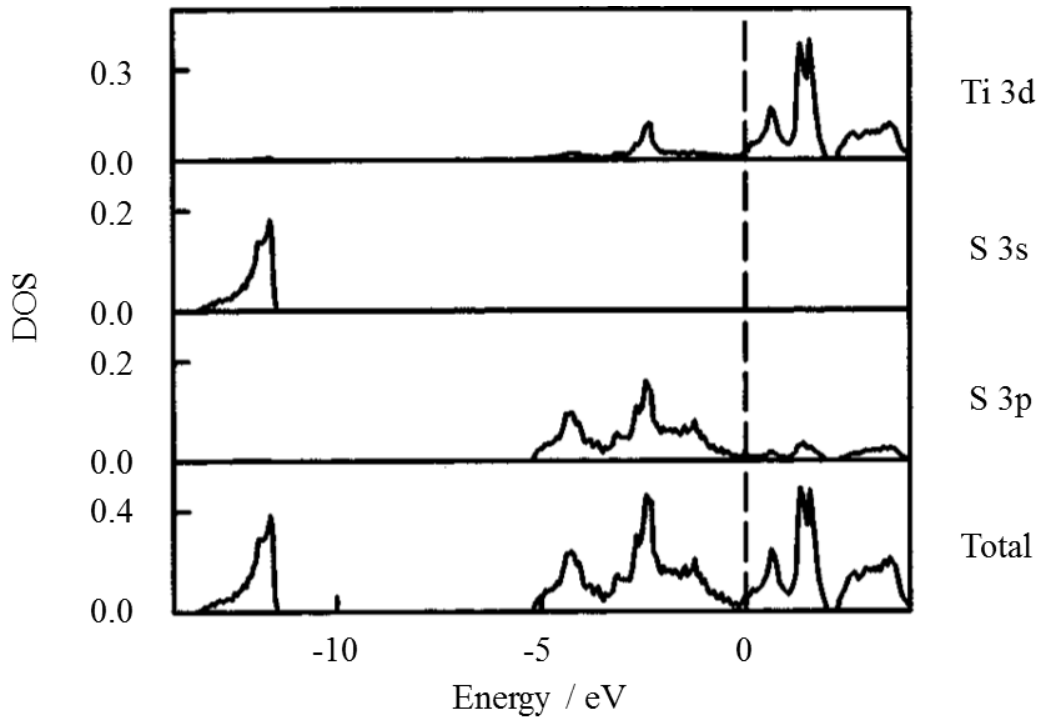

Figure 3.31 Partial and total density of states of TiS_2 adapted from the work Fang *et al.*[168]

From the electrical properties of Co_xTiS_2 series A ($0 \leq x \leq 0.40$), it was observed that intercalation levels above x = 0.10 caused the power factor to decline over the whole temperature range investigated. The power factor was reduced from $S^2\rho^{-1}$ = 1.0 - 1.2 mW m^{-1} K^{-2} down to below $S^2\rho^{-1}$ = 0.3 mW m^{-1} K^{-2} over the whole temperature range for materials with compositions corresponding to $x \geq 0.20$. Conversely, in samples with low intercalation levels ($x \leq 0.10$), the benefits of doping on the electrical resistivity outweigh the degradation of the Seebeck coefficient at temperatures above 473 K. Since no improvement was observed in the thermal properties for samples of composition Co_xTiS_2 ($x > 0.10$), Section 3.2.5.3, the detailed investigation of in-plane and cross-plane thermoelectric properties of Co_xTiS_2 was limited to samples of composition Co_xTiS_2 ($x \leq 0.10$).

The in-plane and cross-plane electrical properties of the ball milled series, series B, of composition Co_xTiS_2 (x = 0; 0.02; 0.04; 0.06; 0.08 and 0.10) are shown in Figure 3.32. The in-plane Seebeck coefficient for TiS_2 at 300 K, S = -232 μV K^{-1}, is in good agreement with the measurements made by Imai et al.[155] with who reported S = -251 μV K^{-1} at 300 K within the *ab* plane of the single crystal. The electrical resistivity is also consistent with measurements within the *ab* plane of a single crystal (ρ = 0.017 mΩ m) which is of the same order of magnitude as ρ = 0.034 mΩ m measured here for the consolidated powder in the in-plane direction. While in-plane measurements on polycrystalline TiS_2 compare favourably with measurements in the *ab* plane of a single crystal, measurements of electrical resistivity made in the cross-plane direction are two orders of magnitude lower than along the crystallographic *c* direction of a single crystal. The anisotropy in the polycrystalline sample is hence not as pronounced as in the single crystal, indicating the less than perfect alignment of plate-like crystallites despite the large orientation effect observed by powder X-ray diffraction. This anisotropy, attributed to the two-dimensional layered structure, is reflected in the electrical resistivity and Seebeck coefficient, both higher for cross-plane measurements compared to in-plane measurements from the same pellet.

Comparison between in-plane measurements of series A and series B reveals an electrical resistivity and a Seebeck coefficient slightly increased for the ball milled series. While these could be in part explained in term of small variations in sulphur deficiency from the synthesis,

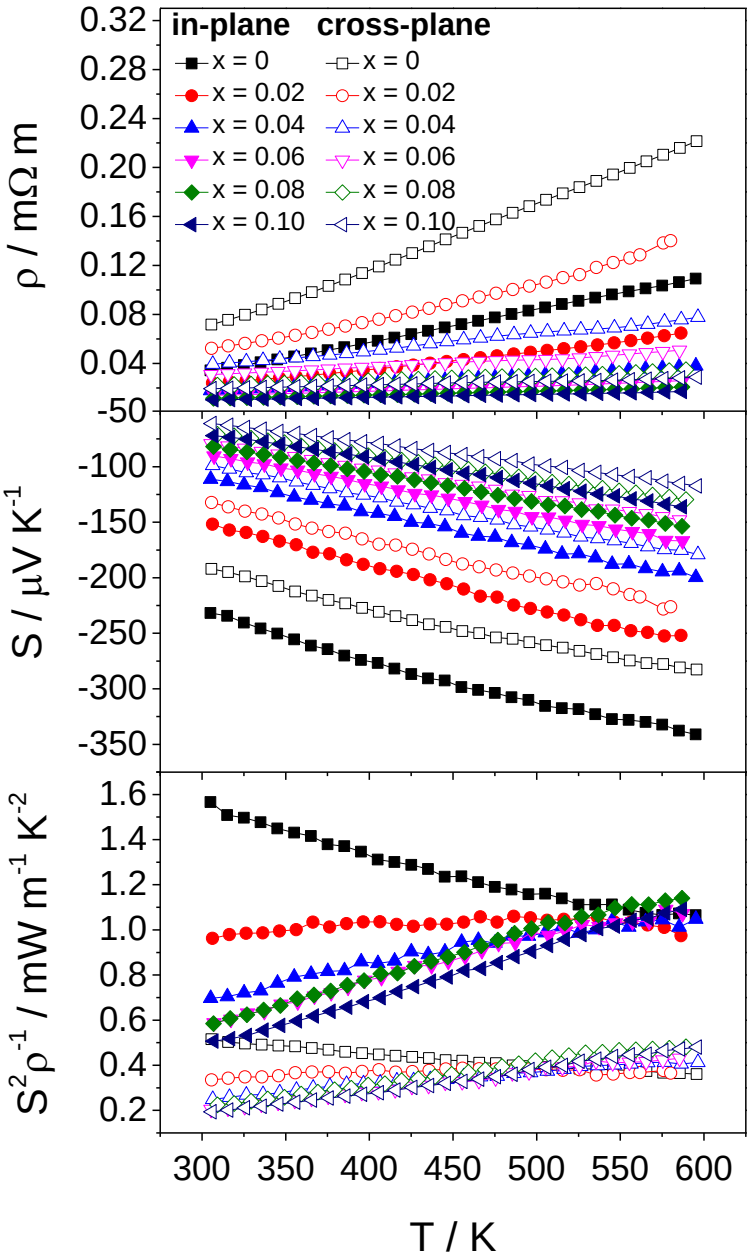

Figure 3.32 Temperature dependence of the electrical resistivity (ρ), Seebeck coefficient (S) and power factor ($S^2\rho^{-1}$) of Co_xTiS_2 ($x \leq 0.10$), Series B. Full symbols represent measurements along the in-plane direction while the empty symbols correspond to cross-plane measurements.

it is more likely to be linked to the added ball mill step as the synthesis and hot-pressing conditions were kept identical. The smaller particle size in the ball milled series increases the grain boundary scattering contribution to the electrical resistivity, for instance ρ increases from 0.026 mΩ m to 0.038 mΩ m at 320 K for TiS_2. The absolute value of the Seebeck coefficient

is also increased, from -145 μV K^{-1} to -237 μV K^{-1} at 320 K in TiS_2. As with the electrical resistivity, a lower sulphur deficiency could partly explain the difference. However, the reduction of the particle size increases the surface area that potentially increases the amount of adsorbed species, probably hydroxide or moisture, in the powder. The oxidation occurring during the hot-pressing step can result in titanium de-intercalation and formation of trace amounts of $TiO_{2-\gamma}$.[161] The consequence of titanium de-intercalation is a lower sulphur deficiency and a decrease in the charge carrier concentration that contributes to the rise in electrical resistivity and Seebeck coefficient. The degree of non-stoichiometry in the consolidated sample, determined by comparison between Seebeck coefficient and electrical resistivity measurements of TiS_2 here and those for $Ti_{1+\gamma}S_2$ reported previously,[157] is estimated to be between 1 % and 1.5 %, corresponding to an upper limit in composition of $Ti_{1.015}S_2$. This is also consistent with the *c* lattice parameter that lies in the range $5.695 \leq c$ / Å ≤ 5.700 and a unit cell volume < 57.3 $Å^3$, both of which are consistent with the deviation from stoichiometry lying in the range 1-1.5 %.

Both the in-plane and cross-plane electrical resistivity of Co_xTiS_2 ($x \leq 0.10$), Series B, increase linearly with temperature and decrease with cobalt intercalation level. This metal-like temperature dependence is accompanied by a high absolute value of the Seebeck coefficient, an unusual combination that suggests the materials are better described as degenerate semiconductors not as metals or semi-metals. The calculation of the in-plane and cross-plane power factor, Figure 3.32, confirms the observations made on series A, Figure 3.30, where the reduction in electrical resistivity compensates for the reduction in Seebeck coefficient above a certain temperature. The rapid fall in electrical resistivity and corresponding decrease of |S| with cobalt intercalation result in a change in the temperature dependence of the power factor at x = 0.02 from a negative to a positive gradient. The power factor ($S^2\rho^{-1}$) is improved upon cobalt intercalation at temperatures above 500 K for cross-plane measurements, ranging from 0.35 to 0.45 mW m^{-1} K^{-2} over the 500 K to 595K range, and above 575 K for in-plane measurements, reaching $S^2\rho^{-1} \approx 1$ - 1.1 mW m^{-1} K^{-2} over the 550 K to 595 K range.

For Co_xTiS_2 ($x \geq 0.25$), Figure 3.33, the absolute Seebeck coefficient continues to decrease with x over the whole temperature range investigated, while the electrical resistivity increases.

The reduction in |S| is consistent with the donation of electrons from cobalt; however, the electrical resistivity increases slightly. This can be explained by the lower density in consolidated samples with high cobalt intercalation levels.

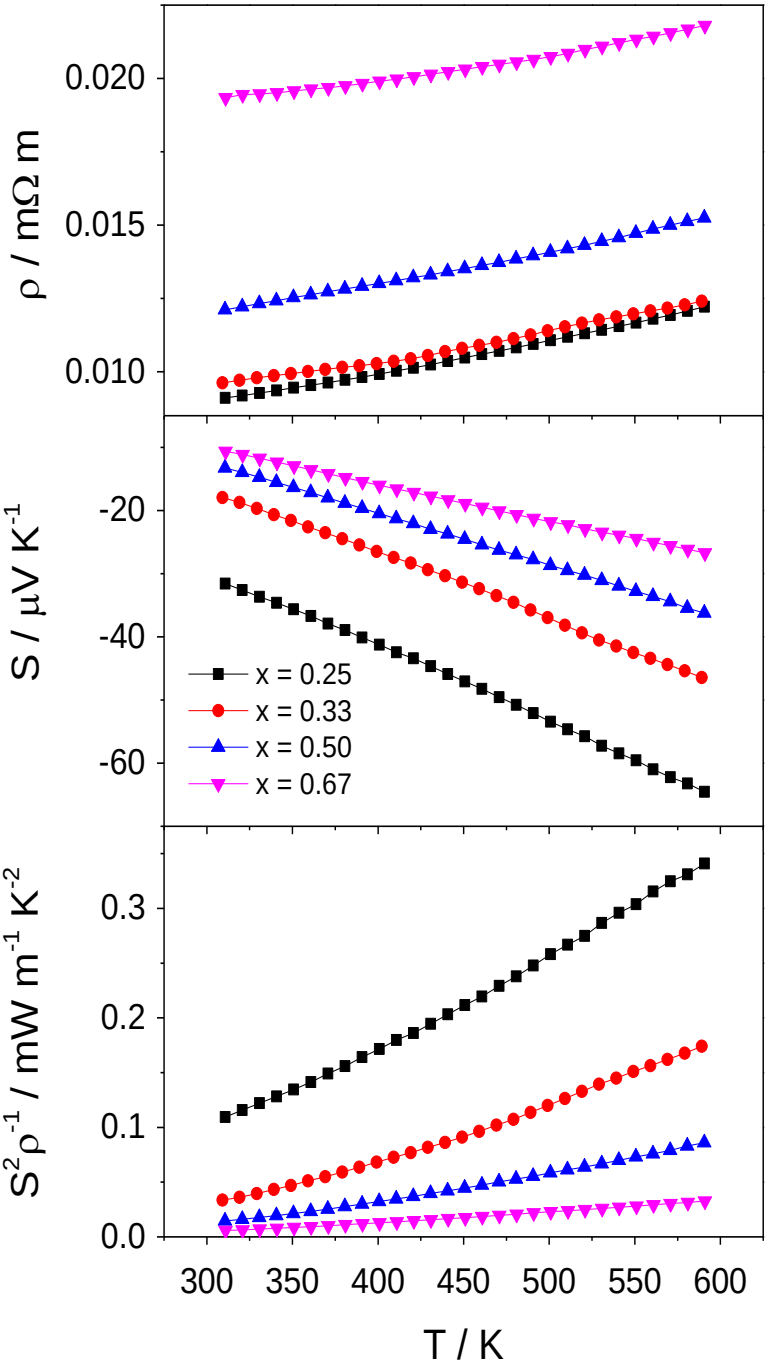

Figure 3.33 Measurements of the in-plane temperature dependence of the electrical resistivity (ρ), Seebeck coefficient (S) and power factor ($S^2\rho^{-1}$) of Co_xTiS_2 ($0.25 \leq x \leq 2/3$), Series B, as a function of x.

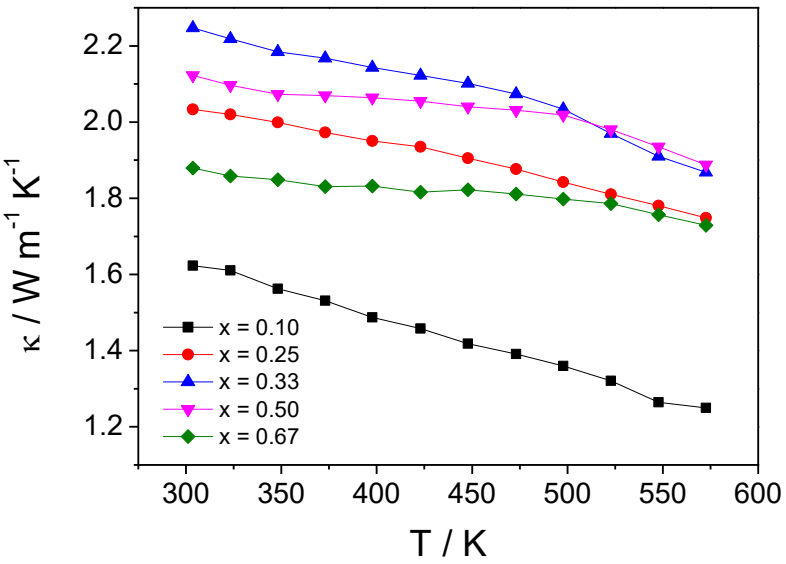

Figure 3.34 Temperature dependence of the cross-plane thermal conductivity (κ) of Co_xTiS_2 (Series B) as a function of x for high doping levels

3.2.5.3 Thermal transport properties and figure of merit

The cross-plane thermal conductivity measurements for Co_xTiS_2 samples (Series B) with $x \geq 0.10$ are presented in Figure 3.34. As with the electrical properties, high cobalt intercalation levels are detrimental to the thermoelectric performance with thermal conductivities substantially higher than that of Co_xTiS_2 materials with $x \leq 0.10$, Figure 3.35. This is illustrated by the compositional dependence of the cross-plane thermal conductivity, Figure 3.36. The higher thermal conductivity in samples with high interaction levels ($x \geq 0.10$) can be in part explained by the increased electronic contribution, κ_{el}, arising from the electron transfer from cobalt to the TiS_2 host. However, the porosity of samples of composition Co_xTiS_2 with $x > 0.25$ ultimately decreases the electronic contribution due to the increased electrical resistivity.

The compositional evolution of the electronic contribution to the thermal conductivity can be verified by estimating the electronic contribution from the electrical conductivity measurements using the Wiedemann-Franz law ($L = 2.44 \times 10^{-8}$ W Ω K^{-2}), Figure 3.37. This can only be done in the in-plane direction as cross-plane electrical properties of Co_xTiS_2 were not measured for $x \geq 0.25$. Despite this decrease in κ_{el}, the total thermal conductivity remains

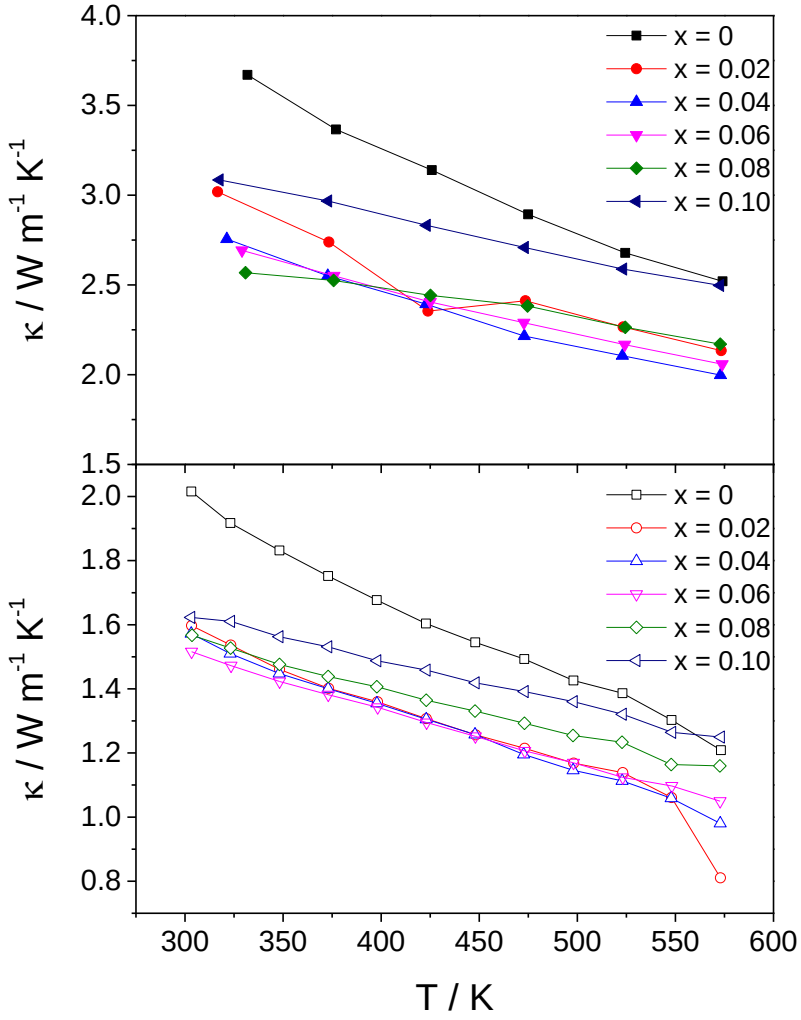

Figure 3.35 Temperature dependence of the in-plane (top) and cross-plane (bottom) thermal conductivity (κ) of Co_xTiS_2 ($0 \leq x \leq 0.10$).

high, suggesting that the second component of the thermal conductivity, from phonon propagation, is also increased with cobalt intercalation. This enhanced phonon propagation might be due to the formation of ordered superstructures and the loss of two-dimensional character.

The thermal transport properties of Co_xTiS_2 materials, series B, with low cobalt contents ($x \leq 0.10$), Figure 3.35, contrast with the observations made on higher doping levels, with significant reductions in thermal conductivity achieved for compositions corresponding to $x \leq 0.08$. The in-plane electronic contribution to the thermal conductivity, Figure 3.37, increases sharply as a result of the electron transfer from Co to the TiS_2 host. The lattice component can

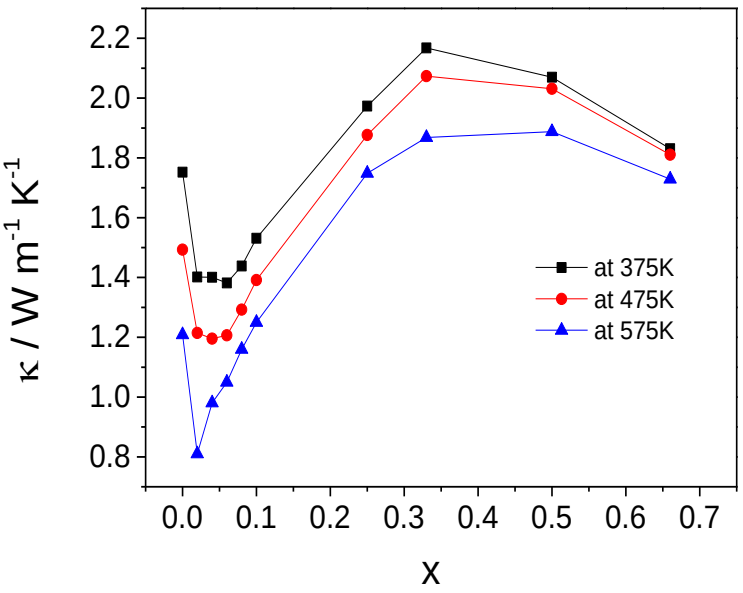

Figure 3.36 Compositional dependence of the cross-plane thermal conductivity (κ) of Co_xTiS_2 ($0 \leq x \leq 2/3$), series B, at 375 K, 475 K and 575 K.

then be deduced by subtracting the electronic contribution to the total, measured, thermal conductivity. The compositional dependence of the lattice contribution, included in Figure 3.39 reveals the marked reduction caused by the presence in low amount of cobalt in the van der Waals' gap of TiS_2. For an intercalation level corresponding to Co_xTiS_2 ($x \leq 0.08$), the benefits

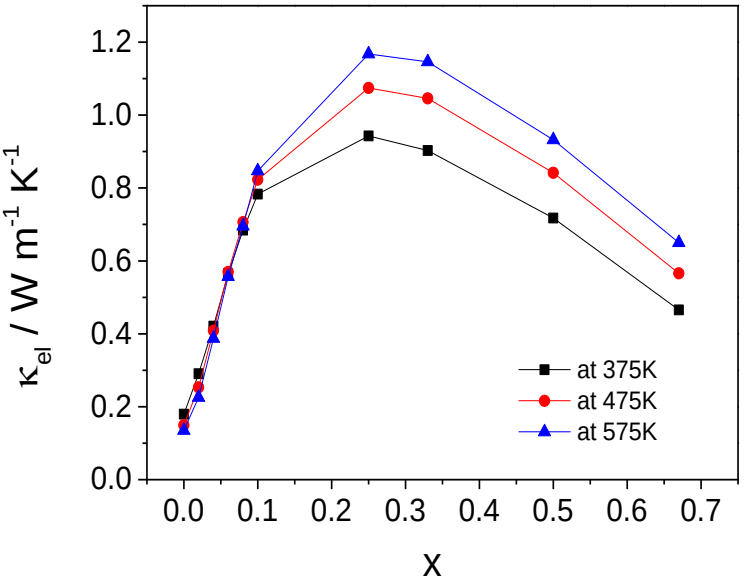

Figure 3.37 Compositional dependence of the in-plane electrical contribution to the thermal conductivity of Co_xTiS_2 ($0 \leq x \leq 2/3$), series B, at 3 selected temperatures, calculated using the Wiedemann-Franz law.

of the phonon scattering caused by the disordered array of cobalt in the inter-layer are greater than the detrimental effects of the electronic contribution. The effect is stronger in the in-plane direction where the total thermal conductivity is around twice as a high as measured in the cross-plane direction. The lowest thermal conductivity is exhibited by $Co_{0.04}TiS_2$ with the total thermal conductivity (κ) decreasing by more than 20 % compared to TiS_2 over the investigated temperature range.

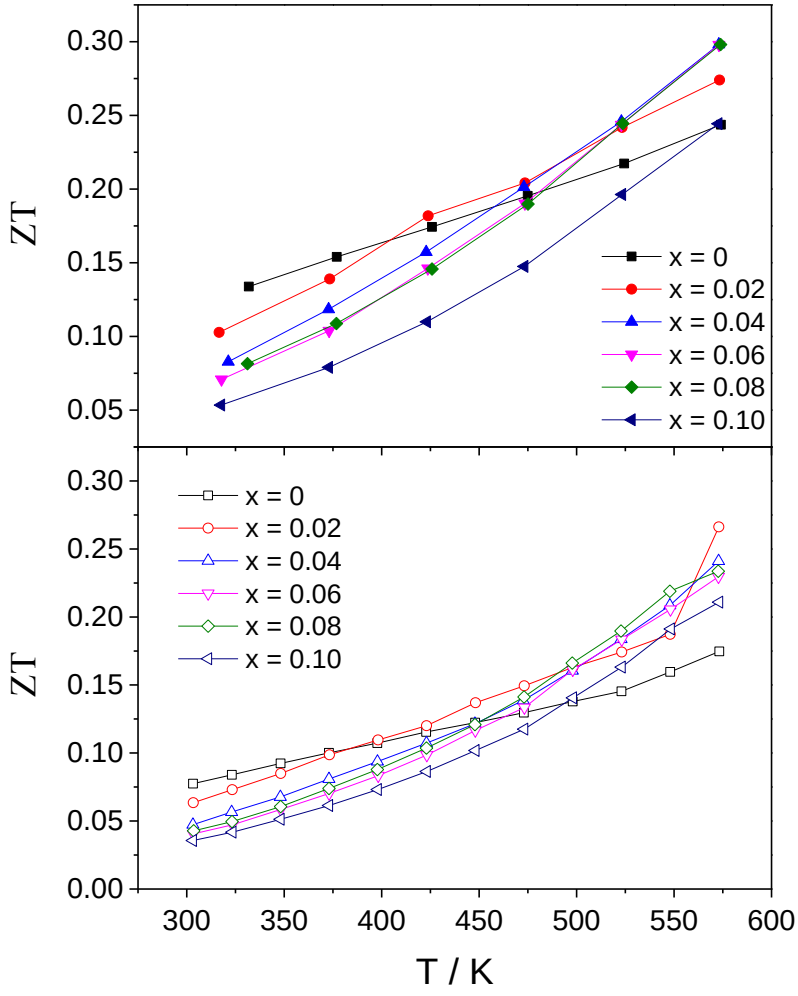

Figure 3.38 Temperature dependence of the in-plane (Top) and cross-plane (Bottom) figure of merit (ZT) of Co_xTiS_2 ($0 \leq x \leq 0.10$), series B.

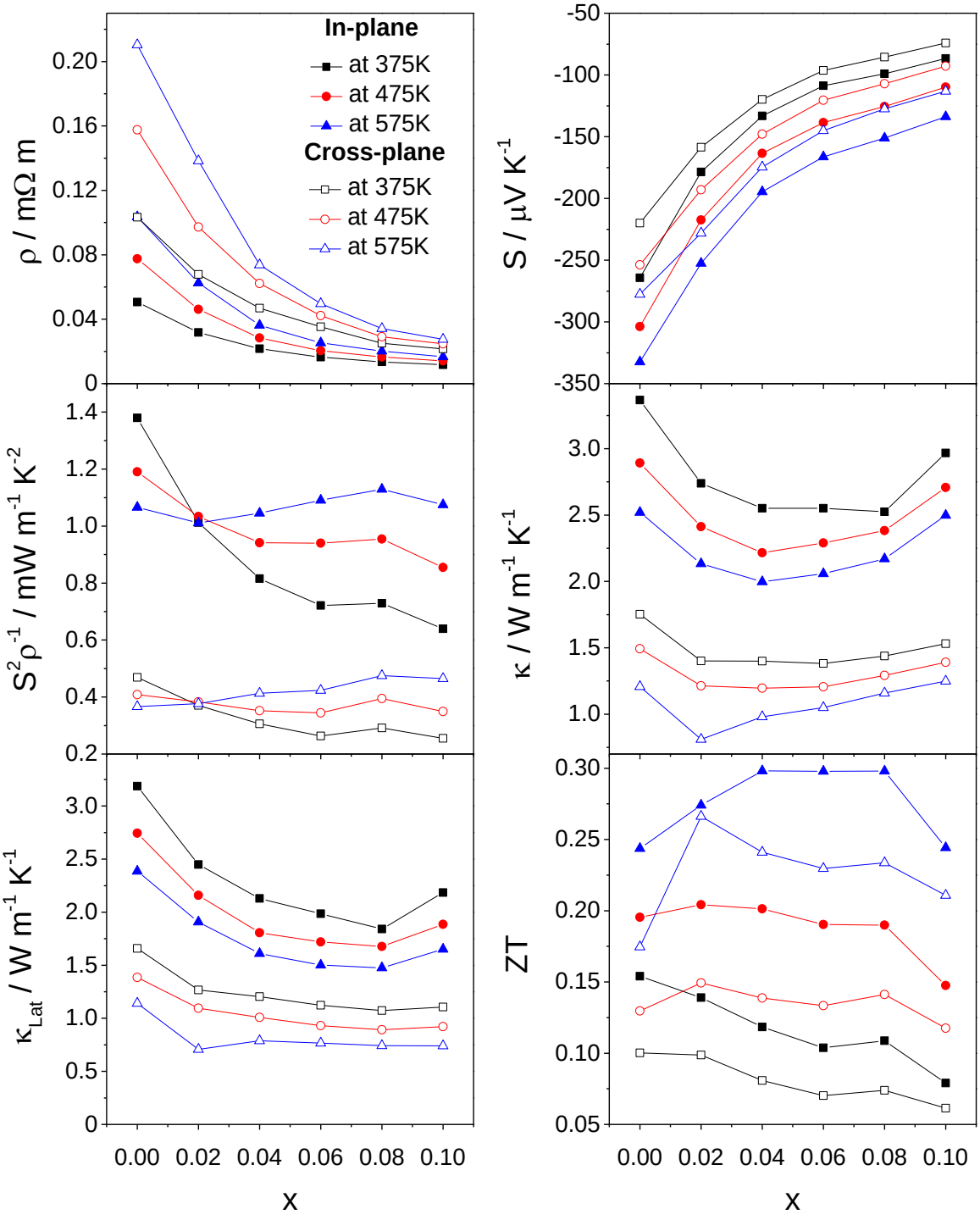

Figure 3.39 Compositional dependence of the in-plane (full symbols) and cross-plane (empty symbols) thermoelectric performance of Co_xTiS_2 ($0 \leq x \leq 0.10$), series B, including electrical resistivity (top left), Seebeck coefficient (top right), power factor (middle left), thermal conductivity (middle right), electronic contribution to thermal conductivity (bottom left) and ZT (bottom right).

The figure of merit, ZT, was calculated in both in-plane and cross-plane directions for Co_xTiS_2 ($x \leq 0.10$), series B, Figure 3.38. Thermoelectric performance is higher in the in-plane direction, mainly due to the much lower electrical resistivity. The highest ZT at low temperature is achieved by pristine TiS_2 and reaches ZT ≈ 0.13 at 330 K; however, the similar power factor and reduced thermal conductivity observed in samples with low cobalt doping increases ZT of intercalated phases at higher temperatures. The best performance at 575 K is achieved for Co_xTiS_2 ($0.02 \leq x \leq 0.06$) with an in-plane ZT ≈ 0.3. This represents a 25 % increase over the maximum value of that for TiS_2 at the same temperature. The impact of low intercalation levels of cobalt on the in-plane and cross-plane properties at 375 K, 475 K and 575 K is summarised in Figure 3.39, for Co_xTiS_2 ($x \leq 0.1$), series B. For all compositions, the in-plane and cross-plane properties exhibit similar compositional dependence. The effect of divalent cobalt intercalation resembles that of monovalent copper[160, 194] and silver[156] with intercalation causing a charge transfer and increased phonon scattering that simultaneously decreases the electrical resistivity and thermal conductivity. The maximum ZT = 0.3 determined for ball milled and hot-pressed samples (series B) of composition Co_xTiS_2 ($0.02 \leq x \leq 0.06$) compares favourably with M_xTiS_2 (M = Cu, Ag, Ti) at 573 K prepared by spark plasma sintering.

3.3 $Mo_xTi_{1-x}S_2$

One of the conventional strategies to chemically dope a material consists in substituting an element with a different one without altering the integrity of the structure. For instance, the tellurides that dominate the thermoelectric market are doped-derivatives of Sb_2Te_3 and Bi_2Te_3.[17] Beside the electronic doping caused by the addition or removal of charge carriers in the electronic structure, substitution can also induce disorder caused by the size difference between the substituent and the substituted elements. This disorder decreases the lattice contribution to the thermal conductivity via phonon scattering processes caused by mass fluctuation or local structural defects. There have been several reports of substitution of titanium in TiS_2, including partial replacement with magnesium,[195] vanadium,[196] chromium, iron,[197] nickel,[198] zirconium,[199] niobium[159, 200] and tantalum,[158, 201-203] or of substitution of sulphur, with selenium[204] or tellurium.[205] The TE properties of $Mg_xTi_{1-x}S_2$,[195] $(Ni_xTi_{1-x})_{1+y}S_2$,[198] TiS_xSe_{2-x},[204, 206, 207] $Ti_{1-x}Ta_xS_2$[158] and $Ti_{1-x}Nb_xS_2$ [159] have been investigated. However,

characterisation of the structural and transport properties of molybdenum substituted TiS_2 that is described here has not been reported previously.

3.3.1 Synthesis

Samples of composition $Mo_xTi_{1-x}S_2$ (x = 0.01; 0.02; 0.03; 0.04; 0.05; 0.06; 0.07; 0.08; 0.09) were synthesised from the elements Ti (Alfa Aesar, dehydrided, 99.99 %), Mo (Alfa Aesar, ≥ 99.95 %) and S (Sigma Aldrich, flakes, 99.99 %) via high temperature solid-state reaction,

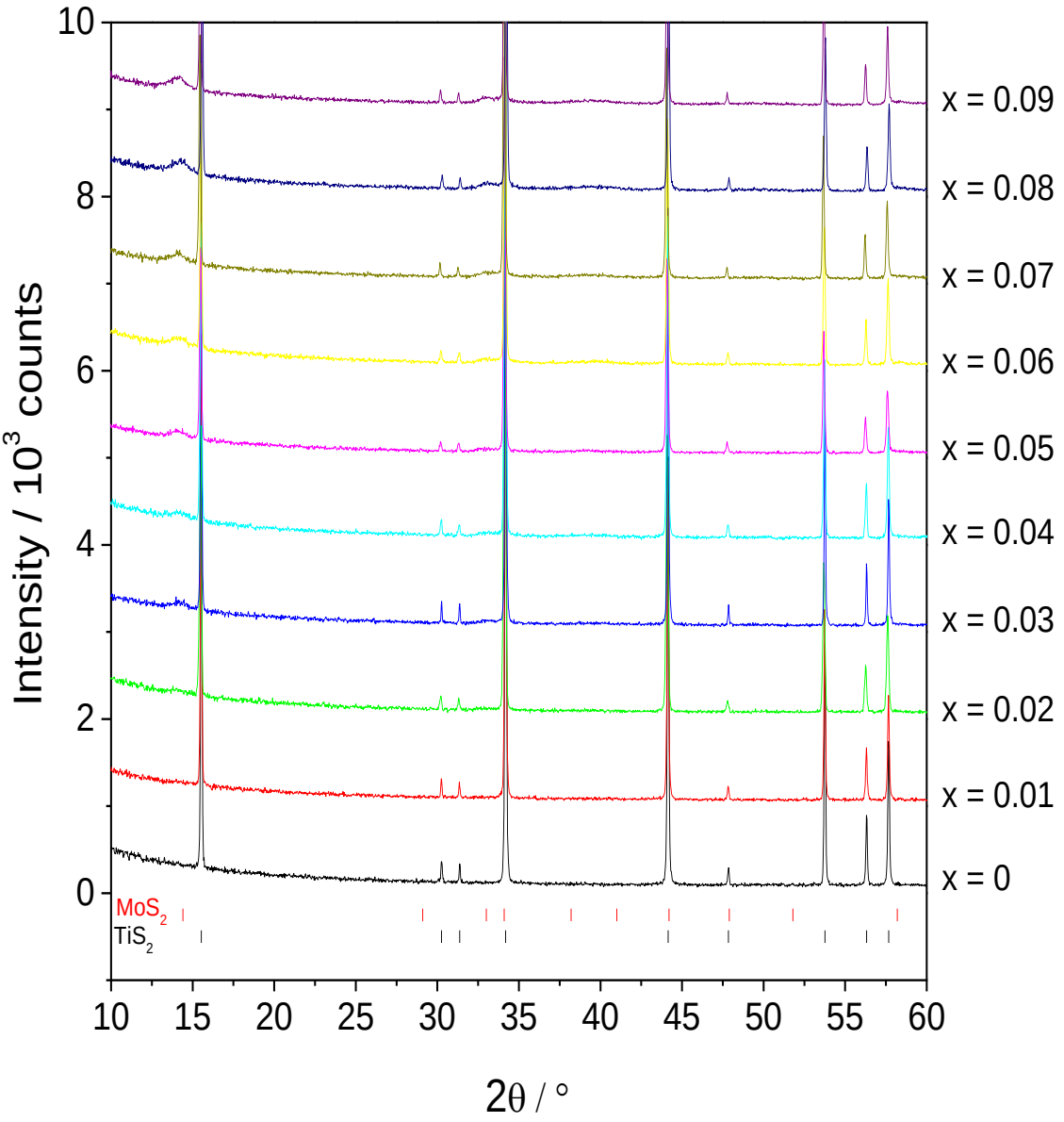

Figure 3.40 Powder X-ray diffraction patterns for $Mo_xTi_{1-x}S_2$ over the range $10 \leq 2\theta / ^{o} \leq 60$ with tick marks corresponding the reflections positions for MoS_2 (in red, top) and TiS_2 (in black, bottom).

Section 2.1.1. The sealed silica tubes containing stoichiometric amounts of dried elements were evacuated down to a pressure of 10^{-4} Torr and placed in a furnace and heated at 350 °C for 4 h and 650 °C for 12 h, using a heating and cooling rate of 1 °C min^{-1}.

3.3.2 Structural investigations

Powder X-ray diffraction patterns of samples with nominal composition $Mo_xTi_{1-x}S_2$ (x = 0; 0.01; 0.02; 0.03; 0.04; 0.05; 0.06; 0.07; 0.08 and 0.09) were collected over the range $5 \leq 2\theta$ / º ≤ 120 with a step size of 0.027646 º for a total of 8 h (Section 2.2). The relatively large step size and long collection time was used to ensure good counting statistics to aid the identification of any minor secondary phases, principally rhombohedral MoS_2, with its strongest reflection (003) at $2\theta = 14.5$ º,[208] which appears at higher substitution levels. The stacked powder X-ray diffraction patterns for $Mo_xTi_{1-x}S_2$ ($0 \leq x \leq 0.09$) over the range $10 \leq 2\theta$ / º ≤ 60, Figure 3.40, show a peak at $2\theta = 14.4$ º from the (003) reflection of rhombohedral MoS_2, indicating that the

Table 3.9 Refined parameters from Rietveld analysis of powder X-ray diffraction data for $Mo_xTi_{1-x}S_2$, $0 \leq x \leq 0.09$ (Space group $P\bar{3}m1$)[a]

		x in $Mo_xTi_{1-x}S_2$				
		0	0.01	0.02	0.03	0.04
	a / Å	3.40676(5)	3.40672(5)	3.40629(6)	3.40646(5)	3.40639(6)
	c / Å	5.69716(8)	5.69733(9)	5.6964(1)	5.69659(8)	5.69652(9)
Ti	*B* / Å^2	0.44(5)	0.76(6)	0.34(6)	0.97(6)	0.16(3)
S	*z*	0.2487(4)	0.2480(4)	0.2493(4)	0.2479(4)	0.2519(4)
	B / Å^2	0.31(4)	0.43(5)	0.08(4)	0.45(5)	0.16(3)
Mo	*B* / Å^2	-	0.76(6)	0.34(6)	0.97(6)	0.16(3)
	d/ g cm^{-3}	3.25	3.26	3.28	3.29	3.31
	R_{wp} / %	8.35	9.26	9.03	9.68	9.57
	χ^2	1.33	1.28	1.36	1.47	1.57
		0.05	0.06	0.07	0.08	0.09
	a / Å	3.40615(6)	3.40671(6)	3.40574(7)	3.40735(7)	3.40630(8)
	c / Å	5.6965(2)	5.6970(2)	5.6954(2)	5.6982(2)	5.6967(2)
Ti	*B* / Å^2	0.06(4)	0.11(4)	0.43(4)	0.28(4)	0.21(5)
S	*z*	0.2504(5)	0.2496(5)	0.2498(5)	0.2502(5)	0.2497(6)
	B / Å^2	0.06(4)	0.11(4)	0.43(4)	0.28(4)	0.21(5)
Mo	*B* / Å^2	0.06(4)	0.11(4)	0.43(4)	0.28(4)	0.21(5)
	d/ g cm^{-3}	3.32	3.33	3.35	3.36	3.36
	R_{wp} / %	10.47	9.79	11.11	10.5	12.68
	χ^2	1.37	1.48	1.65	1.67	2.1

[a] Ti and Mo on 1(a), (0, 0, 0); S on 2(d), (1/3, 2/3, z). SOF(Ti/Mo) constrained at nominal composition.

second phase is formed at a molybdenum substitution level as low as x = 0.03. The structure of $Mo_xTi_{1-x}S_2$ was refined from powder X-ray diffraction data using the Rietveld method based on the CdI_2-type structure (space group: $P\bar{3}m1$) of TiS_2 determined from single crystal X-ray diffraction data.[171] The refined unit cell parameters and atomic positions, Table 3.9, of a given composition were used as a starting model for the next composition in the molybdenum doped series. Output profiles are provided in Figure 3.41 and Figure 3.42.

Rietveld refinements of the X-ray diffraction data were carried out as described in Section 3.2.2.1. The Site Occupancy Factor (SOF) of Ti, Mo and S were fixed to their nominal composition as little or no improvement was observed when allowing them to refine. This is due to the very small variation in electronic density arising from the introduction of $x < 0.1$ of Mo substitution per formula unit. For the same reason, the thermal parameters for Ti and Mo were constrained to be equivalent. There is a continuous decrease in the quality of the fit as the molybdenum content increases and for doping level higher than x = 0.03, it was necessary to constrain all three isotropic thermal parameters to be equal in order to prevent that of sulphur from refining to a physically meaningless negative value. When molybdenum is removed from the model and the SOF for Ti is fixed to unity, the isotropic thermal parameters of Ti and S refine to a sensible positive value but no improvement is made on the overall refinement. No substantial changes can be observed on the lattice parameters, Figure 3.43, and the series does not follow Vegard's law. The variations in lattice parameters *a* and *c* for Co_xTiS_2 are included for comparison. For intercalated systems, M_xTiS_2 (M = Ti, V, Cr, Mn, Fe, Co, Ni, Cu and Ag), the intercalation of a guest element, even as low as $x < 0.1$, is accompanied by variations in the lattice parameters.[114, 157, 161, 173] The absence of compression or stretching of the *c* axis in $Mo_xTi_{1-x}S_2$ despite the large size difference between the cations, 0.605 Å for Ti^{4+} against 0.65 Å for Mo^{4+},[209] supports the fact that molybdenum does not intercalate between TiS_2 layers. For substituted systems $M_xTi_{1-x}S_2$ (M = V, Zr, Nb, Ta and Fe), [159, 197, 199, 203] systematic variations in the lattice parameters were also observed. However, in $M_xTi_{1-x}S_2$ (M = Cr and Ni),[197, 198] substitution levels below x = 0.75 and x = 0.06 for chromium and nickel respectively, do not result in a substantial change in the lattice parameters. A similar behaviour is observed here and the solubility limit of Mo remains low, $x \leq 0.04$, before the formation of MoS_2 impurities.

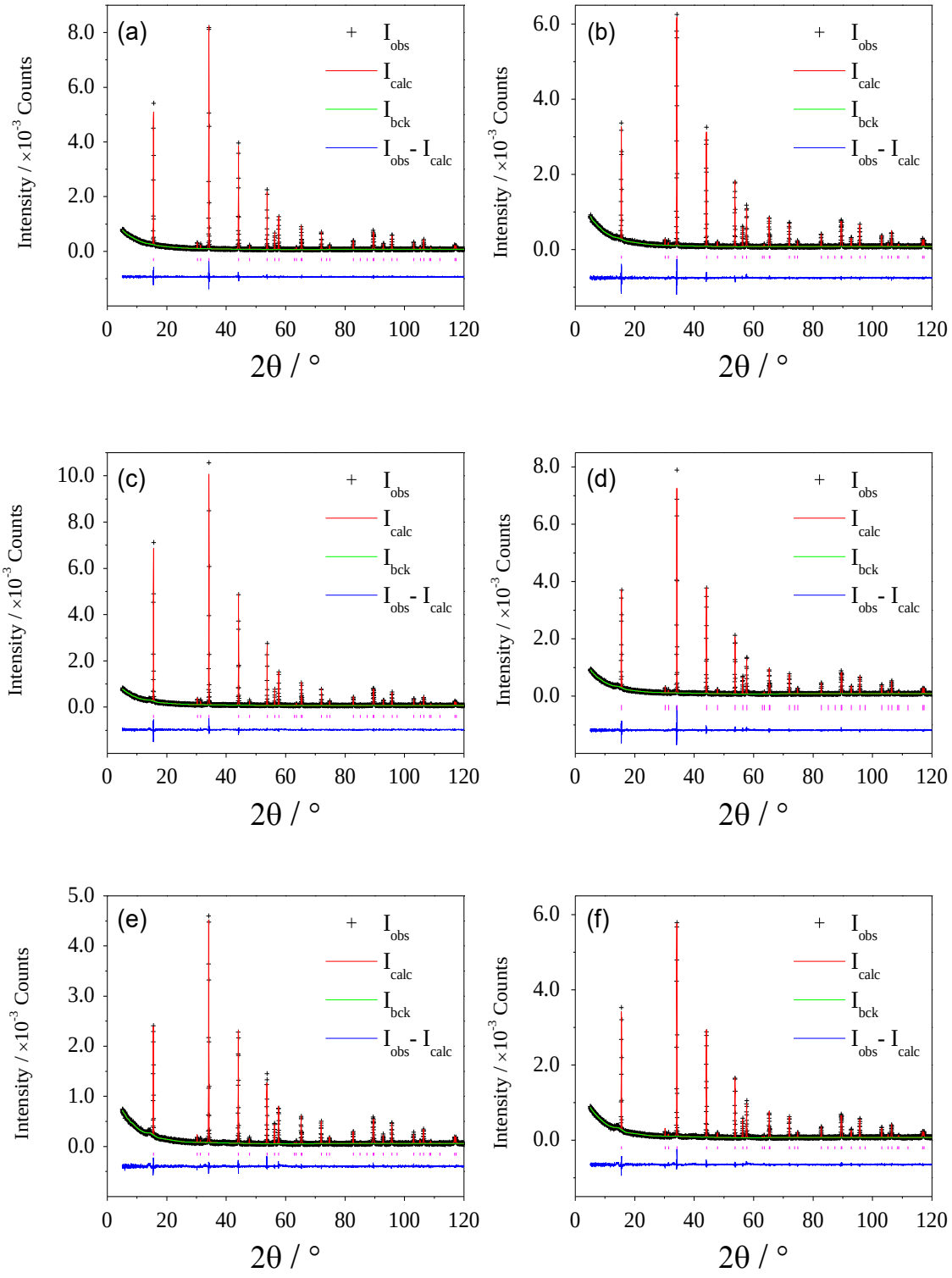

Figure 3.41 Observed (crosses), calculated (full line) and difference (lower full line) profiles for $Mo_xTi_{1-x}S_2$ from Rietveld refinement of XRD data: (a) x = 0.01, (b) x = 0.02, (c) x = 0.03, (d) x = 0.04, (e) x = 0.05 and (f) x = 0.06. Reflection positions are signalled by tick marks.

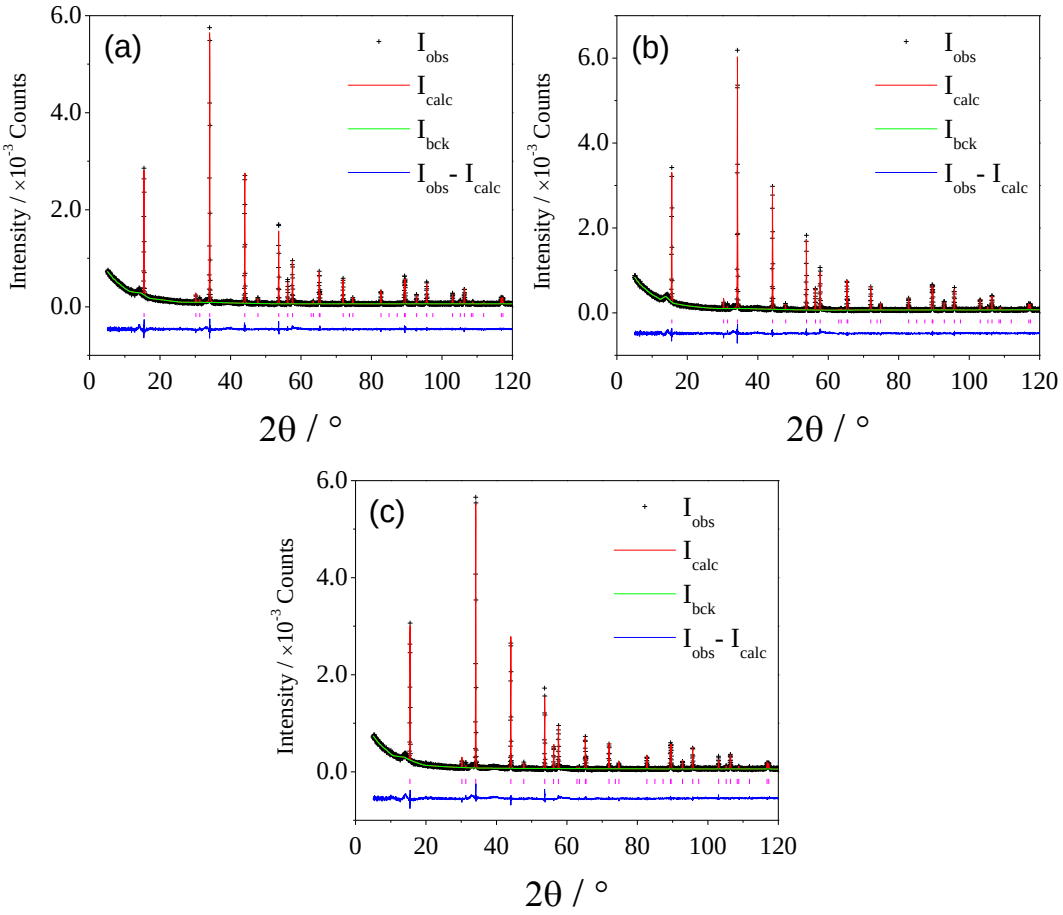

Figure 3.42 Observed (crosses), calculated (full line) and difference (lower full line) profiles for $Mo_xTi_{1-x}S_2$ from Rietveld refinement of XRD data: (a) x = 0.07, (b) x = 0.08 and (C) x = 0.09. Reflection positions are signalled by tick marks.

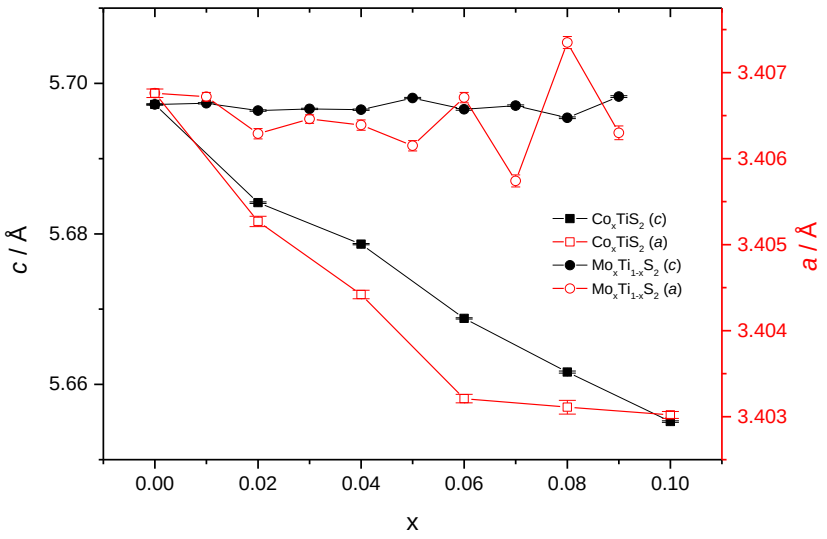

Figure 3.43 Compositional dependence of the lattice parameters *a* and *c* for $Mo_xTi_{1-x}S_2$ ($0 \leq x \leq 0.08$) and Co_xTiS_2 ($0 \leq x \leq 0.10$) from powder X-ray diffraction analysis.

3.3.3 Thermoelectric performance

3.3.3.1 Electrical properties

The electrical resistivity and Seebeck coefficient of selected samples of $Mo_xTi_{1-x}S_2$ ($0 \leq x \leq 0.08$) were measured in the in-plane direction on ingots cut from hot-pressed pellets. The density of the samples was relatively high, reaching 93 % of the crystallographic density for TiS_2 and from 96 % to 98 % of crystallographic value for molybdenum-substituted derivatives. The results, Figure 3.44, show a metallic temperature dependence across the series with an

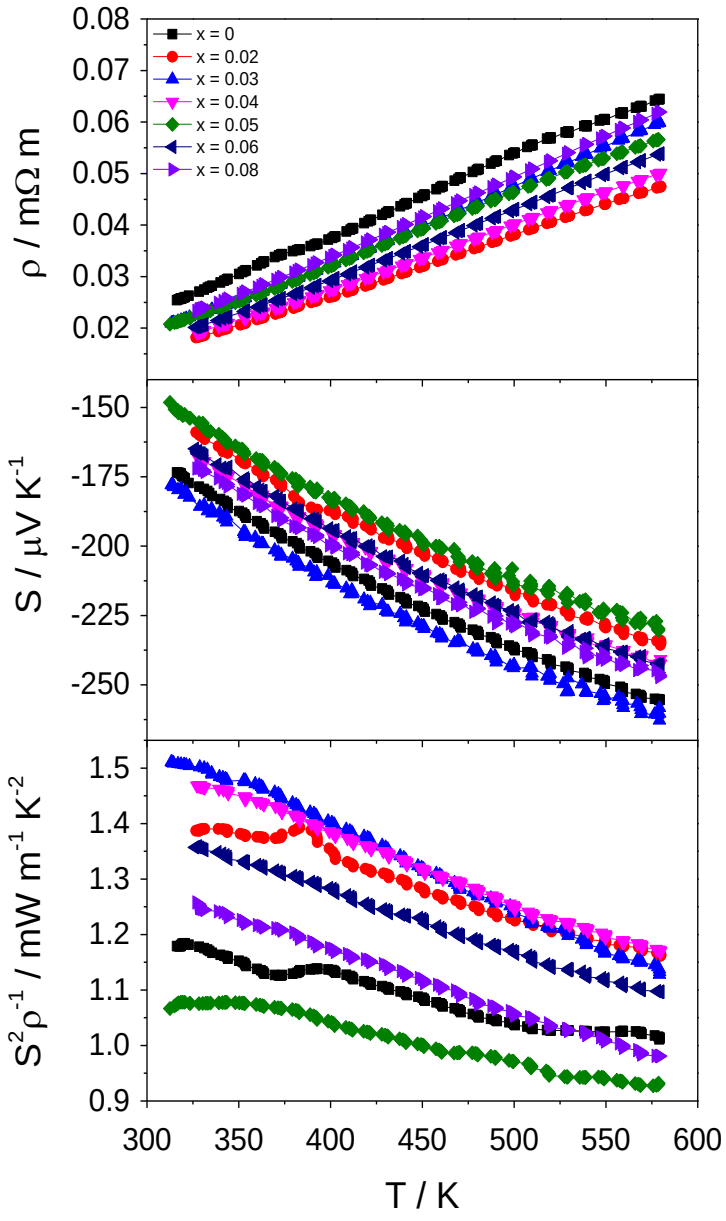

Figure 3.44 Temperature dependence of the electrical resistivity (top), Seebeck coefficient (middle) and power factor (bottom) of hot-pressed $Mo_xTi_{1-x}S_2$ ($0 \leq x \leq 0.08$).

increase of the electrical resistivity with temperature. While molybdenum substitution decreases the resistivity, the decrease is not systematic. However, its temperature dependence is reduced for all values of x investigated. While this could in part be explained by the better densification of doped samples, the value of the Seebeck coefficient, which is less sensitive to density variations, also varies with composition, demonstrating that the compositional evolution of electrical properties cannot solely be explained in term of density variation. The negative sign of the Seebeck coefficient confirms that the main charge carriers are electrons and all materials are *n*-type. The electrical resistivity and Seebeck coefficient measured for TiS_2 are slightly different than previously reported results[155] on TiS_2 single crystal with S = -173 μV K^{-1} and ρ = 0.025 mΩ m at 315 K against S = -251 μV K^{-1} and ρ = 0.017 mΩ m measured along the single crystal's *ab* plane at 300 K. One reason for these differences is the nature of the sample with an expectedly higher electrical resistivity in a polycrystalline sample due to the presence of boundary scattering. The lower absolute value of the Seebeck coefficient is likely to originate from a variation in the charge carrier concentration caused by titanium self-intercalation (as discussed in Section 3.1 and Section 3.2.5.2) and/or molybdenum substitution. The degree of non-stoichiometry for the pure titanium sulphide, TiS_2, was estimated[157] from the Seebeck coefficient, electrical resistivity and unit cell dimension to be *c.a.* 1.5 %. This is consistent with a *c* lattice parameter that lies in the range $5.695 \leq c$ / Å ≤ 5.700 and a unit cell volume of *ca.* 57.26 $Å^3$, both of which suggest a deviation from stoichiometry of 1.5 %. Because all $Mo_xTi_{1-x}S_2$ samples have been prepared in identical conditions of heat and pressure, it is reasonable to consider the degree of titanium self-intercalation arising from sulphur volatilisation to be constant at *ca*. 1.5 % across the series.

In order to investigate the potential effect of molybdenum doping, two new samples were synthesised with composition $Mo_xTi_{1-x}S_2$ (x = 0.015 and 0.035), along with a TiS_2 reference. These samples were divided in two series, one was consolidated after hand grinding and the second after a ball milling step (1 h, 350 rpm, 5 min intervals with change of direction) similar to that used for the Co_xTiS_2 series (Section 3.2.5.1). In an effort to reduce the effects associated with the degree of densification, the powders were consolidated using spark plasma sintering

(SPS), Section 2.7.1, following the sintering profile detailed in Appendix A. The pellets obtained using SPS have a density of 99 % of the crystallographic value.

Electrical measurements, carried out in-plane for $Mo_xTi_{1-x}S_2$ (x = 0; 0.015 and 0.035) for hand ground and ball milled samples processed by SPS are given in Figure 3.45. The electrical resistivity follows a metallic-like behaviour for all samples and the negative Seebeck

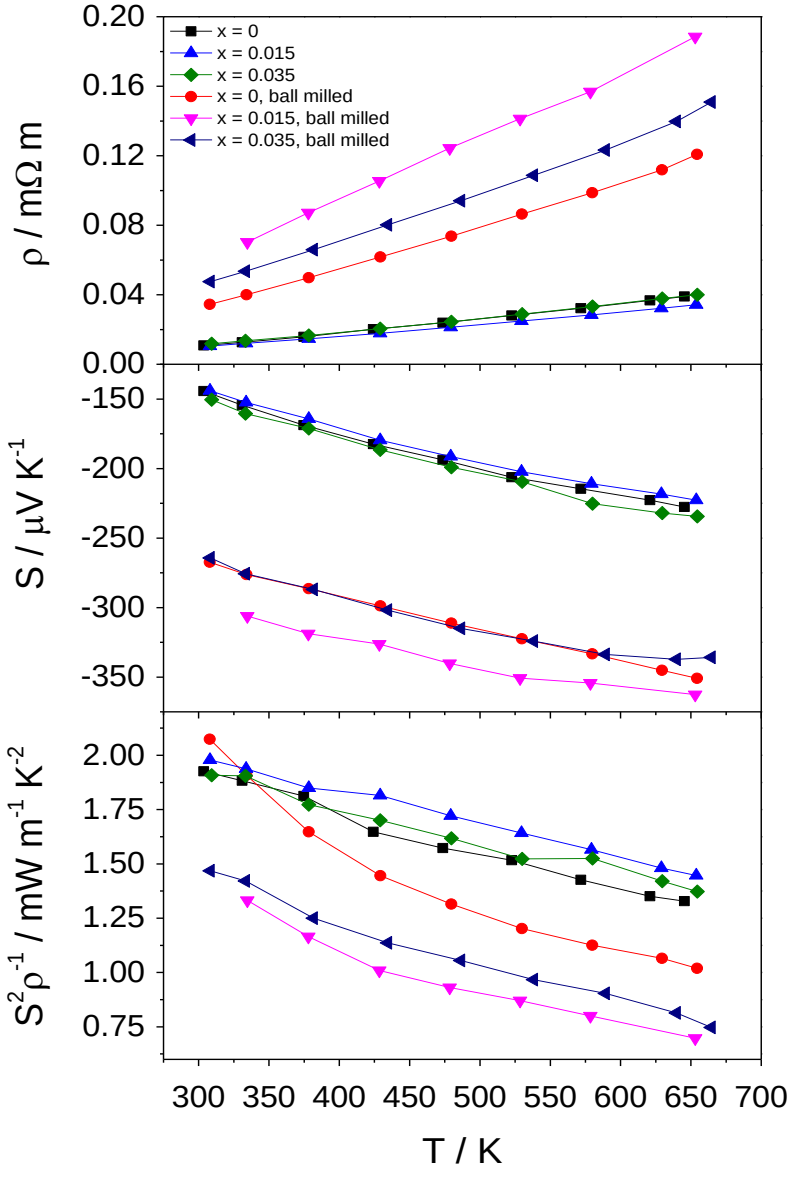

Figure 3.45 Temperature dependence of the electrical resistivity (top), Seebeck coefficient (middle) and power factor (bottom) of $Mo_xTi_{1-x}S_2$ (x = 0; 0.015 and 0.035) with and without ball mill step and processed by SPS.

coefficient values confirm the *n*-type character of the materials. In the case of the hand ground samples, the molybdenum doping seems to have no effect on the electrical properties. In comparison, the measurements made on $Mo_xTi_{1-x}S_2$ hot-pressed samples, Figure 3.44, also showed similar electrical properties between samples in a range of substitution $0.02 \leq x \leq 0.04$, although TiS_2 had a higher electrical resistivity that could be attributed to a poorer densification. However, the properties of ball milled samples consolidated by SPS are drastically different with substantially higher electrical resistivity and absolute Seebeck coefficient compared to hand ground samples. This ultimately results in a degradation of the power factor. Interestingly, the combination of ball milling and SPS densification dramatically increase the effect of molybdenum substitution. The electrical resistivity and the absolute value of the Seebeck coefficient of $Mo_xTi_{1-x}S_2$ initially increase for $x = 0.015$ before decreasing for $x = 0.035$. Nonetheless, the electrical resistivity of molybdenum-substituted samples remains higher than that of pristine TiS_2 and the resulting power factor is lower over the whole temperature range investigated.

Although molybdenum doping does not appear to be a promising approach to improve the electrical performance, ball milled TiS_2 consolidated by SPS reaches a high power factor, $S^2\rho^{-1} \approx 2.1$ mW m^{-1} K^{-2} at room temperature, the highest reported for $Ti_{1+\gamma}S_2$.[156-161, 194] The Seebeck coefficient and electrical resistivity at 300 K enable an estimate to be made of the non-stoichiometry in both TiS_2 samples. For samples prepared from hand ground powder and densified by SPS, the sulphur deficiency is slightly higher than for hot-pressed samples (Section 3.2.5.2) with an estimated composition of ca. $Ti_{1.02}S_2$. The additional ball mill step has the same effect with SPS than with the hot-pressed samples; the electrical resistivity and the absolute Seebeck coefficient increase substantially. The same conclusion can be drawn here with titanium de-intercalation occurring during the consolidation. The higher temperature (1073 K) used in SPS processing is consistent with this process being more pronounced than with hot-pressing (923 K). The composition after consolidation is estimated to be closer to stoichiometric with *ca*. 1 % of self-intercalated titanium.

3.3.3.2 Thermal transport properties

The cross-plane thermal diffusivity of $Mo_xTi_{1-x}S_2$ was measured and the thermal conductivity calculated, Figure 3.46. Measurements on the hot-pressed series were carried out on polished discs of ca. 2 mm width and *ca.* 12.7 mm diameter and measurements on the series consolidated by SPS were carried out on 6 × 6 × 2 mm^3 squares. Details of instrumentation are given in Section 2.7.3.

As with the electrical properties, molybdenum substitution has no apparent effect on the thermal conductivity of hot-pressed samples with values ranging from $\kappa \approx 2.1$ W m^{-1} K^{-1} at 373 K to $\kappa \approx 1.5$ W m^{-1} K^{-1} at 573 K for all investigated samples. These values are consistent with

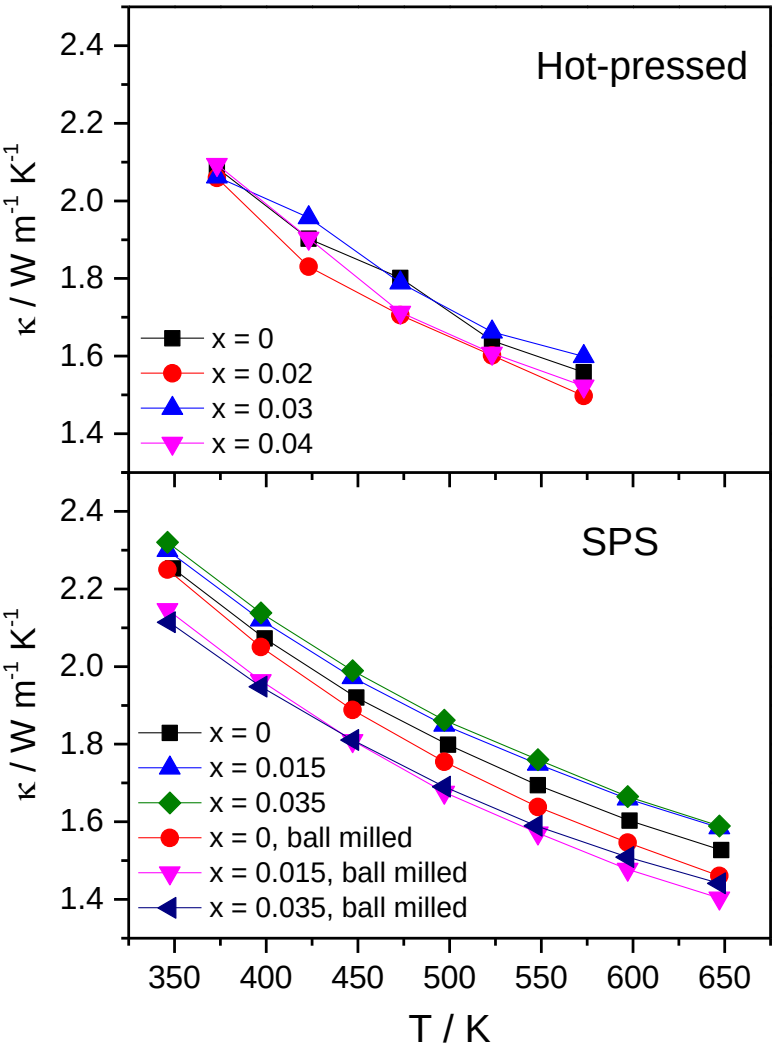

Figure 3.46 Temperature dependence of the cross-plane thermal conductivity of $Mo_xTi_{1-x}S_2$ after hot-pressing (x = 0; 0.02 and 0.04) and after SPS (x = 0; 0.015 and 0.035).

previous measurements, Section 3.2.5.3, with thermal conductivity of ball milled and hot-pressed TiS_2 being slightly lower, *ca.* 1.3 to 2.0 W m^{-1} K^{-1} over the same temperature range.

In samples consolidated by SPS, the effect of molybdenum substitution is again more pronounced in samples prepared from ball milled powders, similar to with the observations on electrical properties. Similarly, the thermal conductivity for samples prepared from hand ground powder is unchanged, within the experimental error, upon molybdenum doping. This suggests that the small differences in the temperature dependence of κ are in part explained by the reduction of the electronic component.

3.3.4 Heat soak experiment

In order to investigate the durability and the reproducibility of the thermoelectric properties of TiS_2, a 26 days heat-soak test was undertaken at 473 K on TiS_2 consolidated by SPS. The sample was left in a furnace, in air, and taken out for electrical measurements after 4, 12, 19 and 26 days. A thin layer of oxide formed and was polished off at the contact points of the sample with the electrical probes. Electrical measurements, represented by the power factor, are shown in Figure 3.47.

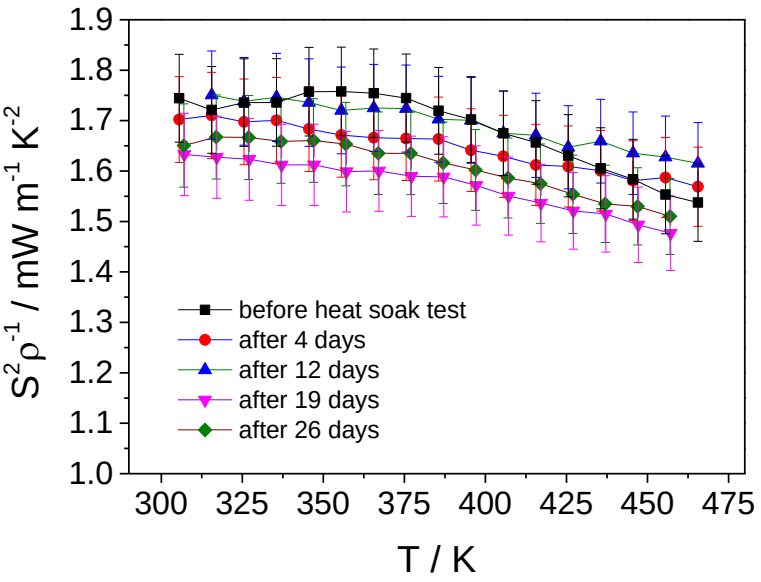

Figure 3.47 Temperature dependence of the power factor of TiS_2 at different points in the heat-soak test (473 K). The error bars correspond to a 5 % variation.

No significant changes are observed with values of power factor all within a 5 % experimental error margin. This experiment combined with thermogravimetric analysis (Figure 3.25) show that TiS_2 can be used in applications requiring working temperatures up to 473 K. However, the observed surface oxidation indicates that a protective coating would greatly improve the longevity of TiS_2 based devices.

3.4 Conclusions

Structural properties of the cobalt intercalates of titanium disulphide, Co_xTiS_2 ($0 \leq x \leq 0.75$), have been studied using a combination of powder X-ray and neutron diffraction. As the cobalt intercalation level increases, the system evolves from a disordered phase, in which Co randomly occupies octahedral sites, through three superstructure types, monoclinic M_5S_8 (x = 0.25), trigonal M_2S_3 (x = 1/3) and monoclinic M_3S_4 (x = 0.5) to a second disordered phase, Figure 3.48. In this high cobalt intercalated disordered phase, both octahedral and tetrahedral interstitial sites are occupied. Neutron diffraction data at temperature below 2 K do not reveal any sign of a long-range magnetically ordered phase. Magnetic susceptibility and muon spectroscopy measurements were used to investigate the magnetic behaviour of these

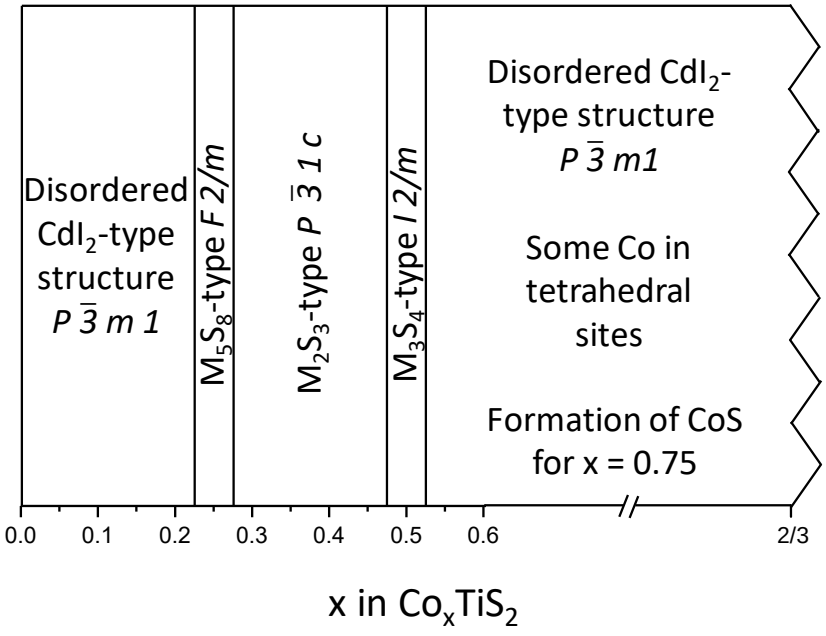

Figure 3.48 Structural arrangements of Co_xTiS_2 ($0 \leq x \leq 2/3$) established from XRD and neutron diffraction analysis.

superstructures and disordered phases. At low cobalt content, Co_xTiS_2 ($x < 1/3$), the effective magnetic moments are in reasonable agreement with a +2 oxidation state of cobalt. Data for higher intercalation levels are consistent with previous reports of the formation of a $(t_{2g})^6(e_g)^1$ low-spin cobalt-based band near the Ti 3*d* band. The presence of a magnetic impurity, possibly CoS, in the range 350 K to 400 K for $Co_{0.75}TiS_2$ suggests that the limit of the single-phase region of Co_xTiS_2 lies in the range $2/3 \leq x \leq 3/4$. Muon spectroscopy experiments revealed the presence of strong internal magnetic fields below 35 K for samples of composition Co_xTiS_2 ($x = 0.25$ and 0.50), giving strong evidence for short-range magnetic ordering and an internal field of *ca*. 0.4 T experienced at the muon site. Cobalt intercalation has a strong impact on the electron-transport properties and thermal behaviour of TiS_2. Electrical property measurements revealed that the electron transfer from Co^{2+} to the conduction band of the TiS_2 host causes a rapid and systematic reduction of the electrical resistivity in well-densified samples. The accompanying fall in the absolute value of the Seebeck coefficient is detrimental to the thermoelectric performance. The resulting power factor is improved for low intercalation level. This motivated a more thorough investigation of the TE properties of Co_xTiS_2 ($x \leq 0.10$), taking into account the anisotropy of the consolidated samples revealed by powder X-ray diffraction. Along with a low power factor, the thermal conductivity for samples with higher cobalt content remains high despite the artificially low electronic contribution arising from the moderate porosity of the samples. The power factor of the Co_xTiS_2 series ($0.02 \leq x \leq 0.1$) is comparable to that of pristine TiS_2 above 500 K for cross-plane and above 550 K for in-plane measurements. The disordered distribution of cobalt cations in interstitial sites reduces the lattice thermal conductivity via increased phonon scattering. This reduction is more pronounced than the increased electronic contribution and the overall thermal conductivity is decreased. Overall, the incorporation of low levels of cobalt is beneficial to the figure of merit with the highest ZT increased by 25 % over that of pristine TiS_2. The maximum value is obtained in in-plane measurements for Co_xTiS_2 ($0.04 \leq x \leq 0.08$) at 573 K with ZT = 0.3. Such a high ZT value at low temperature is encouraging for large scale application. For comparison, this level of performance for *n*-type sulphides is usually achieved at higher temperatures with $ZT \geq 0.4$ at 950 K for $Cu_4Mo_6S_8$[210] and $LaGd_{1.02}S_3$,[89] and $ZT \geq 1$ for doped-Bi_2S_3 at 923 K.[79] For temperatures similar to those investigated here, similar performance is obtained for the

related M_xTiS_2 (M = Cu, Ag)[156, 160] and TiS_2-based superlattices[117, 161] prepared by spark plasma sintering and for the hot-pressed Shandite-type phase $Co_3Sn_{1.6}In_{0.4}S_2$.[100]

Substitution of titanium by molybdenum was attempted in order to improve the thermoelectric properties of TiS_2 via electron doping and increased phonon scattering. Powder X-ray diffraction analysis was carried out on $Mo_xTi_{1-x}S_2$ ($0 \leq x \leq 0.09$) and measurements of thermoelectric properties were carried out on series of molybdenum substituted TiS_2 with different preparation methods, hot-pressed $Mo_xTi_{1-x}S_2$ ($0 \leq x \leq 0.08$) and $Mo_xTi_{1-x}S_2$ (x = 0; 0.015 and 0.035) consolidated by SPS from hand ground and ball milled powder. The impact of molybdenum in samples, consolidated by SPS or hot-pressing, is ambiguous. The conduction band of TiS_2 being mainly composed of the Ti 3*d* orbitals, the substitution of Ti(IV), d^0, by Mo(IV), d^2, should in theory contribute to an increase in the total electron count and increase the charge carrier concentration. However, the increased electrical resistivity and Seebeck coefficient are indicative of a decrease in the charge carrier concentration or in the charge carrier mobility. Evidence for the formation of a second phase, MoS_2, obtained for doping levels as low as $x \geq 0.03$ indicates that the measured electrical and thermal properties could be described in term of variations in the level of titanium self-intercalation that depends on the sample fabrication. To investigate this further, Hall effect measurements could be used to obtain information on the carrier concentration and mobility. Nonetheless, the power factor determined for TiS_2 consolidated by SPS from ball milled powder is higher than those previously reported, approaching $S^2\rho^{-1} \approx 2.1$ mW m^{-1} K^{-2} at 323 K with no change observed in the thermal conductivity. This suggests that a simple 1 h ball milling step can be highly efficient in improving the electrical performance at low temperature. A heat-soak experiment was successful in demonstrating the reproducibility of the electrical properties of TiS_2 consolidated by SPS for application at temperature that do not exceed 473 K.

Cost-efficient, low grade waste heat recovery is promising in many domestic applications where the temperature rarely exceeds those investigated in this chapter. The results obtained are encouraging with ZT comparable to that of the best *n*-type sulphides at these temperatures. Further investigations on the impact of ball milling combined with spark plasma sintering would lead to substantial improvements in the thermoelectric performance of Co_xTiS_2.

Chapter 4 - TiS_2 nanoparticles and nanocompositing

4.1 Introduction

As outlined in Chapter 1, the search for thermoelectric materials with better performance is constrained by the interdependency of the Seebeck coefficient, electrical resistivity and thermal conductivity. The introduction of dimensionality as a new variable brings different strategies that enables the electrical and thermal properties to be tuned more independently.[20, 22, 23, 211, 212] Electrical properties can be tuned using phenomena such as energy filtering[213] or quantum-confinement,[21, 67] which consists of decreasing the system size to the nanoscale with considerable changes being made respectively on the electron scattering dynamics and the density of states. The consequence is a potential control of the Seebeck coefficient with little effect on the electrical resistivity and an improved power factor. Additionally, the reduction in the particle size increases the number of grain boundaries that have been shown to effectively scatter the heat-carrying phonons, decreasing the thermal conductivity more than the electrical conductivity.[21, 39, 214] Decreasing the particle size down to a few nanometres has been found to make dramatic improvements in ZT, such as in chalcopyrite nanocrystals, $CuFeS_2$, with a ZT of *ca*. 0.26 at 500 K, corresponding to an increase by almost two orders of magnitude compared to the bulk material.[97]

Although a few synthesis routes for the production of TiS_2 nanoparticles have already been reported, their potential application as thermoelectric materials still requires investigation. Solution-based synthesis of TiS_2 has been reported to produce particles with a wide range of morphologies such as nanodiscs,[215] fullerene-like nanoparticles,[216, 217] 1-D chains,[218] nanotubes,[219, 220] or amorphous nanoparticles.[221] In the first part of this chapter, nanoparticles with flower-like and flake-like morphologies have been synthesised using an easily scalable liquid-phase route and their potential application as thermoelectric materials is investigated.

Another way of taking advantage of nanostructures is by incorporating nanoparticles within a bulk material matrix. Because reductions in thermal conductivity can be achieved without any ordering of the nanoparticles within the host matrix,[21, 222] improvements in the thermoelectric

performance can be achieved by a simple dispersion of nanoparticles in a host material with techniques such as ball milling. This strategy has been found to improve the ZT of thermoelectric materials by decreasing the thermal conductivity and in some cases by improving the Seebeck coefficient via energy filtering or quantum confinement. For instance, the performance of a zone-melted commercial ingot of Bi_2Te_3 was dramatically increased by the addition of Bi_2Te_3 nanotubes prepared by solvothermal synthesis; the composite reaching a ZT between 0.8 and 1 over the temperature range $330 \leq T / K \leq 510$.[223] The performance of $Bi_{0.3}Sb_{1.7}Te_3$ was largely improved by the dispersion of 0.4 vol% of SiC nanoparticles and the nanocomposite reached a ZT value of 1.33 at 373 K.[26] Overall, many nanocomposites involving the derivatives of bismuth telluride and lead telluride in particular have been studied recently, resulting in improvements in ZT.[24, 26, 27, 214, 223-229] An impressive ZT value of *ca*. 2.2 at 915 K has been reported in *p*-type PbTe endotaxially nanostructured with 4 mol% of SrTe.[68] Embedding PbS nanoparticles in a TiS_2 host has been demonstrated to be a good strategy to improve the thermoelectric performance of the material. The power factor of TiS_2 was increased by *ca*. 110 % at 300 K and by *ca*. 35 % at 673 K owing to an increase in Seebeck coefficient attributed to energy filtering upon the dispersion of 1 mol% of PbS nanoparticles.[230] Similarly, incorporation of MoS_2 nanoparticles has led to a decrease in the charge carrier concentration and improved phonon scattering. As a result, an increase in the absolute value of the Seebeck coefficient and a decrease in the thermal conductivity substantially improved the thermoelectric performance with ZT reaching *ca*. 0.3 at 573 K for TiS_2 with 3 mol% of nano-MoS_2.[231] This corresponds to a 60 % increase over the parent TiS_2 before nanocompositing. In the second and third part of this chapter, the effect of nanocompositing with two types of nanoparticles, TiO_2 and carbon nanotubes, has been investigated.

4.2 TiS_2 nanoflakes and nanoflowers

Sizable application of thermoelectric devices requires synthesis techniques that are adapted to large-scale industrial processes. The thermoelectric properties of TiS_2 with respect to its raw materials cost are excellent, see Chapter 3, but high-temperature solid-state reaction can be difficult to adapt to the industrial scale for multiple reasons. The energy cost to keep the powders at 650 ºC for several hours is important, the need for an evacuated sealed environment

adds to the production cost and the pressure built up by sulphur gas in a closed system can lead to fire and explosion hazards as well as toxic gas emissions. Taking this into consideration, two different synthesis routes have been investigated as part of the InnovTeg project: a top-down approach (mechanochemical synthesis) and a bottom-up approach (liquid-phase reaction). Most of the work on mechanochemical synthesis was completed by collaborators[232] and therefore are not discussed here.

Liquid-phase reaction is widely used in industry as it offers a controlled and relatively cost-efficient route to synthesising large amounts of powdered materials. A number of routes were explored by different groups in the past decades, producing TiS_2 materials with controlled morphology. Solution-based reactions have led to the synthesis of TiS_2 nanoparticles with different morphologies for applications ranging from lithium batteries[45] to cancer therapy.[233] In this section, nanoparticles with flower-like (nanoflowers) and flake-like nanoparticles (nanoflakes) have been synthesised using direct reaction between sulphur and titanium tetrachloride in a high boiling point solvent.

4.2.1 Synthesis

The synthesis, adapted from the work of Prabakar et al.,[234] simultaneously offers a scalable route to TiS_2 materials and the production of nanoparticles with controlled morphology. The two reactions were completed under reflux in a three-necked round bottom flask under flowing nitrogen, Figure 4.1. Sulphur flakes (Sigma Aldrich, 99.99 %) were ground and dissolved in 1-octadecene (Sigma Aldrich, 90 %), slowly heated up to 150 ºC and degassed for 30 min. For the production of nanoflowers, *ca*. 0.2 g of sulphur (6 mmol) was dissolved in 20 mL of 1-octadecene and 0.1 mL of $TiCl_4$ (1 mmol, Sigma Aldrich, ≥ 99.0 %) was rapidly injected at 300 ºC. The mixture quickly turned black and was allowed to react for 10 min before being cooled to room temperature at the natural cooling rate. For the production of nanoflakes, *ca*. 1 g of sulphur (30 mmol) was dissolved in 40 mL of 1-octadecene and 0.5 mL of $TiCl_4$ (5 mmol) was injected at 150 ºC. The reaction temperature was slowly increased to 300 ºC over 25 min and kept for 10 min before being cooled down to room temperature. For both reactions, black precipitates were collected by centrifugation and washed repeatedly with toluene and methanol.

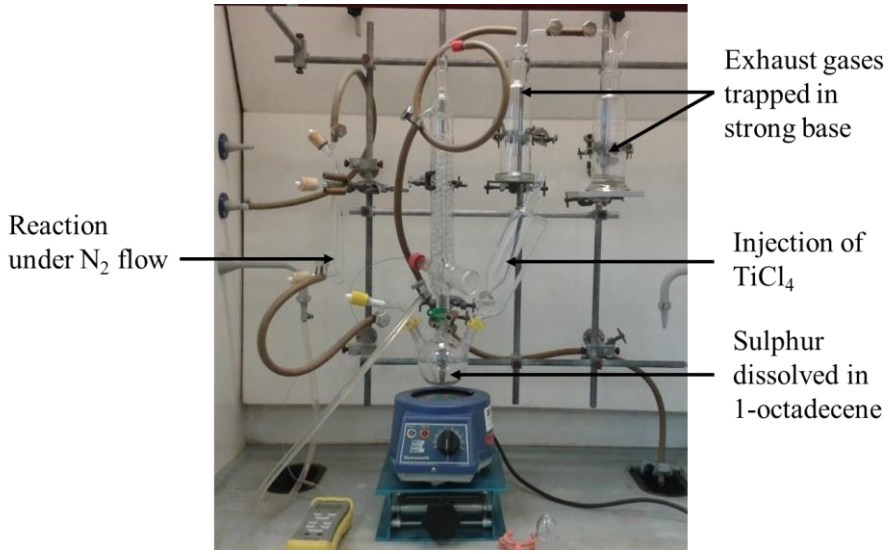

Figure 4.1 The experimental set-up for liquid-phase synthesis of TiS_2

4.2.2 SEM/EDX analysis

Scanning electron micrographs of the samples from the two reactions were taken and EDX analysis was carried out using an Environmental Scanning Electron Microscope (ESEM), Section 2.8. The elemental analysis for each sample was determined from the sum spectrum of at least three scans, with a high magnification ranging from $\times 10^4$ to $\times 10^5$. Injection of titanium tetrachloride at 300 ºC, resulted in the expected flower-like nanoparticles of *ca*. 500 nm in size, Figure 4.2, consistent with the literature.[234] EDX analysis shows the presence of chlorine in the final compounds, with an approximate composition of $TiS_{1.1(1)}Cl_{0.2(1)}$. Prabakar *et al*. described the growth mechanism of TiS_2 nanoflowers, and attributed the presence of chlorine to the formation of amorphous TiS_xCl_y compound in the spherical core of the nanoparticles.[234] Injection of titanium tetrachloride at 150 ºC, followed by an increase in temperature, produces flake-like particles of various size, from a few hundred nanometres to a few microns, Figure 4.3. EDX analysis did not indicate any substantial amount of chlorine, consistent with previous observations[234] and a rapid formation of flakes without the initial formation of amorphous TiS_xCl_y spheres. The determined composition of approximately $TiS_{1.8(1)}$, is much closer to the desired stoichiometry.

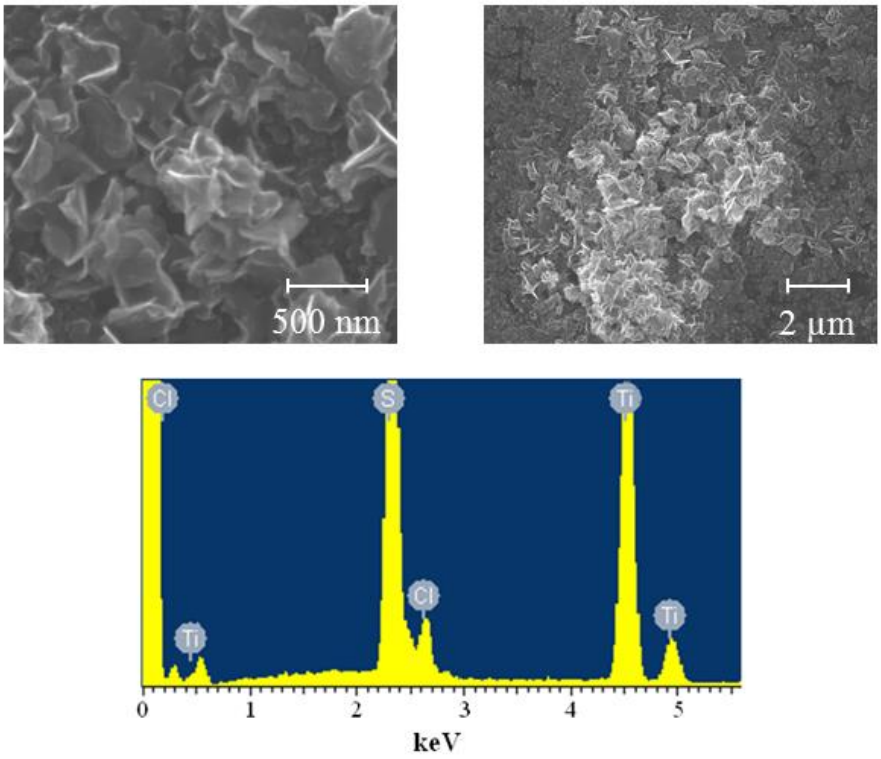

Figure 4.2 Scanning electron micrographs of nanoflowers (top) and EDX analysis (bottom).

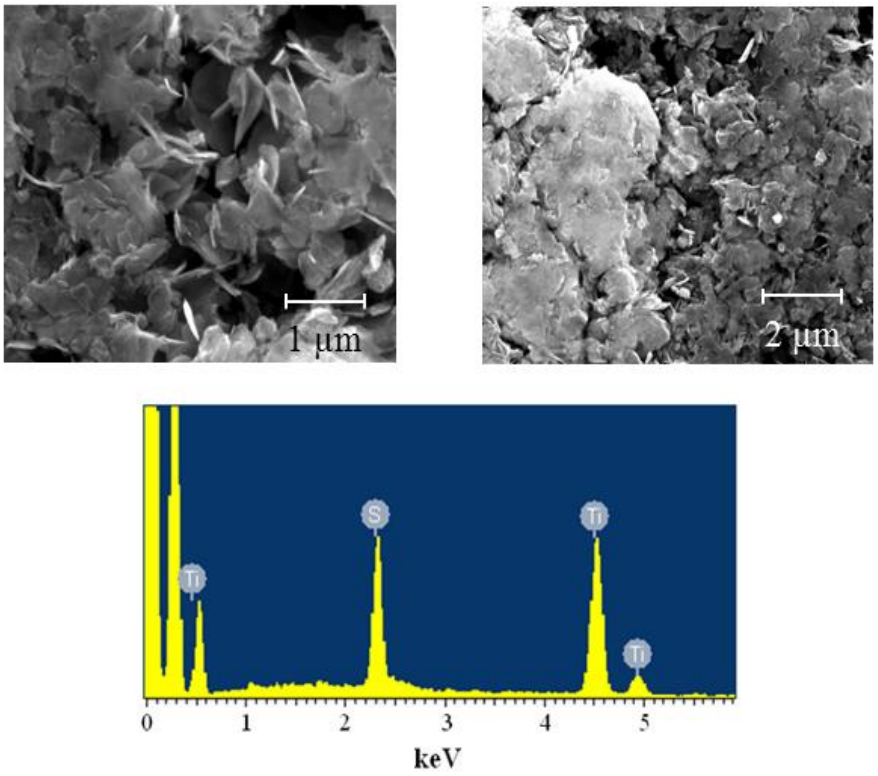

Figure 4.3 Scanning electron micrographs of nanoflakes (top) and EDX analysis (bottom).

4.2.3 TiS_2 nanoflakes as thermoelectric materials

The synthesis of TiS_2 nanoflowers produced only a few milligrams of sample, with a composition too different from the desired Ti to S ratio of 1:2. However, the synthesis of nanoflakes, scaled up by a factor 5 in only twice as much solvent, produced sufficient chlorine-free material (0.15 g, 27 % yield) for the consolidation of a small pellet of 5 mm in diameter. The powder was cold-pressed in a 5 mm diameter stainless steel mould for 30 min with a pressure of 1 GPa and sintered in a sealed tube at 650 °C for 12 h. The obtained shiny-gold pellet had a density of 2.21 g cm^{-3}, 69 % of theoretical value. Powder X-ray diffraction data for the sintered material, Figure 4.4, confirm the formation of TiS_2 with only trace amounts of impurities, likely to be a mixture of anatase and rutile TiO_2 from the hydrolysis of residual titanium chloride or from reaction of TiS_2 with adsorbed moisture during the sintering step. The sintered pellet, with a thickness of 3.2 mm, only permitted measurement of the Seebeck coefficient in an adapted sample mount, Figure 4.5, at temperatures below 340 K. The measurement was carried out in air, from room temperature to 340 K. The apparatus used for this measurement is described in the Section 2.7.2.2. The Seebeck coefficient can then be compared with the literature values for $Ti_{1+x}S_2$ to estimate the level of non-stoichiometry in the material.[157] The results are plotted in Figure 4.5, alongside TiS_2 prepared by conventional solid-

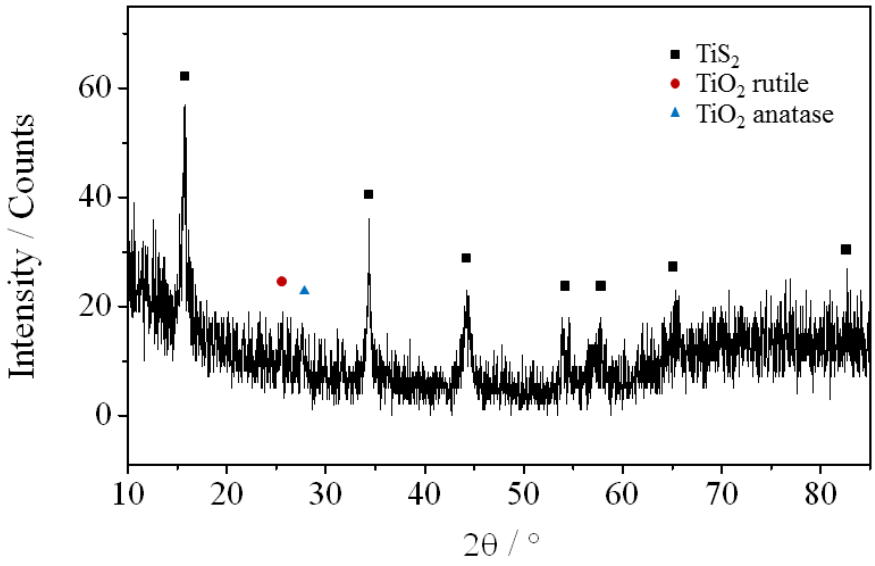

Figure 4.4 Powder X-ray diffraction pattern of the surface of the TiS_2 nanoflakes cold-pressed and sintered pellet.

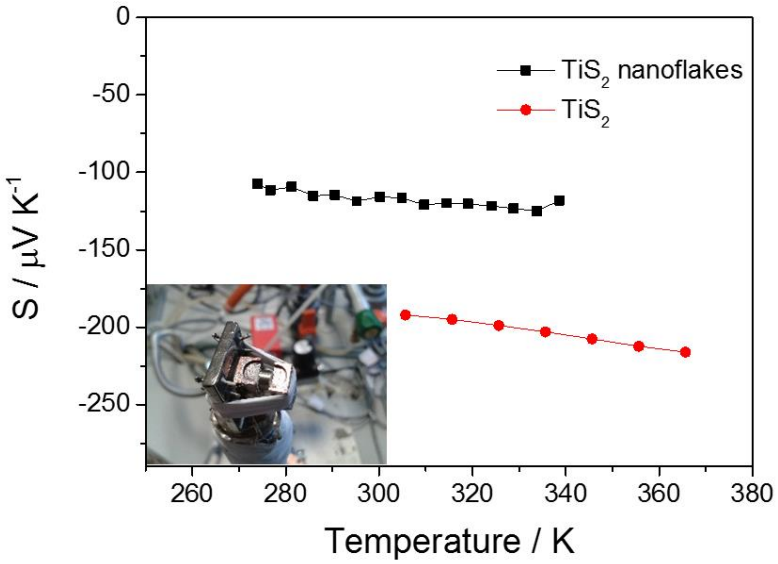

Figure 4.5 Temperature dependence of the Seebeck coefficient of the TiS_2 nanoflakes compared with cross-plane measurement on hot-pressed TiS_2.

state reaction and hot-pressed, see Section 3.2.5.2, in the cross-plane direction, *i.e.* in the direction of pressing. At 300 K, the Seebeck coefficient was measured to be around -115 μV K^{-1}, which is halved compared with conventional TiS_2 and would correspond to a stoichiometry of $Ti_{1+x}S_2$ where x is within the range $0.02 \leq x \leq 0.03$. After the measurement, a second powder X-ray diffraction analysis was carried out, Figure 4.6, and data revealed a large increase in the

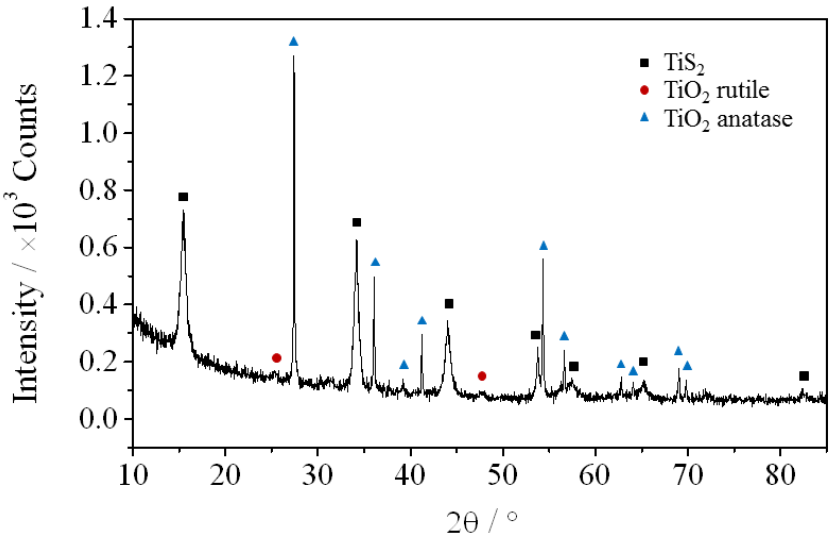

Figure 4.6 Powder X-ray diffraction of the surface of the TiS_2 nanoflakes cold-pressed/sintered pellet after measurement of the Seebeck coefficient.

amount of TiO_2 impurities in the sample. The formation of anatase is likely to have occurred during the measurement as the temperature increased, up to 350 K on the hot side. The large surface-to-volume ratio from the very small particle size allows for substantial amounts of moisture from the air to be adsorbed. It is likely that the energy transferred as heat during the measurement caused a reaction at the surface of the grains and the high porosity of the sample may have contributed to the extent of the oxidation.

These results indicate that direct reaction between sulphur in solution and titanium tetrachloride can offer a scalable route to the production of TiS_2 nanoparticles. Unfortunately, the available lab-scale equipment did not allow for larger samples to be synthesised and subsequently no pellet with good size and density could be produced. Substantial oxidation occurs in TiS_2 nanoparticles even at a temperature as low as 340 K. Nevertheless, it is possible to remedy to the oxidation issue by producing samples with high density and using a protective coating. The thermal conductivity of a sample with nanoscale grains is expected to be much lower than that of the bulk material[235] and TiS_2 nanoflakes are still highly promising thermoelectric materials. However, more suitable laboratory equipment is required to complete the investigation.

4.3 TiS_2/nano-TiO_2 nanocomposites

A series of titanium disulphide nanocomposites containing 0.5 %, 1.0 % and 1.5 % in volume of titanium oxide nanoparticles has been prepared. Powder X-ray diffraction analysis and the electrical and thermal transport property measurements were carried out. Nanocompositing with insulating TiO_2 nanoparticles carried out in an effort to decrease the thermal conductivity by the addition of grain boundaries and to investigate the effect of controlled addition of oxides on the electrical properties.

4.3.1 Sample preparation

A series of nanocomposites of bulk TiS_2 and TiO_2 nanoparticles was obtained by mechanically milling titanium disulphide with 0.5 %, 1 % and 1.5 % in volume of nano-TiO_2. The parent TiS_2 powder was prepared by conventional solid-state reaction between stoichiometric amounts of Ti (Alfa Aesar, dehydrided, 99.99 %) and S (Sigma Aldrich, flakes, 99.99 %) in evacuated and sealed silica tubes following the process detailed in Section 3.2.1. Each one of

the 6 g batches was checked using powder X-ray diffraction and only the samples with no evidence for TiO_2 impurities were kept and mixed together. By doing so, all nanocomposites were prepared from the same large batch of TiS_2. The next step involved ball milling (400 rpm, 2 h, 5 min interval with change of direction) TiS_2 with TiO_2 nanoparticles (Sigma Aldrich, mixture of rutile and anatase, 21 nm, 99.5 %) in a stainless steel jar in an inert argon atmosphere with a powder to ball weight ratio of 1:6. All samples were stored in an argon glove box to prevent unwanted oxidation of TiS_2. The ball milled powder was hot-pressed (650 °C, 100 MPa, 30 min) into two pellets, one with a thickness of *ca*. 2 mm and the other *ca*. 8-10 mm which were then cut into ingots following the process detailed in Section 3.2.5.1 in order to measure the electrical and thermal properties in the in-plane and cross-plane direction. The densities of the samples were all higher than 95 % of the theoretical value.

4.3.2 Powder X-ray diffraction

Powder X-ray diffraction data for the TiS_2/nano-TiO_2 nanocomposites series, Figure 4.7, were acquired on ground fragments of pellet. In some cases, trace amounts of SiO_2 were detected, likely to be coming from small shards of the quartz tubes used during the synthesis of TiS_2.

The commercial nanoparticles used for compositing contain both the anatase and rutile phases of TiO_2, Figure E.1 (Appendix E). Peaks corresponding to the highest intensity reflection of anatase and rutile are marked and their intensities increase, as expected, with the level of nanoparticles introduced. Rietveld refinements were carried out on XRD data, Figure

Table 4.1 Refined parameters from Rietveld analysis of powder X-ray diffraction data for TiS_2/nano-TiO_2 nanocomposites. (Space group $P\bar{3}m1$)[a]

		Vol% of nano-TiO_2			
		0	0.5	1	1.5
	a / Å	3.40795(3)	3.4077(2)	3.40851(8)	3.40817(8)
	c / Å	5.69926(7)	5.7007(3)	5.7014(3)	5.7007(3)
Ti	B / Å^2	0.90(6)	0.04(5)	1.5(2)	1.24(7)
S	z	0.2480(3)	0.2451(4)	0.2496(6)	0.2488(4)
	B / Å^2	0.70(6)	0.04(5)	1.3(2)	0.98(7)
	R_{wp} / %	6.78	8.90	9.29	9.25
	χ^2	3.61	1.71	1.71	1.78

[a] Ti on 1(a), (0, 0, 0); S on 2(d), (1/3, 2/3, z); Co on 1(b) (0, 0, 1/2), constrained at nominal composition.

4.8 and Table 4.1, and small variations were observed in the lattice parameters, plotted in Figure 4.9. The scale of these variations, *ca*. 0.001 Å and 0.002 Å for the *a* and *c* lattice parameters respectively, is small compared with the effect of titanium self-intercalation, from TiS_2 (c = 5.678 Å) to $Ti_{1.05}S_2$ (c = 5.715 Å).[157] It is likely that only very small differences in the amount of self-intercalated titanium are the reasons for such variations.

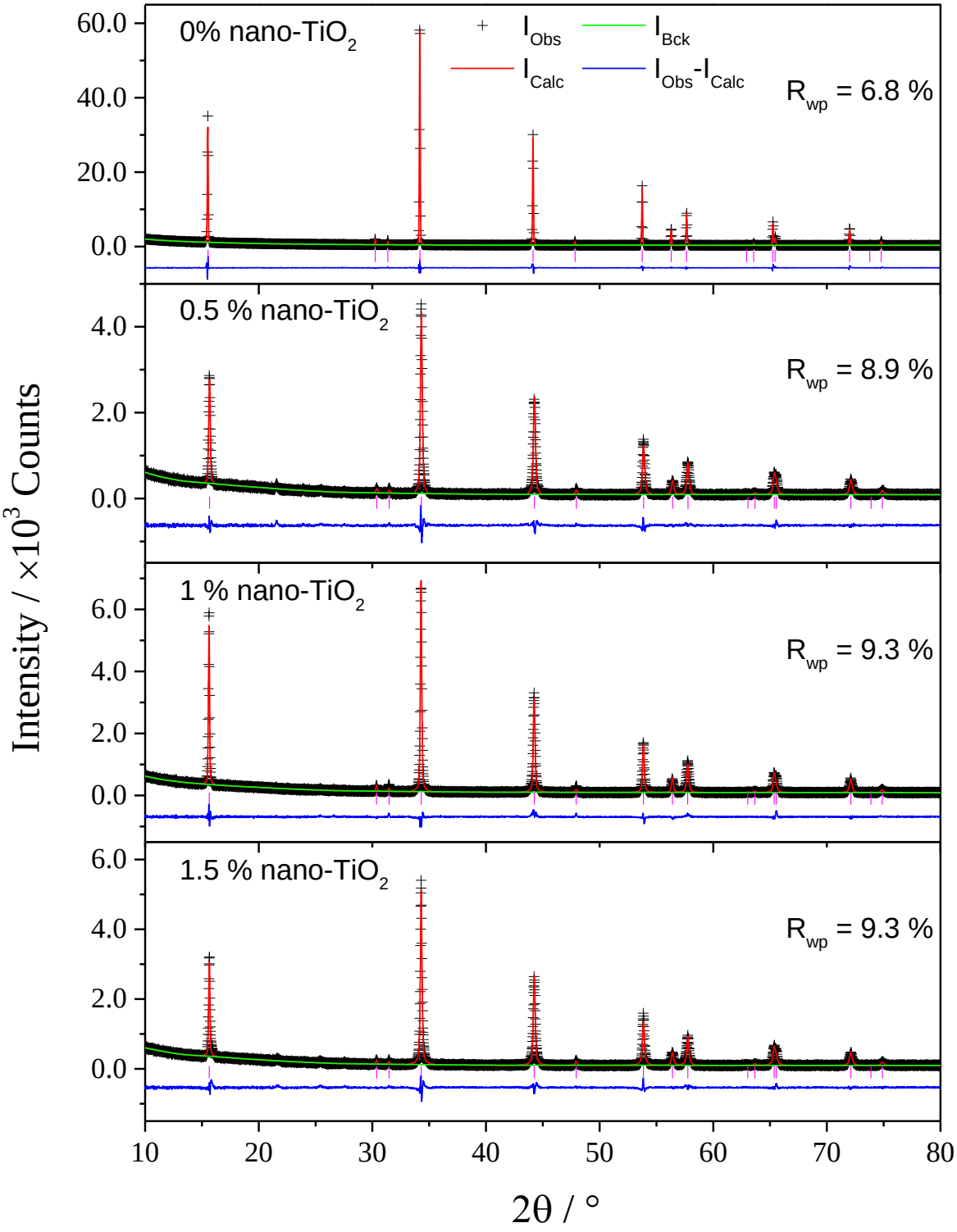

Figure 4.8 Observed (crosses), calculated (full line) and difference (lower full line) profiles for TiS_2/nano-TiO_2 nanocomposites from Rietveld refinement of XRD data. Reflection positions of TiS_2 are signalled by tick marks.

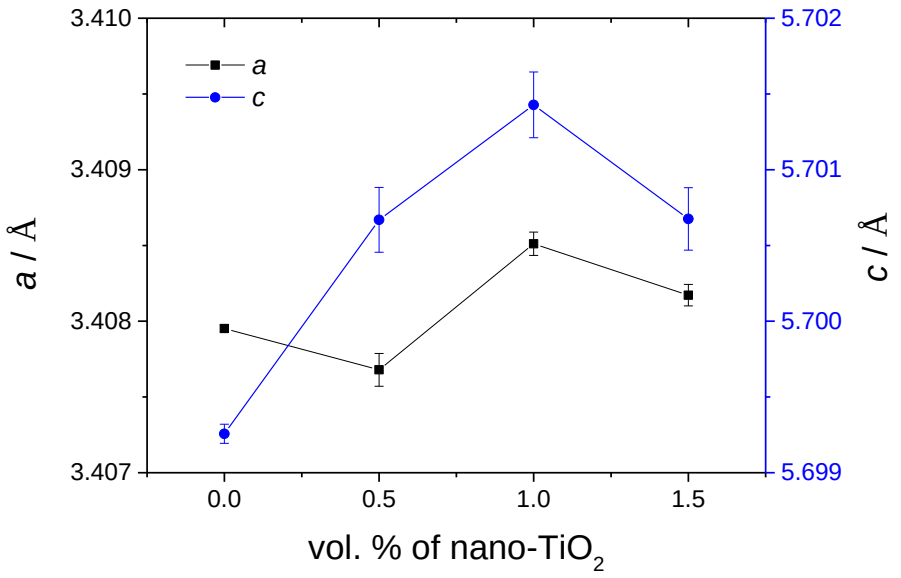

Figure 4.8 Unit-cell parameters of TiS_2/nano-TiO_2 nanocomposites as a function of the vol% of TiO_2 nanoparticles from Rietveld refinements of XRD data.

4.3.3 Thermoelectric performance

4.3.3.1 Electrical properties

Because of the highly anisotropic electrical and thermal properties of TiS_2 samples, established in Section 3.2.5.1, the temperature dependence of the electrical resistivity and Seebeck coefficient of the TiS_2/nano-TiO_2 series were measured in both in-plane (i.e. in the direction perpendicular to the pressing) and cross-plane (i.e. along the pressing axis) directions. Measurements on pristine TiS_2 carried out in-plane, Figure 4.10, are in very good agreement with those reported in Section 3.2.5.2 and measurements made on a single crystal by Imai et al.[155] All samples are *n*-type materials with a metallic behaviour of the electrical resistivity. The in-plane Seebeck coefficient for TiS_2 at 300 K was measured to be S = -226 μV K^{-1}, comparable to the single crystal value (S = -251 μV K^{-1} at 300 K) measured within the *ab* plane. The electrical resistivity, ρ = 0.028 mΩ m at 300 K, is also comparable with measurements on a single crystal (ρ = 0.017 mΩ m). The addition of 0.5 vol% of TiO_2 nanoparticles causes a reduction in the electrical resistivity and in the absolute value of the Seebeck coefficient. This could be indicative of an increase in the charge carrier concentration. Stoichiometric TiO_2 has no *3d* electrons and is an electrical insulator,[236] hence this increase in charge carrier

concentration could be explained by variations in the level of Ti self-intercalation in TiS_2. For higher nano-TiO_2 incorporation, the effect is reversed and both the absolute value of the Seebeck coefficient and the electrical resistivity are increased. A similar observation was made by Li et *al*. with the dispersion of 0.4 vol% of SiC nanoparticles into bulk $Bi_{0.3}Sb_{1.7}Te_3$, causing a decrease in the electrical resistivity, although SiC has a higher electrical resistivity than $Bi_{0.3}Sb_{1.7}Te_3$.[26] In the case of TiS_2/nano-TiO_2, however, this is accompanied by a decrease in |S|, consistent with a small increase in the charge carrier concentration for 0.5 vol% of nano-TiO_2. This could be in part explained by an increase in the number of defects in the structure and in part by an increase in the amount of intercalated titanium, causing the charge carrier concentration to increase slightly with nanocompositing. The presence of small amounts of intercalated Ti is supported by the increase in the *c* lattice parameter of nanocomposites compared with parent TiS_2, observed in Section 4.3.2. There are two simple mechanisms for the intercalation of Ti in the van der Waals' gap of TiS_2, either by sulphur volatilisation and self-intercalation or by the incorporation of titanium from an external source. Because TiO_2 allows for some small level of non-stoichiometry,[237] it is possible that Ti atoms migrating from TiO_2 to the van der Waals' gap of TiS_2 also contribute to the apparent increase in the charge carrier concentration. For samples with 1 vol% and 1.5 vol% of nano-TiO_2, however, the electrical resistivity and the absolute value of the Seebeck coefficient increase. This could be explained by a reduction in the charge carrier mobility from the increased number of grain boundaries and by the addition of an electrically insulating second phase. Unlike the sample with 0.5 vol% of nano-TiO_2, the small increase in charge carrier concentration, caused by possible structural defects and intercalation of a small amount of Ti from TiO_2, does not compensate any more for the loss of carrier mobility and the amount of insulating material. Hall effect measurements on the series, in order to determine the evolution of the charge carrier concentration and mobility, would help to understand the mechanisms involved here. The consequence on the power factor is beneficial for 0.5 vol% with the highest calculated value of $S^2\rho^{-1} = 1.91$ mW m^{-1} K^{-2} reached at 305 K, a small improvement from parent TiS_2 with a power factor of $S^2\rho^{-1} = 1.82$ mW m^{-1} K^{-2} at the same temperature. Nanocomposites with higher vol% of nano-TiO_2 have lower power factors due to the increased electrical resistivity.

Measurements of Seebeck coefficient and electrical resistivity of the parent TiS_2 phase carried out in the cross-plane direction, Figure 4.11, compare favourably with those presented in Chapter 3 with S = -194 μV K^{-1} and ρ = 0.039 mΩ m at 310 K. The anisotropy of the electrical properties of the hot-pressed samples is not as pronounced as the anisotropy in single-crystal measurements with electrical resistivity values two orders of magnitude lower than

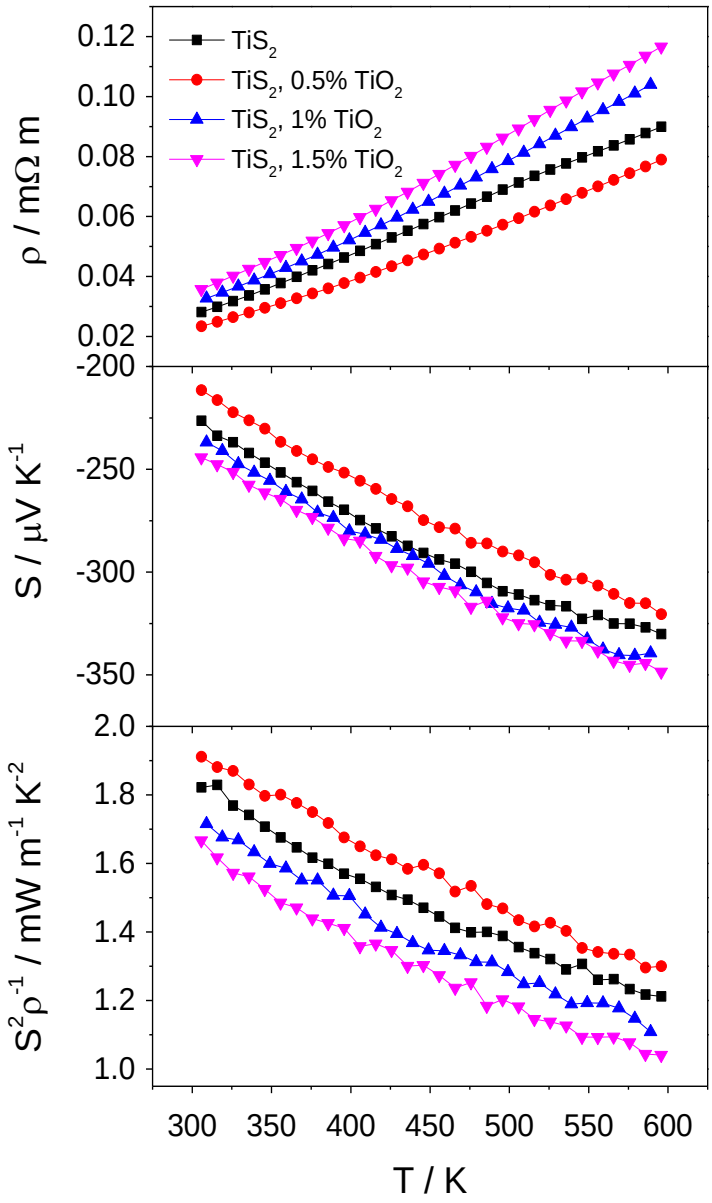

Figure 4.9 Temperature dependence of the electrical resistivity (ρ), Seebeck coefficient (S) and power factor ($S^2\rho^{-1}$) of TiS_2/nano-TiO_2 nanocomposites measured along the in-plane direction.

measurements carried out along the *c* axis of a single crystal.[155] The electrical resistivity of the TiS_2/nano-TiO_2 series measured in the cross-plane direction shows a metallic temperature dependence and a systematic increase with the addition of TiO_2 nanoparticles. The lowest electrical resistivity value is obtained for the parent TiS_2 with $\rho = 0.039$ mΩ m at 310 K, which is about twice that of the in-plane value. In parallel, the Seebeck coefficient, while lower in absolute value compared to in-plane measurements, behaved in a very similar way with respect to the volume % of nanoparticles. The addition of nano-TiO_2 initially lowers the absolute value of the Seebeck coefficient from S = -190 μV K^{-1} for TiS_2 to S = -180 μV K^{-1} for TiS_2 with 0.5 vol% of nano-TiO_2 at 305 K, before increasing again and reaches a maximum of S = -197 μV K^{-1} at 305 K for TiS_2 with 1.5 vol% of TiO_2. Overall, the cross-plane power factor decreases systematically with nanocompositing and the maximum value is observed for TiS_2 at 310 K with a power factor of *ca*. 0.97 mW m^{-1} K^{-2}.

The principal difference in the effect of nanocompositing observed between in-plane and cross-plane measurements is the absence of an initial decrease in the cross-plane electrical resistivity with the addition of 0.5 vol% of nano-TiO_2. In parallel, the absolute value of the Seebeck coefficient behaves similarly for both in-plane and cross-plane compositional dependence. This provides further evidence for the slight increase in the charge carrier concentration with the addition of 0.5 vol% of nano-TiO_2. However, the anisotropy of the structure and the resulting higher electrical resistivity in the cross-plane direction may prevent any improvement from being effective. High-resolution Transmission Electron Microscopy (HR-TEM) combined with electronic structure calculations could be useful in order to explain why the possible increase in charge carrier concentration, via Ti intercalation or induced structural defects, only causes the in-plane electrical resistivity to decrease.

4.3.3.2 Thermal transport properties and figure of merit

The thermal conductivity of the TiS_2/nano-TiO_2 nanocomposites was measured along both the in-plane, Figure 4.12, and cross-plane directions, Figure 4.13. In-plane measurements of thermal diffusivity were carried out on square-cut samples with sides of *ca*. 6 mm and a thickness of *ca*. 1.5 mm, as detailed in Section 3.2.5.1. Cross-plane thermal diffusivity was measured on discs with a diameter of *ca*. 12.7 mm a thickness of *ca*. 2 mm. The thermal

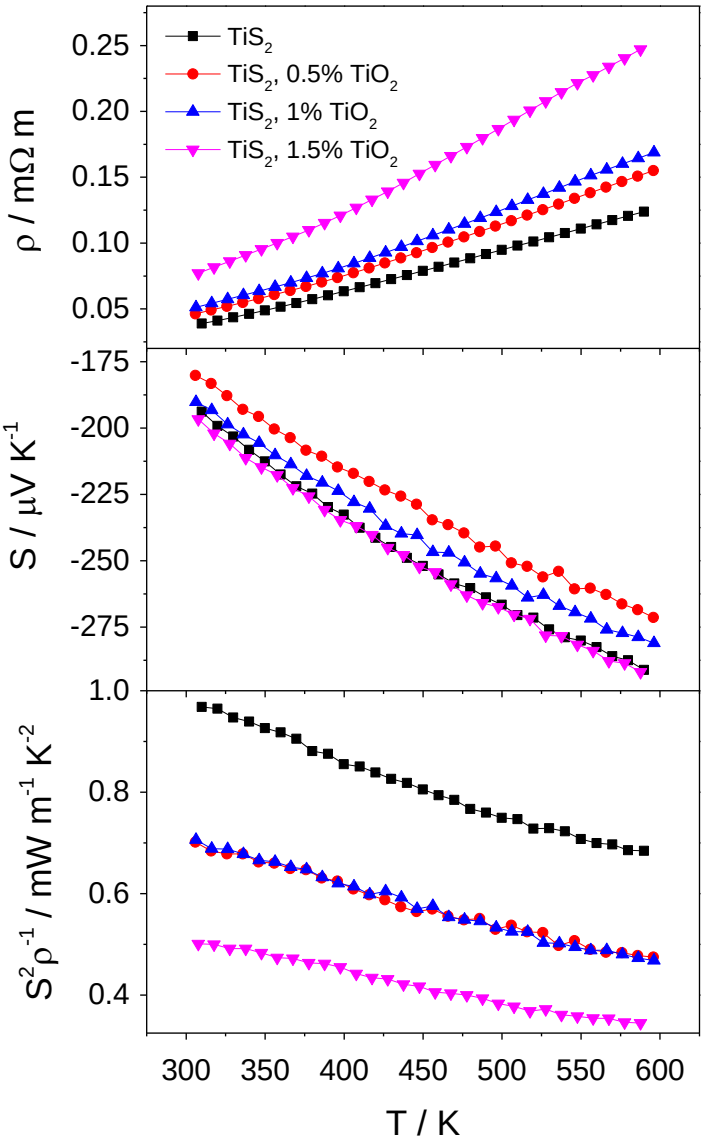

Figure 4.10 Temperature dependence of the electrical resistivity (ρ), Seebeck coefficient (S) and power factor ($S^2\rho^{-1}$) of TiS_2/nano-TiO_2 nanocomposites measured along the cross-plane direction.

conductivity was then calculated using the Dulong-Petit specific heat (Cp = 0.668 J K^{-1} g^{-1}). In both cases, the electronic contribution to the thermal conductivity was estimated using the Wiedemann-Franz law ($L = 2.44 \times 10^{-8}$ W Ω K^{-2}) and the lattice contribution was determined by subtraction, using the equation $\kappa_{lat} = \kappa_{tot} - \kappa_{el}$. The electronic contribution to the thermal conductivity remains very small in both directions and the observed effect of nanocompositing on the electrical resistivity does not impact greatly on the thermal conductivity.

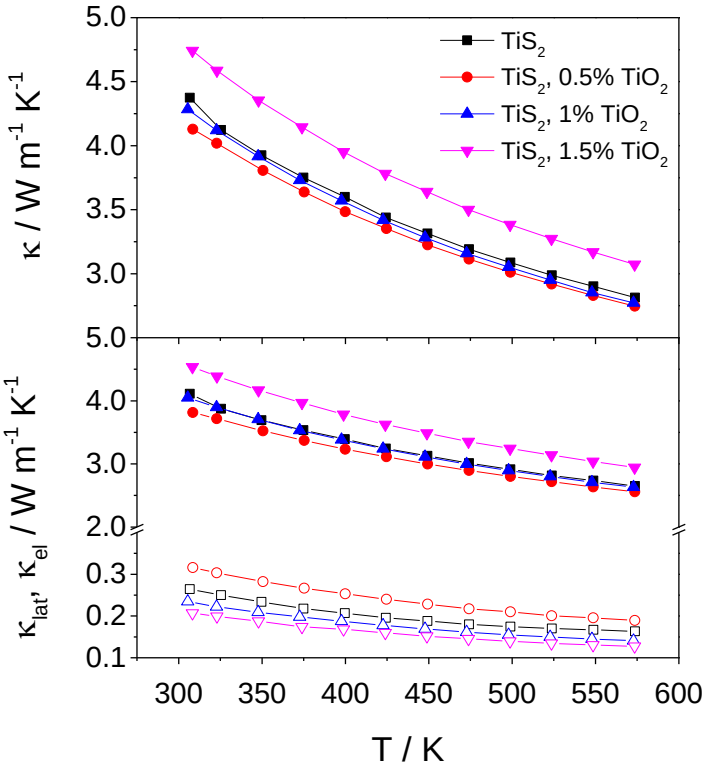

Figure 4.12 Temperature dependence of the total in-plane thermal conductivity (top) and the lattice and electronic contributions (bottom) of the TiS_2/TiO_2 nanocomposites, determined using the Wiedemann-Franz law. Electronic contributions are shown as open symbols.

The in-plane thermal conductivity is about twice as large as the cross-plane value, consistent with the TiS_2 measurements carried out in Section 3.2.5.3. Contrary to what was expected, the in-plane thermal conductivity remains initially the same, within error, for nanocompositing levels up to 1 vol%, before increasing for TiS_2 with 1.5 vol% of nano-TiO_2. The thermal conductivity of bulk TiO_2 is higher than that of TiS_2, with $\kappa \approx 13$ W m^{-1} K^{-1} in the in-plane direction and $\kappa \approx 9$ W m^{-1} K^{-1} in the cross-plane direction at 273 K.[238] This higher thermal conductivity may be the cause for the increase observed for TiS_2 with 1.5 vol% of nano-TiO_2 in the in-plane direction. In the cross-plane direction, all measurements are similar within the experimental error and the thermal conductivity remains almost unchanged with nanocompositing. As a result, the figure of merit of the TiS_2/TiO_2 nanocomposites, Figure 4.14, follows a similar compositional trend to the power factor. In the in-plane direction, the best performance is achieved by TiS_2 with 0.5 vol% of nano-TiO_2 and reaches ZT = 0.28 at 573 K

while pristine TiS_2, prepared in the same way, reaches ZT ≈ 0.25. In the cross-plane direction, no improvement was achieved with nanocompositing because of the dramatic decrease in the power factor. However, the highest ZT of *ca*. 0.28 at 573 K, measured for pristine TiS_2, is slightly higher than the in-plane value. This contrasts with measurements made in Section 3.2.5.3, where the cross-plane ZT at 573 K was lower by *ca*. 30 % compared with in-plane measurements for TiS_2. Because the consolidation step was kept identical, this difference may be attributed to the ball milling step used to prepare the powders (twice as long in the present results). The electrical and thermal properties still suggest a strong anisotropy in the compacted samples; however, the power factor remains high enough in the cross-plane direction and the resulting ZT is equivalent or better than in the in-plane direction. Overall, only a small improvement was achieved by nanocompositing with TiO_2 nanoparticles.

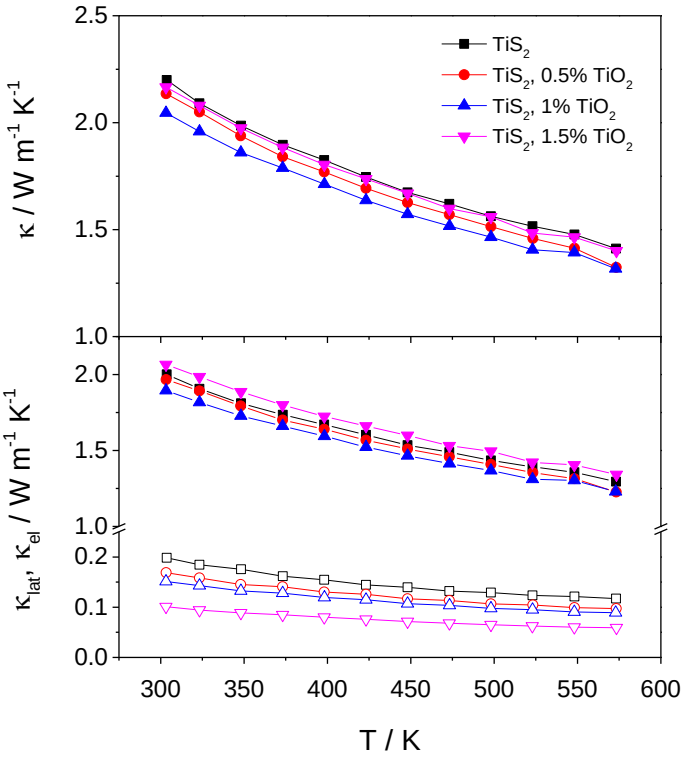

Figure 4.13 Temperature dependence of the total cross-plane thermal conductivity (top) and the lattice and electronic contributions (bottom) of the TiS_2/TiO_2 nanocomposites, determined using the Wiedemann-Franz law. Electronic contributions are shown as open symbols.

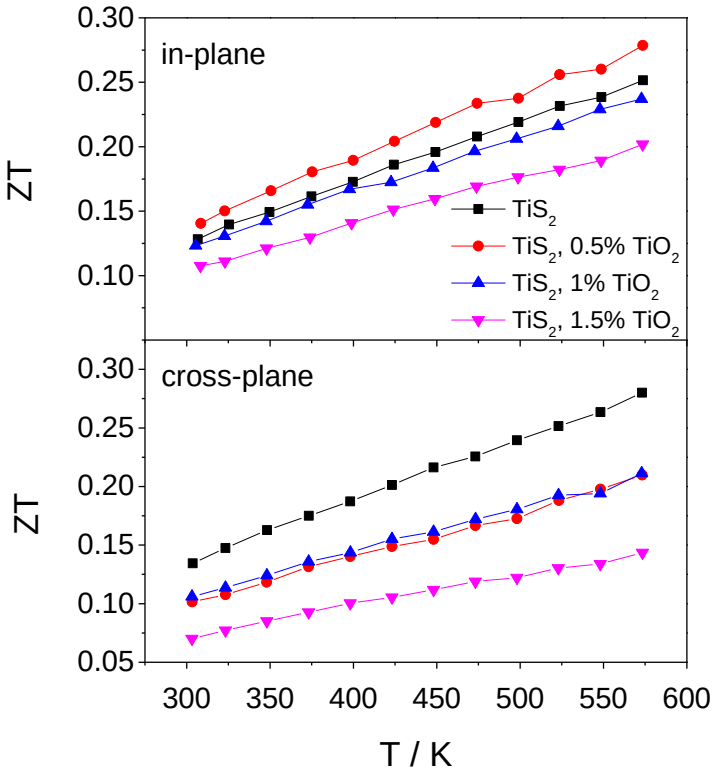

Figure 4.14 Temperature dependence of the figure of merit, ZT, of the TiS_2/TiO_2 nanocomposites in the in-plane (top) and cross-plane direction (bottom).

4.4 TiS_2/CNTs nanocomposites

The structure of multi-walled carbon nanotubes (MWNTs) were reported by Iijima in 1991[239] and a large-scale synthesis method was developed the following year by Ebbesen and Ajayan.[240] Since then, carbon nanotubes have found their way to a wide range of applications such as military equipment because of their strength, light weight and chemical stability.[241] The electrical properties of carbon nanotubes are sensitively dependent on structural parameters such as the number of concentric cylinders, their diameter and length as well as variations in carrier density and π-bonding caused by chemical treatments.[242, 243] Therefore, carbon nanotubes can have very different electrical properties, from insulating to metallic behaviour, depending on the synthesis conditions.[244]

A series of titanium disulphide nanocomposites containing 0.5 %, 1.0 % and 1.5 % by volume of commercial multi-walled carbon nanotubes has been prepared. Powder X-ray diffraction

analysis and the electrical and thermal transport property measurements were carried out. Nanocompositing with carbon nanotubes (CNTs) was primarily aimed to decrease the thermal conductivity by the addition of grain boundaries. Additionally, the effect on the electrical properties of nanocompositing with carbon nanotubes of small diameter (6 - 9 nm) and with a high anisotropy is investigated.

4.4.1 Sample preparation

A second series of nanocomposites, TiS_2/CNTs, was obtained by mechanical milling of bulk TiS_2 with commercial carbon nanotubes (Sigma Aldrich, Multi-walled, 6-9 nm × 5 µm, > 95 %). The parent TiS_2 powder was taken from the same large batch as the TiS_2/nano-TiO_2 series, detailed in Section 4.3.1, and similar nanocompositing levels were used with 0.5 vol%, 1 vol% and 1.5 vol% of carbon nanotubes. Ball millings of TiS_2 and CNTs were carried out using stainless steel jar in an inert argon atmosphere with a powder to ball weight ratio of 1:6. The same milling conditions as TiS_2/nano-TiO_2 nanocomposites were used with 400 rpm, 2 h and 5 min interval with change of direction. All samples were stored in an argon glove box and the ball milled powders were hot-pressed (650°C, 100 MPa, 30 min) into two pellets with a thickness of *ca*. 2 mm and *ca*. 8-10 mm respectively. The pellets were cut following the process detailed in Section 3.2.5.1 in order to measure the electrical and thermal properties in the in-plane and cross-plane direction. The densities of the nanocomposite samples were all higher than 94 % of the theoretical value.

4.4.2 Powder X-ray diffraction

Powder X-ray diffraction data were acquired for the commercial carbon nanotubes on a zero background sample holder, Figure E.2 (Appendix E). Reflections are consistent with graphite-2H[245] with traces of at least one unidentified crystalline phase. Overall, the XRD data are consistent with the commercial materials being multi-walled CNTs of reasonably high purity.[246] Rietveld refinements were carried out on PXRD data acquired on ground fragments of pellet of the TiS_2/CNTs series, Figure 4.15. For the nanocomposites, no signals coming from carbon nanotubes were detected, probably owing to the very low intensity coming from nanoscale crystallites in only 0.5 to 1.5 vol%. In the samples with 1 vol% CNTs, some traces

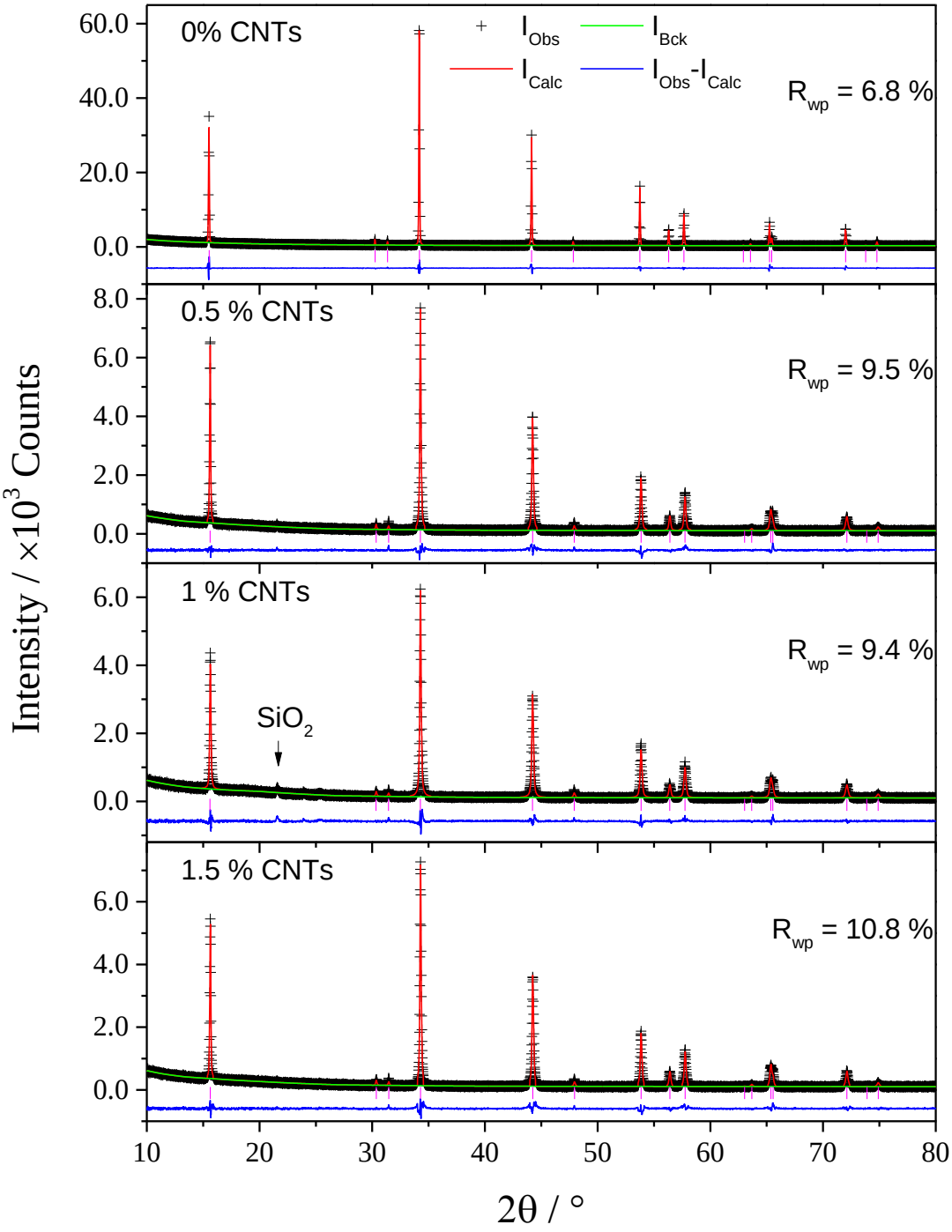

Figure 4.15 Observed (crosses), calculated (full line) and difference (lower full line) profiles for TiS_2/CNTs nanocomposites from Rietveld refinement of XRD data. Reflection positions of TiS_2 are signalled by tick marks.

of SiO_2 were detected, likely to be coming from the ball milling of a small shard of silica tubes from the solid-state reaction of TiS_2. As with the TiS_2/nano-TiO_2 series (Section 4.3.2),

Table 4.2 Refined parameters from Rietveld analysis of powder X-ray diffraction data for TiS_2/CNTs nanocomposites. (Space group $P\bar{3}m1$)[a]

		Vol% of CNTs			
		0	0.5	1	1.5
	a / Å	3.40795(3)	3.40676(5)	3.40578(9)	3.40707(6)
	c / Å	5.69926(7)	5.6983(2)	5.6973(3)	5.6979(2)
Ti	*B* / Å^2	0.90(6)	2.5(2)	2.7(2)	1.9(3)
S	*z*	0.2480(3)	0.2498(5)	0.2512(6)	0.2493(6)
	B / Å^2	0.70(6)	2.2(2)	2.4(2)	1.5(3)
	R_{wp} / %	6.78	9.54	9.40	10.80
	χ^2	3.61	2.08	1.97	2.58

[a] Ti on 1(a), (0, 0, 0); S on 2(d), (1/3, 2/3, z); Co on 1(b) (0, 0, 1/2), constrained at nominal composition.

Rietveld refinements revealed some very small variations of *ca*. 0.001 Å and 0.002 Å for the *a* and *c* lattice parameters respectively, Table 4.2 and Figure 4.16. However, the overall decrease in the unit cell parameters does not suggest that more titanium was intercalated in the van der Waals' gap of TiS_2.

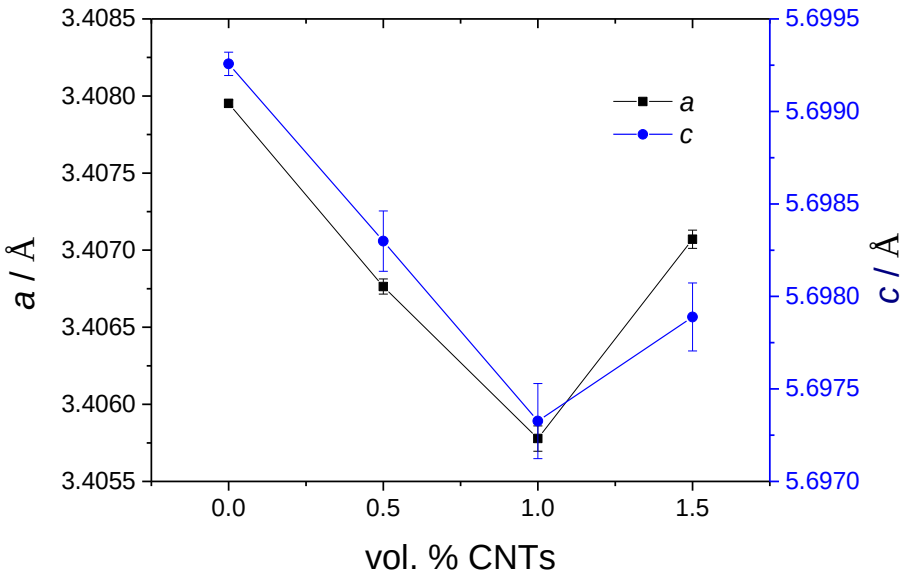

Figure 4.16 Unit-cell parameters of TiS_2/CNTs nanocomposites as a function of the vol% of carbon nanotubes from Rietveld refinements of XRD data.

4.4.3 Thermoelectric performance

4.4.3.1 Electrical Properties

The temperature dependence of the electrical resistivity and Seebeck coefficient were measured and the power factor calculated for the TiS_2/CNTs series in both in-plane, Figure 4.17, and cross-plane direction, Figure 4.18. The process for measuring electrical properties in these two directions has been detailed in Section 3.2.5.1. All samples in both in-plane and cross-plane

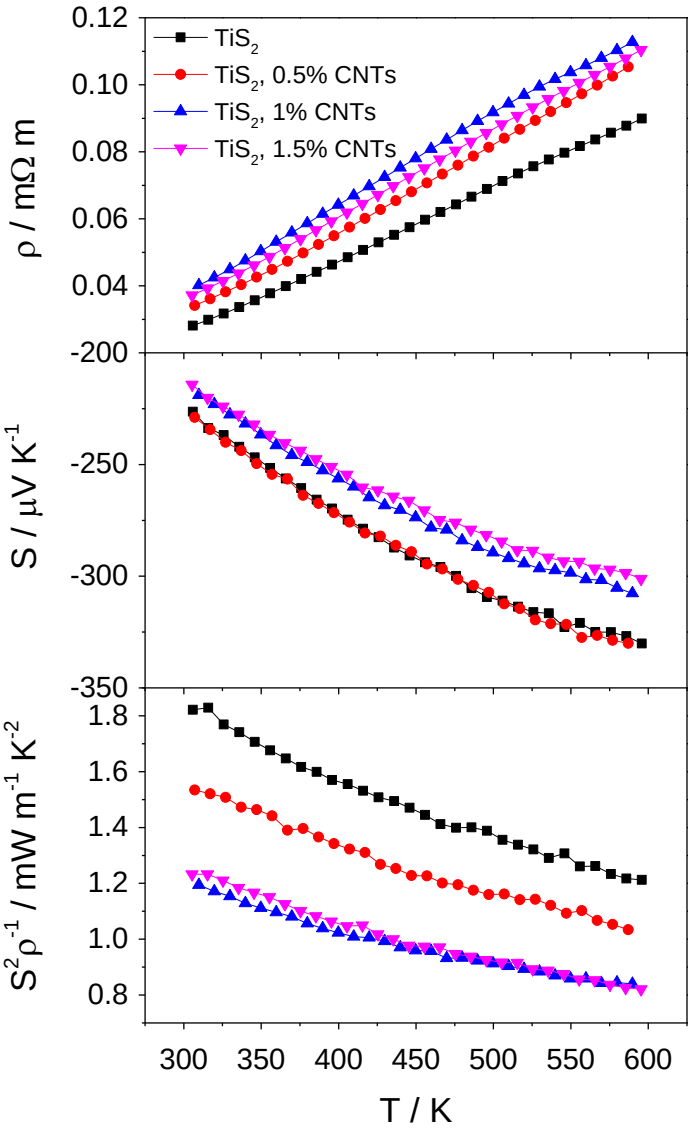

Figure 4.16 Temperature dependence of the electrical resistivity (ρ), Seebeck coefficient (S) and power factor ($S^2\rho^{-1}$) of TiS_2/CNTs nanocomposites measured along the in-plane direction.

directions are *n*-type materials with a metallic behaviour of the electrical resistivity. Unlike nanocompositing with TiO_2, the addition of a small vol% of carbon nanotubes has a pronounced detrimental impact on the electrical properties over the whole composition range and temperature range investigated. The overall increase in electrical resistivity and decrease in the absolute value of the Seebeck coefficient with nanocompositing is observed in both in-plane and cross-plane measurements. As a result of the simultaneous decrease in |S| and

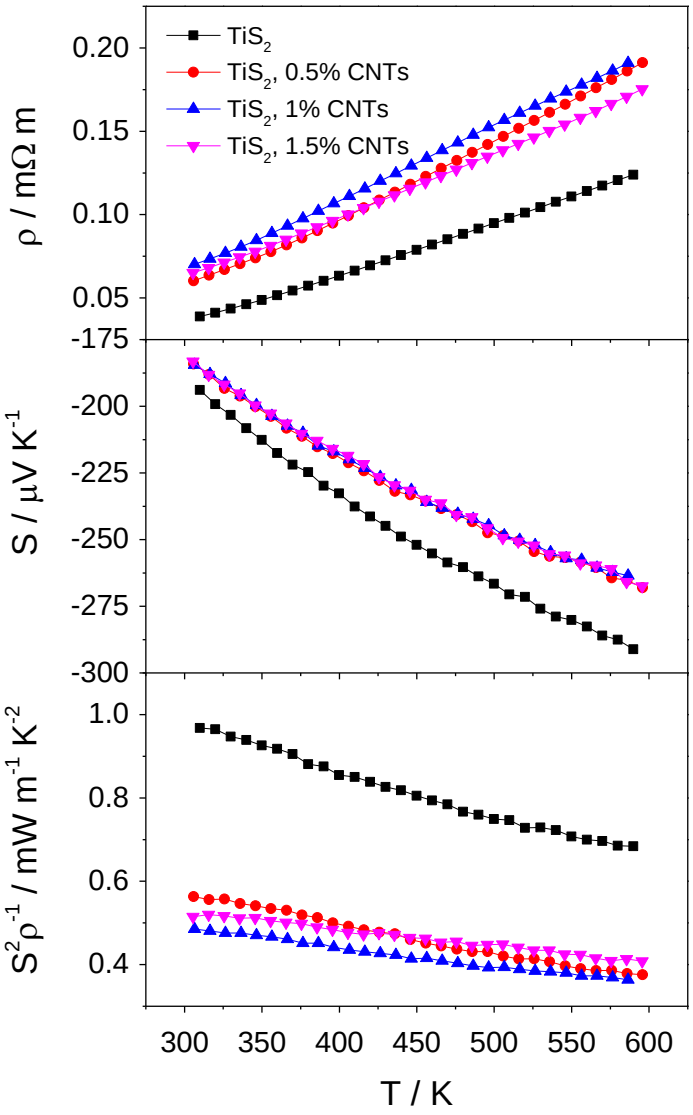

Figure 4.17 Temperature dependence of the electrical resistivity (ρ), Seebeck coefficient (S) and power factor ($S^2\rho^{-1}$) of TiS_2/CNTs nanocomposites measured along the cross-plane direction.

increase in ρ, the power factor is dramatically reduced by a third in the in-plane direction and halved in the cross-plane direction. The very similar effect of nanocompositing on the in-plane and cross-plane electrical properties suggests that the high anisotropy of the carbon nanotubes is not reflected in the electrical properties of the nanocomposites and the structural integrity of the nanotubes may have been altered by the ball milling step. Data do not show any sign of energy-filtering or quantum confinement as |S| is systematically decreased with the amount of nanotubes introduced. Overall, the highest power factors are obtained for the parent TiS_2 with $S^2\rho^{-1}$ = 1.82 mW m^{-1} K^{-2} at 305 K in in-plane direction and $S^2\rho^{-1}$ = 0.97 mW m^{-1} K^{-2} at 310 K in cross-plane direction.

Additional experiments are needed in order to understand what causes this simultaneous decrease in electrical conductivity and absolute value of Seebeck coefficient. Microscopy techniques such as scanning or transmission electron microscopy (SEM, TEM) combined with EDX analysis would be useful to identify the possible alterations caused to the carbon nanotubes. Additionally, Hall effect measurements should be carried out to measure their potential impact on charge carrier concentration and mobility.

4.4.3.2 Thermal transport properties and figure of merit

The in-plane, Figure 4.19, and cross-plane thermal conductivity, Figure 4.20, of the TiS_2/CNTs nanocomposite series have been determined using the measured thermal diffusivity and the Dulong-Petit specific heat (Cp = 0.668 J K^{-1} g^{-1}). In-plane thermal diffusivity measurements were carried out on square-cut samples with sides of *ca*. 6 mm and a thickness of *ca*. 1.5 mm and cross-plane thermal diffusivity was measured on discs with a diameter of *ca*. 12.7 mm a thickness of *ca*. 2 mm. The electronic contribution to the thermal conductivity was estimated using the Wiedemann-Franz law (L = 2.44 × 10^{-8} W Ω K^{-2}), and the lattice contribution determined by subtraction, using the equation $\kappa_{lat} = \kappa_{tot} - \kappa_{el}$.

Unlike TiS_2/nano-TiO_2 nanocomposites, the samples with dispersed carbon nanotubes show a decrease in both in-plane and cross-plane thermal conductivity with the nanocompositing level. In the in-plane direction, the lowest value, $\kappa \approx 2.28$ W m^{-1} K^{-1}, is obtained for TiS_2 with 1.5 vol% of CNTs at 573 K while the parent TiS_2 reaches $\kappa \approx 2.65$ W m^{-1} K^{-1} at the same

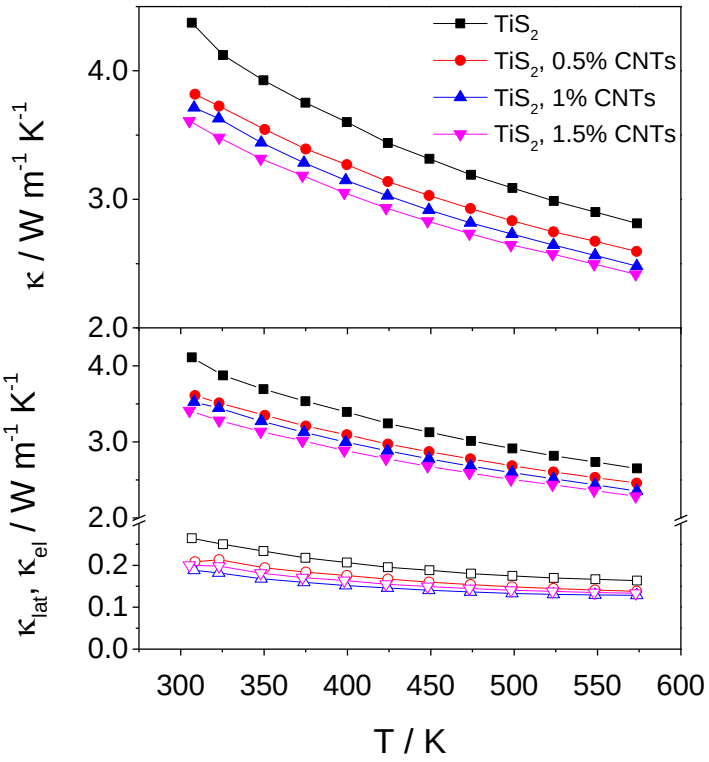

Figure 4.18 Temperature dependence of the total in-plane thermal conductivity (top) and the lattice and electronic contributions (bottom) of the TiS_2/CNTs nanocomposites, determined using the Wiedemann-Franz law. Electronic contributions are shown as open symbols.

temperature, corresponding to a 14 % decrease upon nanocompositing. In the cross-plane direction, the lowest value at 573 K is obtained for all three nanocomposites with $\kappa \approx 1.04$ W m^{-1} K^{-1}, a 20 % reduction from parent TiS_2 with a thermal conductivity of *ca*. 1.29 W m^{-1} K^{-1}.

In both directions, the electronic contribution, κ_{el}, although decreasing slightly with nanocompositing, does not play an important role in the overall reduction in the thermal conductivity and only accounts for 5 % to 10 % of the total value. The bulk of the reduction is due to a decrease in the lattice contribution, κ_{lat}, with nanocompositing over the whole temperature range. This gives evidence for an increase in the phonon scattering rate in samples with a percentage of carbon nanotubes added to the TiS_2 matrix. The effect is more pronounced in the in-plane direction where a steady reduction in κ_{lat} and κ_{tot} with nanocompositing is observed, whereas in the cross-plane direction, there is little difference between 0.5 vol% and

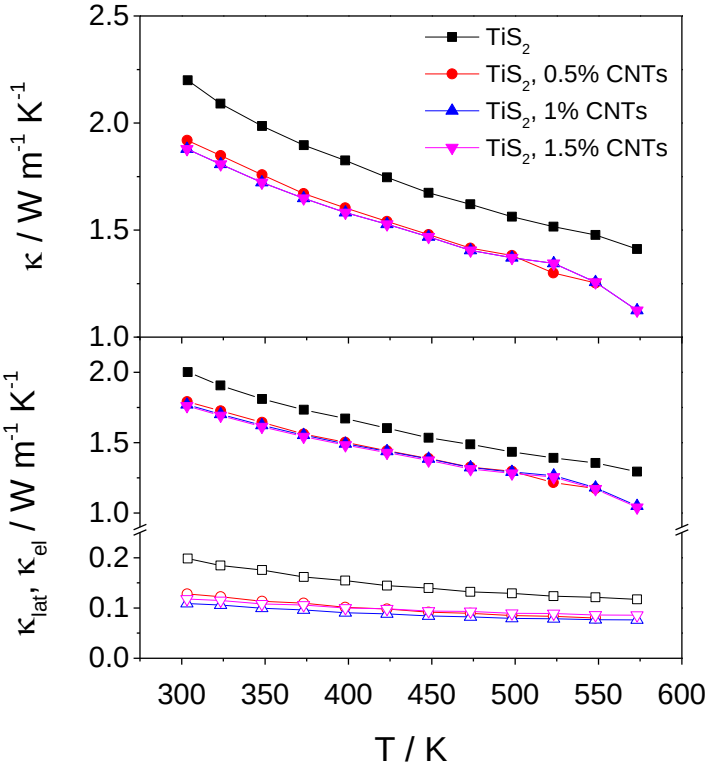

Figure 4.19 Temperature dependence of the total cross-plane thermal conductivity (top) and the lattice and electronic contributions (bottom) of the TiS_2/CNTs nanocomposites, determined using the Wiedemann-Franz law. Electronic contributions are shown as open symbols.

1.5 vol% of CNTs. The figure of merit, ZT, calculated in both in-plane and cross-plane directions, is not improved with nanocompositing over the investigated temperature range, Figure 4.21. The reduction observed in the thermal conductivity is not sufficient to offset the large decrease in the power factor. The best performance is still achieved by pristine TiS_2 with ZT = 0.25 and ZT 0.28 at 573 K in in-plane and cross-plane directions, respectively.

4.5 Conclusion

The synthesis of nanoparticles of TiS_2 and the preparation of TiS_2 nanocomposites were achieved in an effort to investigate the impact of reduced length scale on the thermoelectric performance of TiS_2-based materials. Nanoparticles of TiS_2 with controlled morphology were successfully synthesised in small amounts, and the Seebeck coefficient was measured on a cold-pressed and sintered pellet of TiS_2 nanoflakes. Powder X-ray diffraction and SEM/EDX

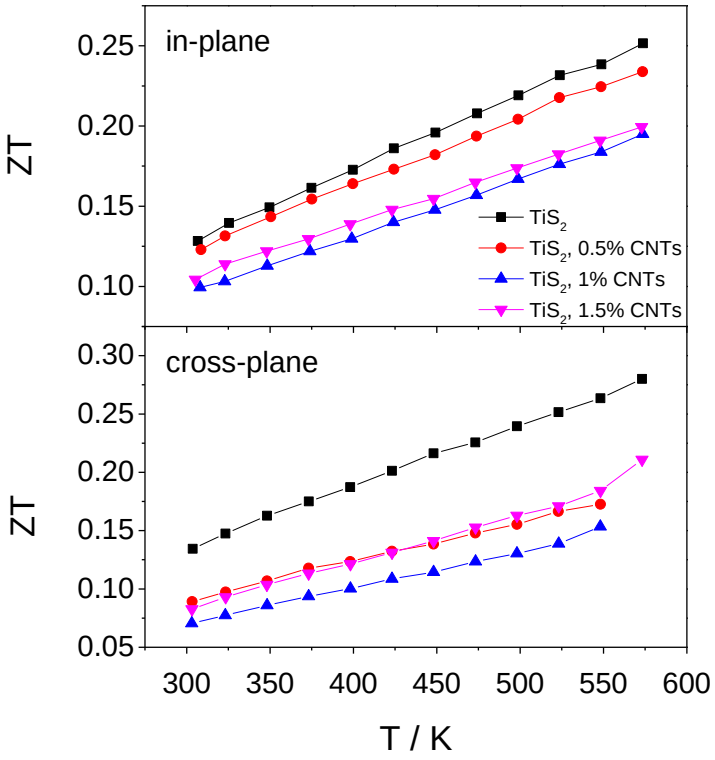

Figure 4.20 Temperature dependence of the figure of merit, ZT, of the TiS_2/CNTs nanocomposites in the in-plane (top) and cross-plane direction (bottom).

analysis confirmed the morphology and good purity of the sample. Furthermore, the value of the Seebeck coefficient was consistent with a stoichiometry $Ti_{1+x}S_2$ where x is within the range $0.02 \leq x \leq 0.03$. While the stability in air appeared to be an issue with such small particles, this method is very promising for the large-scale synthesis of cost-efficient non-toxic nanoparticles with good thermoelectric response. Further work should seek to synthesise larger batches of TiS_2 nanoflakes in an adapted apparatus in order to allow the production of large pellets with higher density suitable for measurement of thermoelectric properties. In order to obtain dense samples while retaining the particle size, a rapid pressing using a spark plasma sintering instrument should be attempted.

Two types of nanocomposites have been investigated for their thermoelectric properties, ball milling TiS_2 with titanium oxide nanoparticles and with multi-walled carbon nanotubes. Powder X-ray diffraction analysis was carried out on ground fragments of pellets and

confirmed the high purity of the nanocomposites after consolidation. The ball milling conditions used, have led to a larger ZT in the cross-plane direction with ZT = 0.28 at 573 K for pristine TiS_2. Only the nanocomposite with 0.5 vol% of nano-TiO_2 has shown slightly better performance than pristine TiS_2 with a 12 % increase in the figure of merit, from ZT = 0.25 to ZT = 0.28 at 573 K in the in-plane direction. No improvement was measured in the cross-plane direction, suggesting that the effect of nanocompositing with TiO_2 is anisotropic. Surprisingly, the addition of nano-TiO_2 causes an increase in the thermal conductivity that can be attributed to the higher thermal conductivity of TiO_2, while the addition of carbon nanotubes causes a systematic decrease, consistent with an increase phonon scattering. However, the increase in the electrical resistivity with the addition of CNTs is too large for any improvement to be made on the figure of merit.

Chapter 5 - Copper-containing sulphide minerals as thermoelectric materials

5.1 Introduction

This chapter focuses on the thermoelectric properties of two naturally-occurring families of copper-containing mineral, tetrahedrites and bornites. Both minerals have been known and mined for decades;[247-250] however, their thermoelectric properties have been overlooked until very recently. Although measurements of the Seebeck coefficient and electrical resistivity have been carried out on bornite, tetrahedrite and many other natural minerals,[251] the first complete reports on thermoelectric performance were published only in 2012 and 2014 for doped-tetrahedrites, $Cu_{10}M_2Sb_4S_{13}$ (M = Mn, Fe, Co, Ni, Cu, and Zn),[252] and bornite, Cu_5FeS_4,[253] respectively. These families are extremely promising as thermoelectric materials with the cost of raw materials, Appendix F,[90] being much lower than the current materials and made of non-toxic and widely available elements.

The thermoelectric performance of tetrahedrite materials has been under the spotlight since 2012 due to their low thermal conductivity and a high power factor. The low thermal conductivity is a consequence of a complex crystal structure with a large unit cell[254] and strong phonon scattering caused by the out-of-plane vibrations of the Cu atom in the trigonal planar position.[255] The thermoelectric properties of materials based on natural tetrahedrite have been recently re-investigated[255-257] with various compositions of the form $Cu_{12-x}(Zn, Fe)_x(Sb, As)_4S_{13}$ ($0 \leq x \leq 2$) mixed with synthetic $Cu_{12}Sb_4S_{13}$ reaching ZT over 0.8 for temperatures between 600 K and 700 K.[256, 257] However, the natural component of these synthetic/natural composite materials constitutes only 25 % to 50 % of the total mass, the remaining actually being the arsenic-containing tennantite, $Cu_{12}As_4S_{13}$. Fully synthetic, arsenic-free, tetrahedrite has also reached an impressively high ZT with the best performance achieved so far by $Cu_{11}MnSb_4S_{13}$ at 575 K with ZT = 1.13.[258] Conversely, Chetty *et al.* observed a degradation of the thermoelectric properties of tetrahedrite with manganese substitution over the whole investigated temperature range.[259] Recent improvements, obtained by systematic investigations

of doped tetrahedrites, have been surveyed in an extensive review by Chetty *et al*.[254] A few examples include $Cu_{12-x}Zn_xSb_4S_{13}$ ($0 \leq x \leq 2$)[255] with a ZT close to 1 at 723 K, $Cu_{10.5}NiZn_{0.5}Sb_4S_{13}$ with a ZT above unity at 723 K,[260] or $Cu_{11.5}Co_{0.5}Sb_4S_{13}$ with ZT = 0.98 at 673 K.[261] Doping on the antimony position was also investigated with the substitution of Sb with Te resulting in a ZT of 0.92 at 723 K.[262] Degradation of the properties of tetrahedrite samples can be associated with the presence of impurities such as Cu_3SbS_3. Tetrahedrite is found to be stable over a wide range of compositions that involve large excess of Cu and Sb.[104, 263, 264] Studies of the phase diagram of the Cu-Sb-S system has led to compositions $Cu_{12-x}Sb_4S_{13}$ ($0 \leq x \leq 2$) and $Cu_{12}Sb_{4+y}S_{13}$ ($0 \leq y \leq 2/3$).[265] However, the composition range strongly depends on the temperature and a mixture of Cu-rich, $Cu_{14}Sb_4S_{13}$, and Cu-poor, $Cu_{12}Sb_4S_{13}$, phases is found at room temperature.[248, 264, 266] The charge carrier concentration of $Cu_{12+y}Sb_4S_{13}$ can be controlled by the introduction of excess copper and the thermoelectric properties of the material can be tuned.

Bornite is another copper-containing naturally occurring mineral with an ultralow thermal conductivity and was recently identified as a potential candidate for thermoelectric power generation.[253] It is a naturally-occurring mineral with an anti-fluorite related structure that undergoes order-disorder transitions over the temperature range $473 \leq T / K \leq 543$.[105, 107, 111] Details of the structure of the different polymorphs in bornite are discussed in Section 1.6.1.2. Doped derivatives of bornite are a new family of potential thermoelectric materials for sustainable energy recovery with reported ZT of *ca*. 0.4 and *ca*. 0.5 at 700 K for Cu_5FeS_4 and $Cu_{5.04}Fe_{0.96}S_4$, respectively.[253]

In this chapter, the structural and thermoelectric properties of tetrahedrite phases, $Cu_{12-x}Mn_xSb_4S_{13}$ ($0 \leq x \leq 1$) and $Cu_{12+y}Sb_4S_{13}$ (y = 0; 0.3; 1; 1.5 and 2), and manganese-doped bornite $Cu_5Fe_{1-x}Mn_xS_4$ ($0 \leq x \leq 0.10$) prepared via mechanical alloying, are investigated.

5.2 Tetrahedrite phases $Cu_{12}Sb_4S_{13}$ and $Cu_{11}MnSb_4S_{13}$

When the work on manganese doped tetrahedrite described in this section was initiated, no report of the thermoelectric properties had been published. The two reports, by Heo *et al*.[258] and Chetty *et al*.,[259] both on $Cu_{12-x}Mn_xSb_4S_{13}$ ($0 \leq x \leq 2$) contains conflicting results. The first

studies have shown a substantial improvement from ZT = 0.3 to ZT = 1.13 at 575 K with the incorporation of Mn while the second reported a systematic degradation of the thermoelectric properties of tetrahedrite with manganese substitution. In this section, the structural properties of $Cu_{12-x}Mn_xSb_4S_{13}$ (x = 0; 1) are investigated using a combination of powder X-ray and temperature dependent neutron diffraction. Electrical and thermal property measurements were carried out and the resulting thermoelectric figure of merit was calculated.

5.2.1 Synthesis

Stoichiometric amounts of Cu (Sigma Aldrich, 99.5 %), Mn (Alfa Aesar, 99.95 %), Sb (Alfa Aesar, 99.5 %), and S (Sigma Aldrich, flakes, 99.99 %) corresponding to the composition $Cu_{12-x}Mn_xSb_4S_{13}$ (x = 0; 1) were pre-reacted by ball milling (see Section 2.1.2). The pre-reaction of the elemental precursors (Ar atmosphere, 600 rpm, 16 × 30 min interval steps with change of direction and weight ratio of powder to balls 3:10) was needed in order to prevent an early reaction between copper and sulphur inside the silica tube. The pre-reacted powders were sealed in evacuated silica tubes at 10^{-4} Torr and placed in a furnace for firing (Section 2.1.1). The two tetrahedrite samples followed different heat treatments, optimised individually for the highest purity. The un-substituted tetrahedrite was cold-pressed and heated to 773 K at a rate of 1 K min^{-1} for 64 h and rapidly cooled to room temperature by removing the tube from the furnace. The manganese substituted sample underwent two successive firing with intermediate grinding and cold-pressing. The sample was first heated to 973 K at a rate of 1.6 K min^{-1} for 3 h, cooled down to 823 K at a rate of 1 K min^{-1} and held at that temperature for 30 h before being cooled down to room temperature at the natural cooling rate. A second firing was done on a cold-pressed pellet at 823 K for 30 h with a heating rate of 1 K min^{-1}.

5.2.2 Structural investigations

5.2.2.1 Powder X-ray diffraction

Powder X-ray diffraction data for $Cu_{12-x}Mn_xSb_4S_{13}$ (x = 0; 1) were collected at room temperature using a Bruker D8 Advance powder diffractometer (Section 2.2) over the angular range $10 \leq 2\theta / ° \leq 85$ with a step size of 0.027646 º for a period of 6 hours. The structure of $Cu_{12-x}Mn_xSb_4S_{13}$ (x = 0; 1) was refined using the Rietveld method[142, 143] and the GSAS software

package,[130] Figure 5.1, with an initial structural model derived from single-crystal X-ray data (space group $I\bar{4}3m$)[259] for $Cu_{12-x}Mn_xSb_4S_{13}$. The corresponding structural parameters are gathered in Table 5.1. The background was described using the reciprocal interpolation, the scale factor, zero shift, unit cell parameters, atomic coordinates, isotropic thermal parameters of Cu(1), Sb, S(1), S(2) and anisotropic thermal parameters of Cu(2) for the tetrahedrite phase were then refined. The peak shape was described using a pseudo-Voigt function[146, 147] (Section

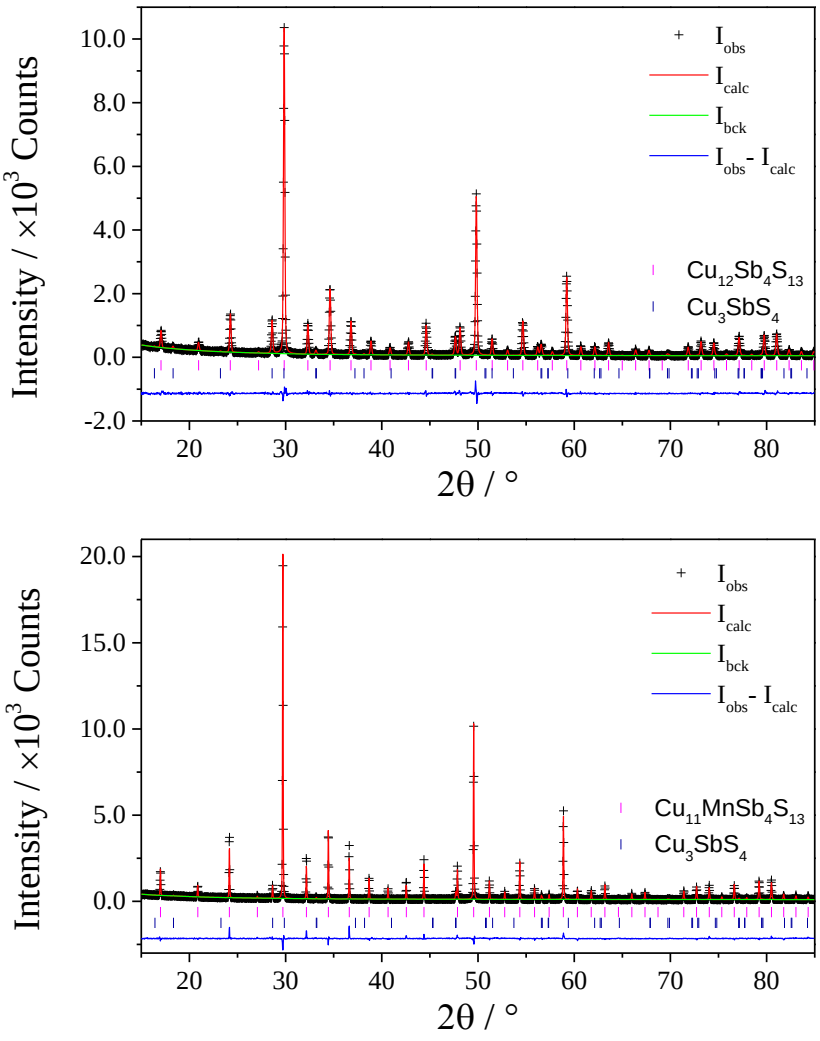

Figure 5.1 Observed (crosses), calculated (full line) and difference (lower full line) profiles for $Cu_{12}Sb_4S_{13}$ (top) and $Cu_{11}MnSb_4S_{13}$ (bottom), from Rietveld refinement of XRD data. Reflection positions for the minority impurity phase, Cu_3SbS_4, are given below the main phase positions.

Table 5.1 Refined parameters from Rietveld analysis of powder X-ray diffraction data for $Cu_{12-x}Mn_xSb_4S_{13}$, x = 0; 1, (Space group $I\bar{4}3m$)[a]

		$Cu_{12}Sb_4S_{13}$	$Cu_{11}MnSb_4S_{13}$
	a / Å	10.3234(2)	0.3865(3)
Cu(1)	B / Å^2	1.3(2)	2.7(2)
	SOF	1	0.833
Mn	B / Å^2	-	4.7(2)
	SOF	-	0.167
Cu(2)	x	0.2173(6)	0.2112(6)
	U_{11} / ×10^{-2} Å^2	3.4(6)	7.1(7)
	U_{22}, U_{33} / ×10^{-2} Å^2	7.5(3)	7.5(3)
	U_{23} / ×10^{-2} Å^2	-5.7(3)	-3.4(3)
Sb	x, y, z	0.2685(1)	0.2681(2)
	B / Å^2	0.9(2)	2.2(2)
S(1)	x, y	0.1146(5)	0.1098(5)
	z	0.3620(6)	0.3634(6)
	B / Å^2	0.9(2)	2.1(2)
S(2)	B / Å^2	1.4(5)	3.5(6)
	wt% impurity	8.4	3.9
	R_{wp} / %	9.12	9.15
	χ^2	1.736	2.149

[a] Cu(1) on 12(d), (1/4, 1/2, 0); Cu(2) on 12(e), (x, 0, 0); Sb on 8(c), (x, y, z); S(1) on 24(g), (x, y, z) and S(2) on 2(a), (0, 0, 0)

2.4.1). All coefficients were refined individually until the refinement was stable enough for all non-zero coefficients to be refined simultaneously. Subsequently, all parameters related to the tetrahedrite phase were fixed and the second phase, Cu_3SbS_4, was added.[267] Unit-cell parameters, phase scale factor, and isotropic thermal parameters for the second phase were refined until convergence. Parameters for both phases were then allowed to refine simultaneously. The site occupancy factors (SOF) were fixed to their nominal values as no significant improvement in the quality of fit was observed when allowing them to refine.

The two phases contain a small amount of Cu_3SbS_4 impurity phase, greatly reduced in the manganese substituted sample. The structure of natural tetrahedrite was first confirmed using least-squares refinement by Wuensch in 1963.[268] It has since been observed that solid solutions only, formed by various substitutions on the copper or antimony sites, are found in nature.[263] This accounts for the difficulty of synthesizing stoichiometric tetrahedrite and why copper-rich phases up to a composition of $Cu_{14}Sb_4S_{13}$ are stable.[248, 249, 263, 264]

The refined unit-cell parameters, a = 10.3234(2) Å and a = 10.3865(3) Å for $Cu_{12}Sb_4S_{13}$ and $Cu_{11}MnSb_4S_{13}$, respectively, and the presence of small amounts of Cu_3SbS_4 are consistent with the work of Chetty *et al.*[259] No comparison could be done with the work of Heo *et al.*[258] on $Cu_{12-x}Mn_xSb_4S_{13}$ as no details on the structural analysis were provided. The added manganese was placed on the Cu(1) site but no clear conclusion can be drawn here because of the small difference in the X-ray scattering power of copper and manganese. For this reason, powder neutron diffraction experiments were performed to provide a more detailed structural analysis of $Cu_{12-x}Mn_xSb_4S_{13}$ (x = 0; 1).

5.2.2.2 Powder neutron diffraction

Time-of-flight powder neutron diffraction data for $Cu_{12-x}Mn_xSb_4S_{13}$ (x = 0; 1) were collected at the ISIS facility on the Polaris diffractometer described in Section 2.3.2. Powdered samples were sealed in evacuated low-boron content silica tubes and fitted in thin-walled vanadium cans. Measurements were carried out over the temperature range $303 \leq T / K \leq 773$ inside a furnace, evacuated to a pressure < 10^{-4} Torr, on heating and cooling for $Cu_{12}Sb_4S_{13}$ and on heating only for $Cu_{11}MnSb_4S_{13}$. A background measurement was carried out using an empty evacuated ampoule and the data were subsequently subtracted from each total data set using the Mantid software package.[136, 137] Figure 5.2 and Figure 5.3, display the temperature dependence of powder neutron data of the highest resolution bank (bank 5, back scattering, 2θ = 146.72 °) for $Cu_{12}Sb_4S_{13}$ and $Cu_{11}MnSb_4S_{13}$ respectively. In both cases, the thermal expansion of the unit cell may be clearly observed through the shifting of the peaks at higher d-spacing. Additionally, systematic variations can be observed in the intensity of the main reflections. This was investigated by a series of multibank Rietveld refinements performed using the GSAS software package[130] and data from bank 5 (2θ = 146.72 °), bank 4 (2θ = 92.59 °) and bank 3 (2θ = 52.21 °). Refinements of the data collected at room temperature were conducted using the lattice parameters obtained from powder X-ray diffraction in the initial model. The refinements using data collected at higher temperature were carried out successively, using data from the previous temperature as an initial model for the next. In all cases, the refinement was initiated with the tetrahedrite phase only, using the highest resolution bank (bank 5, 2θ = 146.72 °). The scale factor and the structural parameters, including the

lattice parameters, atom coordinates and thermal displacement parameters were refined successively. Once convergence was achieved, a second phase was added, corresponding to the impurity Cu_3SbS_4. Data from the remaining detector banks were added in turn following the same method than previously detailed for the refinement of the Co_xTiS_2 phases in Section 3.2.2.2. Multibank refinements were repeated for all data sets acquired over the temperature range $303 \leq T / K \leq 773$. The results of the Rietveld refinements from data collected at room temperature for $Cu_{12}Sb_4S_{13}$ and $Cu_{11}MnSb_4S_{13}$ are given in Figure 5.4 and Figure 5.5, respectively and the refined parameters of the temperature dependent investigations are tabulated in Table 5.2 and Table 5.3. Excellent fits were obtained for both compositions at each temperature investigated, with R_{wp} values ranging between 2 % and 3 % and almost no features were present in the difference curve. Because the background was subtracted in the initial manipulation of the raw data, the value of χ^2 is underestimated and often resulted in values below unity.

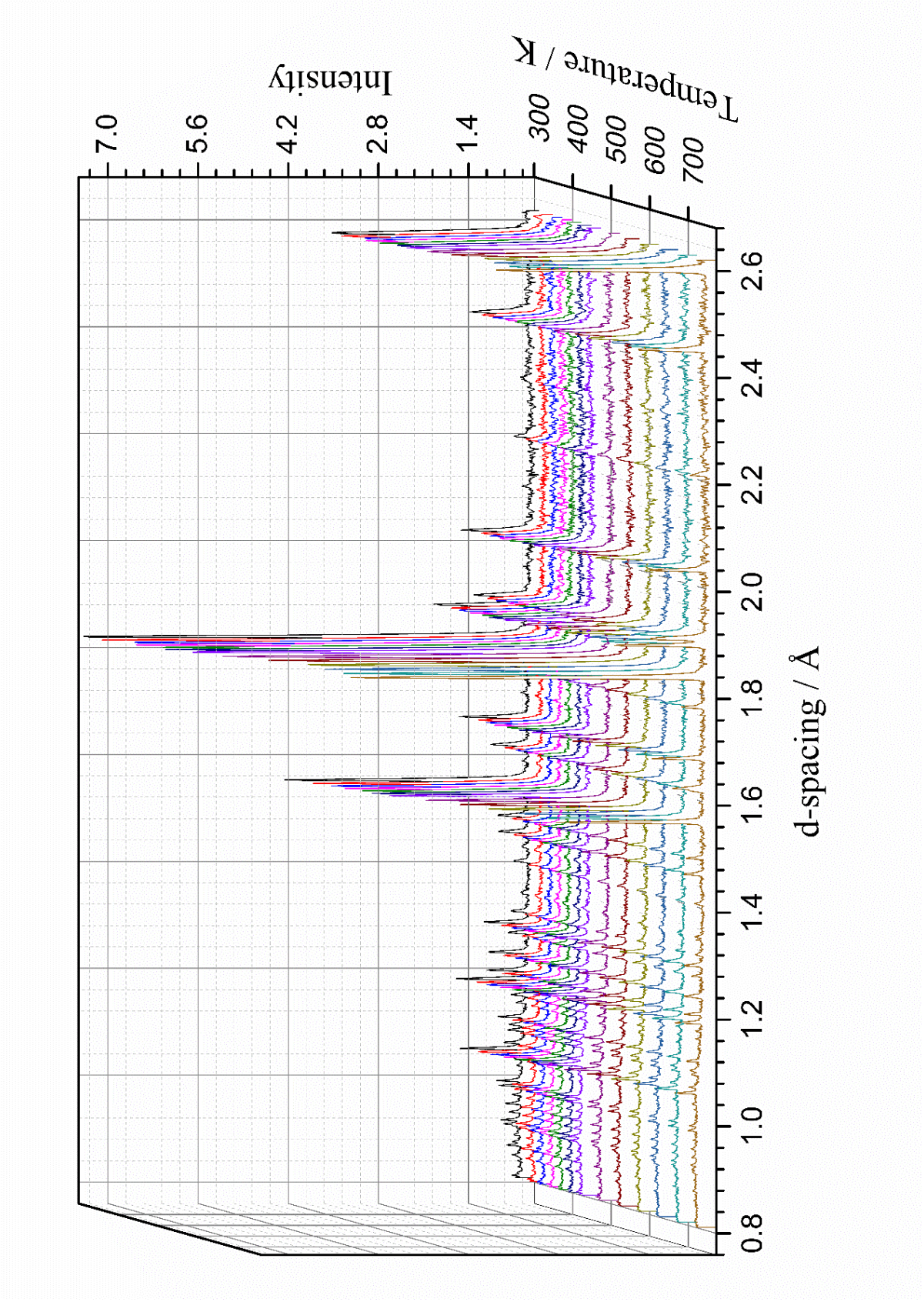

Figure 5.2 Waterfall plot of neutron diffraction patterns of $Cu_{12}Sb_4S_{13}$ from 313 to 773 K.

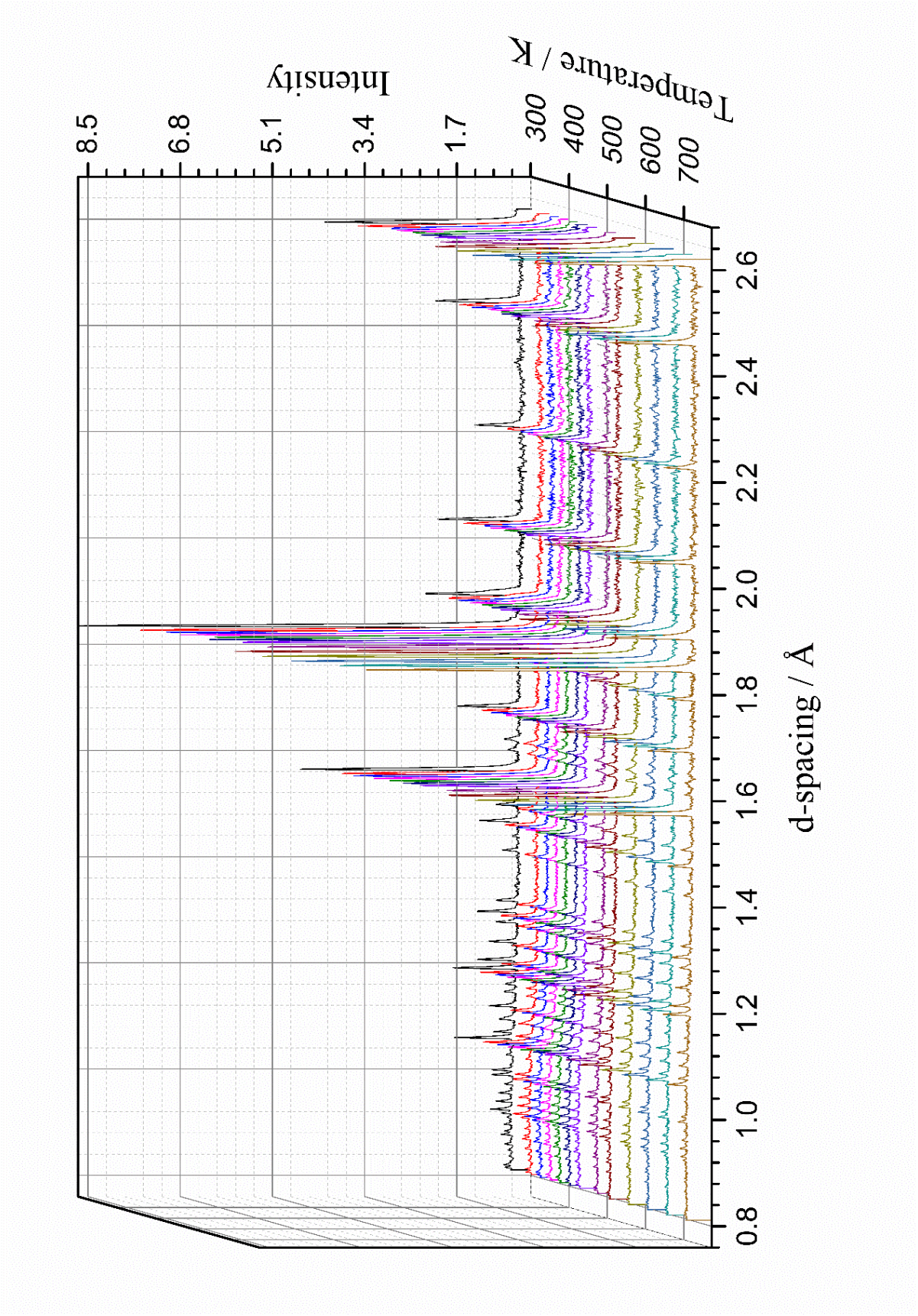

Figure 5.3 Waterfall plot of neutron diffraction patterns of $Cu_{11}MnSb_4S_{13}$ from 303 to 773 K.

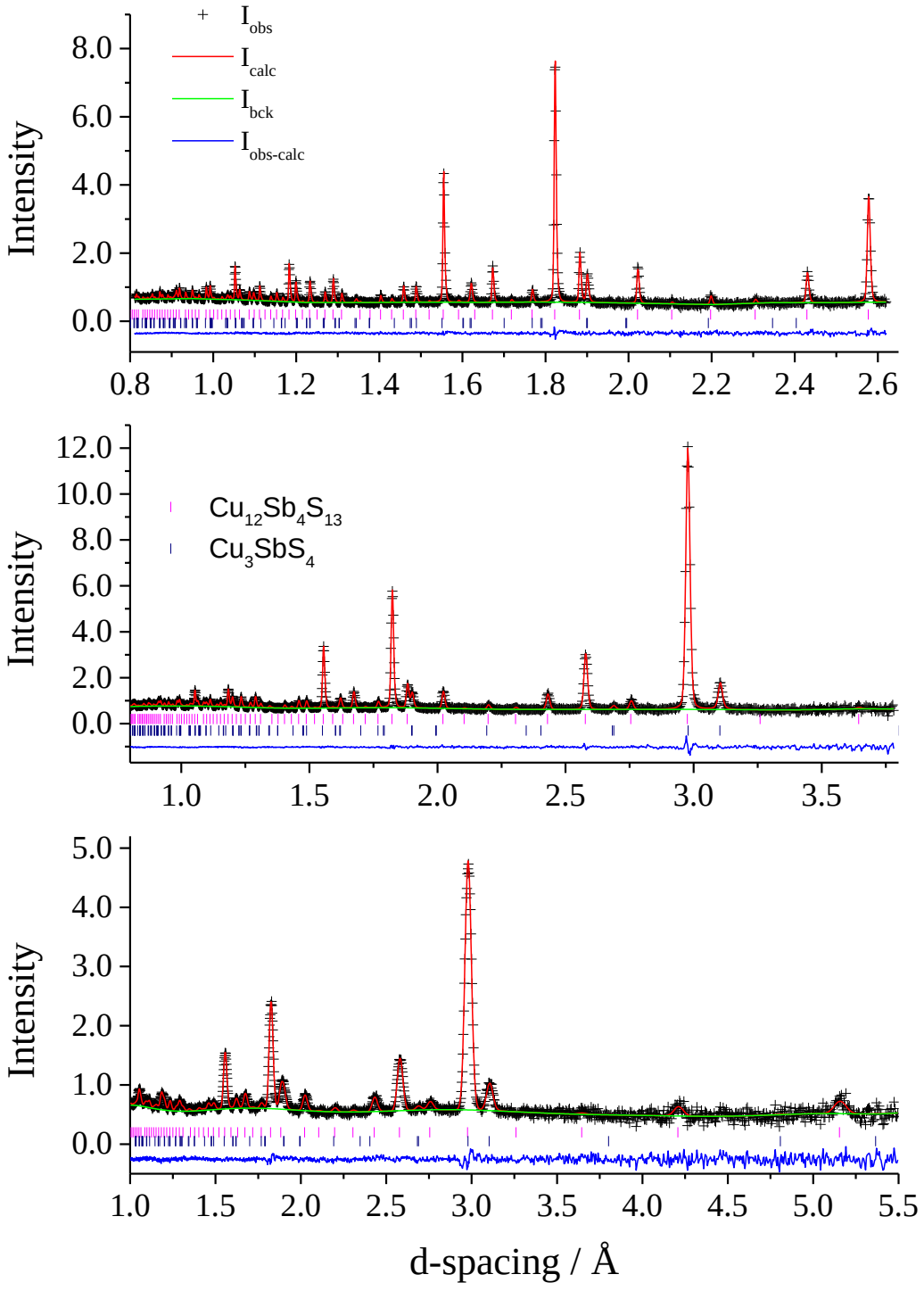

Figure 5.4 Observed (crosses), calculated (full line) and difference (lower full line) profiles for $Cu_{12}Sb_4S_{13}$ at 313 K from Rietveld refinements of powder neutron diffraction data acquired on the Polaris diffractometer. From top to bottom, bank 5 (146.72 °), bank 4 (92.59 °) and bank 3 (52.21 °). Bragg reflection positions for $Cu_{12}Sb_4S_{13}$ (top) and the minority impurity phase, Cu_3SbS_4, (bottom) are signalled by tick marks.

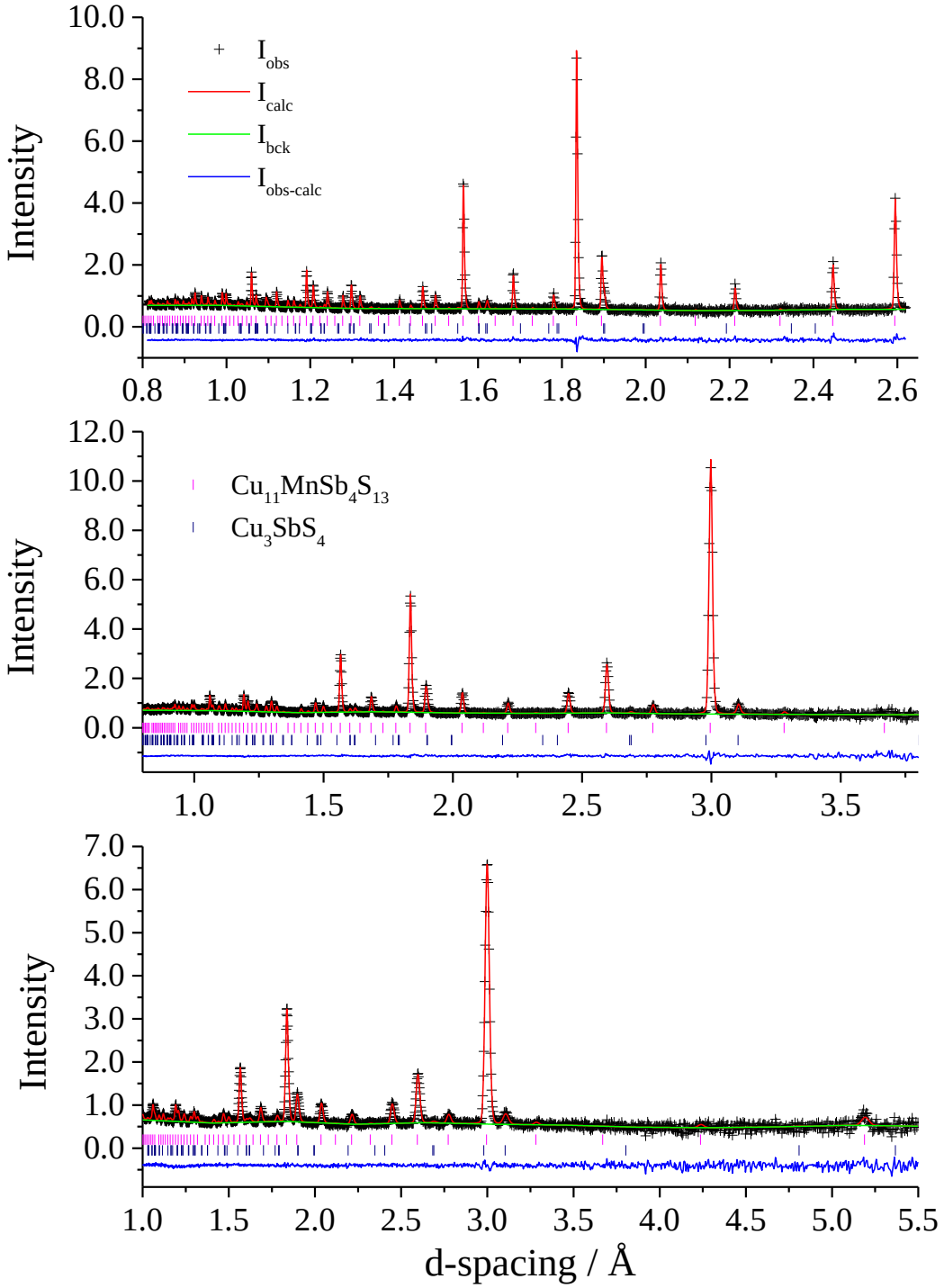

Figure 5.5 Observed (crosses), calculated (full line) and difference (lower full line) profiles for $Cu_{11}MnSb_4S_{13}$ at 303 K from Rietveld refinements of powder neutron diffraction data acquired on the Polaris diffractometer. From top to bottom, bank 5 (146.72 °), bank 4 (92.59 °) and bank 3 (52.21 °). Bragg reflection positions for $Cu_{11}MnSb_4S_{13}$ (top) and the minority impurity phase, Cu_3SbS_4, (bottom) are signalled by tick marks.

Table 5.2 Refined parameters from Rietveld analysis of neutron diffraction data for $Cu_{12}Sb_4S_{13}$, (Space group $I\bar{4}3m$)[a]

	T / K	313	348	373	398	423	448	473	523	573
	a / Å	10.30747(4)	10.31234(4)	10.31383(4)	10.31612(5)	10.31956(5)	10.32324(5)	10.32742(5)	10.33849(5)	10.35325(5)
Cu(1)	B / Å^2	1.86(4)	2.11(5)	2.31(5)	2.41(5)	2.70(6)	2.76(6)	2.91(6)	3.29(7)	3.71(8)
Cu(2)	x	0.2185(2)	0.2186(2)	0.2190(2)	0.2194(2)	0.2187(3)	0.2186(3)	0.2189(3)	0.2185(3)	0.2184(3)
	U_{11} / Å^2	0.014(2)	0.013(2)	0.016(2)	0.014(2)	0.015(2)	0.017(2)	0.017(2)	0.023(2)	0.021(2)
	U_{22}, U_{33} / Å^2	0.088(2)	0.091(2)	0.099(2)	0.102(2)	0.107(2)	0.109(2)	0.112(2)	0.124(3)	0.132(3)
	U_{23} / Å^2	-0.051(2)	-0.050(2)	-0.057(2)	-0.055(2)	-0.057(2)	-0.057(2)	-0.057(2)	-0.066(3)	-0.066(3)
Sb	x	0.2685(2)	0.2684(2)	0.2682(3)	0.2685(3)	0.2680(3)	0.2678(3)	0.2679(3)	0.2677(3)	0.2673(3)
	B / Å^2	1.33(6)	1.53(7)	1.51(7)	1.68(7)	1.72(8)	1.76(8)	1.83(9)	2.15(9)	2.2(2)
S(1)	x	0.1147(3)	0.1143(3)	0.1150(4)	0.1147(4)	0.1145(4)	0.1148(4)	0.1150(4)	0.1150(4)	0.1152(5)
	z	0.3646(4)	0.3652(4)	0.3647(5)	0.3646(5)	0.3659(5)	0.3645(5)	0.3647(5)	0.3635(6)	0.3641(6)
	B / Å^2	1.29(5)	7.7(3)	1.49(6)	1.58(6)	1.66(6)	1.76(6)	1.78(7)	2.13(7)	2.22(8)
S(2)	B / Å^2	1.29(5)	1.4(2)	1.5(2)	1.5(2)	1.5(2)	1.6(2)	1.7(2)	1.8(2)	1.5(2)
	wt% impurity	8.3(3)	7.7(3)	7.8(3)	7.6(3)	7.8(3)	7.9(3)	7.9(3)	8.2(3)	9.7(4)
	R_{wp} / %	2.45	2.45	2.51	2.53	2.53	2.46	2.54	2.45	2.46
	χ^2	0.9591	0.9601	0.9695	0.9958	1.002	0.9351	0.9898	0.8982	0.9087

	T / K	623	673	723	773	673[b]	573[b]	473[b]	373[b]	323[b]
	a / Å	10.36433(5)	10.37499(6)	10.38741(5)	10.40143(5)	10.37038(5)	10.34794(4)	10.33320(4)	10.32009(4)	10.31352(3)
Cu(1)	B / Å^2	4.14(8)	4.6(1)	5.0(2)	5.5(2)	4.51(9)	3.54(7)	2.91(6)	2.27(5)	1.89(4)
Cu(2)	x	0.2176(3)	0.2186(4)	0.2180(4)	0.2176(4)	0.2182(3)	0.2181(3)	0.2187(3)	0.2184(2)	0.2185(2)
	U_{11} / Å^2	0.027(2)	0.024(2)	0.035(3)	0.031(3)	0.027(2)	0.023(2)	0.018(2)	0.016(2)	0.013(1)
	U_{22}, U_{33} / Å^2	0.138(3)	0.147(4)	0.156(4)	0.160(4)	0.142(3)	0.126(3)	0.112(2)	0.099(2)	0.090(2)
	U_{23} / Å^2	-0.069(3)	-0.069(3)	-0.079(3)	-0.077(3)	-0.070(3)	-0.065(2)	-0.060(2)	-0.058(2)	-0.052(2)
Sb	x	0.2663(3)	0.2670(3)	0.2660(3)	0.2659(3)	0.2667(3)	0.2673(3)	0.2675(3)	0.2680(2)	0.2682(2)
	B / Å^2	2.3(2)	2.7(2)	2.5(2)	2.9(2)	2.6(2)	2.16(9)	1.90(8)	1.56(7)	1.40(6)
S(1)	x	0.1146(5)	0.1150(6)	0.1154(6)	0.1147(6)	0.1146(5)	0.1144(4)	0.1141(4)	0.1143(3)	0.1143(3)
	z	0.3636(6)	0.3639(7)	0.3619(8)	0.3642(7)	0.3629(7)	0.3642(5)	0.3647(5)	0.3646(4)	0.3647(4)
	B / Å^2	2.31(8)	2.56(9)	2.7(1)	2.9(1)	2.41(9)	2.18(7)	1.72(6)	1.49(5)	1.32(5)
S(2)	B / Å^2	1.5(2)	1.7(2)	1.9(3)	1.6(3)	2.2(3)	1.9(2)	1.5(2)	1.4(2)	1.4(2)
	wt% impurity	9.8(4)	9.2(4)	9.5(4)	11.1(5)	8.4(4)	7.5(3)	7.4(3)	7.3(2)	7.3(2)
	R_{wp} / %	2.35	2.49	2.43	2.34	2.6	2.39	2.47	2.42	2.44
	χ^2	0.8426	0.9191	0.865	0.8357	1.005	0.9015	0.9644	0.9641	0.979

[a] Cu(1) on 12(d), (1/4, 1/2, 0); Cu(2) on 12(e), (x, 0, 0); Sb on 8(c), (x, x, x); S(1) on 24(g), (x, x, z) and S(2) on 2(a), (0, 0, 0)

[b] Data acquired on cooling

Table 5.3 Refined parameters from Rietveld analysis of neutron diffraction data for $Cu_{11}MnSb_4S_{13}$, (Space group $I\bar{4}3m$)[a]

	T / K	303	348	373	398	423	448	473
	a / Å	10.37655(4)	10.38329(4)	10.38638(4)	10.38950(4)	10.39261(5)	10.39584(4)	10.39933(5)
Cu(1)/Mn	B / Å^2	1.77(5)	2.17(6)	2.38(7)	2.51(7)	2.70(8)	2.84(8)	2.99(8)
Cu(2)	x	0.2169(2)	0.2173(2)	0.2169(2)	0.2172(3)	0.2174(3)	0.2169(3)	0.2167(3)
	U_{11} / Å^2	0.010(1)	0.007(1)	0.009(2)	0.010(2)	0.008(2)	0.012(2)	0.010(2)
	U_{22}, U_{33} / Å^2	0.078(1)	0.086(2)	0.091(2)	0.094(2)	0.097(2)	0.099(2)	0.101(2)
	U_{23} / Å^2	-0.047(2)	-0.049(2)	-0.052(2)	-0.054(2)	-0.053(2)	-0.053(2)	-0.052(2)
Sb	x	0.2675(2)	0.2673(3)	0.2668(3)	0.2672(3)	0.2672(3)	0.2671(3)	0.2668(3)
	B / Å^2	1.49(6)	1.68(8)	1.84(9)	2.0(1)	2.0(1)	2.0(1)	2.1(1)
S(1)	x	0.1139(3)	0.1138(3)	0.1137(3)	0.1137(4)	0.1136(4)	0.1144(4)	0.1139(4)
	z	0.3626(3)	0.3635(4)	0.3633(4)	0.3635(4)	0.3641(5)	0.3626(4)	0.3632(5)
	B / Å^2	1.18(5)	1.30(6)	1.37(6)	1.45(7)	1.51(7)	1.56(7)	1.52(7)
S(2)	B / Å^2	1.3(2)	1.1(2)	1.2(2)	1.1(2)	1.0(2)	1.2(2)	1.1(2)
	wt% impurity	3.3(2)	3.1(2)	3.1(2)	3.1(3)	3.1(2)	3.2(2)	3.5(3)
	R_{wp} / %	2.5	2.99	2.89	2.95	3.16	2.91	3
	χ^2	0.9949	1.287	1.182	1.273	1.388	1.149	1.212

	T / K	523	573	623	673	723	773
	a / Å	10.40571(4)	10.41252(4)	10.41866(4)	10.42600(4)	10.43482(4)	10.44559(4)
Cu(1)/Mn	B / Å^2	3.45(8)	3.75(7)	4.07(9)	4.28(9)	4.9(1)	5.4(2)
Cu(2)	x	0.2167(3)	0.2157(2)	0.2155(3)	0.2157(3)	0.2154(3)	0.2154(3)
	U_{11} / Å^2	0.017(2)	0.025(2)	0.035(2)	0.033(2)	0.035(2)	0.038(2)
	U_{22}, U_{33} / Å^2	0.109(2)	0.117(2)	0.123(2)	0.129(2)	0.135(3)	0.144(3)
	U_{23} / Å^2	-0.058(2)	-0.064(2)	-0.069(2)	-0.067(2)	-0.069(2)	-0.073(3)
Sb	x	0.2668(3)	0.2663(2)	0.2665(3)	0.2666(3)	0.2658(3)	0.2659(3)
	B / Å^2	2.3(2)	2.26(9)	2.3(1)	2.5(1)	2.8(2)	2.9(2)
S(1)	x	0.1134(4)	0.1138(4)	0.1142(5)	0.1136(5)	0.1135(5)	0.1139(6)
	z	0.3629(5)	0.3611(4)	0.3596(5)	0.3600(5)	0.3600(5)	0.3605(6)
	B / Å^2	1.81(7)	2.13(7)	2.22(8)	2.32(8)	2.49(8)	2.8(1)
S(2)	B / Å^2	1.6(2)	2.2(2)	2.5(2)	2.7(3)	2.7(3)	2.9(3)
	wt% impurity	3.5(3)	3.2(2)	2.9(2)	2.5(2)	2.6(2)	3.1(3)
	R_{wp} / %	2.78	2.1	2.23	2.17	2.14	2.13
	χ^2	1.045	0.7858	0.914	0.852	0.7909	0.8084

[a] Cu(1) (SOF = 5/6) and Mn (SOF = 1/6) on 12(d), (1/4, 1/2, 0); Cu(2) on 12(e), (x, 0, 0); Sb on 8(c), (x, x, x); S(1) on 24(g), (x, x, z) and S(2) on 2(a), (0, 0, 0)

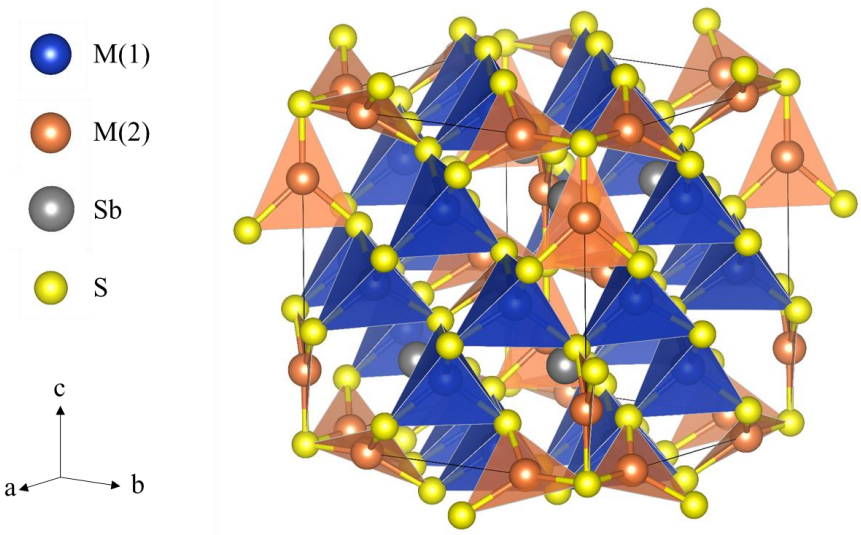

Figure 5.6 Structure of $M(1)_6M(2)_6[SbS_3]_4S$. $M(1)S_4$ tetrahedra are shown in blue and $M(2)S_3$ trigonal planar polyhedra are shown in orange.

Stoichiometric tetrahedrite can be described a defect sphalerite structure and expressed in the form $M(1)_6M(2)_6[SbS(1)_3]_4S(2)$, where M(1) and M(2) are transition-metal atoms in tetrahedral and trigonal planar coordination respectively, Figure 5.6. $SbS(1)_3$ forms a trigonal pyramid and S(2) is in octahedral position at the centre of the cube, coordinated to six M(2) atoms. Since the tetrahedrite structure was confirmed by Wuensch,[268] the bonding and the possible oxidation states of Cu have been disputed. Using the Brillouin-zone model, based on a nearly-free electron model, Johnson and Jeanloz predicted that stoichiometric tetrahedrite with a nominal composition $Cu_{12}Sb_4S_{13}$ is highly unlikely to be formed.[265] A similar conclusion was previously drawn by Makovicky and Skinner, in a systematic study of the $Cu_{12+x}Sb_{4+y}S_{13}$ solid solution.[248] In $Cu_{12+x}Sb_{4+y}S_{13}$, some of the Cu in M(1) become mobile in order to accommodate up to two more atoms, and form a copper-rich phase with a composition up to $Cu_{14}Sb_4S_{13}$. Recent studies have shown that stoichiometric tetrahedrite can be synthesised with high levels of purity,[254, 259-262, 269-271] but often with trace amounts of Cu_3SbS_4. In the cases where no impurity was detected, some level of substitution on the Cu site was involved. The beneficial effect of substitution is confirmed in the present studies with a clear diminution in the weight percentage of Cu_3SbS_4 on going from $Cu_{12}Sb_4S_{13}$ (*ca*. 8 wt%) to $Cu_{11}MnSb_4S_{13}$ (*ca*. 3 wt%). Table 5.2 and Table 5.3. This also corroborates the observation that naturally occurring

tetrahedrite is always found in the form of a solid solution with at least two different transition metals in M(1) and M(2) sites.[254] The very different coherent neutron scattering length of Cu (7.718 fm) and Mn (-3.73 fm) and the resulting excellent contrast strongly support the manganese substitution on the M(1) site rather than the M(2) site and confirm previous studies using powder X-ray diffraction on Mn-substituted tetrahedrite.[252, 259, 272] Neutron diffraction experiments on iron-substituted tetrahedrite led to the same conclusion that substitution occurs on the M(1) site.[273] The substitution of Cu^{+} (0.60 Å) by the larger ionic radius element Mn^{2+} (0.66 Å), in tetrahedral coordination, causes the unit cell to expand with the incorporation of manganese, Figure 5.7. The thermal expansion of $Cu_{11}MnSb_4S_{13}$ is linear over the whole temperature range $303 \leq T / K \leq 773$, while $Cu_{12}Sb_4S_{13}$ shows a slight change of slope around 400 K. Above this temperature, the thermal expansion coefficient, estimated using a simple linear fit, decreases from $2.31(6) \times 10^{-4}$ Å K^{-1} to $1.39(4) \times 10^{-4}$ Å K^{-1} upon manganese

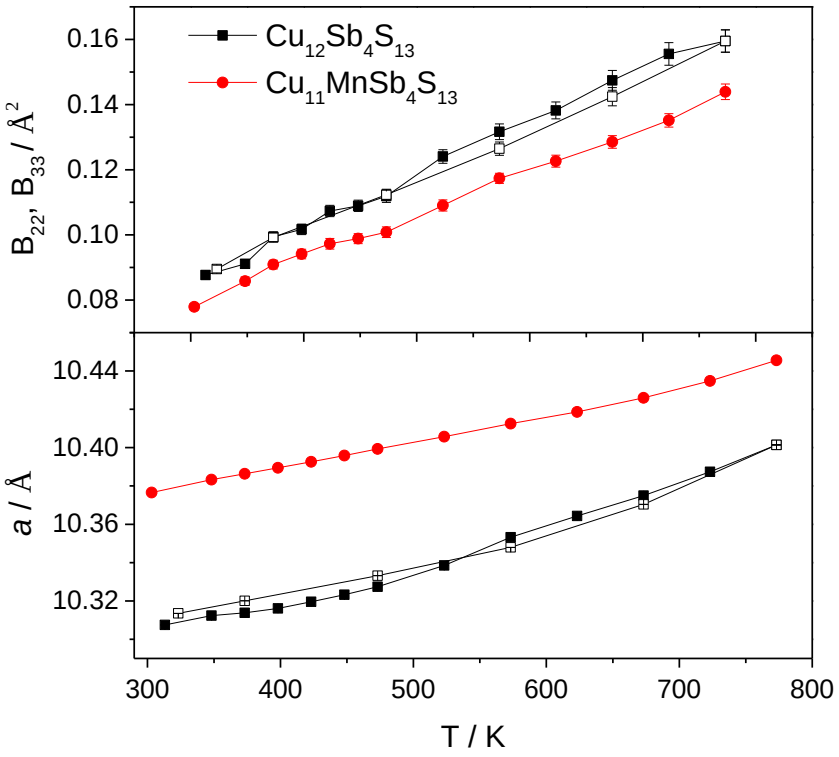

Figure 5.7 Temperature dependence of the anisotropic thermal parameters, $U_{22} = U_{33}$, (top) and unit cell parameter *a* (bottom) for $Cu_{12-x}Mn_xSb_4S_{13}$ (x = 0; 1). Data from measurements carried out on cooling are shown as open symbols. Error bars lie within the symbols.

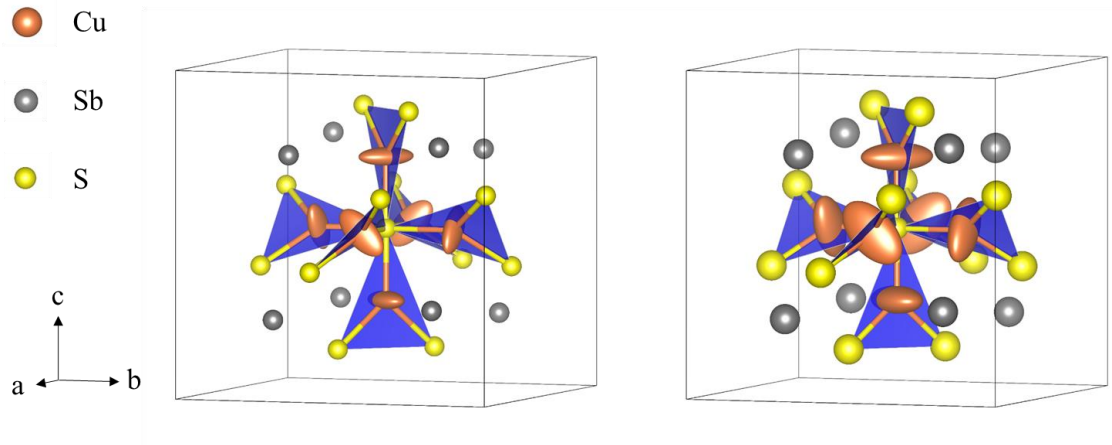

Figure 5.8 Structure of $Cu_{12}Sb_4S_{13}$, highlighting the CuS_3 trigonal planar polyhedra in blue. Thermal ellipsoids are shown with a 90 % probability at 313 K (left) and 773 K (right). S(1) and S(2) are respectively located outside corners of the triangle and at the centre of the unit cell. Cu(1) atoms have been omitted for clarity.

substitution. This information is useful when considering tetrahedrite as a thermoelectric material, as devices can be damaged by the differential thermal expansion of materials. The refinements revealed a large anisotropic thermal displacement parameter for Cu(2) in the direction perpendicular to the trigonal plane formed by two S(1) atoms and the S(2) atom at the centre of the $S(2)Cu(2)_6$ octahedron, Figure 5.8. The anisotropic thermal displacement parameter in this direction is 4 to 6 times larger than the isotropic thermal displacement parameters of the other atoms and increases linearly with increasing temperature, Figure 5.7. The nature of the chemical bonding and the unusual dynamics of the Cu(2) atoms has been investigated in depth by Lai *et al.* using a combination of X-ray synchrotron diffraction and first-principles simulations.[274] The Cu(2) atom forms strong covalent bonds with S(1) and S(2) with a bond order of 0.75 and 0.66, respectively. Additionally, there is a bonding fluctuation between Cu(2) and Sb, with a weak covalent bonding (bond order ≈ 0.10) alternating with the presence of a Sb lone pair. The asymmetry around Cu(2) can be considered as partially static and can be split into two positions, Cu(2)' on 24(g), on each side of trigonal planar polyhedron, Figure 5.9.[273] The bonding fluctuations at the Sb site modifies the initial SbS_3 trigonal pyramid by partially bonding to three Cu(2)/Cu(2)' atoms and forming a distorted S_3SbCu_3 trigonal

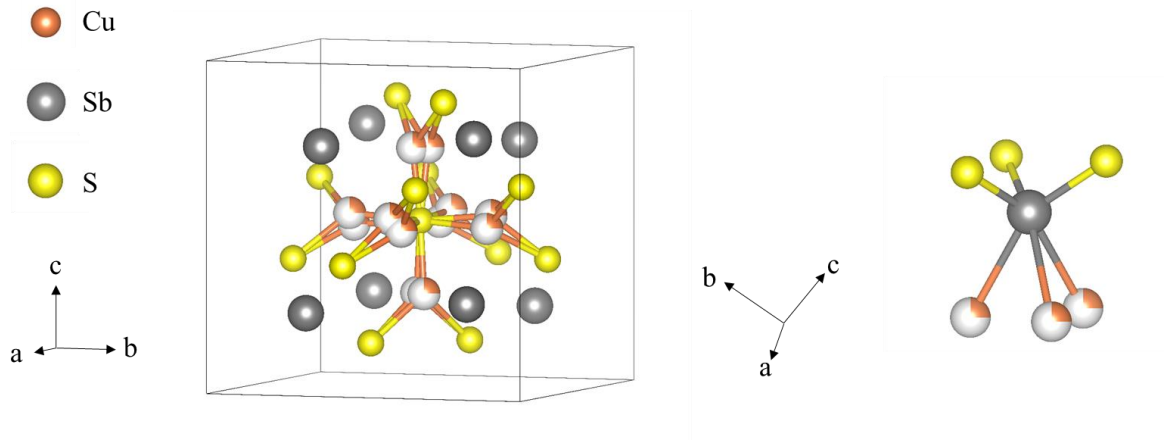

Figure 5.9 Structure of $Cu_{12}Sb_4S_{13}$, showing the split site Cu(2)' (left) and the resulting S_3SbCu_3 trigonal antiprism (right). The white/orange spheres represent the partial occupancy of the Cu(2)' site. Cu(1) atoms have been omitted for clarity.

antiprism.[274] Because the neutron diffraction studies presented here were performed at elevated temperature, the Cu atom in trigonal planar position was treated as Cu(2) with a large anisotropy in the thermal displacement rather than the Cu(2)' split site. Such an anharmonic rattling mode is expected to strengthen the resonant phonon scattering[275] and to contribute to the low lattice contribution to the thermal conductivity of tetrahedrite.

5.2.3 Thermoelectric performance of $Cu_{12}Sb_4S_{13}$ and $Cu_{11}MnSb_4S_{13}$

5.2.3.1 Electrical properties

Measurements of the electrical properties of $Cu_{12-x}Mn_xSb_4S_{13}$ (x = 0; 1) were carried out on hot-pressed pellets with densities > 95 % of the crystallographic value. Hot-pressing was carried out on the apparatus described in Section 2.7.1 under a pressure of 80 MPa at 723 K for 30 min and carried out under a constant nitrogen flow to prevent oxidation. The pressure was maintained during cooling until the temperature decreased below 373 K. Tetrahedrite pellets being hard and brittle, electrical measurements were carried out on disc samples using an adapted sample holder to avoid issues with crack formation and chipping around the edges during the cutting step. Figure 5.10 shows the temperature dependence of the electrical

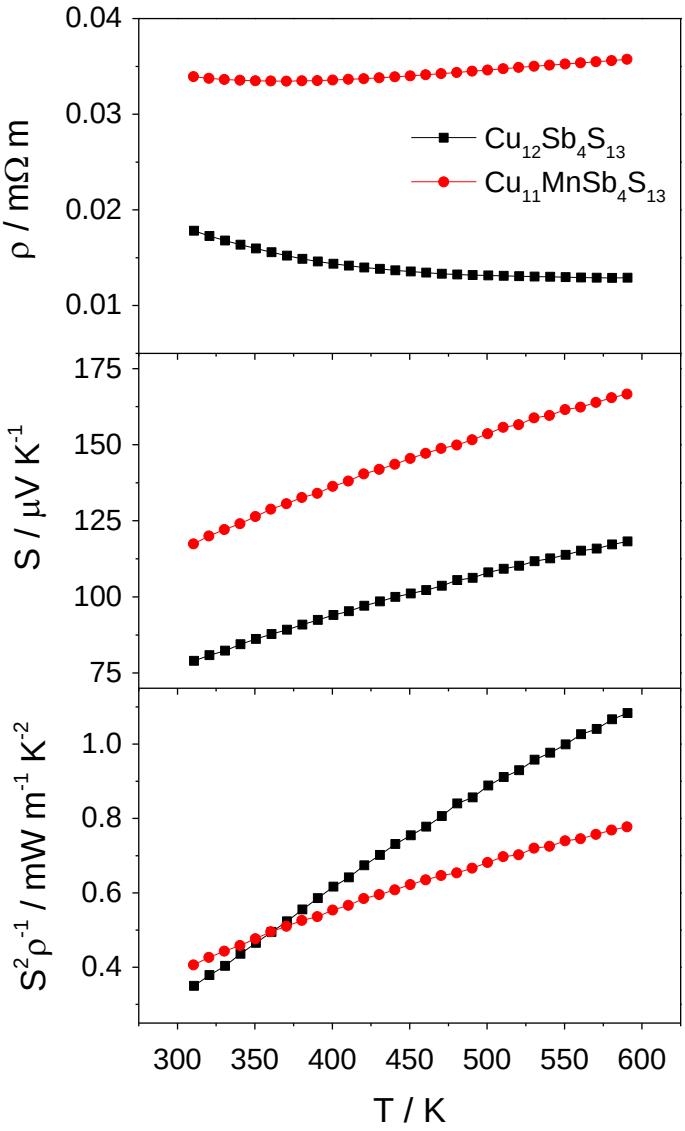

Figure 5.10 Temperature dependence of the electrical properties of $Cu_{12-x}Mn_xSb_4S_{13}$ (x = 0; 1), including the electrical resistivity (top), Seebeck coefficient (middle) and the resulting power factor (bottom).

resistivity, ρ, Seebeck coefficient, S, and calculated power factor, $S^2\rho^{-1}$, for $Cu_{12-x}Mn_xSb_4S_{13}$ (x = 0; 1) measured over the temperature range $310 \leq T / K \leq 580$. The data indicate that unsubstituted tetrahedrite is a *p*-type semiconductor with a low electrical resistivity, $\rho < 0.02$ mΩ m at room temperature, consistent with recent measurements of the thermoelectric properties of tetrahedrite.[255, 258, 259, 271] Substitution of Cu by Mn at the M(1) site causes the electrical resistivity and Seebeck coefficient to increase simultaneously with a change in the

temperature behaviour of the electrical resistivity. For $Cu_{11}MnSb_4S_{13}$, ρ becomes almost temperature independent with a change in the sign of $^{d\rho}/_{dT}$ from negative below 350 K to positive above 400 K, consistent with extrinsic semiconducting behaviour and a decrease in the charge carrier concentration compared with $Cu_{12}Sb_4S_{13}$.

Recent DFT (density-functional theory) band structure calculations,[255] Figure 5.11, predicted $Cu_{12}Sb_4S_{13}$ to be a metal with all copper ions being in the monovalent Cu^+ state. This contradicts earlier X-ray absorption spectroscopy measurements that indicated a mixture of divalent and monovalent cations at the M(1) position.[276, 277] A complete filling of the valence band, and the resulting semiconducting state, is expected for $Cu_{12}Sb_4S_{13}$ when Cu is in a mixed valence state with formal oxidation states corresponding to $Cu_{10}^{+}Cu_2^{2+}Sb_4^{3+}S_{13}^{2-}$. The substitution of copper by manganese is likely to correspond to a partial filling of the valence band and a decrease in the charge carrier (hole) concentration via the substitution of monovalent Cu^+ by divalent Mn^{2+}. This results in an increase in both electrical resistivity and Seebeck coefficient. Additionally, the disorder induced by manganese substitution may contribute to the increase in electrical resistivity. The large increase in Seebeck coefficient with substitution (more than 50 % over the temperature range investigated) is only sufficient to counterweigh the loss of electrical conductivity below 360 K. Overall, the highest power factor is observed for $Cu_{12}Sb_4S_{13}$ with $S^2\rho^{-1}$ = 1.08 mW m^{-1} K^{-2} at 590 K while the maximum value

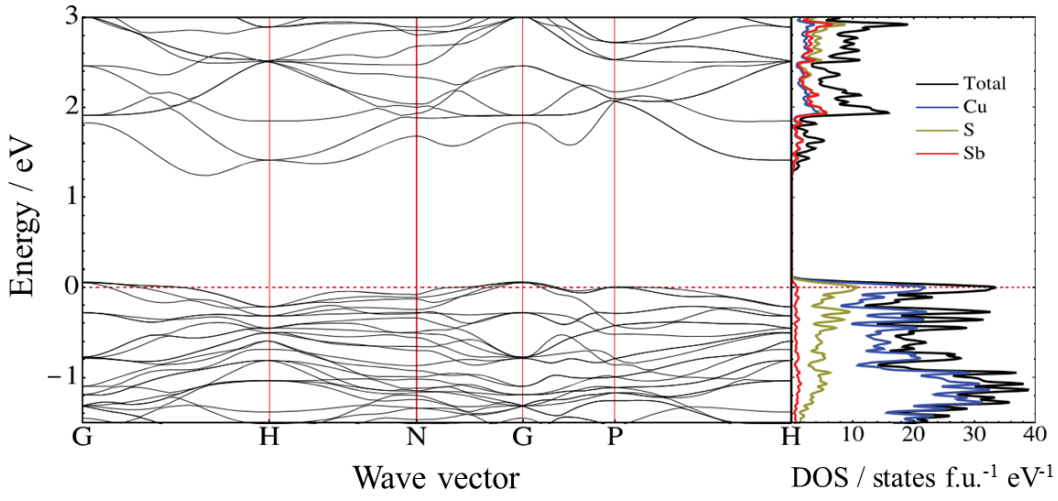

Figure 5.11 Electronic band structure and density of states (DOS) of $Cu_{12}Sb_4S_{13}$ from DFT calculations, the dotted lines represent the Fermi level. From the work of Lu *et al.*[255]

for $Cu_{11}MnSb_4S_{13}$ is $S^2\rho^{-1}$ = 0.78 mW m^{-1} K^{-2} at the same temperature. At 310 K, however, the manganese substituted tetrahedrite has the highest power factor with $S^2\rho^{-1}$ = 0.40 mW m^{-1} K^{-2} against $S^2\rho^{-1}$ = 0.35 mW m^{-1} K^{-2} for $Cu_{12}Sb_4S_{13}$. These values are of a comparable order of magnitude to that of the best thermoelectric materials, *e.g.* $S^2\rho^{-1}$ = 1 - 5 mW m^{-1} K^{-2} for nanostructured BiSbTe alloys.[27]

5.2.3.2 Thermal transport properties and figure of merit

The thermal diffusivity of $Cu_{12-x}Mn_xSb_4S_{13}$ (x = 0; 1) was measured on discs with a thickness of *ca.* 2 mm. Because of the cubic structure of tetrahedrite, the thermal diffusivity was only measured in the direction parallel to the pressing. The specific heat used to calculate the thermal conductivity was determined using the Dulong-Petit law, *Cp* = 0.434 J K^{-1} g^{-1} and *Cp* = 0.436 J K^{-1} g^{-1} for $Cu_{12}Sb_4S_{13}$ and $Cu_{11}MnSb_4S_{13}$, respectively. These values were corroborated by

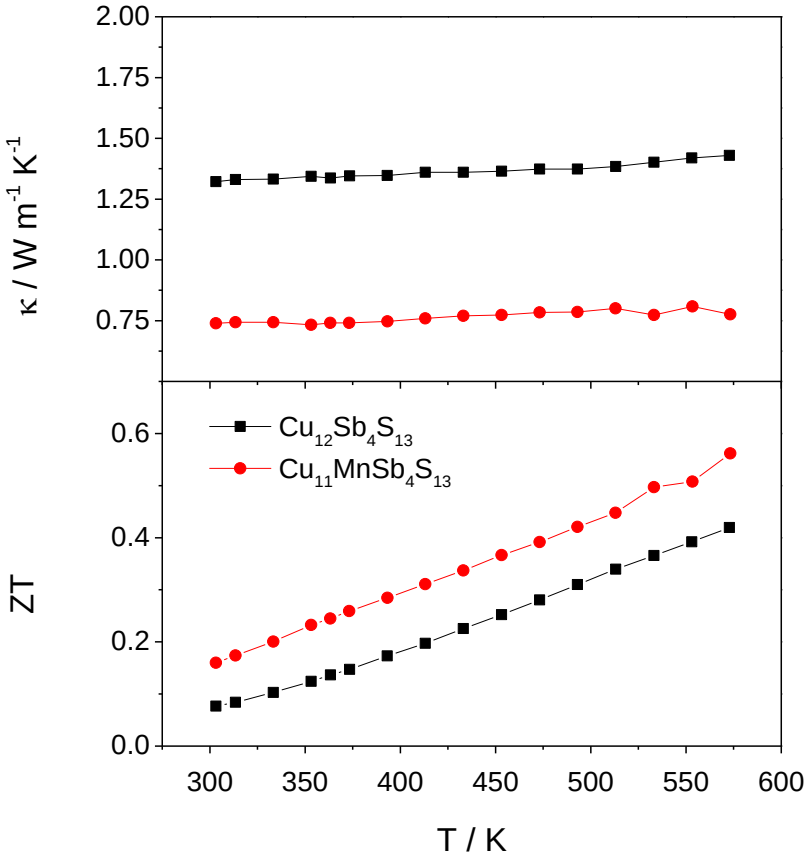

Figure 5.12 Temperature dependence of the thermal conductivity and the figure of merit, ZT, of $Cu_{12-x}Mn_xSb_4S_{13}$ (x = 0; 1).

side-by-side measurements with a pyroceram reference, Appendix G. The temperature dependence of the thermal conductivity, κ, and the figure of merit, ZT, of $Cu_{12-x}Mn_xSb_4S_{13}$ (x = 0; 1) are shown in Figure 5.12. The values for κ range from κ = 1.32 W m^{-1} K^{-1} and κ = 1.43 W m^{-1} K^{-1} over the temperature range investigated for $Cu_{12}Sb_4S_{13}$. The low thermal conductivity is, in part, attributed to the complex crystal structure with a large number of atoms, 58 per unit cell. Moreover, the recent in-depth studies[274] of Lai *et al.* on the chemical bonding and atomic dynamics in tetrahedrites have shed light on the anharmonic rattling of the Cu(2) site, detailed in Section 5.2.2.2. The low energy vibration is expected to play an important role in phonon scattering and therefore contribute to the low thermal conductivity of tetrahedrite.[271] For $Cu_{11}MnSb_4S_{13}$, manganese substitution leads to a large reduction in thermal conductivity and an almost temperature independent behaviour and a value of κ ≈ 0.75 W m^{-1} K^{-1}. This represents a reduction of more than 40 % across the temperature range. The electronic and

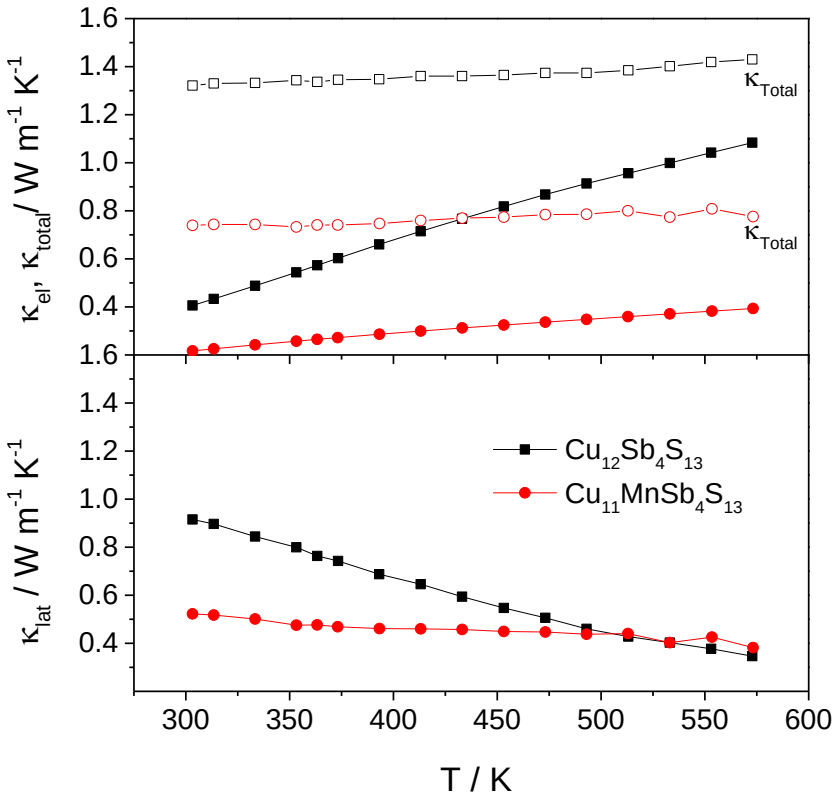

Figure 5.13 Electronic component (top) and lattice component (bottom) of the thermal conductivity of $Cu_{12-x}Mn_xSb_4S_{13}$ (x = 0; 1), calculated using the Wiedemann-Franz law. The total thermal conductivity is shown in open symbols for comparison.

lattice contributions to the total thermal conductivity, Figure 5.13, have been determined using the Wiedemann-Franz law with $L = 2.44 \times 10^{-8}$ W Ω K^{-2}. The reduction caused by manganese substitution can be attributed to a large reduction in the electronic contribution resulting from the increase in electrical resistivity. Additionally, the lower lattice contribution is responsible for a significant part of the reduction at low temperature and could be explained by the disorder that accompanies the substitution of copper by lighter manganese. Ultimately, the figure of merit is improved over the whole temperature range investigated upon manganese substitution with a 100 % increase over $Cu_{12}Sb_4S_{13}$ at 300 K and a 33 % increase at 573 K. The highest ZT is observed for $Cu_{11}MnSb_4S_{13}$ with ZT = 0.56 at 573 K; at the same temperature $Cu_{12}Sb_4S_{13}$ reaches a ZT of 0.42.

The results on unsubstituted tetrahedrite are in agreement with previous research, Appendix H, with the exception of the work of Chetty *et al*., where the electrical resistivity is very low, *ca*. 0.01 mΩ m, and ZT reaches the highest reported value of 0.76 at 623 K, Table 5.4.[259] Because of the presence of Cu_3SbS_4 impurities, it may be that these differences arise from variations in the weight percentage of the second phase. Of the two recent systematic studies on $Cu_{12-x}Mn_xSb_4S_{13}$, Chetty et al. reported a systematic decrease in the figure of merit. At 575 K, the ZT of $Cu_{12-x}Mn_xSb_4S_{13}$ was reported to be *ca*. 0.4 for x = 0.9 and *ca*. 0.27 for x = 1.4. Conversely, Heo *et a*l. reported a large increase in ZT upon manganese substitution with a maximum ZT of 1.13 at 573 K for $Cu_{11}MnSb_4S_{13}$.[258] However, the exceptionally low thermal conductivity values observed for Mn-substituted tetrahedrite in the work of Heo *et a*l., κ < 0.3

Table 5.4 Reported thermoelectric properties of $Cu_{12-x}Mn_xSb_4S_{13}$.

x in $Cu_{12-x}Mn_xSb_4S_{13}$	$T_{ZT\text{-}max}$ / K	S / μV K^{-1}	ρ / mΩ m	$S^2 \rho^{-1}$ / mW m^{-1} K^{-2}	κ / W m^{-1} K^{-1}	ZT_{max}	Ref
0	623	140	0.01	1.70	1.4	0.76	
0.4	673	150	0.02	1.25	1.3	0.65	
0.9	723	175	0.04	0.77	1.0	0.55	259
1.4	723	260	0.14	0.49	0.9	0.40	
1.8	723	400	0.9	0.18	0.6	0.20	
0	575	105	0.020	0.562	1.08	0.30	
0.5	575	117	0.020	0.691	0.37	1.07	
1	575	141	0.037	0.536	0.27	1.13	258
1.5	575	187	0.118	0.297	0.21	0.78	
2	575	247	0.270	0.226	0.17	0.76	

W m^{-1} K^{-1}, have not been reproduced. These differences in thermal conductivity are likely to be due to the difference in density between the consolidated samples prepared by Heo *et al*., with a measured density ≥ 85 % of the crystallographic against > 95 % achieved by Chetty *et al*. and in the present work. The resulting thermal conductivity, κ, is directly reduced by its dependence on the density, *d*, of the sample via the relationship $\kappa = d \times \alpha \times C_p$, where C_p is the heat capacity and α is the thermal diffusivity. The porosity of the sample contributes to the apparent reduction in thermal conductivity through the relationship, $\kappa = \kappa_0 \times (1 - P^{2/3})$, where κ_0 is the thermal conductivity of the fully densified material and *P* is the pore fraction.

Although the thermoelectric properties of on $Cu_{12-x}Mn_xSb_4S_{13}$ (x = 0; 1) differ from those reported in the literature,[254, 258, 259] the figure of merit remains very high for a tellurium and selenium-free material and is comparable to that of the state-of-the-art materials such as doped derivatives of Sb_2Te_3, $CeFe_4Sb_{12}$ or PbTe with ZT ranging from 0.4 to 1.3 at 573 K.[17, 22]

5.3 Tetrahedrite phases $Cu_{12+y}Sb_4S_{13}$

The thermoelectric properties of a series of copper-enriched tetrahedrites with composition $Cu_{12+y}Sb_4S_{13}$ (y = 0; 0.3; 1; 1.5 and 2) has been investigated. Powder X-ray diffraction was used to confirm the presence of a Cu-rich and a Cu-poor phase and to identify potential impurities. The electrical properties and thermal conductivity have been measured and the thermoelectric figure of merit of the samples has been calculated.

5.3.1 Synthesis and structure confirmation

Powdered samples with composition $Cu_{12+y}Sb_4S_{13}$ (y = 0.3; 1; 1.5 and 2), were prepared by Dr A. Kaltzoglou, of this laboratory, through solid-state reaction (Section 2.1.1) of stoichiometric amounts of Cu (Sigma Aldrich, 99.5 %), Sb (Alfa Aesar, 99.5 %), and S (Sigma Aldrich, flakes, 99.99 %). Two successive firings were applied to the powders, at 773 K for 48 h, using a heating and cooling rate of 1 K min^{-1}, with an intermediate grinding step. Le bail refinements of XRD data on the pellets confirmed the presence of a mixture of a Cu-poor phase and a Cu-rich phase, Figure 5.14. For comparison, the data from Rietveld refinement of $Cu_{12}Sb_4S_{13}$, from Section 5.2.2.1, are also included. Traces of Cu_3SbS_4 were found only in $Cu_{12.3}Sb_4S_{13}$.

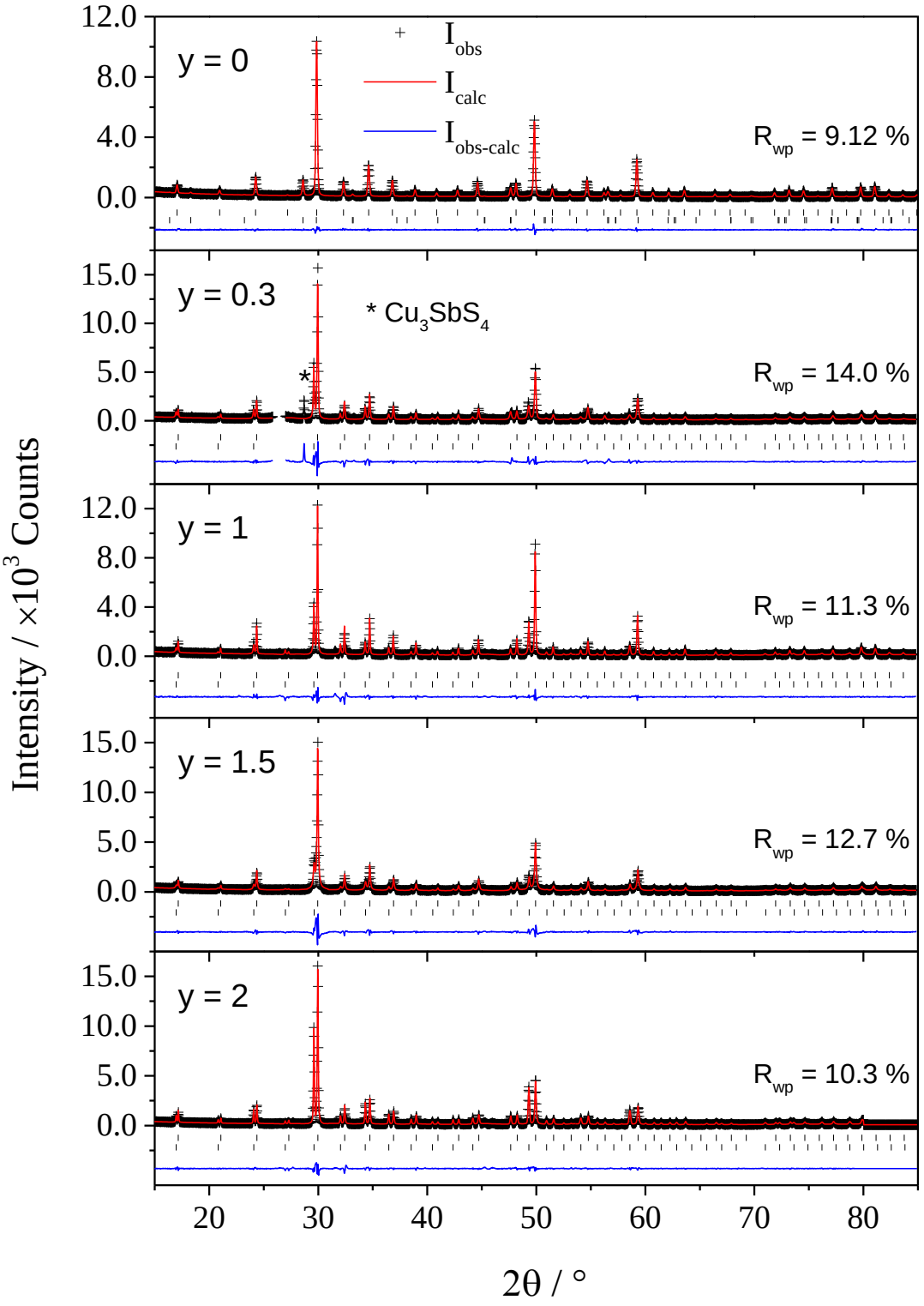

Figure 5.14 Observed (black crosses), calculated (red line) and difference (blue line) profiles for $Cu_{12}Sb_4S_{13}$ from Rietveld refinement and $Cu_{12+y}Sb_4S_{13}$ (y = 0.3; 1; 1.5; 2) from Le Bail refinement of XRD data. The top tick marks correspond to the Bragg reflections from the Cu-poor phase and the bottom tick marks to the second phase; Cu_3SbS_4 in the case of $Cu_{12}Sb_4S_{13}$, and the Cu-rich phase in the case of $Cu_{12+y}Sb_4S_{13}$.

Table 5.5 Lattice parameter, *a*, of the Cu-poor and Cu-rich tetrahedrite phases in $Cu_{12+y}Sb_4S_{13}$ from Le Bail refinement of XRD data.

y in $Cu_{12+y}Sb_4S_{13}$	*a* (Cu-poor) / Å	*a* (Cu-rich) / Å
0	10.3234(2)[a]	-
0.3	10.3287(4)	10.4469(5)
1	10.3302(3)	10.4463(3)
1.5	10.3248(4)	10.4390(5)
2	10.3228(3)	10.4439(3)

[a] From Rietveld refinement

The lattice parameters, *a*, determined from the Le Bail refinements are shown in Table 5.5. The values of $a \approx 10.32$ Å and $a \approx 10.44$ Å correspond to the Cu-poor and Cu-rich tetrahedrite respectively and are consistent with previous reports.[249, 264] Detailed structural refinement of the copper-enriched tetrahedrites using the Rietveld method was impeded by the superposition of reflections from the Cu-poor and Cu-rich phases. Previous studies on the structure of tetrahedrite suggested that the presence of interstitial sites and the lower apparent occupancy of Cu(1) sites in Cu-rich tetrahedrite offer a preferred pathway for the migration of mobile Cu ions.[104, 249] Higher resolution analysis, such as neutron diffraction, is required to determine accurately the structural parameters.

5.3.2 Thermoelectric performance of $Cu_{12+y}Sb_4S_{13}$

5.3.2.1 Electrical properties

As with stoichiometric tetrahedrite, the electrical properties of $Cu_{12+y}Sb_4S_{13}$ (y = 0.3; 1; 1.5 and 2) were determined from hot-pressed pellets with densities > 95 % of the crystallographic value. The hot-pressed pellets were obtained using the same method as for $Cu_{12}Sb_4S_{13}$, described in Section 5.2.3.1. The electrical properties, Figure 5.15, were measured directly on discs. For $Cu_{12+y}Sb_4S_{13}$ samples with y > 0, the electrical properties show two distinct behaviours, below and above an apparent transition, at $T_M \approx 380$ K for y = 0.3, up to $T_M \approx 410$ K for y = 2.

At the temperature T_M, the electrical resistivity changes from an abrupt fall with increasing temperature, as expected for a semiconductor, to an almost temperature independent behaviour reminiscent of that of $Cu_{12}Sb_4S_{13}$. The behaviour of the Seebeck coefficient also changes from a parabolic decrease to a linear increase with temperature at T_M. Below the transition

temperature, this behaviour is consistent with the presence of a copper-rich phase, with a predicted filled valence band leading to a semiconductor with a large band gap.[255, 265] Above T_M, the excess copper leads to a reduction in charge carrier concentration due to partial filling of the valence band. This produces an increase in both the Seebeck coefficient and the electrical resistivity. As a result, the power factor of $Cu_{12+y}Sb_4S_{13}$ (y = 0.3; 1; 1.5 and 2), is reduced with respect to stoichiometric tetrahedrite (y = 0) as the increase in the Seebeck coefficient is not sufficient to outweigh the increase in electrical resistivity. The maximum power factor is

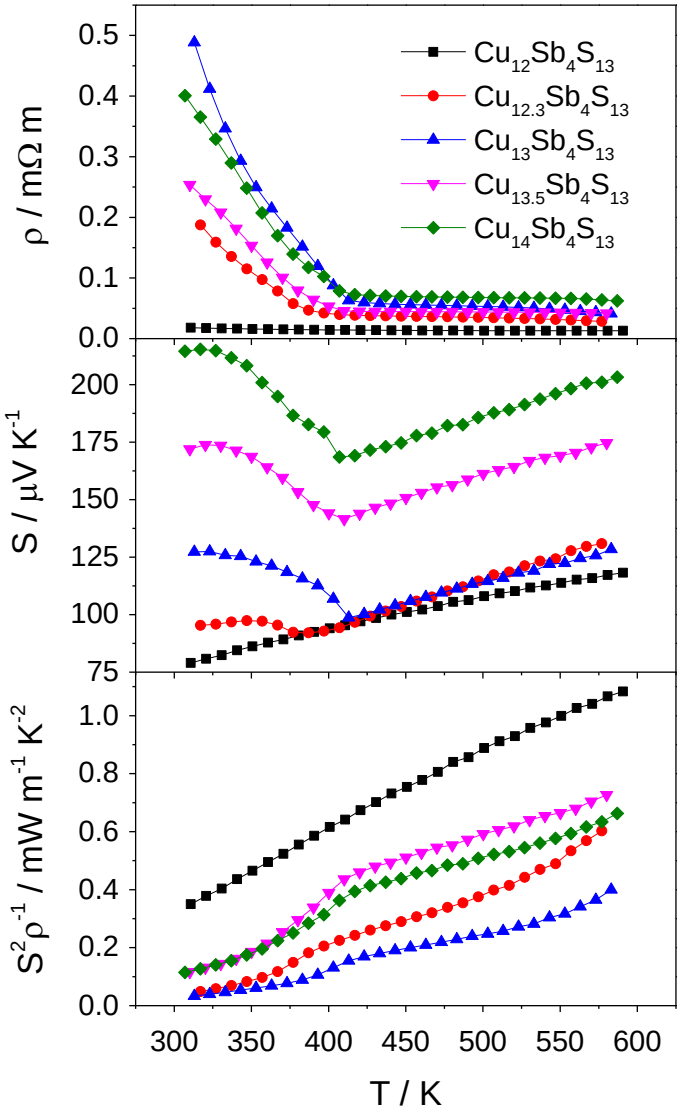

Figure 5.15 Temperature dependence of the electrical properties of $Cu_{12+y}Sb_4S_{13}$ (y = 0; 0.3; 1; 1.5; 2), including the electrical resistivity (top), Seebeck coefficient (middle) and the power factor (bottom).

observed for $Cu_{12}Sb_4S_{13}$ over the whole temperature range investigated with $S^2\rho^{-1}$ = 0.35 mW m^{-1} K^{-2} at 310 K and $S^2\rho^{-1}$ = 1.08 mW m^{-1} K^{-2} at 590 K. The power factor of copper-enriched tetrahedrites $Cu_{12+y}Sb_4S_{13}$ decreases up to y = 1 before increasing for y = 1.5 and 2, as a result of a large increase in the Seebeck coefficient, reaching $S^2\rho^{-1}$ = 0.73 mW m^{-1} K^{-2} at 590 K.

A study of the unit cell parameters determined from powder X-ray diffraction data, reported that the copper-rich and copper-poor phases merged into a single tetrahedrite phase with nominal composition $Cu_{12+y}Sb_4S_{13}$ (y > 0) at a temperature transition around 400 K.[248] However, this observation is contradicted by an on-going investigation, including temperature-dependent neutron diffraction analysis, carried out on the same samples than the ones used in this work.[278] While the two tetrahedrite phases do merge into one, neutron diffraction data unequivocally locate the merging temperatures at 553 K and 493 K on heating for $Cu_{12.3}Sb_4S_{13}$ and $Cu_{14}Sb_4S_{13}$, respectively. Discontinuities in bond lengths and residual density distributed throughout the unit cell in Fourier maps occur at the same temperature than the anomalies in the unit cell parameters.[278] Similar transitions have been observed in Cu_3SbS_3,[279] Cu_3BiS_3[280] and Cu_3SbSe_3,[281] and have been attributed to a change from stationary to mobile copper atoms, that could be responsible for the dramatic changes of behaviours observed in the electrical properties in the present work.

5.3.2.2 Thermal transport properties and figure of merit

The thermal diffusivity of $Cu_{12+y}Sb_4S_{13}$ (y = 0.3; 1; 1.5 and 2) was measured on discs with a thickness of *ca.* 2 mm in the direction parallel to the pressing. As with stoichiometric tetrahedrite, the electrical and thermal properties of $Cu_{12+y}Sb_4S_{13}$ are regarded as being isotropic because of the cubic structure. The thermal conductivity was calculated using the Dulong-Petit specific heat, which ranges from Cp = 0.434 J K^{-1} g^{-1} for y = 0.3 to Cp = 0.431 J K^{-1} g^{-1} for y = 2. The addition of copper atoms in tetrahedrite has a large impact on the thermal conductivity, Figure 5.16, with the lowest values being obtained for the copper-rich end of the series, $Cu_{14}Sb_4S_{13}$. At 573 K, the thermal conductivity of $Cu_{14}Sb_4S_{13}$ is reduced by *ca.* 60 % compared to the stoichiometric tetrahedrite and reaches κ = 0.58 W m^{-1} K^{-1}. For copper-

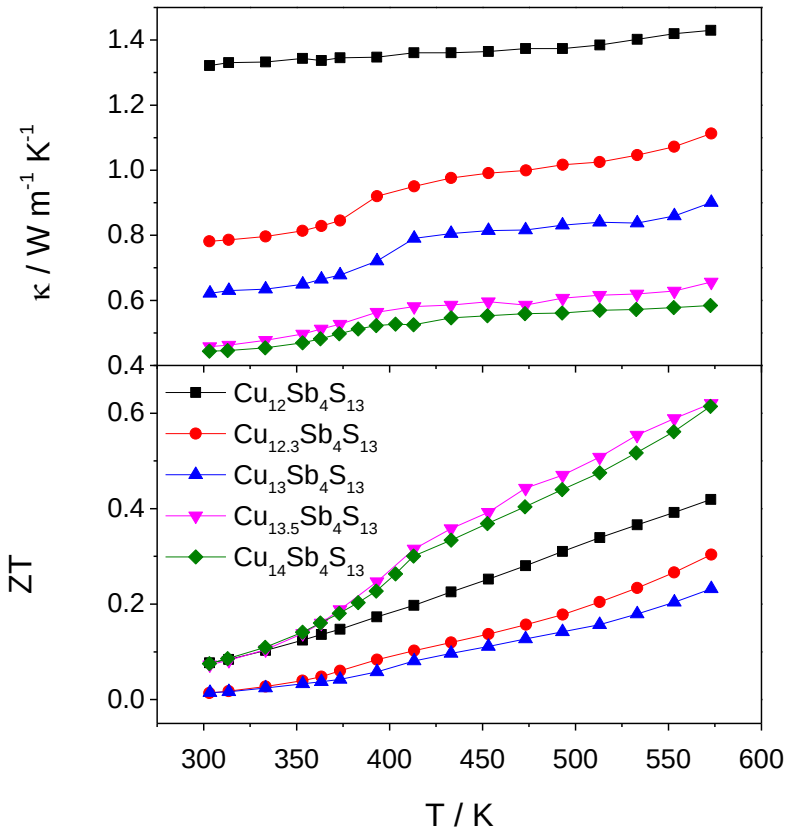

Figure 5.16 Temperature dependence of the thermal conductivity and the figure of merit, ZT, of $Cu_{12+y}Sb_4S_{13}$ (y = 0; 0.3; 1; 1.5; 2).

enriched tetrahedrites, the thermal conductivity increases slightly with temperature with a step observed at T_M. The electronic and lattice contributions to the total thermal conductivity, Figure 5.17, have been determined using the Wiedemann-Franz law with $L = 2.44 \times 10^{-8}$ W Ω K^{-2}. While the extra copper also helps to decrease the lattice component, κ_{lat}, of the thermal conductivity at low temperature, it is the reduction in the electronic component, κ_{el}, that is principally responsible for the reduction over the whole temperature range investigated. The lattice contribution to the thermal conductivity is largely independent of temperature for the copper-enriched samples and decreases with additional copper. This may be associated with an increase in the phonon scattering rate caused by the highest number of atoms per unit cell. Ultimately, the large decrease in the thermal conductivity is sufficient to compensate for the decrease in power factor for $Cu_{12+y}Sb_4S_{13}$ when $y \geq 1.5$, Figure 5.16. The highest figure of

merit is observed for $Cu_{12+y}Sb_4S_{13}$ (y = 1.5 and 2) with ZT = 0.62 at 573 K. This represents a 48 % increase over stoichiometric tetrahedrite, $Cu_{12}Sb_4S_{13}$, at the same temperature. The thermoelectric properties of copper-enriched tetrahedrite are very promising; however, there is a risk of copper-ion mobility as some copper atoms are expected to become mobile to accommodate the extra Cu.[263] Because of this, more data including neutron diffraction, SEM/EDX analysis and ionic conductivity measurements are needed to complete the investigation.

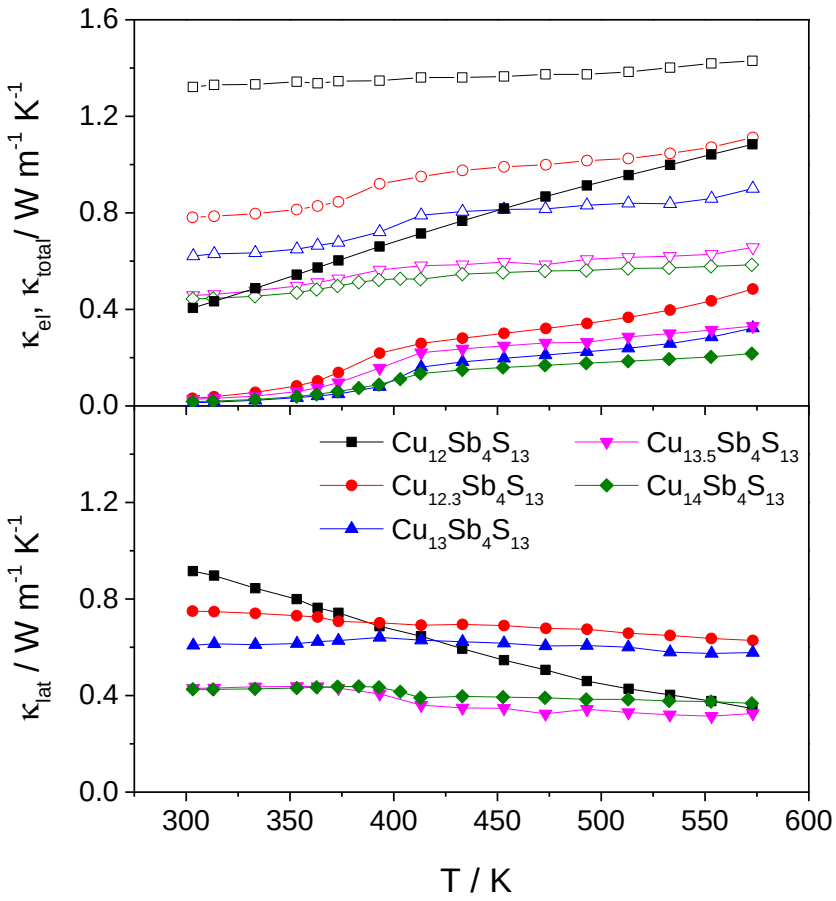

Figure 5.17 Electronic component (top) and lattice component (bottom) of the thermal conductivity of $Cu_{12+y}Sb_4S_{13}$ (y = 0; 0.3; 1; 1.5; 2), calculated using Wiedemann-Franz law. The total thermal conductivity is shown in open symbols for comparison.

5.4 Bornite phase $Cu_5Fe_{1-x}Mn_xS_4$

This section presents the first report of the thermoelectric properties of doped bornite, along with a new synthetic route, via mechanical alloying. The results have been published in a special issue on thermoelectricity of the Journal of Materials Chemistry C.[282] The low thermal conductivity and moderately high electrical resistivity of bornite are in part due to the low charge carrier concentration.[253] Therefore, there is room for improvement through an enhancement of the electrical properties provided the low thermal conductivity can be maintained. In this context, substitution of the trivalent Fe by transition metals Zn and Mn was attempted. However, Zn doping was unsuccessful with the formation of sphalerite ZnS. A series of compositions $Cu_5Fe_{1-x}Mn_xS_4$ ($0 \leq x \leq 0.10$), has been prepared and characterised by powder X-ray diffraction, electrical and thermal transport property measurements, thermal analysis and scanning electron microscopy coupled with EDX analysis.

5.4.1 Synthesis

The established synthesis route for the preparation of bornite is by high-temperature solid-state reaction in evacuated sealed tubes, involving a large energy consumption over several days.[107, 111, 253] Bornite has been investigated as a potential photovoltaic material because of a band gap of approximately 1 eV,[283] and has subsequently been successfully synthesised using solution-based methods.[284, 285] Using solvents such as oleic acid or ethylene glycol in reflux is not usually a problem for large scale production; however, it induces complications for thermoelectric applications as the adsorbed solvent is often difficult to eliminate fully. This leads to unwanted side-reactions during the consolidation step that ultimately change the physical properties of the sample.

The samples investigated in the following section have been synthesised using mechanical alloying as detailed in Section 2.1.2. Bornite samples with composition $Cu_5Fe_{1-x}Mn_xS_4$ (x = 0; 0.01; 0.02; 0.03; 0.04; 0.05; 0.10) were mechanically alloyed from Cu (Sigma Aldrich, 99.5 %), Fe (Sigma Aldrich, 99.9 %), Mn (Alfa Aesar, 99.95 %) powders and S flakes (Sigma Aldrich, 99.99 %). Stoichiometric amounts of each element were ground using a pestle and mortar and placed in a 25 ml stainless-steel jar together with 6 mm stainless-steel balls, under

an argon atmosphere. The weight ratio of powder to balls was 3:7. Two successive millings were carried out at 500 rpm with 5 min interval steps, with a change of direction, for 20 h each.

5.4.2 Structural investigations

5.4.2.1 Powder X-ray diffraction

Two successive ball millings of elemental precursors with composition $Cu_5Fe_{1-x}Mn_xS_4$ ($0 \leq x \leq 0.10$) produce a fine black powder from the mechanical alloying of the elements. Powder X-ray diffraction data, Figure 5.18, are consistent with the presence of poorly crystalline cubic bornite and a small quantity of unreacted iron. Following hot-pressing at 823 K, detailed in Section 2.7.1, the crystallinity of the sample increased and the products adopt the low-temperature orthorhombic structure of bornite. Le Bail refinement using X-ray diffraction data, Figure 5.18, obtained for the consolidated pellet of Cu_5FeS_4 resulted in lattice parameters (a =

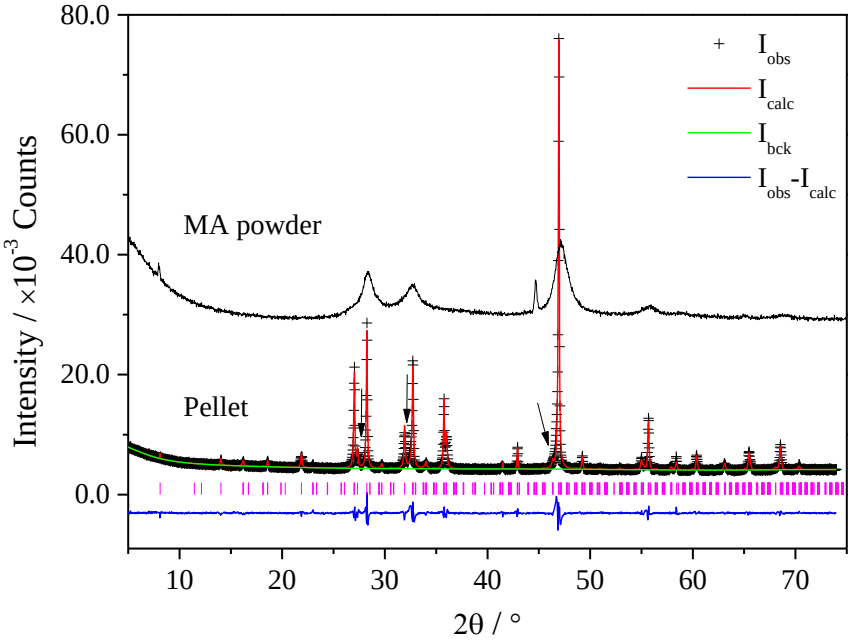

Figure 5.18 Powder X-ray diffraction pattern of mechanically alloyed (MA) Cu_5FeS_4 (upper full line) and the observed (black crosses), calculated (red line) and difference (lower blue line) profiles from Le Bail refinement using X-ray diffraction data collected on the hot-pressed bornite pellet. Reflection positions for the orthorhombic $2a \times 4a \times 2a$ phase are marked. Arrows indicate peak shoulders that can be indexed with a 1a unit cell.

10.9484(3) Å, *b* = 21.8647(8) Å and *c* = 10.9484(3) Å) that are consistent with previous reports for the low-temperature orthorhombic phase.[106] The absence of impurities such as chalcopyrite, pyrrhotite or pyrite is confirmed. Full structural refinement using the Rietveld method was not possible owing to the superposition of reflections arising from trace amounts of a cubic phase which can be indexed with a lattice parameter a ≈ 5.50 Å, indicated by arrows in Figure 5.18. Morimoto *et al.* observed that quenching bornite from elevated temperatures results in the isolation of the intermediate 2*a* phase that subsequently converts to the thermodynamically favoured orthorhombic polymorph after several weeks at room temperature.[107] The strongest Bragg reflections of both the intermediate, 2*a*, and high-temperature, 1*a*, cubic phases all occur at the same 2θ angles as those of the low-temperature orthorhombic phase. Therefore, it was not possible from the data available to unequivocally identify the trace polymorph as the 1*a* or 2*a* phase or even both, as suggested by Ding *et al.*, who described a highly heterogeneous structure with the coexistence of several domains, 1*a*, 2*a* and 4*a* or 6*a*.[113]

Powder X-ray diffraction data for the manganese doped samples are given in Figure 5.19. They are very similar to that of unsubstituted bornite; however, traces of alabandite (MnS) can be detected for $Cu_5Fe_{0.9}Mn_{0.1}S_4$, suggesting that the solubility limit of manganese in bornite is approximately 0.1 per formula unit. The compositional evolution of the *a* and *b* parameters of the orthorhombic phase with manganese substitution is shown in Figure 5.20. Whilst the *a* (and *c*) lattice parameter changes little with manganese content, the *b* parameter changes quite markedly. The compositional variation of the *b* parameter is not entirely linear but exhibits a weak anomaly for x ≤ 0.03 suggesting that manganese may occupy different atom positions, depending on the composition.

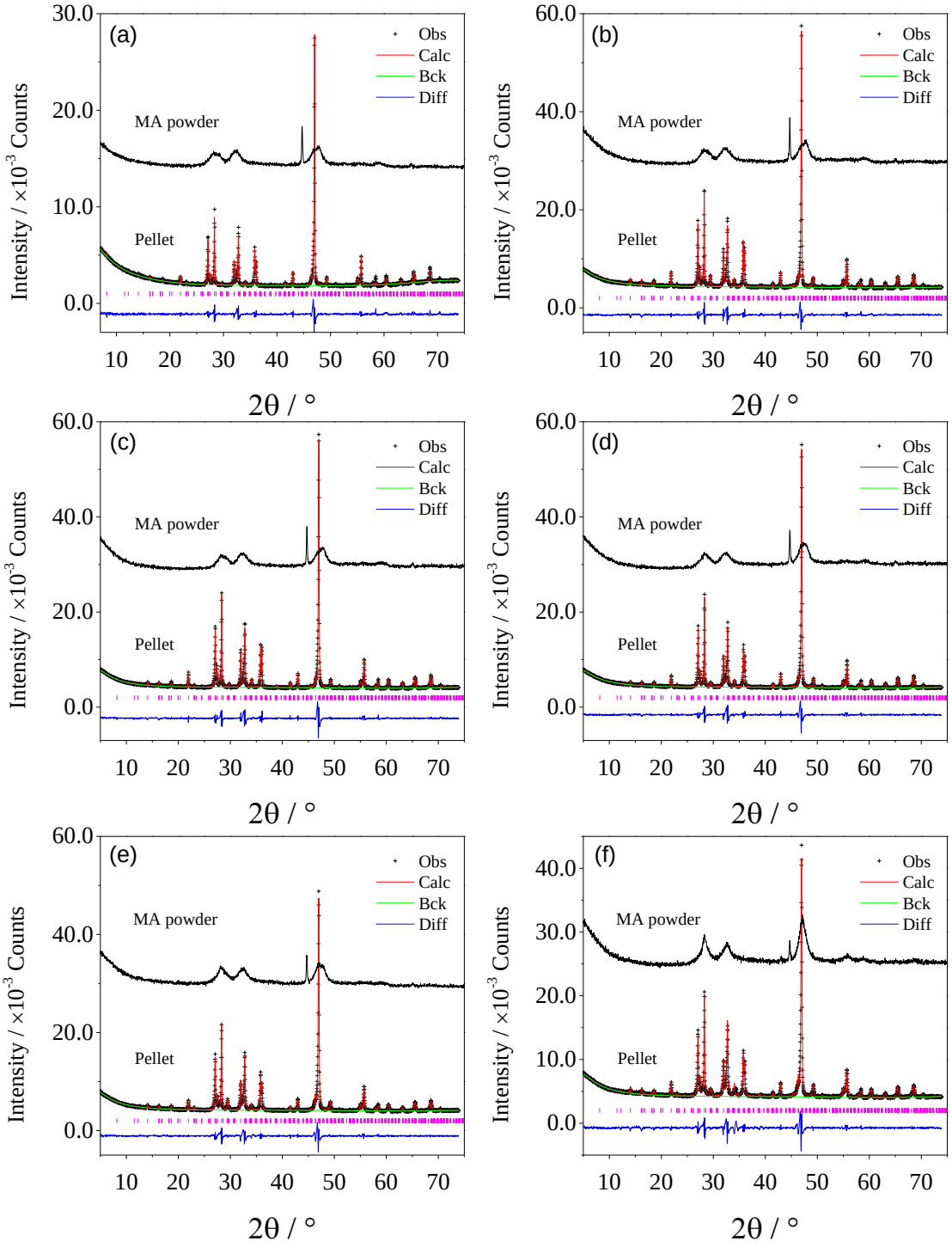

Figure 5.19 Observed (crosses), calculated (red line) and difference (blue line) profiles for $Cu_5Fe_{1-x}Mn_xS_4$ from Le Bail refinement using XRD data: (a) x = 0.01 (R_{wp} = 4.21 %), (b) x = 0.02 (R_{wp} = 3.97 %), (c) x = 0.03 (R_{wp} = 4.29 %), (d) x = 0.04 (R_{wp} = 3.96 %), (e) x = 0.05 (R_{wp} = 3.77 %), (f) x = 0.10 (R_{wp} = 4.15 %). Reflection positions are indicated by tick marks.

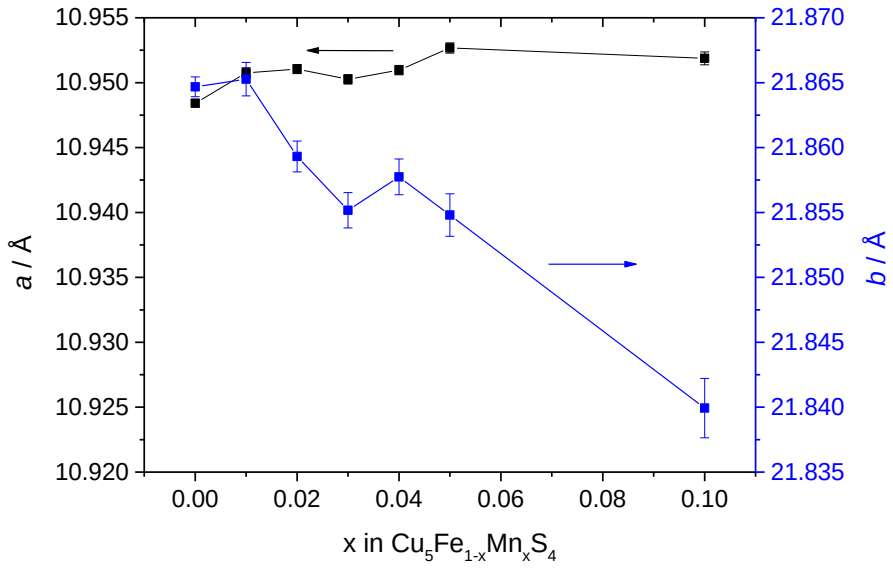

Figure 5.20 Lattice parameters of $Cu_5Fe_{1-x}Mn_xS_4$ determined from Le Bail refinement using XRD data as a function of manganese content. Error bars are shown.

5.4.2.1 SEM/EDX analysis

Scanning electron micrographs were taken and EDX analysis was carried out using an Environmental Scanning Electron Microscope (ESEM), as described in Section 2.8. Two sites per consolidated sample were investigated, one at the centre of the pellet and one closer to the edge. The elemental analysis for each site was calculated from the sum spectrum of three scans, acquired over at least 300 s with an ×100 magnification. The experimental compositions determined on both sites were similar and subsequently averaged. The scanning electron micrograph and the corresponding elemental maps for $Cu_5Fe_{0.95}Mn_{0.05}S_4$, indicate a homogeneous distribution of constituent elements. The experimental compositions determined

Table 5.6 Composition of the $Cu_5Fe_{1-x}Mn_xS_4$ samples determined by EDX analysis. Standard deviations are given in brackets.

x	Experimental composition	x	Experimental composition
0	$Cu_{4.89(2)}Fe_{1.00(1)}S_{4.11(3)}$	0.04	$Cu_{4.91(3)}Fe_{0.97(1)}Mn_{0.042(4)}S_{4.08(3)}$
0.01	$Cu_{4.91(3)}Fe_{1.00(1)}Mn_{0.016(4)}S_{4.08(3)}$	0.05	$Cu_{4.93(3)}Fe_{0.94(1)}Mn_{0.044(5)}S_{4.09(3)}$
0.02	$Cu_{4.87(3)}Fe_{0.98(1)}Mn_{0.019(5)}S_{4.13(4)}$	0.10	$Cu_{4.88(3)}Fe_{0.91(1)}Mn_{0.107(5)}S_{4.10(3)}$
0.03	$Cu_{4.90(3)}Fe_{0.97(1)}Mn_{0.042(4)}S_{4.09(3)}$	-	-

from EDX analysis, Table 5.6, determined on consolidated ingots are in good agreement with the initial composition of the reaction mixtures, suggesting that no significant loss of elements has taken place during the synthesis and consolidation process. The EDX spectra of Cu_5FeS_4 and $Cu_5Fe_{0.95}Mn_{0.05}S_4$ are given in Figure 5.21. Because of the relatively large uncertainty arising from such elemental analysis, it is not possible to exclude the possibility of sulphur volatilisation occurring during the consolidation step. However, it is important to notice that the quantity of iron remains very close to the nominal composition and the material does not appear to be iron-doped as a result of ball milling in stainless steel.

5.4.3 Thermoelectric performance

5.4.3.1 Electrical properties

Electrical property measurements were carried out for the bornite series with composition $Cu_5Fe_{1-x}Mn_xS_4$ (x = 0; 0.01; 0.02; 0.03; 0.04; 0.05 and 0.10). Because bornite is a very brittle material, cutting rectangular shapes using a laboratory-scale diamond saw may result in crack formation and chipping around the edges. To circumvent this issue, the electrical properties

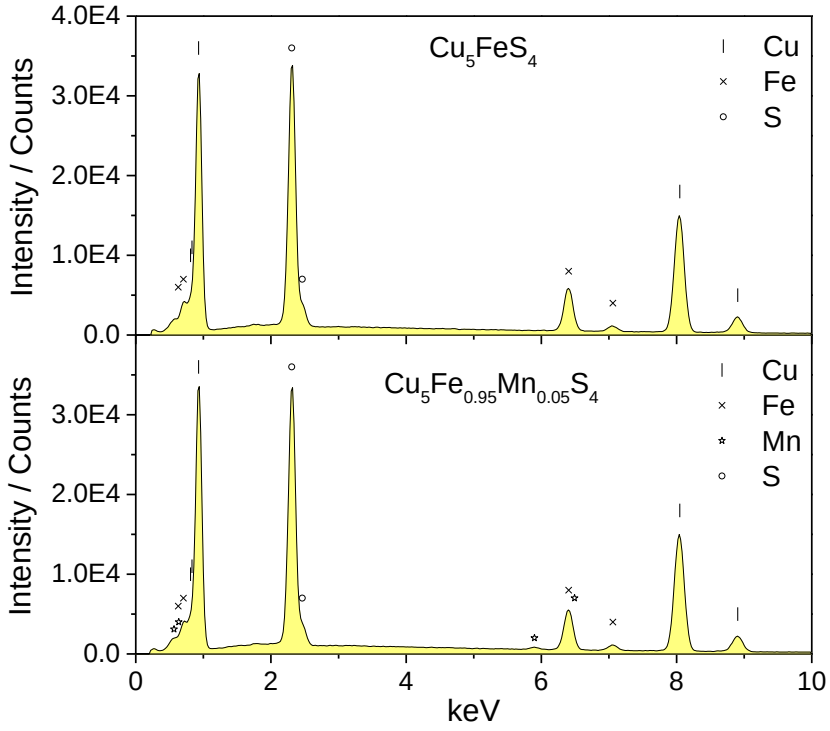

Figure 5.21 EDX spectra for Cu_5FeS_4 and $Cu_5Fe_{0.95}Mn_{0.05}S_4$ acquired at the centre of the consolidated pellets.

were directly measured on disc samples using an adapted sample holder. The temperature dependence of the electrical properties of $Cu_5Fe_{1-x}Mn_xS_4$, Figure 5.22, measured over the temperature range $310 \leq T / K \leq 580$ indicate that all samples behave as semiconductors with a large *p*-type Seebeck coefficient, and exhibit an anomaly at the temperature at which the transition from the orthorhombic to the intermediate cubic phase occurs, Section 1.6.1.2. The electrical resistivity of bornite follows an Arrhenius law, Figure 5.23, in the low-temperature phase, $300 \leq T / K \leq 416$, and in the high-temperature phase, $520 \leq T / K \leq 580$. The determined activation energies, $E_a \approx 0.04$ eV and $E_a' \approx 0.1$ eV respectively for the low and high-temperature

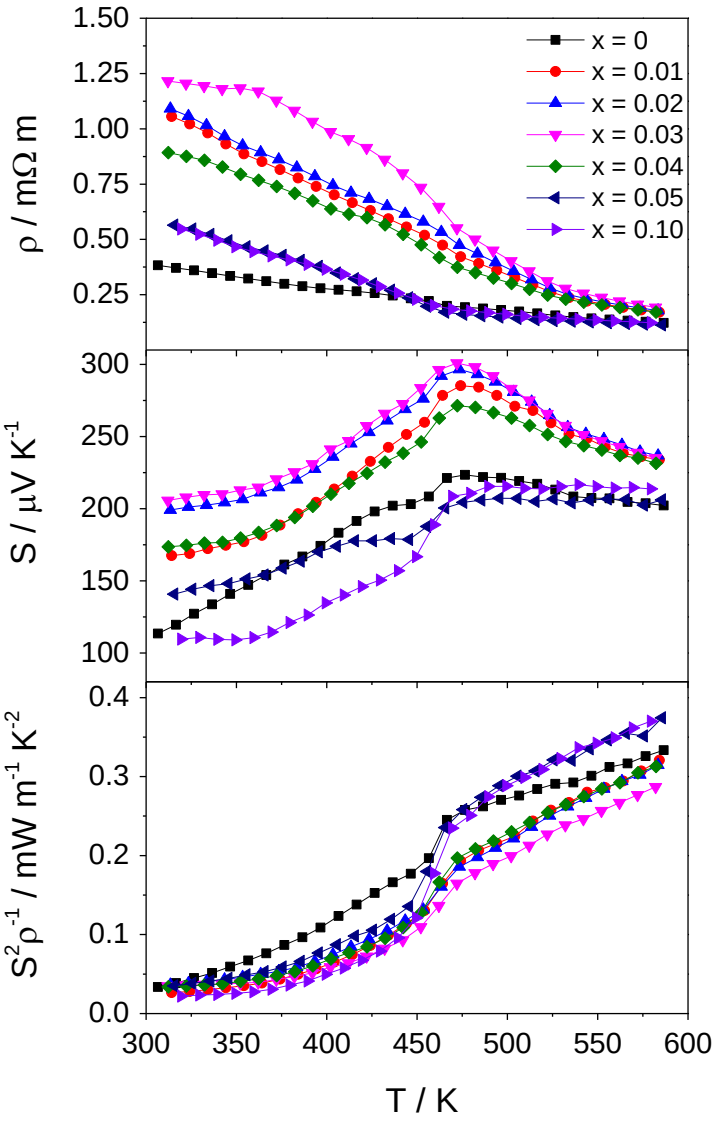

Figure 5.22 From top to bottom: Temperature dependence of the electrical resistivity, the Seebeck coefficient and the resulting power factor for $Cu_5Fe_{1-x}Mn_xS_4$.

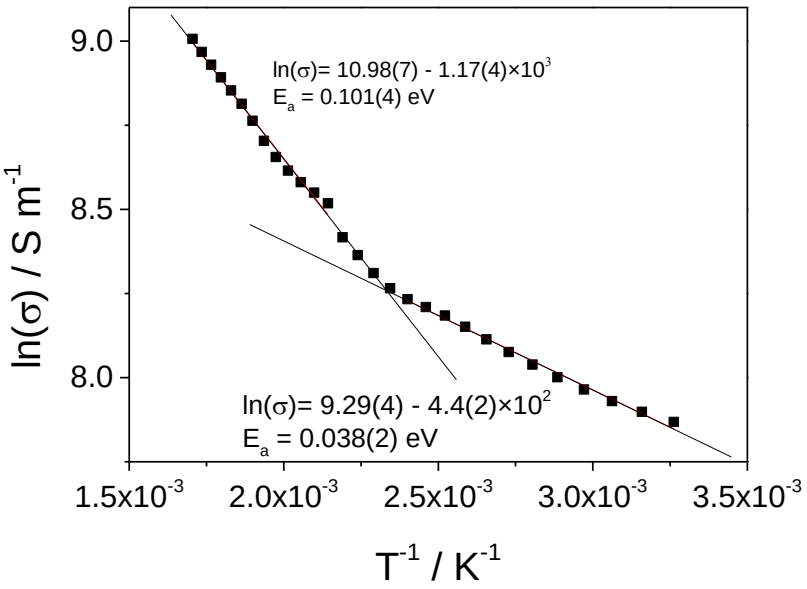

Figure 5.23 Arrhenius behaviour of Cu_5FeS_4 and activation energy determination for the low-temperature ($E_a \approx 0.04$ eV) and high-temperature ($E_a' \approx 0.1$ eV) phases.

phases, are similar to those reported previously for stoichiometric bornite with $E_a \approx 0.1$ eV.[253] However, given that diffuse reflectance measurements indicate that the optical band gap of bornite is of the order of 1 eV,[283, 284] these activation energies are likely to originate from the promotion of extrinsic charge carriers. The maximum Seebeck coefficient of $Cu_5Fe_{1-x}Mn_xS_4$ is reached at *ca*. 470 K, corresponding to the first phase transition temperature, with the highest value, S = 300 μV K^{-1}, being obtained for x = 0.03. This corresponds to an increase of about 35 % over the un-doped bornite. Similarly, the highest electrical resistivity increases with the level of manganese substitution up to a maximum for x = 0.03. It has been established that the oxidation state of iron in bornite is Fe(III),[286] hence substitution of Fe(III) with Mn(II) should result in an increase in the hole concentration. However, it is clear from Figure 5.24 that both the Seebeck coefficient and electrical resistivity increase up to x = 0.03 before decreasing again. This behaviour is much more pronounced in the low-temperature ordered phase and the compositional dependence of the electrical transport properties appears to show an anomaly at a similar composition to that observed for the lattice parameters of the orthorhombic phase, Figure 5.20. This suggests that manganese may occupy different crystallographic sites depending on the substitution levels. There are several atom sites available to accommodate manganese, with copper and iron being located in similar tetrahedral sites and the structure

containing additional tetrahedral vacancies. The cation distribution of $Cu_5Fe_{1-x}Mn_xS_4$, however, cannot be determined using powder X-ray diffraction only. As demonstrated by the high-resolution transmission electron spectroscopy studies by Ding et al.,[113] it is likely that the low-temperature phase of bornite consists of an heterogeneous combination of different phases. This is supported by the X-ray diffraction patterns, Figure 5.18 and Figure 5.19, in which a shoulder is consistently observed at 2θ positions corresponding to a cubic phase. The compositional dependence, as a function of manganese substitution of the electrical properties

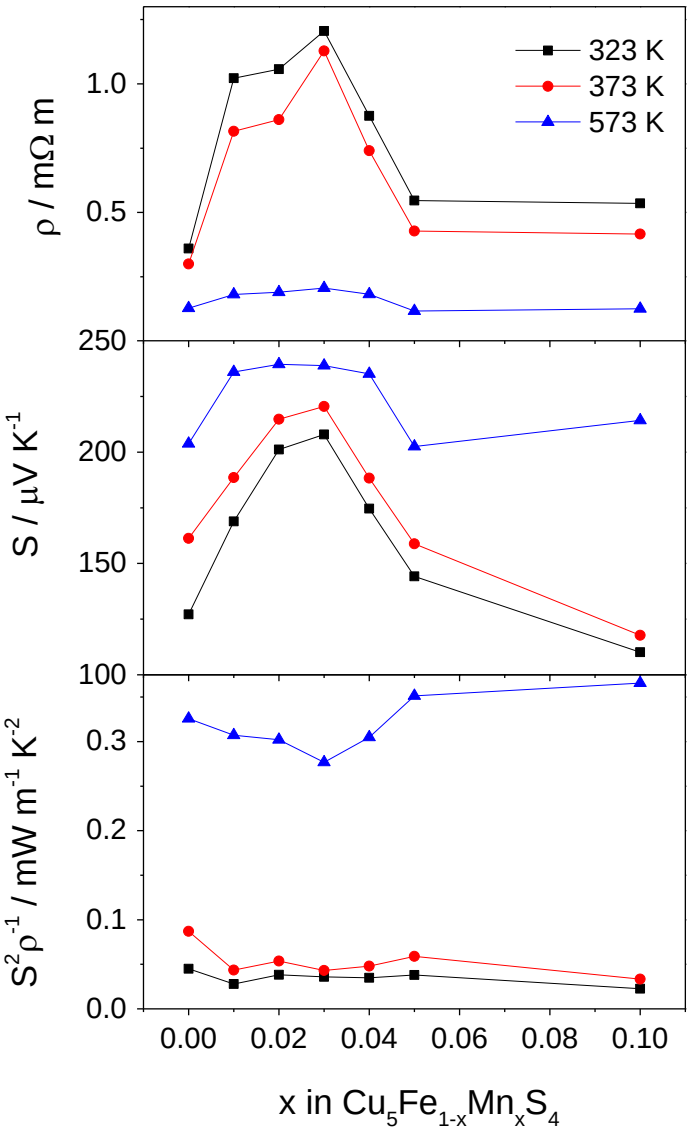

Figure 5.24 Transport properties of $Cu_5Fe_{1-x}Mn_xS_4$ at 323, 373 and 573 K, as a function of the manganese substitution level, from top to bottom: electrical resistivity, Seebeck coefficient and power factor.

of $Cu_5Fe_{1-x}Mn_xS_4$ at 3 selected temperatures, 323 K, 373 K and 573 K, is given in Figure 5.24. In the temperature region (above 530 K) where the disordered 1*a* cubic phase exists, the maximum in ρ and S is substantially reduced, suggesting that the absence of an ordered superstructure has a significant effect on the band structure of bornite. This is supported by the marked change in the magnitude of the optical band gap between the low-temperature (0.86 eV) and the high-temperature (1.25 eV) phases[284], and between the values of electronic band gaps determined in Figure 5.23. The calculated power factor of $Cu_5Fe_{1-x}Mn_xS_4$ varies only slightly across the series because of the balance between variations in Seebeck coefficient and electrical resistivity. The power factor of the un-substituted bornite reaches $S^2\rho^{-1} = 0.33$ mW m^{-1} K^{-2} at 580 K and a small improvement is observed for $Cu_5Fe_{0.95}Mn_{0.05}S_4$ and $Cu_5Fe_{0.90}Mn_{0.10}S_4$ with $S^2\rho^{-1} = 0.37$ mW m^{-1} K^{-2} for both phases at the same temperature.

5.4.3.2 Thermal transport properties

The thermal conductivity of $Cu_5Fe_{1-x}Mn_xS_4$ (x = 0; 0.01; 0.02; 0.03; 0.04; 0.05 and 0.10) was measured on discs in the direction parallel to the pressing. Unlike layered samples, the bornite pellets do not show any sign of preferred orientation. The first-order phase transitions, occurring in the temperature range $473 \leq T / K \leq 543$, involve latent heat. Therefore, the specific heat calculated using the Dulong-Petit law was preferred to side-by-side measurements using a reference material. Calculation of the total thermal conductivity was carried out using $Cp = 0.497$ J K^{-1} g^{-1} and the measured thermal diffusivity, α, given in Figure I.1 (Appendix I). The temperature dependence of the total thermal conductivity and its evolution as a function of manganese substitution at three selected temperatures are given in Figure 5.25. In all samples, changes in the slope of the thermal conductivity occur at temperatures corresponding to phase transitions. Above the first transition temperature, a large decrease in the thermal conductivity results in extremely low values at 543 K with a minimum of $\kappa \approx 0.28$ W m^{-1} K^{-1} for $Cu_5Fe_{0.97}Mn_{0.03}S_4$. After the intermediate-to-high-temperature phase transition, the thermal conductivity of the series reaches values of the order of $\kappa \approx 0.4$ W m^{-1} K^{-1} which is about 70 % of the thermal conductivity of water.[287] Such a low magnitude of the thermal conductivity could in part be attributed to the complete disordering of the cation sublattice of the cubic phase, and is comparable to that found for the ‘‘phonon-liquid electron-crystal’’ (PLEC) $Cu_{2-x}S$.[34]

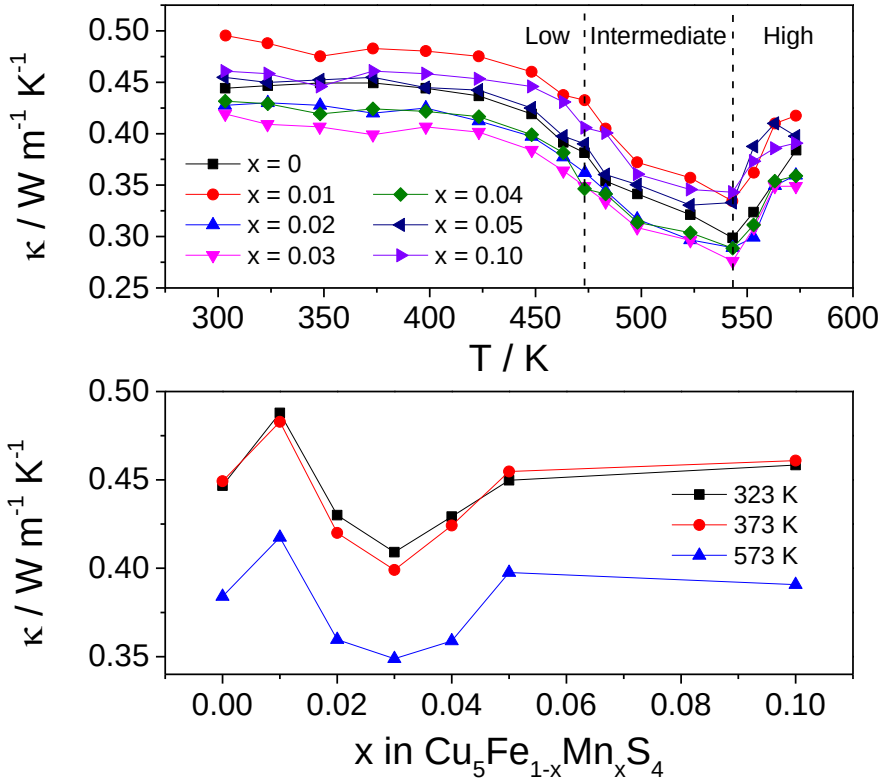

Figure 5.25 Thermal transport properties of $Cu_5Fe_{1-x}Mn_xS_4$: Temperature dependence of the thermal conductivity (top) and compositional dependence of the thermal conductivity (bottom) at 323 K, 373 K and 573 K.

In the low-temperature phase region, the thermal conductivity is comparable to that of the high temperature cubic phase. This is surprising owing to the long-range ordering of vacancies in the low-temperature superstructure and the high level of disorder in the cubic phase. However, the complex microstructure of bornite in the low-temperature phase may serve to reduce the thermal conductivity, with the co-existence of domains with different superstructures,[113] or twinning domains.[106, 107] Manganese substitution up to x = 0.03 causes a drop in thermal conductivity that can be explained in term of additional disorder created by the substitution of iron by manganese. Higher substitution levels lead to an increase in the thermal conductivity that cannot be solely explained by an increased contribution from the charge carriers. Lattice and electronic contributions to the thermal conductivity, Figure I.2 (Appendix I), have been determined using the Wiedemann-Franz law with $L = 2.44 \times 10^{-8}$ W Ω K^{-2}. The compositional evolution of the lattice component of the thermal conductivity, κ_{lat}, shows an anomaly at x =

0.01 and a change of behaviour at x ≥ 0.04. These compositions are similar to those corresponding to anomalies in the lattice parameters, Figure 5.20, suggesting that the location of Mn in the crystal structure may change as x increases.

5.4.3.3 Figure of merit

As a result of the ultralow thermal conductivity, manganese-doped bornite, $Cu_5Fe_{1-x}Mn_xS_4$, shows excellent ZT values at temperatures above the first structural phase transition at *ca*. 460 K, Figure 5.26, with a maximum of ZT = 0.55 being reached at 543 K for the un-substituted bornite. This value is higher than the highest ZT previously reported for bornite, ZT ≈ 0.4 at 673 K, prepared by conventional solid-state reaction.[253] In the same study, the highest ZT reported for bornite derivative was ZT ≈ 0.52 at 700 K for $Cu_{5.04}Fe_{0.96}S_4$.

Low levels of manganese substitution lead to a decrease in the thermal conductivity. However, the power factors have also been reduced by the increased electrical resistivity. Higher substitution levels produce an increase in both power factor and thermal conductivity. As a result, the figure of merit remains comparable, within experimental error, with that of un-substituted bornite across the whole manganese-doped series. The ZT remains above 0.5 between 523 K and the maximum temperature investigated of 573 K. This performance is promising for waste-heat recovery, and also compares favourably with other tellurium and

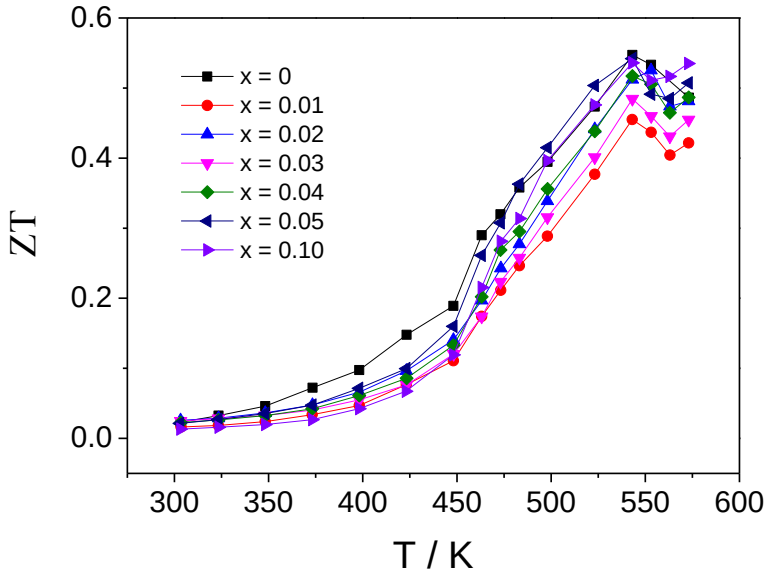

Figure 5.26 Temperature dependence of the figure of merit, ZT, for $Cu_5Fe_{1-x}Mn_xS_4$.

selenium-free thermoelectric materials, including $Ti_{1+x}S_2$,[157] $LaGd_{1.03}S_3$,[89] or $Cu_4Mo_6S_8$ [210] that exhibit ZT = 0.4 at higher temperatures.

5.4.4 Stability of $Cu_5Fe_{1-x}Mn_xS_4$

5.4.4.1 Thermogravimetric analysis

Thermogravimetric analysis was carried out in air over the temperature range 290 ≤ T / K ≤ 773 and under a flowing N_2 atmosphere over the temperature range 295 ≤ T / K ≤ 973 K on un-doped bornite powder, Figure 5.27. Under an inert atmosphere, Cu_5FeS_4 begins to lose

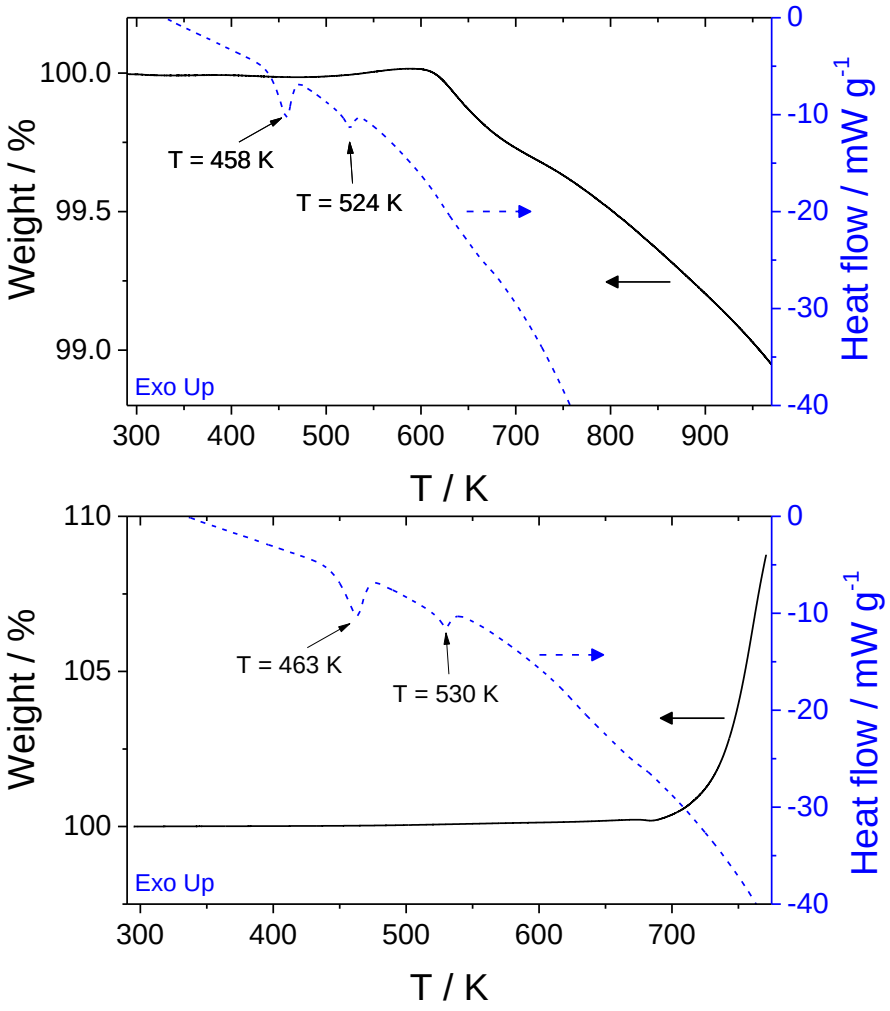

Figure 5.27 Combined TGA/DSC data for Cu_5FeS_4 powder under a nitrogen flow (top) and in air (bottom), showing the temperature dependence of the weight percentage of the sample and the heat flow.

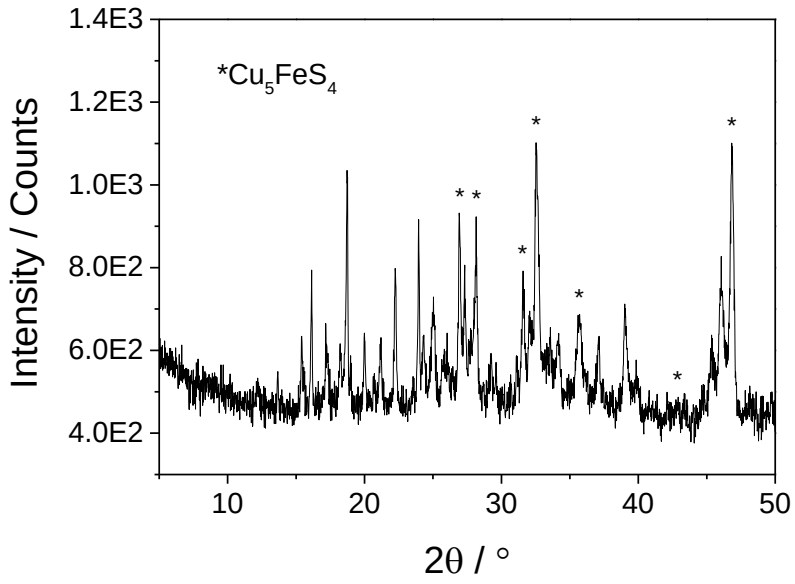

Figure 5.28 Powder X-ray diffraction data for bornite after the TGA/DSC experiment in air. Peaks with no marks correspond to a mixture of copper sulphates, copper oxides and copper sulphides.

weight above *ca*. 600 K, consistent with sulphur loss. This may result in exsolution of chalcopyrite ($CuFeS_2$) or $Cu_{2-x}S$ upon cooling, a process which has been reported to occur in non-stoichiometric bornites when cooling from high temperatures.[288] Under an atmosphere of air, the onset of oxidation occurs at *ca*. 673 K. The data suggest a maximum operating temperature of *ca*. 600 K in the absence of any protective coating. The DSC measurements, Figure 5.27, show two transitions at *ca*. 460 K and 530 K, corresponding to the phase transitions. These values are consistent with previous reports[109, 111] and correspond to the transition from the low-temperature orthorhombic ($2a \times 4a \times 2a$ supercell)[106] to low intermediate bornite ($2a$ supercell)[108] at 460 K, and from the intermediate to the high temperature cubic bornite ($1a$ unit cell)[107] at 530 K. Powder X-ray diffraction data on powders after the TGA/DSC measurement in air, Figure 5.28, show the extent of the degradation that the sample suffers above 700 K, with the formation of a significant level of copper-containing impurities.

5.4.4.2 Repeatability and $Cu_{2-x}S$ exsolution

The electrical properties of two samples, Cu_5FeS_4 and $Cu_5Fe_{0.96}Mn_{0.04}S_4$, were measured repeatedly up to 580 K over a period of 10 weeks, Figure J.1 and J.2 (Appendix J). The power factor remains unchanged, within experimental error, above the first phase transition temperature when repeating measurements on the same ingot. This shows that the electrical properties of bornite do not degrade with time over a period of time of a few weeks. However, when the measurement temperature is extended to 890 K, well above the temperature at which sulphur loss starts to occur, the samples deteriorate markedly and their initial properties cannot be recovered, Figure 5.29. Powder X-ray diffraction data acquired on the pellet after the third measurement, carried out over the temperature range $300 \leq T / K \leq 890$ K, Figure J.3, confirm that exsolution of $Cu_{2-x}S$ occurs at high temperatures. Consequently, the Seebeck coefficient becomes negative for $T \leq 600$ K and the electrical resistivity is markedly increased. The temperature dependence of the Seebeck coefficient and the large electrical resistivity is

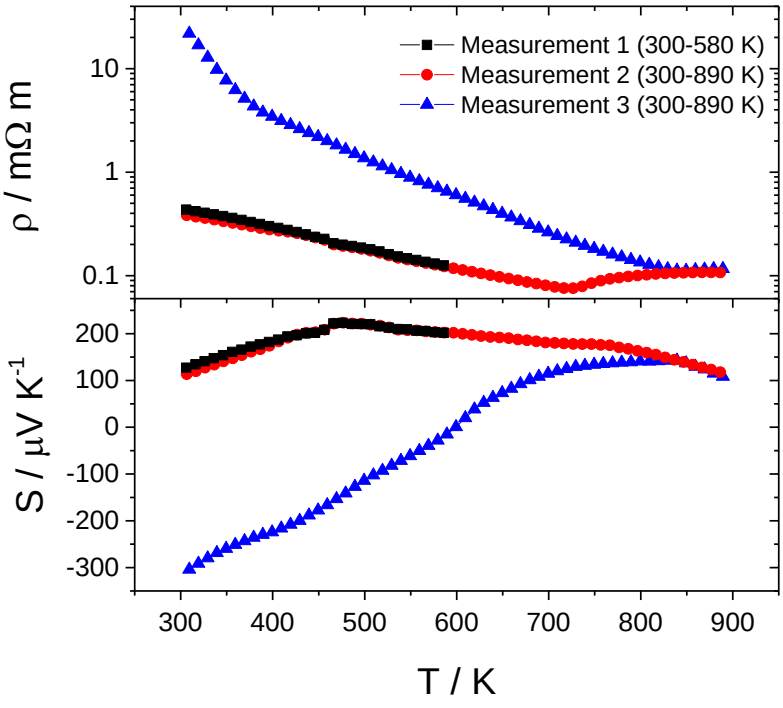

Figure 5.29 Repeated measurements of the temperature dependence of the electrical resistivity (top) and the Seebeck coefficient (bottom) for one ingot of Cu_5FeS_4. The first measurement was carried out over the temperature range $300 \leq T / K \leq 580$, whilst the second and third measurements were carried out back-to-back, up to 890 K.

reminiscent of bornite prepared by conventional solid-state reaction.[253] The poorer performance measured in conventional bornite compared with the mechanically alloyed samples may therefore be explained by the presence of exsolved $Cu_{2-x}S$.

5.5 Conclusions

Two alternative doping techniques, involving manganese substitution and the addition of excess copper, have been investigated in an effort to improve the thermoelectric performance of tetrahedrite (ZT = 0.4 at 573 K). Manganese substitution was successful and temperature dependent neutron diffraction studies confirmed the position of Mn in the structure as well as giving information on the unusual dynamics of Cu(2) in the trigonal planar position. The high anisotropy in the thermal displacement of Cu(2) may be associated with the low thermal conductivity of tetrahedrite. Substitution of Cu(1) for Mn provides a means of controlling the filling of the valence band ultimately allowing the electrical properties of the material to be tuned. Although the power factor was reduced in comparison with un-doped tetrahedrite, the decrease in both electronic and lattice contributions to the thermal conductivity contributed to an overall increase in the figure of merit, ZT, with a maximum value being reached for $Cu_{11}MnSb_4S_{13}$ (ZT = 0.56 at 573 K).

The addition of excess copper in tetrahedrite leads to the formation of two phases, a Cu-rich and a Cu-poor phase, that coalesce into a stable single phase at 553 K and 493 K on heating for $Cu_{12.3}Sb_4S_{13}$ and $Cu_{14}Sb_4S_{13}$, respectively.[278] However, changes in the electrical and thermal properties of $Cu_{12+y}Sb_4S_{13}$ (y = 0.3; 1; 1.5; 2) were observed over the temperature range $380 \leq T / K \leq 410$, with the lowest and highest transition temperatures observed for $Cu_{12.3}Sb_4S_{13}$ and $Cu_{14}Sb_4S_{13}$, respectively. Therefore, these changes of behaviour may be more related to a change from stationary to mobile copper atoms rather than the coalescence of the Cu-poor and Cu-rich phases into a single phase. As with manganese substitution, the addition of excess copper enables the tuning of the electrical and thermal properties and the reduction of the charge carrier concentration with increasing Cu excess leads to a large reduction in the electronic contribution to the thermal conductivity and an increase in the Seebeck coefficient. The highest ZT is observed for $Cu_{12+y}Sb_4S_{13}$ (y = 1.5 and 2) with 0.62 at 573 K.

A new synthetic path for the production of bornite was developed. This methodology involves mechanical alloying of the elemental precursors, followed by hot-pressing, and offers many advantages over high-temperature solid-state reactions, as it is faster, safer and readily scalable. Additionally, ball milling leads to a material with a superior thermoelectric performance (ZT = 0.55 at 543 K) when compared to conventionally prepared samples (ZT ≈ 0.4 at 573 K). The thermoelectric properties of bornite are degraded above 600 K because of sulphur loss. However, the material is stable up to 580 K when measured repeatedly over a period of a few weeks. Manganese substitution was successfully attempted and a solubility limit of $Cu_5Fe_{0.9}Mn_{0.1}S_4$ established; however, no substantial improvement in the thermoelectric performance was observed with manganese substitution. Structural phase transitions have been found to have a marked effect on the thermoelectric properties of bornite. Such variations have been observed in other thermoelectric materials such as the structurally-related $Cu_{2-x}Se$, that exhibits a change of behaviour of the thermal conductivities at *ca*. 400 K, the temperature at which $Cu_{2-x}Se$ undergoes a phase transition from α-$Cu_{2-x}Se$ to β-$Cu_{2-x}Se$.[289]

Overall, the thermoelectric performance of two families of minerals, tetrahedrite and bornite, have been described in this chapter. Both are particularly attractive because of the low cost, non-toxicity and widespread occurrence of constituting elements. However, binary copper sulphides are known to suffer major intrinsic issues that prevent their large scale utilisation as thermoelectric materials, such as copper mobility.[35] The change of electrical and thermal behaviours at temperatures that may be related to a change from stationary to mobile copper in Cu-enriched tetrahedrites and the close structural relationship between the high-temperature phase of bornite and $Cu_{2-x}S$ raise the question about copper ion mobility and its involvement in the low thermal conductivity. To investigate this, Qiu *et al*. have measured repeatedly the electrical resistivity of bornite at 573 K under a current density of 12 A cm^{-2}, and compared with Cu_2S.[253] Results suggest that copper ion migration in bornite is largely suppressed by the pinning effect of immobile iron atoms. Similar experiments, combined with ionic conductivity measurements, could be carried out on the Mn-doped bornite series and Cu-enriched tetrahedrites in order to inspect the combined pinning effect of manganese and iron in the former and the extent of the copper mobility in the latter.

Chapter 6 - Conclusions

6.1 Titanium disulphide derivatives

6.1.1 Cobalt intercalation in titanium disulphide

The work on titanium disulphide derivatives involved a study of the structural and physical property changes associated with the intercalation of cobalt within the van der Waals' gap of TiS_2. A combination of powder X-ray and neutron diffraction experiments has established the compositional dependence of the structural arrangements in Co_xTiS_2 ($0 \leq x \leq 0.75$). For cobalt intercalation levels of $x < 1/3$, Co atoms are found to randomly occupy octahedral sites within the van der Waals' gap. At intermediate intercalation levels, the ordering of Co atoms and vacancies leads to the formation of three superstructure types, monoclinic M_5S_8 ($x = 0.25$), trigonal M_2S_3 ($x = 1/3$) and monoclinic M_3S_4 ($x = 0.5$). A second disordered phase is found at high intercalation levels, $x \geq 2/3$, where Co atoms are randomly distributed but occupy both octahedral and tetrahedral interstitial sites. Low-temperature neutron diffraction, magnetic susceptibility measurements and muon spectroscopy experiments were combined in order to study the magnetic properties of Co_xTiS_2 ($0 \leq x \leq 0.75$). No long-range structural arrangements could be observed; however, muon spectroscopy brought strong evidence for short-range ordering in Co_xTiS_2 ($x = 0.25$ and 0.50). The effective magnetic moments, μ_{eff}, of Co in Co_xTiS_2 ($x < 1/3$) are consistent with Co being in a +2 oxidation state, while for higher intercalation levels, μ_{eff} decreases, indicating and increasing degree of electron delocalisation. The single-phase region was determined to lie in the range $2/3 \leq x \leq 0.75$ from the presence of a magnetic impurity in $Co_{0.75}TiS_2$. Well-densified samples were obtained from the hot-pressing of ball milled powders of Co_xTiS_2 prepared by solid-state reaction. As a result of the electron transfer from Co^{2+} to the conduction band of TiS_2, the electrical resistivity can be reduced systematically and the thermoelectric performance for Co_xTiS_2 with low intercalation levels ($x \leq 0.10$) is improved compared with pristine TiS_2. Additionally, the thermal conductivity is systematically reduced, attributed to an increase in phonon scattering from the higher level of disorder in the van der Waals' gap with low levels of cobalt intercalation. A 25 % increase in

the figure of merit over the whole temperature range investigated is achieved for Co_xTiS_2 ($0.04 \leq x \leq 0.08$), with a maximum value ZT = 0.3 at 573 K in the in-plane direction. Such a figure of merit at 573 K is one of the highest reported for a *n*-type sulphide, especially without involving heavy elements such as Bi or Pb. Comparatively, a figure of merit of 0.3 was reported for $Cu_{0.02}TiS_2$ and $Ag_{0.02}TiS_2$ consolidated by SPS at 600 K and 540 K, respectively.[156, 160] Such a thermoelectric performance is highly promising for large-scale application because of the low-cost and low density (d = 3.24 g cm^{-3}) of TiS_2 derivatives. Materials with higher performance have been reported for several *n*-type materials but involved higher temperature and heavy elements such as ZT ≥ 0.4 at 950 K for $Cu_4Mo_6S_8$[210] and $LaGd_{1.02}S_3$[89], and ZT ≥ 1 for doped-Bi_2S_3 at 923 K.[79]

6.1.2 Molybdenum substitution in titanium disulphide

The substitution of titanium by molybdenum, $Mo_xTi_{1-x}S_2$ ($0 \leq x \leq 0.09$), has been successful in increasing the in-plane power factor in hot-pressed samples. However, substitution has a detrimental effect on samples consolidated by SPS. The effect of substitution is not systematic and powder X-ray diffraction data reveal trace amounts of MoS_2 in $Mo_xTi_{1-x}S_2$ for substitution levels as low as x = 0.03. The effect of molybdenum substitution is highly dependent on the consolidation of the sample, indicating that molybdenum doping might be closely related to the level of Ti self-intercalation. In hot-pressed samples, both the electrical resistivity and the absolute value of the Seebeck coefficient are reduced upon substitution, resulting in a power factor 25 % higher than that of TiS_2 for $Mo_xTi_{1-x}S_2$ (x = 0.03; 0.04), reaching $S^2\rho \approx 1.5$ mW m^{-1} K^{-2} and $S^2\rho \approx 1.2$ mW m^{-1} K^{-2} at 323 K and 573 K, respectively. The power factor reported for TiS_2, $S^2\rho^{-1}$ = 2.1 mW m^{-1} K^{-2} at 323 K, achieved for ball milled samples consolidated by SPS, is the highest reported for $Ti_{1+\gamma}S_2$.[156-161, 194] No significant changes were observed in the cross-plane thermal conductivity upon molybdenum substitution.

6.1.3 TiS_2 nanoparticles and nanocomposites

Following the excellent thermoelectric properties of TiS_2 derivatives, nanoparticles were synthesised using a scalable solution-based route, involving the reaction between S dissolved in a high boiling point solvent and $TiCl_4$. Control over the morphology of the particles was

achieved and a cold-pressed pellet of TiS_2 nanoflakes was produced. Measurements of the Seebeck coefficient are consistent with a stoichiometry $Ti_{1+x}S_2$ where x lies within the range $0.02 \leq x \leq 0.03$. Much work remains to be done on TiS_2 nanoparticles as only the Seebeck coefficient could be measured.

Bulk titanium disulphide was ball milled with nanoparticles of titanium oxide and carbon nanotubes. A 12 % increase in the figure of merit at 573 K, ZT = 0.28, was observed for the nanocomposite with 0.5 vol% of nano-TiO_2 in the in-plane direction. The decrease in both the electrical resistivity and thermal conductivity with the addition of 0.5 vol% of nano-TiO_2 is consistent with an increase in the charge carrier concentration. Titanium dioxide, allowing for a small level of non-stoichiometry, could be responsible for titanium intercalation within the van der Waals' gap of TiS_2. This is supported by the increase in the *c* lattice parameter for 0.5 vol% and 1.0 vol% of nano-TiO_2. While compositing with nano-TiO_2 does not yield any significant changes in the thermal conductivity, the addition of carbon nanotubes causes a systematic decrease in thermal conductivity. Nevertheless, the poor electrical performance of TiS_2/CNTs samples prevents any improvement to be made on the figure of merit. The longer and faster ball milling conditions used in the nanocomposite series have led to an improvement in the cross-plane properties and the highest figure of merit ZT = 0.28 at 573 K is observed for TiS_2.

6.1.4 Further work

Further work on TiS_2 derivatives should include a systematic investigation of the effect of ball milling and spark plasma sintering on the thermoelectric properties of Co_xTiS_2. Measurements of the in-plane thermal conductivity on $Mo_xTi_{1-x}S_2$ ($x \leq 0.1$) should be carried out along with SEM/TEM investigations and Hall effect measurements in order to determine the solubility limit of $Mo_xTi_{1-x}S_2$ and the impact of molybdenum substitution on the charge carrier concentration and mobility. Larger batches of TiS_2 nanoparticles with controlled morphologies should be produced with a more suitable apparatus and consolidated using a hot-press or a SPS apparatus. The problems relative to the reaction between adsorbed solvent and TiS_2 during the measurements should be addressed. As the electrical properties of carbon nanotubes can vary

greatly with their size and synthesis conditions, more samples should be prepared and measured with CNTs of variable sizes. Nanocompositing TiS_2 with TiS_2 nanoflakes should also be investigated.

6.2 Copper-containing ternary sulphides

6.2.1 Manganese substitution in tetrahedrite

Recently, tetrahedrites minerals have attracted a lot of interest because of the low thermal conductivity, attributed to the large unit cell and anharmonic rattling of the Cu(2) atom. In this work, two strategies have been attempted in order to improve the thermoelectric response of *p*-type tetrahedrite, manganese substitution and copper enrichment. Manganese substitution was successful and neutron diffraction analysis unequivocally located Mn on the Cu(1) site in tetrahedral position. Control over the valence band filling of tetrahedrite via Mn substitution has led to a dramatic reduction in the thermal conductivity, with $\kappa \approx 0.75$ W m^{-1} K^{-1} measured for $Cu_{11}MnSb_4S_{13}$ over the temperature range $303 \leq T / K \leq 573$ through a reduction in both electronic and lattice contributions. A maximum figure of merit, ZT = 0.56, was obtained for $Cu_{11}MnSb_4S_{13}$ at 573 K.

6.2.2 Copper-enriched tetrahedrite

The thermoelectric properties of copper-enriched tetrahedrite $Cu_{12+y}Sb_4S_{13}$ (y = 0.3; 1; 1.5; 2) have been investigated. At room temperature, $Cu_{12+y}Sb_4S_{13}$ exists as a mixture of a Cu-poor and a Cu-rich phase that coalesce into a single phase over the temperature range $493 \leq T / K \leq 553$, depending on the amount of excess copper. Dramatic changes in the behaviour of the electrical and thermal properties of $Cu_{12+y}Sb_4S_{13}$ (y = 0.3; 1; 1.5; 2) were observed at a temperature lower than the phase transition temperature and are more likely to be related to a change from stationary to mobile copper atoms. Large reductions in the thermal conductivity and the increase in Seebeck coefficient with Cu excess leads to a large improvement in the figure of merit with ZT = 0.62 at 573 K for $Cu_{12+y}Sb_4S_{13}$ (y = 1.5 and 2).

6.2.3 Manganese substitution in bornite

Bornite has been identified recently as a potential *p*-type thermoelectric material with a high figure of merit ZT ≈ 0.4 at 573 K.[253] In this work, manganese-doped bornite was synthesised using mechanical alloying for the first time, a synthetic route that is suitable for large scale production. The thermoelectric properties of mechanically alloyed bornite are substantially improved over those of bornite prepared by conventional solid-state reaction with a maximum ZT of 0.55 at 543 K. The solubility limit of $Cu_5Fe_{1-x}Mn_xS_4$ was determined to be x = 0.1 using powder X-ray diffraction data but no substantial improvements in the thermoelectric properties were obtained. The stability of the consolidated samples was tested and the materials are found to be stable up to 580 K with no degradation of the electrical properties over a few weeks. However, evidences for sulphur loss were found at temperatures above 600 K and $Cu_{2-x}S$ exsolution occurs, permanently degrading the thermoelectric properties.

6.2.4 Performance comparison and further work

The thermoelectric performance of *p*-type manganese-doped tetrahedrite, $Cu_{11}MnSb_4S_{13}$, and mechanically alloyed bornite, Cu_5FeS_4, are similar with ZT ≈ 0.55 over the temperature range 543 ≤ T / K ≤ 573. Although these performances are excellent for transition-metal sulphides, the highest reported ZT of 1.13 at 573 K for $Cu_{11}MnSb_4S_{13}$[258] was not reproduced. Cu-enriched tetrahedrite reached the highest figure of merit measured in this thesis with ZT = 0.62 at 573 K for $Cu_{12+y}Sb_4S_{13}$ (y = 1.5 and 2). This is comparable to other tetrahedrites such as $Cu_{12-x}Zn_xSb_4S_{13}$,[256] $Cu_{10.5}NiZn_{0.5}Sb_4S_{13}$,[260] $Cu_{11.5}Co_{0.5}Sb_4S_{13}$[261] that have a similar ZT at 573 K and reach ZT ≈ 1 at 723 K, 723 K and 673 K, respectively. The figure of merit achieved by manganese-doped tetrahedrite and mechanically alloyed bornite are comparable to that of $Cu_{1.97}S$, which has the highest reported ZT for a sulphide with 0.8 at 650 K and 1.7 at 1000 K.[34] However, copper mobility in binary copper sulphides results in virtually high electrical conductivity and low thermal conductivity in so-called "phonon-liquid electron-crystal" thermoelectric materials.[289] Copper ion mobility prevents the large scale utilisation of such materials in current thermoelectric devices.[35] The change of behaviour in the electrical and thermal properties of Cu-enriched tetrahedrite may be associated with a change from stationary

to mobile copper ion, thus further work should include ionic conductivity measurements in order to determine if copper-enriched tetrahedrite could be implemented to large scale thermoelectric application. Similar measurements should be carried out on $Cu_{12}Sb_4S_{13}$ and $Cu_{11}MnSb_4S_{13}$. Future work on bornite should include a combination of neutron diffraction analysis and X-ray absorption near edge structure (XANES) in order to establish the location of Mn in the structure and to confirm the oxidation states of the elements involved. Owing to the high Seebeck coefficient and the ultralow thermal conductivity of doped-tetrahedrites and mechanically alloyed bornite, there is significant scope for further improvement of the thermoelectric figure of merit through the identification of suitable/additional doping elements.

6.3 Final comments

Thermoelectric power generation has the potential to be a cost-efficient, highly reliable source of electricity. The figure of merit around unity, previously restricted to materials composed of toxic and costly heavy elements, is being reached by environmentally benign materials based on widely available sulphides. However, in the temperature range $473 \leq T / K \leq 673$, at which domestic waste heat is available, the thermoelectric performance of current materials needs to be improved. In this thesis, some of the highest figure of merit values in the temperature range $543 \leq T / K \leq 573$ have been reported for *n*-type and *p*-type sulphides.

References

1. C. John, N. Dana, A. G. Sarah, R. Mark, W. Bärbel, P. Rob, W. Robert, J. Peter and S. Andrew, *Environ. Res. Lett.*, 2013, **8**, 024024.
2. *Directive 2009/28/EC of the European Parliament and of the Council of 23 April 2009 on the promotion of the use of energy from renewable sources and amending and subsequently repealing Directives 2001/77/EC and 2003/30/EC [accessed 15 May 2016]*
3. J. Hansen, R. Ruedy, M. Sato and K. Lo, *Rev. of Geophys.*, 2010, **48**.
4. R. B. Schmunk, *NASA/Goddard Space Flight Center Scientific Visualization Studio, Five-Year Global Temperature Anomalies from 1880 to 2015*, http://svs.gsfc.nasa.gov/4419, 2016. *[accessed 21 June 2016]*
5. D. M. Rowe, *Renew. Ener.*, 1999, **16**, 1251 - 1256.
6. G. Min and D. M. Rowe, in *CRC Handbook of Thermoelectrics*, ed. D. M. Rowe, CRC Press, 1995.
7. L. E. Bell, *Science*, 2008, **321**, 1457-1461.
8. I. H. Association, *2015 Hydropower Status Report*, International Hydropower Association, Online, 2015. *[accessed 23 May 2016]*

9. C. W. E. Association, *World Wind Energy Association Bulletin Issue 1*, 2016.
10. D. R. Walwyn and A. C. Brent, *Renew. Sust. Energ. Rev.*, 2015, **41**, 390-401.
11. I. E. Agency, *World Energy Outlook, Global Energy Trends*, Online, 2015.
12. B. C. H. Steele and A. Heinzel, *Nature*, 2001, **414**, 345-352.
13. M. K. Debe, *Nature*, 2012, **486**, 43-51.
14. M. Z. Jacobson, *Energy Environ. Sci.*, 2009, **2**, 148-173.
15. J. Curie and P. Curie, *J. Phys. Theor. Appl.*, 1882, **1** 245-251.
16. T. J. Seebeck, *Abh. K. Akad. Wiss.*, 1822, 289.
17. D. M. Rowe, in *CRC Handbook of Thermoelectrics*, ed. D. M. Rowe, CRC Press, 1995.
18. J. Yang and T. Caillat, *MRS Bull.*, 2006, **31**, 224-229.
19. J. R. Sootsman, D. Y. Chung and M. G. Kanatzidis, *Angew. Chem.*, 2009, **48**, 8616-8639.
20. A. J. Minnich, M. S. Dresselhaus, Z. F. Ren and G. Chen, *Energy Environ. Sci.*, 2009, **2**, 466-479.
21. M. S. Dresselhaus, G. Chen, M. Y. Tang, R. G. Yang, H. Lee, D. Z. Wang, Z. F. Ren, J. P. Fleurial and P. Gogna, *Adv. Mater.*, 2007, **19**, 1043-1053.
22. G. J. Snyder and E. S. Toberer, *Nat. Mater.*, 2008, **7**, 105-114.
23. P. Vaqueiro and A. V. Powell, *J. Mater. Chem.*, 2010, **20**, 9577-9584.
24. Y. C. Dou, X. Y. Qin, D. Li, L. L. Li, T. H. Zou and Q. Q. Wang, *J. Appl. Phys.*, 2013, **114**, 044906.
25. L. D. Zhao, B. P. Zhang, J. F. Li, H. L. Zhang and W. S. Liu, *Solid State Sci.*, 2008, **10**, 651-658.
26. J. Li, Q. Tan, J.-F. Li, D.-W. Liu, F. Li, Z.-Y. Li, M. Zou and K. Wang, *Adv. Funct. Mater.*, 2013, **23**, 4317-4323.
27. B. Poudel, Q. Hao, Y. Ma, Y. Lan, A. Minnich, B. Yu, X. Yan, D. Wang, A. Muto, D. Vashaee, X. Chen, J. Liu, M. S. Dresselhaus, G. Chen and Z. Ren, *Science*, 2008, **320**, 634-638.
28. K. F. Hsu, S. Loo, F. Guo, W. Chen, J. S. Dyck, C. Uher, T. Hogan, E. K. Polychroniadis and M. G. Kanatzidis, *Science*, 2004, **303**, 818-821.
29. R. Venkatasubramanian, T. Colpitts, E. Watko, M. Lamvik and N. El-Masry, *J. Cryst. Growth*, 1997, **170**, 817-821.
30. T. C. Harman, D. L. Spears and M. J. Manfra, *J. Electron. Mater.*, 1996, **25**, 1121-1127.
31. H. Beyer, J. Nurnus, H. Böttner, A. Lambrecht, T. Roch and G. Bauer, *Appl. Phys. Lett.*, 2002, **80**, 1216-1218.
32. R. Venkatasubramanian, E. Slivola, T. Colpitts and B. O'Quinn, *Nature*, 2001, **413**, 597-602.
33. G. C. Tewari, T. S. Tripathi and A. K. Rastogi, *J. Electron. Mater.*, 2010, **39**, 1133-1139.
34. Y. He, T. Day, T. Zhang, H. Liu, X. Shi, L. Chen and G. J. Snyder, *Adv. Mater.*, 2014, **26**, 3974-3978.
35. G. Dennler, R. Chmielowski, S. Jacob, F. Capet, P. Roussel, S. Zastrow, K. Nielsch, I. Opahle and G. K. H. Madsen, *Adv. Energy Mater.*, 2014, **4**, 12.
36. H. J. Goldsmid and J. W. Sharp, *J. Electron. Mater.*, 1999, **28**, 869-872.
37. Z. M. Gibbs, H.-S. Kim, H. Wang and G. J. Snyder, *Appl. Phys. Lett.*, 2015, **106**, 022112.
38. R. P. Chasmar and R. Stratton, *J. Electron. Control*, 1959, **7**, 52-72.
39. W. Chunlei, W. Yifeng, W. Ning, N. Wataru, K. Michiko and K. Kunihito, *Sci. Technol. Adv. Mater.*, 2010, **11**, 044306.
40. G. A. Slack, in *CRC Handbook of Thermoelectrics*, ed. D. M. Rowe, CRC Press, 1995.
41. S. Furuseth, L. Brattas and A. Kjekshus, *Acta Chem. Scand. A*, 1975, **29**, 623-631.

42. E. Guilmeau, D. Berthebaud, P. R. N. Misse, S. Hébert, O. I. Lebedev, D. Chateigner, C. Martin and A. Maignan, *Chem. Mater.*, 2014, **26**, 5585-5591.
43. I. G. Gorlova, V. Y. Pokrovskii, S. G. Zybtsev, A. N. Titov and V. N. Timofeev, *J. Exp. Theor. Phys.*, 2010, **111**, 298-303.
44. J. O. Island, R. Biele, M. Barawi, J. M. Clamagirand, J. R. Ares, C. Sanchez, H. S. J. van der Zant, I. J. Ferrer, R. D'Agosta and A. Castellanos-Gomez, *Sci. Rep.*, 2016, **6**, 22214.
45. M. S. Whittingham, *Chem. Rev.*, 2004, **104**, 4271-4301.
46. A. Madhukar, *Solid State Commun.*, 1975, **16**, 383-388.
47. A. F. Wells, *Structural Inorganic Chemistry*, Clarendon Press; Oxford University Press, Oxfordshire, 5th edn., 1984.
48. K. Kosuge, *Chemistry of Non-stoichiometric Compounds*, Oxford University Press, 1994.
49. D. J. Vaughan and J. R. Craig, *Mineral Chemistry of Metal Sulfides*, Cambridge University Press, Cambridge 1978.
50. P. Vaqueiro and A. V. Powell, *Chem. Mater.*, 2000, **12**, 2705-2714.
51. A. R. West, *Solid State Chemistry and its Applications*, John Wiley & Sons, Ltd, United Kingdom, 2014.
52. W. Meissner and R. Ochsenfeld, *Naturwissenschaften*, 1933, **21**, 787-788.
53. S. J. Blundell, *Contemp. Phys.*, 1999, **40**, 175-192.
54. P. D. d. Réotier and A. Yaouanc, *J. Phys.: Condens. Matter*, 1997, **9**, 9113.
55. P. A. Cox, *The Electronic Structure and Chemistry of Solids*, 1987.
56. P. Atkins, *Atkins' Physical Chemistry*, 2002.
57. C. N. R. Rao and J. Gopalakrishnan, *New Directions in Solid State Chemistry*, Cambridge University Press, Cambridge, 2nd edn., 1997.
58. C. Wood, *Rep. Prog. Phys.*, 1988, **51**, 459.
59. B. C. Sales, D. Mandrus and R. K. Williams, *Science*, 1996, **272**, 1325-1328.
60. R. P. Hermann, R. Jin, W. Schweika, F. Grandjean, D. Mandrus, B. C. Sales and G. J. Long, *Phys. Rev. Lett.*, 2003, **90**, 135505.
61. V. Keppens, D. Mandrus, B. C. Sales, B. C. Chakoumakos, P. Dai, R. Coldea, M. B. Maple, D. A. Gajewski, E. J. Freeman and S. Bennington, *Nature*, 1998, **395**, 876-878.
62. J. Zou and A. Balandin, *J. Appl. Phys.*, 2001, **89**, 2932-2938.
63. D. Narducci, E. Selezneva, G. Cerofolini, S. Frabboni and G. Ottaviani, *J. Solid State Chem.*, 2012, **193**, 19-25.
64. A. I. Hochbaum, R. Chen, R. D. Delgado, W. Liang, E. C. Garnett, M. Najarian, A. Majumdar and P. Yang, *Nature*, 2008, **451**, 163-167.
65. A. I. Boukai, Y. Bunimovich, J. Tahir-Kheli, J.-K. Yu, W. A. Goddard Iii and J. R. Heath, *Nature*, 2008, **451**, 168-171.
66. L. D. Hicks and M. S. Dresselhaus, *Phys. Rev. B*, 1993, **47**, 12727-12731.
67. J. P. Heremans, M. S. Dresselhaus, L. E. Bell and D. T. Morelli, *Nat. Nanotechnol.*, 2013, **8**, 471-473.
68. K. Biswas, J. He, I. D. Blum, C.-I. Wu, T. P. Hogan, D. N. Seidman, V. P. Dravid and M. G. Kanatzidis, *Nature*, 2012, **489**, 414-418.
69. W. Liu, Q. Jie, H. S. Kim and Z. Ren, *Acta Mater.*, 2015, **87**, 357-376.
70. J. He, Y. Liu and R. Funahashi, *J. Mater. Res.*, 2011, **26**, 1762-1772.
71. S. Hébert, D. Berthebaud, R. Daou, Y. Breard, D. Pelloquin, E. Guilmeau, F. Gascoin, O. Lebedev and A. Maignan, *J. Phys.: Condens. Matter*, 2016, **28**, 013001/013023.
72. B. Chen, C. Uher, L. Iordanidis and M. G. Kanatzidis, *Chem. Mater.*, 1997, **9**, 1655-1658.

73. M. G. Kanatzidis, T. J. McCarthy, T. A. Tanzer, L.-H. Chen, L. Iordanidis, T. Hogan, C. R. Kannewurf, C. Uher and B. Chen, *Chem. Mater.*, 1996, **8**, 1465-1474.
74. L.-D. Zhao, B.-P. Zhang, W.-S. Liu, H.-L. Zhang and J.-F. Li, *J. Solid State Chem.*, 2008, **181**, 3278-3282.
75. Z.-H. Ge, B.-P. Zhang, Z.-X. Yu and J.-F. Li, *J. Mater. Res.*, 2011, **26**, 2711-2718.
76. Z.-H. Ge, B.-P. Zhang, Y. Liu and J.-F. Li, *Phys. Chem. Chem. Phys.*, 2012, **14**, 4475-4481.
77. K. Biswas, L. Zhao and M. G. Kanatzidis, *Adv. Energy Mater.*, 2012, **2**, 634-638.
78. L. Zhao, J. He, C. Wu, T. P. Hogan, X. Zhou, C. Uher, V. P. Dravid and M. G. Kanatzidis, *J. Am. Chem. Soc.*, 2012, **134**, 7902-7912.
79. L.-D. Zhao, S.-H. Lo, J. He, H. Li, K. Biswas, J. Androulakis, C.-I. Wu, T. P. Hogan, D.-Y. Chung, V. P. Dravid and M. G. Kanatzidis, *J. Am. Chem. Soc.*, 2015, **133**, 20476-20487.
80. L.-D. Zhao, J. He, S. Hao, C.-I. Wu, T. P. Hogan, C. Wolverton, V. P. Dravid and M. G. Kanatzidis, *J. Am. Chem. Soc.*, 2012, **134**, 16327-16336.
81. T. Caillat, J. P. Fleurial and G. J. Snyder, *Solid State Sci.*, 1999, **1**, 535-544.
82. J. K. Burdett and J. H. Lin, *Inorg. Chem.*, 1982, **21**, 5-10.
83. T. Tsubota, M. Ohtaki and K. Eguchi, *J. Ceram. Soc. Jpn.*, 1999, **107**, 697-701.
84. M. Ohta, A. Yamamoto and H. Obara, *J. Electron. Mater.*, 2010, **39**, 2117-2121.
85. M. Ohta, H. Obara and A. Yamamoto, *Mater. T. JIM*, 2009, **50**, 2129-2133.
86. C. Wood, A. Lockwood, J. Parker, A. Zoltan, D. Zoltan, L. R. Danielson and V. Raag, *J. Appl. Phys.*, 1985, **58**, 1542-1547.
87. T. Takeshita, K. A. Gschneidner and B. J. Beaudry, *J. Appl. Phys.*, 1985, **57**, 4633-4637.
88. M. Ohta and S. Hirai, *J. Electron. Mater.*, 2009, **38**, 1287-1292.
89. M. Ohta, S. Hirai and T. Kuzuya, *J. Electron. Mater.*, 2011, **40**, 537-542.
90. U. S. G. Survey and U. S. D. Interior, *Mineral Commodity Summaries*, 2016.
91. T. Kambara, *J. Phys. Soc. Jpn.*, 1974, **36**, 1625-1635.
92. S. R. Hall and J. M. Stewart, *Acta Crystallogr. B*, 1973, **29**, 579-585.
93. T. Naohito and M. Takao, *Appl. Phys. Express*, 2013, **6**, 043001.
94. N. Tsujii, *J. Electron. Mater.*, 2013, **42**, 1974-1977.
95. D. Berthebaud, O. I. Lebedev and A. Maignan, *J. Materiomics*, 2015, **1**, 68-74.
96. J. Li, Q. Tan and J.-F. Li, *J. Alloys Compd.*, 2013, **551**, 143-149.
97. D. Liang, R. Ma, S. Jiao, G. Pang and S. Feng, *Nanoscale*, 2012, **4**, 6265-6268.
98. A. Suzumura, M. Watanabe, N. Nagasako and R. Asahi, *J. Electron. Mater.*, 2014, **43**, 2356-2361.
99. J. Corps, P. Vaqueiro and A. V. Powell, *J. Mater. Chem. A*, 2013, **1**, 6553-6557.
100. J. Corps, P. Vaqueiro, A. Aziz, R. Grau-Crespo, W. Kockelmann, J.-C. Jumas and A. V. Powell, *Chem. Mater.*, 2015, **27**, 3946-3956.
101. A. E. Becquerel, *Ann. Chim. Phys.* , 1866, **48**, 389.
102. E. Makovicky, *Rev. Mineral. Geochem.*, 2006, **61**, 7-125.
103. Hudson Institute of Mineralogy, (http://www.mindat.org/). *[accessed 8 July 2016]*
104. A. Pfitzner, M. Evain and V. Petricek, *Acta Crystallogr. B*, 1997, **B53**, 337-345.
105. A. J. Frueh, Jr., *Am. Mineral.*, 1950, **35**, 185-192.
106. K. Koto and N. Morimoto, *Acta Crystallogr. B*, 1975, **31**, 2268-2273.
107. N. Morimoto and G. Kullerud, *Am. Mineral.*, 1961, **46**, 1270-1282.
108. Y. Kanazawa, K. Koto and N. Morimoto, *Can. Mineral.*, 1978, **16**, 397-404.
109. B. A. Grguric and A. Putnis, *Can. Mineral.*, 1998, **36**, 215-227.
110. J. Grace and A. Putnis, *Econ. Geol.*, 1976, **71**, 1058-1059.
111. B. A. Grguric, A. Putnis and R. J. Harrison, *Am. Mineral.*, 1998, **83**, 1231-1239.

112. Y. Ding, D. R. Veblen and C. T. Prewitt, *Am. Mineral.*, 2005, **90**, 1265-1269.
113. Y. Ding, D. R. Veblen and C. T. Prewitt, *Am. Mineral.*, 2005, **90**, 1256-1264.
114. M. Inoue, H. P. Hughes and A. D. Yoffe, *Adv. Phys.*, 1989, **38**, 565-604.
115. J. A. Wilson and A. D. Yoffe, *Adv. Phys.*, 1969, **18**, 193-335.
116. G. A. Wiegers and R. J. Haange, *Eur. J. Solid State Inorg. Chem.*, 1991, **28**, 1071-1078.
117. C. Wan, Y. Wang, N. Wang and K. Koumoto, *Materials*, 2010, **3**, 2606-2617.
118. C. Wan, X. Gu, F. Dang, T. Itoh, Y. Wang, H. Sasaki, M. Kondo, K. Koga, K. Yabuki, G. J. Snyder, R. Yang and K. Koumoto, *Nat. Mater.*, 2015, **14**, 622-627.
119. B. Mohanty, in *Forensic Investigation of Explosions*, ed. A. Beveridge, Taylor and Francis, 1998.
120. C. Suryanarayana, *Prog. Mater Sci.*, 2001, **46**, 1-184.
121. J. S. Benjamin, *Metall. Trans.*, 1970, **1**, 2943-2951.
122. B. S. Murty and S. Ranganathan, *Int. Mater. Rev.*, 1998, **43**, 101-141.
123. P. S. Gilman and J. S. Benjamin, *Annu. Rev. Mater. Sci.*, 1983, **13**, 279-300.
124. C. C. Koch, *Nanostruct. Mater.*, 1997, **9**, 13-22.
125. P. P. Chattopadhyay, I. Manna, S. Talapatra and S. K. Pabi, *Mater. Chem. Phys.*, 2001, **68**, 85-94.
126. M. Abdellaoui and E. Gaffet, *J. Alloys Compd.*, 1994, **209**, 351-361.
127. M. Abdellaoui and E. Gaffet, *Acta Metall. Mater.*, 1995, **43**, 1087-1098.
128. L. E. Smart and E. A. Moore, *Solid State Chemistry : An Introduction, Fourth Edition*, CRC Press, 2012.
129. *Bruker AXS GmbH, "EVA"*, Karlsruhe, Germany, 2007.
130. A. C. Larson and R. B. V. Dreele, *Los Alamos National Laboratory Report LAUR 86-748*, 1994.
131. B. Toby, *J. Appl. Crystallogr.*, 2001, **34**, 210-213.
132. L. Koester, H. Rauch and E. Seymann, *Atomic Data and Nuclear Data Tables*, 1991, **49**, 65-120.
133. V. F. Sears, *Neutron News*, 1992, **3**, 26-37.
134. *ISIS Neutron and Muon Source Annual Review*, 2015.
135. A. C. Hannon, *Nucl. Instr. Meth. Phys. Res. A*, 2005, **551**, 88-107.
136. F. Akeroyd et al., *Mantid: Manipulation and Analysis Toolkit for Instrument Data*, Mantid Project.
137. O. Arnold et al., *Nucl. Instr. Meth. Phys. Res. A*, 2014, **764**, 156-166.
138. *http://www.isis.stfc.ac.uk/instruments/polaris/. [accessed 2 July 2016]*
139. *Bruker AXS GmbH, "Topas3"*, Karlsruhe, Germany, 2005.
140. J. Rodriguez-Carvajal, *Physica B* 1993, **192**, 55-69.
141. T. Roisnel and J. Rodriguez-Carvajal, *Mater. Sci. Forum*, 2001, **378-381**, 118-123.
142. H. Rietveld, *Acta Crystallogr.*, 1967, **22**, 151-152.
143. H. Rietveld, *J. Appl. Crystallogr.*, 1969, **2**, 65-71.
144. R. A. Young, *The Rietveld Method*, Oxford University Press, Oxford, 1996.
145. L. B. McCusker, R. B. Von Dreele, D. E. Cox, D. Louer and P. Scardi, *J. Appl. Crystallogr.*, 1999, **32**, 36-50.
146. C. Howard, *J. Appl. Crystallogr.*, 1982, **15**, 615-620.
147. P. Thompson, D. E. Cox and J. B. Hastings, *J. Appl. Crystallogr.*, 1987, **20**, 79-83.
148. A. Le Bail, H. Duroy and J. L. Fourquet, *Mater. Res. Bull.*, 1988, **23**, 447-452.
149. A. Le Bail, *Powder Diffr.*, 2005, **20**, 316-326.
150. S. De Franceschi, L. Kouwenhoven, C. Schonenberger and W. Wernsdorfer, *Nat. Nanotechnol.*, 2010, **5**, 703-711.
151. *http://www.isis.stfc.ac.uk/instruments/emu/. [accessed 7 July 2016]*

152. W. J. Parker, R. J. Jenkins, C. P. Butler and G. L. Abbott, *J. Appl. Phys.*, 1961, **32**, 1679-1684.
153. R. D. Cowan, *J. Appl. Phys.*, 1963, **34**, 926-927.
154. A. T. Petit and P. L. Dulong, *Ann. Chim. Phys.*, 1819, **10**, 395–413.
155. H. Imai, Y. Shimakawa and Y. Kubo, *Phys. Rev. B*, 2001, **64**, 241104.
156. T. Barbier, O. I. Lebedev, V. Roddatis, Y. Breard, A. Maignan and E. Guilmeau, *Dalton Trans.*, 2015, **44**, 7887-7895.
157. M. Beaumale, T. Barbier, Y. Breard, G. Guélou, A. V. Powell, P. Vaqueiro and E. Guilmeau, *Acta Mater.*, 2014, **78**, 86-92.
158. M. Beaumale, T. Barbier, Y. Breard, S. Hébert, Y. Kinemuchi and E. Guilmeau, *J. Appl. Phys.* , 2014, **115**, 043704.
159. M. Beaumale, T. Barbier, Y. Breard, B. Raveau, Y. Kinemuchi, R. Funahashi and E. Guilmeau, *J. Electron. Mater.*, 2014, **43**, 1590-1596.
160. E. Guilmeau, Y. Breard and A. Maignan, *Appl. Phys. Lett.*, 2011, **99**, 052107.
161. E. Guilmeau, A. Maignan, C. Wan and K. Koumoto, *Phys. Chem. Chem. Phys.*, 2015, **17**, 24541-24555.
162. M. Ohta, S. Satoh, T. Kuzuya, S. Hirai, M. Kunii and A. Yamamoto, *Acta Mater.*, 2012, **60**, 7232-7240.
163. S. Hébert, W. Kobayashi, H. Muguerra, Y. Bréard, N. Raghavendra, F. Gascoin, E. Guilmeau and A. Maignan, *Phys. Status Solidi A*, 2012, **210**, 69-81.
164. G. A. Wiegers, *Prog. Solid State Chem.*, 1996, **24**, 1-139.
165. C. Wan, Y. Wang, W. Norimatsu, M. Kusunoki and K. Koumoto, *Appl. Phys. Lett.*, 2012, **100**, 101913/101911-101913/101914.
166. C. Wan, Y. Wang, N. Wang, W. Norimatsu, M. Kusunoki and K. Koumoto, *J. Electron. Mater.*, 2011, **40**, 1271-1280.
167. A. H. Reshak and S. Auluck, *Phys. Rev. B*, 2003, **68**, 245113.
168. C. M. Fang, R. A. de Groot and C. Haas, *Phys. Rev. B*, 1997, **56**, 4455-4463.
169. P. C. Klipstein, A. G. Bagnall, W. Y. Liang, E. A. Marseglia and R. H. Friend, *J. Phys. C*, 1981, **14**, 4067-4081.
170. G. Guélou, P. Vaqueiro, J. Prado-Gonjal, T. Barbier, S. Hebert, E. Guilmeau, W. Kockelmann and A. V. Powell, *J. Mater. Chem. C*, 2016, **4**, 1871-1880.
171. R. R. Chianelli, J. C. Scanlon and A. H. Thompson, *Mater. Res. Bull.*, 1975, **10**, 1379-1382.
172. N. Suzuki, T. Yamasaki and K. Motizuki, *J. Phys. Soc. Jpn.*, 1989, **58**, 3280-3289.
173. M. Inoue and H. Negishi, *J. Phys. Chem.*, 1986, **90**, 235-238.
174. W. Bensch and J. Koy, *Inorg. Chim. Acta*, 1993, **206**, 221-223.
175. A. B. De Vries and F. Jellinek, *Rev. Chim. Miner.*, 1974, **11**, 624-636.
176. I. Kawada, M. Nakano-Onoda, M. Ishii, M. Saeki and M. Nakahira, *J. Solid State Chem.*, 1975, **15**, 246 - 252.
177. A. V. Powell, D. C. Colgan and C. Ritter, *J. Solid State Chem.*, 1999, **143**, 163-173.
178. A. V. Powell, D. C. Colgan and P. Vaqueiro, *J. Mater. Chem.*, 1999, **9**, 485-492.
179. T. Kawasaki and K.-i. Ohshima, *J. Phys. Soc. Jpn.*, 2011, **80**, 044601.
180. M. Danot and R. Brec, *Acta Crystallogr. B*, 1975, **31**, 1647-1652.
181. M. Danot and J. Rouxel, *C. r. hebd. séances Acad. sci. C*, 1970, **271**, 998-1001.
182. M. Danot, J. Rouxel and O. Gorochov, *Mater. Res. Bull.*, 1974, **9**, 1383-1392.
183. F. Jellinek, *Acta Crystallogr.*, 1957, **10**, 620-628.
184. L. W. Finger, M. Kroeker and B. H. Toby, *J. Appl. Crystallogr.*, 2007, **40**, 188-192.
185. M. Inoue, M. Matsumoto, H. Negishi and H. Sakai, *J. Mag. Magn. Mater.*, 1985, **53**, 131-138.
186. L. Neel and R. Benoit, *C. r. hebd. séances Acad. sci.*, 1953, **237**, 444-447.

187. J. B. Goodenough and F. A. Cotton, *Magnetism and the Chemical Bond*, Wiley, New York, 1963.
188. S. Miyahara and T. Teranishi, *J. Appl. Phys.*, 1968, **39**, 896-897.
189. K. Sanchez, P. Palacios and P. Wahnon, *Phys. Rev. B*, 2008, **78**, 235121/235121-235121/235126.
190. A. H. Reshak, I. V. Kityk and S. Auluck, *J. Chem. Phys.*, 2008, **129**, 074706/074701-074706/074705.
191. H. E. Brauer, H. I. Starnberg, L. J. Holleboom, H. P. Hughes and V. N. Strocov, *J. Phys.: Condens. Matter*, 1999, **11**, 8957-8973.
192. Y.-S. Kim, M. Mizuno, I. Tanaka and H. Adachi, *Mater. T. JIM*, 1998, **39**, 709-713.
193. Z. Y. Wu, F. Lemoigno, P. Gressier, G. Ouvrard, P. Moreau, J. Rouxel and C. R. Natoli, *Phys. Rev. B*, 1996, **54**, R11009-R11013.
194. A. Maignan, E. Guilmeau, F. Gascoin, Y. Breard and V. Hardy, *Sci. Technol. Adv. Mater.*, 2012, **13**, 053003.
195. X. Y. Qin, J. Zhang, D. Li, H. Z. Dong and L. Wang, *J. Appl. Phys.*, 2007, **102**, 073703.
196. H. P. Vaterlaus, F. Levy and H. Berger, *J. Phys. C Solid State*, 1983, **16**, 1517.
197. J. M. Tarascon, F. J. DiSalvo, M. Eibschutz, D. W. Murphy and J. V. Waszczak, *Phys. Rev. B*, 1983, **28**, 6397-6406.
198. J. Zhang, X. Y. Qin, D. Li and H. Z. Dong, *J. Phys. D: Appl. Phys.*, 2006, **39**, 1230-1236.
199. D. T. Hodul and A. M. Stacy, *J. Solid State Chem.*, 1986, **62**, 328-334.
200. M. Shimakawa, H. Maki, H. Nishihara and K. Hayashi, *Mater. Res. Bull.*, 1997, **32**, 689-699.
201. A. H. Thompson, K. R. Pisharody and R. F. Koehler, Jr., *Phys. Rev. Lett.*, 1972, **29**, 163-166.
202. J. A. Benda, *Phys. Rev. B*, 1974, **10**, 1409-1420.
203. Y. Tison, H. Martinez, I. Baraille, M. Loudet and D. Gonbeau, *Surface Science*, 2004, **563**, 83-98.
204. F. Gascoin, N. Raghavendra, E. Guilmeau and Y. Breard, *J. Alloys Compd.*, 2012, **521**, 121-125.
205. H. P. B. Rimmington and A. A. Balchin, *J. Cryst. Growth*, 1974, **21**, 171-181.
206. Y. Hirota, K. Ichiyama, N. Hosoi, Y. Oikawa, Y. Miyahara, V. A. Kulbachinskii and H. Ozaki, *21st Int. Conf. Thermoelectr.*, 2002, 159-162.
207. A. A. Lakhani, S. Jandl, C. Ayache and J. P. Jay-Gerin, *Phys. Rev. B*, 1983, **28**, 1978-1982.
208. F. Jellinek, G. Brauer and H. Muller, *Nature*, 1960, **185**, 376-377.
209. R. Shannon, *Acta Crystallogr. A*, 1976, **32**, 751-767.
210. M. Ohta, H. Obara and A. Yamamoto, *Mater. T. JIM*, 2009, **50**, 2129-2133.
211. D. L. Medlin and G. J. Snyder, *Curr. Opin. Colloid In.*, 2009, **14**, 226-235.
212. M. G. Kanatzidis, *Chem. Mater.*, 2010, **22**, 648-659.
213. S. V. Faleev and F. Léonard, *Phys. Rev. B*, 2008, **77**, 214304.
214. M. S. Dresselhaus, G. Chen, Z. Ren, J.-P. Fleurial, P. Gogna, M. Y. Tang, D. Vashaee, H. Lee, X. Wang, G. Joshi, G. Zhu, D. Wang, R. Blair, S. Bux and R. Kaner, *Mater. Res. Soc. Symp. Proc.*, 2008, **1044**, 1044-U1002-1004.
215. J. H. Han, S. Lee and J. Cheon, *Chem. Soc. Rev.*, 2013, **42**, 2581-2591.
216. A. Margolin, R. Popovitz-Biro, A. Albu-Yaron, L. Rapoport and R. Tenne, *Chem. Phys. Lett.*, 2005, **411**, 162-166.
217. S. Prabakar, S. Collins, B. Northover and R. D. Tilley, *Chem. Commun.*, 2011, **47**, 439-441.

218. R. A. L. Morasse, T. Li, Z. J. Baum and J. E. Goldberger, *Chem. Mater.*, 2014, **26**, 4776-4780.
219. J. Chen, Z.-L. Tao and S.-L. Li, *Angew. Chem.*, 2003, **42**, 2147-2151.
220. J. Chen, S.-L. Li, Z.-L. Tao and F. Gao, *Chem. Commun.*, 2003, DOI: 10.1039/B300054K, 980-981.
221. A. Bensalem and D. M. Schleich, *Mater. Res. Bull.*, 1988, **23**, 857-868.
222. R. Yang and G. Chen, *Phys. Rev. B*, 2004, **69**, 195316.
223. X. B. Zhao, X. H. Ji, Y. H. Zhang, T. J. Zhu, J. P. Tu and X. B. Zhang, *Appl. Phys. Lett.*, 2005, **86**, 062111.
224. J.-f. Li and J. Liu, *Phys. Status Solidi A*, 2006, **203**, 3768-3773.
225. J. He, J. R. Sootsman, S. N. Girard, J.-C. Zheng, J. Wen, Y. Zhu, M. G. Kanatzidis and V. P. Dravid, *J. Am. Chem. Soc.*, 2010, **132**, 8669-8675.
226. M. Zebarjadi, G. Joshi, G. Zhu, B. Yu, A. Minnich, Y. Lan, X. Wang, M. Dresselhaus, Z. Ren and G. Chen, *Nano Lett.*, 2011, **11**, 2225-2230.
227. A. Soni, Y. Shen, M. Yin, Y. Zhao, L. Yu, X. Hu, Z. Dong, K. A. Khor, M. S. Dresselhaus and Q. Xiong, *Nano Lett.*, 2012, **12**, 4305-4310.
228. L.-D. Zhao, B.-P. Zhang, J.-F. Li, M. Zhou, W.-S. Liu and J. Liu, *J. Alloys Compd.*, 2008, **455**, 259-264.
229. W. Liu, X. Yan, G. Chen and Z. Ren, *Nano Energy*, **1**, 42-56.
230. Y. Wang, J. Wen, Z. Fan, N. Bao, R. Huang, R. Tu and Y. Wang, *AIP Advances*, 2015, **5**, 047126.
231. Y. Ye, Y. Wang, Y. Shen, Y. Wang, L. Pan, R. Tu, C. Lu, R. Huang and K. Koumoto, *J. Alloys Compd.*, 2016, **666**, 346-351.
232. C. Bourgès, T. Barbier, G. Guélou, P. Vaqueiro, A. V. Powell, O. I. Lebedev, N. Barrier, Y. Kinemuchi and E. Guilmeau, *J. Eur. Ceram. Soc.*, 2016, **36**, 1183-1189.
233. X. Qian, S. Shen, T. Liu, L. Cheng and Z. Liu, *Nanoscale*, 2015, **7**, 6380-6387.
234. S. Prabakar, C. W. Bumby and R. D. Tilley, *Chem. Mater.*, 2009, **21**, 1725-1730.
235. D. M. Rowe, V. S. Shukla and N. Savvides, *Nature*, 1981, **290**, 765-766.
236. L. E. Smart and E. A. Moore, in *Section 9: Magnetic and Dielectric Properties, Solid state chemistry: an introduction*, Taylor & Francis, 3rd edn., 2005.
237. L. E. Smart and E. A. Moore, in *Section 5: Defects and non-stoichiometry, Solid state chemistry: an introduction*, Taylor & Francis, 3rd edn., 2005.
238. W. M. Haynes and D. R. Lide, in *CRC handbook of chemistry and physics*, CRC Press, 2004.
239. S. Iijima, *Nature*, 1991, **354**, 56-58.
240. T. W. Ebbesen and P. M. Ajayan, *Nature*, 1992, **358**, 220-222.
241. M. S. Dresselhaus and M. Terrones, *Proc. IEEE*, 2013, **101**, 1522-1535.
242. R. Saito, G. Dresselhaus and M. S. Dresselhaus, *J. Appl. Phys.*, 1993, **73**, 494-500.
243. J. C. Charlier and J. P. Michenaud, *Phys. Rev. Lett.*, 1993, **70**, 1858-1861.
244. L. Langer, V. Bayot, E. Grivei, J. P. Issi, J. P. Heremans, C. H. Olk, L. Stockman, C. Van Haesendonck and Y. Bruynseraede, *Phys. Rev. Lett.*, 1996, **76**, 479-482.
245. P. Trucano and R. Chen, *Nature*, 1975, **258**, 136-137.
246. A. Cao, C. Xu, J. Liang, D. Wu and B. Wei, *Chem. Phys. Lett.*, 2001, **344**, 13-17.
247. B. J. Wuensch, *Z. Kristallogr., Kristallgeom., Kristallphys., Kristallchem.*, 1964, **119**, 437-453.
248. E. Makovicky and B. J. Skinner, *Can. Mineral.*, 1978, **16**, 611-623.
249. E. Makovicky and B. J. Skinner, *Can. Mineral.*, 1979, **17**, 619-634.
250. A. F. Rogers, *Science*, 1915, **42**, 386-388.
251. M. Telkes, *Am. Mineral.*, 1950, **35**, 536-555.

252. K. Suekuni, K. Tsuruta, T. Ariga and M. Koyano, *Appl. Phys. Express*, 2012, **5**, 051201/051201-051201/051203.
253. P. Qiu, T. Zhang, Y. Qiu, X. Shi and L. Chen, *Energy Environ. Sci.*, 2014, **7**, 4000-4006.
254. R. Chetty, A. Bali and R. C. Mallik, *J. Mater. Chem. C*, 2015, **3**, 12364-12378.
255. X. Lu, D. T. Morelli, Y. Xia, F. Zhou, V. Ozolins, H. Chi, X. Zhou and C. Uher, *Adv. Energy Mater.*, 2013, **3**, 342-348.
256. X. Lu and D. T. Morelli, *MRS Commun.*, 2013, **3**, 129-133.
257. X. Lu and D. T. Morelli, *Phys. Chem. Chem. Phys.*, 2013, **15**, 5762-5766.
258. J. Heo, G. Laurita, S. Muir, M. A. Subramanian and D. A. Keszler, *Chem. Mater.*, 2014, **26**, 2047-2051.
259. R. Chetty, D. S. Prem Kumar, G. Rogl, P. Rogl, E. Bauer, H. Michor, S. Suwas, S. Puchegger, G. Giester and R. C. Mallik, *Phys. Chem. Chem. Phys.*, 2015, **17**, 1716-1727.
260. X. Lu, D. T. Morelli, Y. Xia and V. Ozolins, *Chem. Mater.*, 2015, **27**, 408-413.
261. R. Chetty, A. Bali, M. H. Naik, G. Rogl, P. Rogl, M. Jain, S. Suwas and R. C. Mallik, *Acta Mater.*, 2015, **100**, 266-274.
262. X. Lu and D. Morelli, *J. Electron. Mater.*, 2014, **43**, 1983-1987.
263. D. W. Bullett and W. G. Dawson, *J. Phys. C: Solid State Phys.*, 1986, **19**, 5837-5847.
264. E. Makovicky and B. J. Skinner, *Neues Jahrb. Mineral., Monatsh.*, 1976, 141-143.
265. M. L. Johnson and R. Jeanloz, *Am. Mineral.*, 1983, **68**, 220-226.
266. K. Tatsuka and N. Morimoto, *Am. Mineral.*, 1973, **58**, 425-434.
267. A. Pfitzner and S. Reiser, *Z. Kristallogr.*, 2002, **217**, 51-54.
268. B. J. Wuensch, *Science*, 1963, **141**, 804-805.
269. T. Barbier, S. Rollin-Martinet, P. Lemoine, F. Gascoin, A. Kaltzoglou, P. Vaqueiro, A. V. Powell and E. Guilmeau, *J. Am. Ceram. Soc.*, 2016, **99**, 51-56.
270. T. Barbier, P. Lemoine, S. Gascoin, O. I. Lebedev, A. Kaltzoglou, P. Vaqueiro, A. V. Powell, R. I. Smith and E. Guilmeau, *J. Alloys Compd.*, 2015, **634**, 253-262.
271. K. Suekuni, K. Tsuruta, M. Kunii, H. Nishiate, E. Nishibori, S. Maki, M. Ohta, A. Yamamoto and M. Koyano, *J. Appl. Phys.*, 2013, **113**, 043712.
272. N. E. Johnson, *Powder Diffraction*, 1991, **6**, 43-47.
273. J. W. Andreasen, E. Makovicky, B. Lebech and S. K. Møller, *Physics and Chemistry of Minerals*, 2008, **35**, 447-454.
274. W. Lai, Y. Wang, D. T. Morelli and X. Lu, *Adv. Funct. Mater.*, 2015, **25**, 3648-3657.
275. X. Shi, J. Yang, J. R. Salvador, M. Chi, J. Y. Cho, H. Wang, S. Bai, J. Yang, W. Zhang and L. Chen, *J. Am. Chem. Soc.*, 2011, **133**, 7837-7846.
276. G. van der Laan, R. A. D. Pattrick, C. M. B. Henderson and D. J. Vaughan, *J. Phys. Chem. Solids*, 1992, **53**, 1185-1190.
277. R. A. D. Pattrick, G. van der Laan, D. J. Vaughan and C. M. B. Henderson, *Phys. Chem. Miner.*, 1993, **20**, 395-401.
278. P. Vaqueiro, G. Guélou, A. Kaltzoglou, R. I. Smith, T. Barbier, E. Guilmeau and A. V. Powell, unpublished work.
279. A. Pfitzner, *Z. Kristallogr.*, 1998, **213**, 228-236.
280. E. Makovicky, *J. Solid State Chem.*, 1983, **49**, 85-92.
281. W. Qiu, L. Wu, X. Ke, J. Yang and W. Zhang, *Sci. Rep.*, 2015, **5**, 13643.
282. G. Guélou, A. V. Powell and P. Vaqueiro, *J. Mat. Chem. C*, 2015, **3**, 10624-10629.
283. Y. Xu and M. A. A. Schoonen, *Am. Mineral.*, 2000, **85**, 543-556.
284. A. M. Wiltrout, N. J. Freymeyer, T. Machani, D. P. Rossi and K. E. Plass, *J. Mater. Chem.*, 2011, **21**, 19286-19292.

285. P. Kumar, M. Gusain, P. S. Kumar, S. Uma and R. Nagarajan, *RSC Adv.*, 2014, **4**, 52633-52636.
286. M. G. Townsend, J. R. Gosselin, R. J. Tremblay, L. G. Ripley, D. W. Carson and W. B. Muir, *J. Phys. Chem. Solids*, 1977, **38**, 1153-1159.
287. M. L. V. Ramires, C. A. Nieto de Castro, Y. Nagasaka, A. Nagashima, M. J. Assael and W. A. Wakeham, *J. Phys. Chem. Ref. Data*, 1995, **24**, 1377-1381.
288. R. Brett and R. A. Yund, *Am. Mineral.*, 1964, **49**, 1084-1098.
289. H. Liu, X. Shi, F. Xu, L. Zhang, W. Zhang, L. Chen, Q. Li, C. Uher, T. Day and G. J. Snyder, *Nat. Mater.*, 2012, **11**, 422-425.

Appendix A Spark Plasma Sintering conditions of $Mo_xTi_{1-x}S_2$ (x = 0; 0.015 and 0.035).

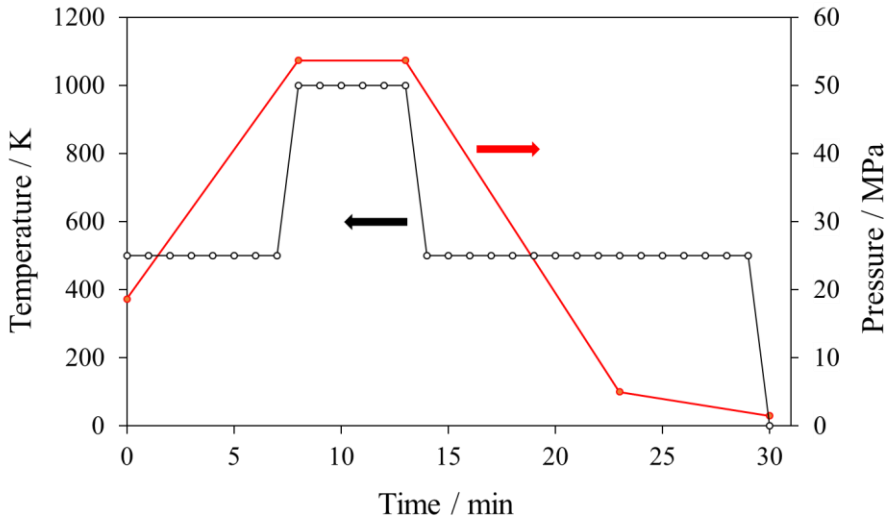

Figure A.1 Pressure and temperature conditions for a SPS sintering.

Appendix B Low temperature powder neutron diffraction of Co_xTiS_2.

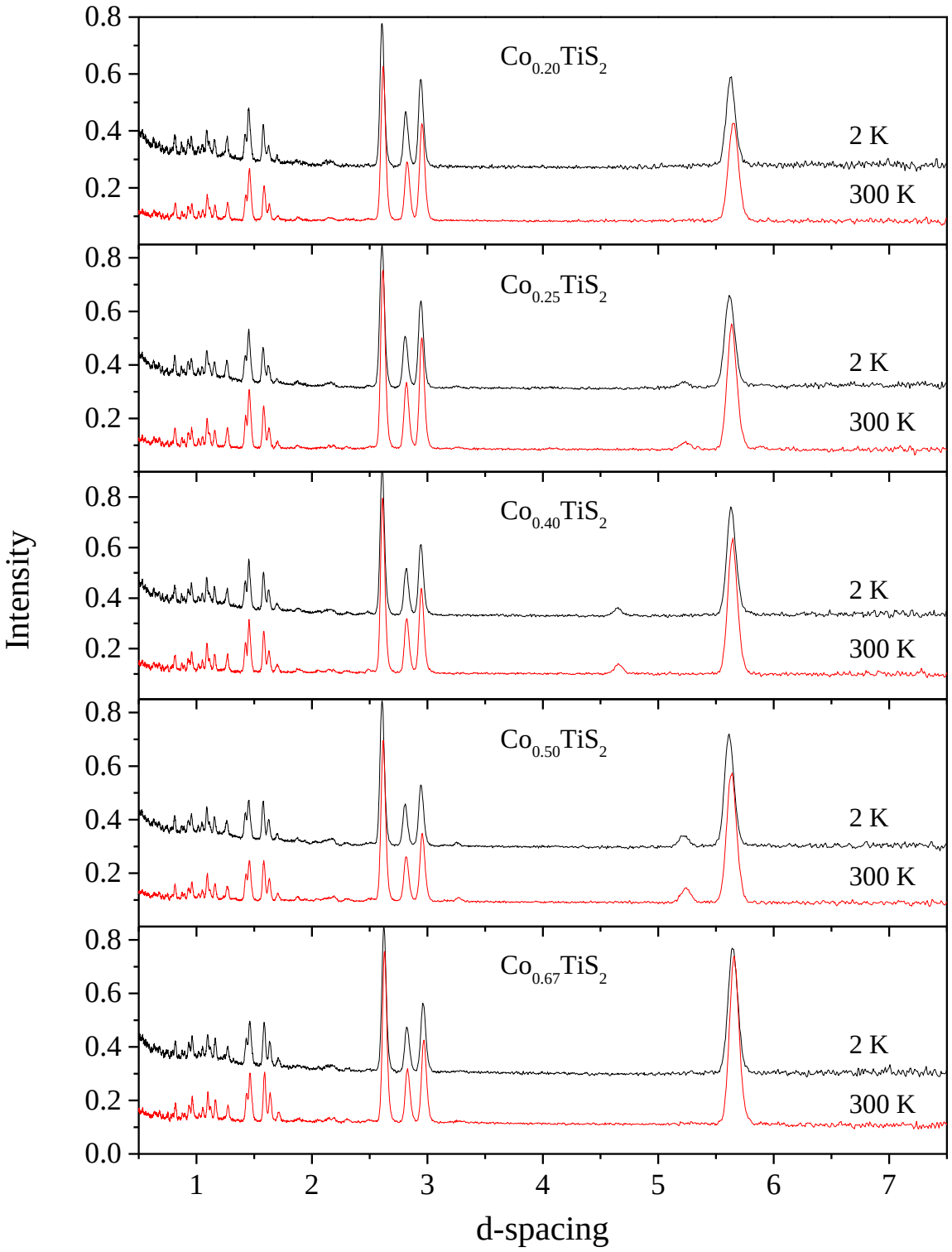

Figure B.1 Powder neutron diffraction data (bank 3, 2θ = 34.96º) of Co_xTiS_2 (x = 0.20; 0.25; 0.40; 0.50 and 0.6) at 2 K (black line) and at 300 K (red line).

Appendix C Muon spin relaxation of Co_xTiS_2 (x = 0.20 and 2/3).

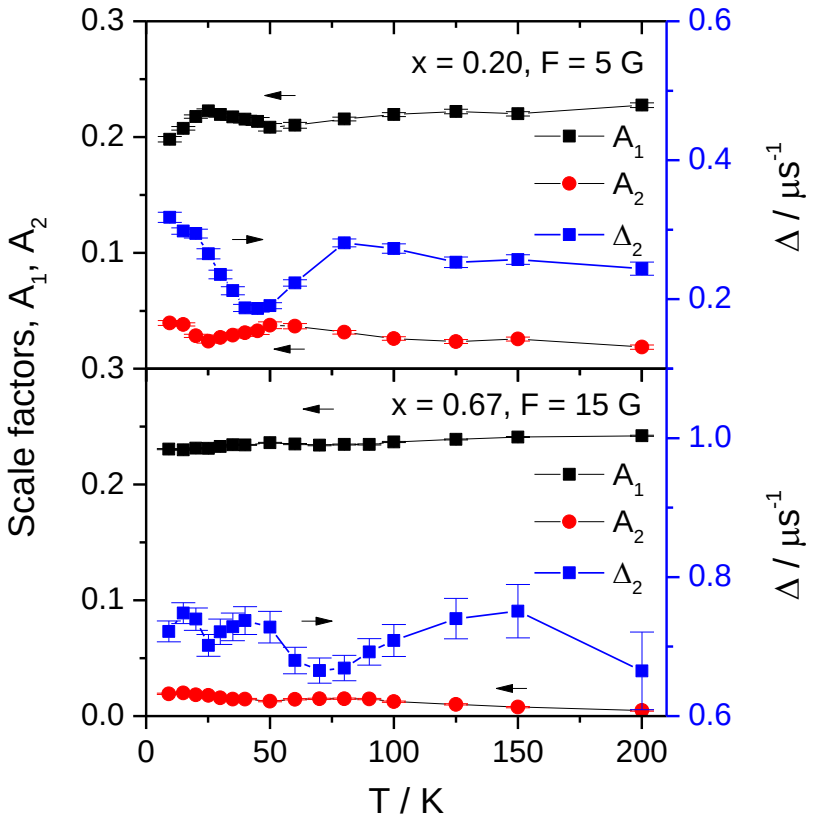

Figure C.1 Temperature dependence of the scale factor of the exponential decay function, A_1, and Kubo-Toyabe function, A_2, of Co_xTiS_2 (x = 0.20 and 2/3). The Gaussian field distribution of the Kubo-Toyabe function, Δ_2, is also shown. For $Co_{1/3}TiS_2$, a slightly stronger longitudinal field was applied (F = 20 G) and $A_2 \approx 0$ over the whole range.

Appendix D XRD of TGA/DSC residues of Co_xTiS_2 (x = 0; 0.08; 0.25 and 1/3).

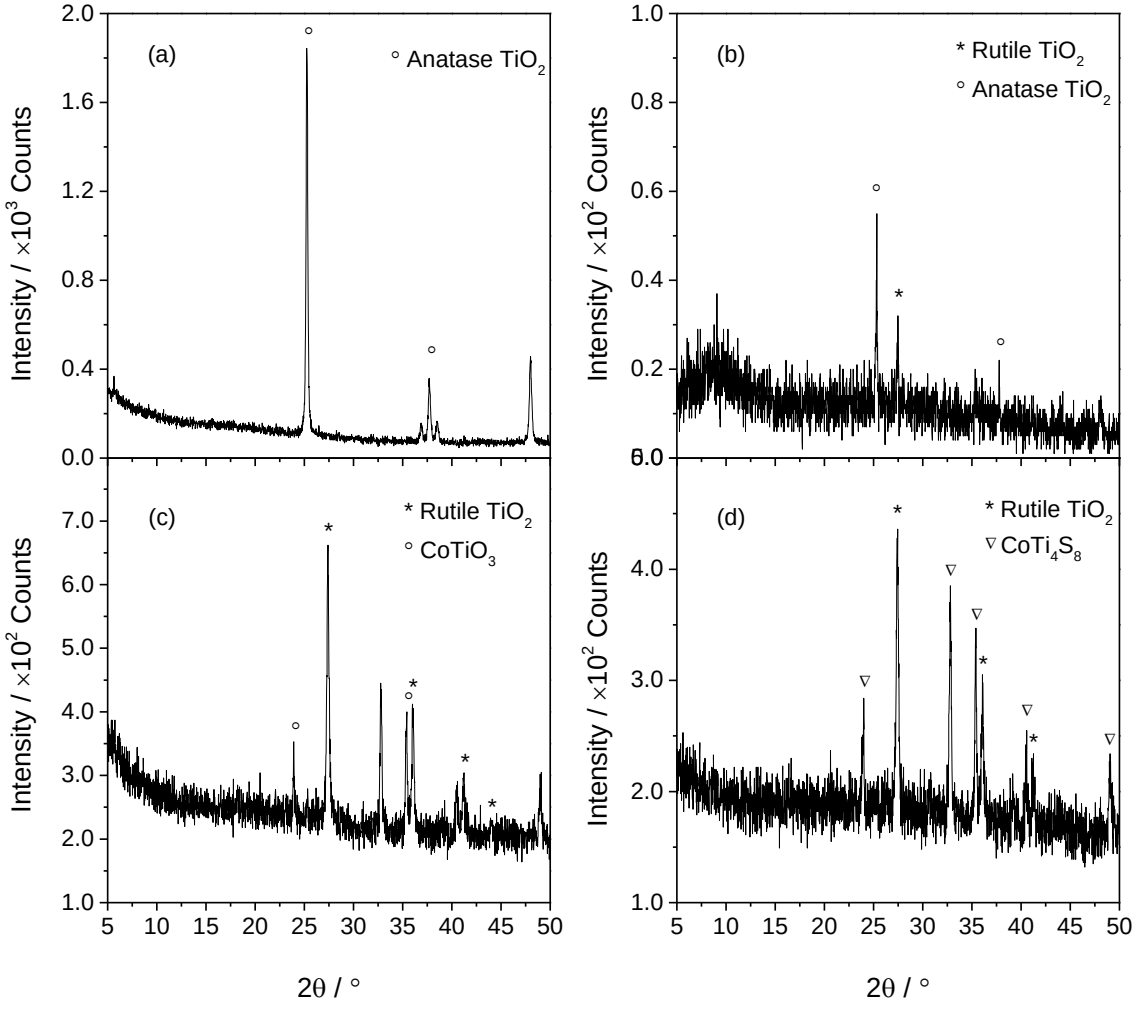

Figure D.1 Powder X-ray diffraction patterns of TGA/DSC residues of (a) TiS_2, (b) $Co_{0.08}TiS_2$, (c) $Co_{0.25}TiS_2$ and (d) $Co_{1/3}TiS_2$ in air.

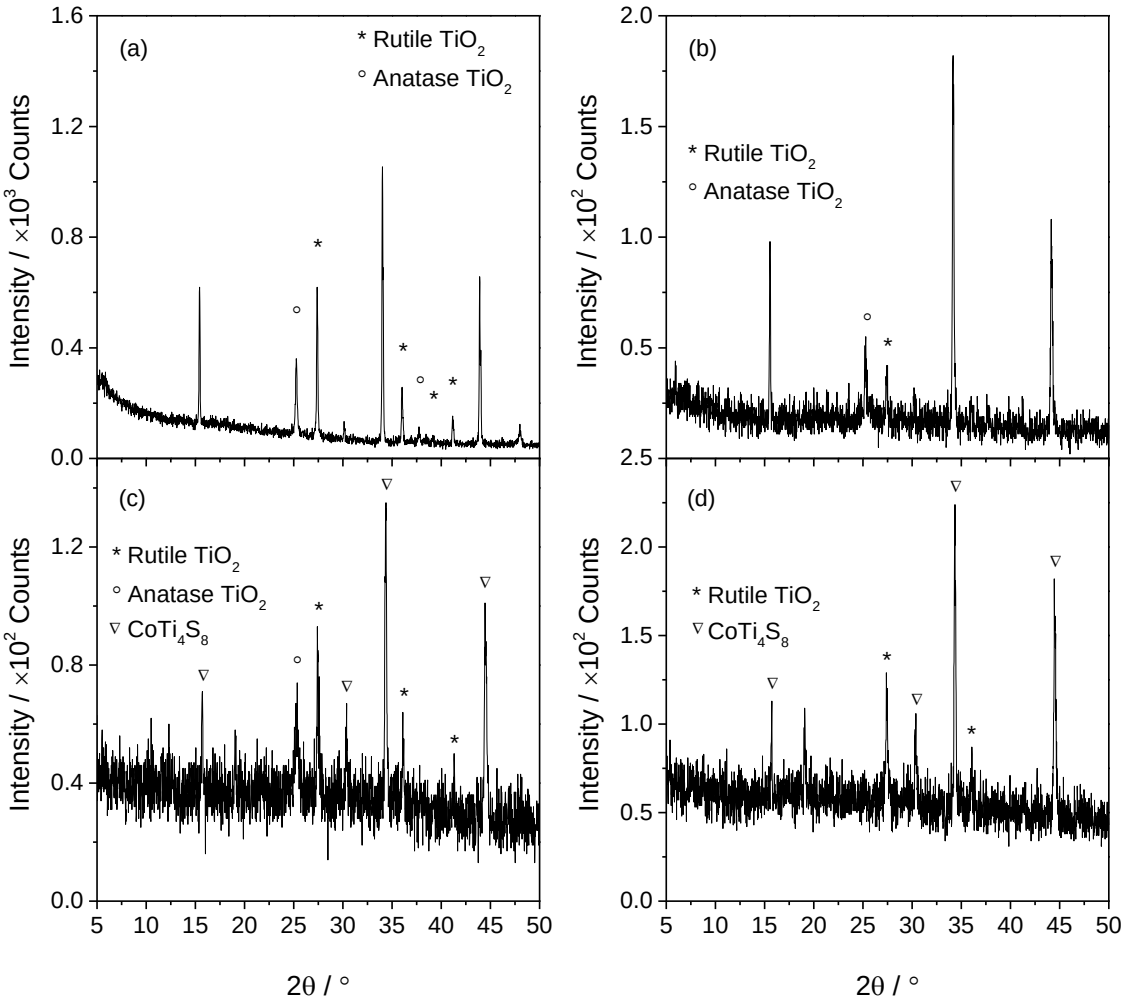

Figure D.2 Powder X-ray diffraction patterns of TGA/DSC residues of (a) TiS_2, (b) $Co_{0.08}TiS_2$, (c) $Co_{0.25}TiS_2$ and (d) $Co_{1/3}TiS_2$ in N_2 atmosphere.

Appendix E Additional powder X-ray diffraction data for the commercial nanoparticles used for the preparation of TiS_2 nanocomposites.

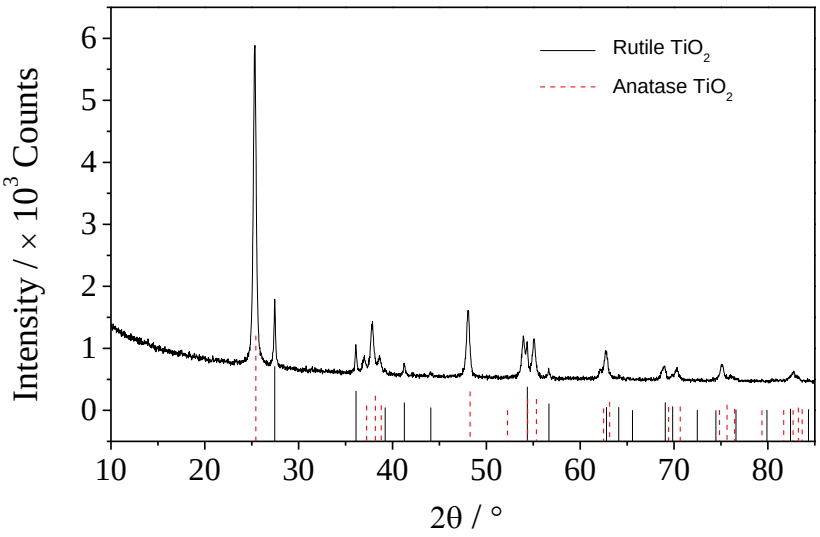

Figure E.1 Powder X-ray diffraction data of commercial TiO_2 nanoparticles used for nanocompositing.

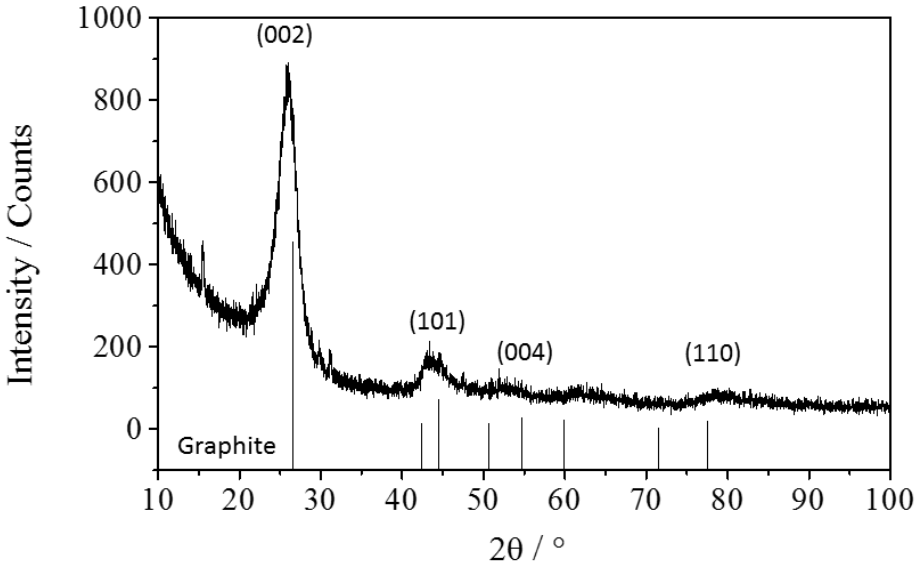

Figure E.2 Powder X-ray diffraction pattern of the commercial carbon nanotubes used for nanocompositing. The main reflections for graphite-2H (Space group *P* 63/*m m c*) are shown.[245]

Appendix F Prices of raw materials according to the USGS Mineral Commodity Summaries.

Table F.1 USGS Mineral Commodity Summaries average raw cost.[90]

Element	Sb	Cu	Fe	S	Bi	Se	Te
Price / \$ kg^{-1}	7.58	5.95	0.09	0.1	16.53	50.27	89

Appendix G Specific heat of $Cu_{12-x}Mn_xSb_4S_{13}$ (x = 0; 1).

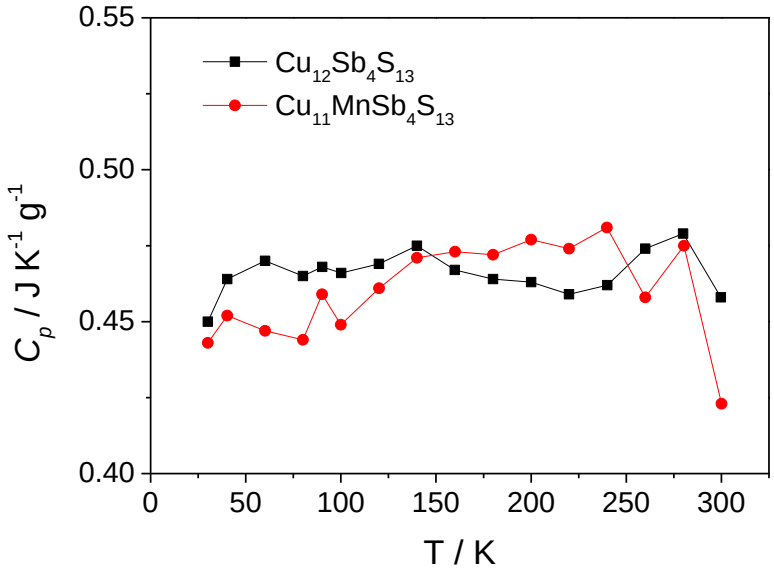

Figure G.1 Temperature dependence of the specific heat of $Cu_{12-x}Mn_xSb_4S_{13}$ (x = 0; 1) determined by side-by-side measurements with a pyroceram reference.

Appendix H Figure of merit, ZT, of $Cu_{12}Sb_4S_{13}$ determined by other workers.

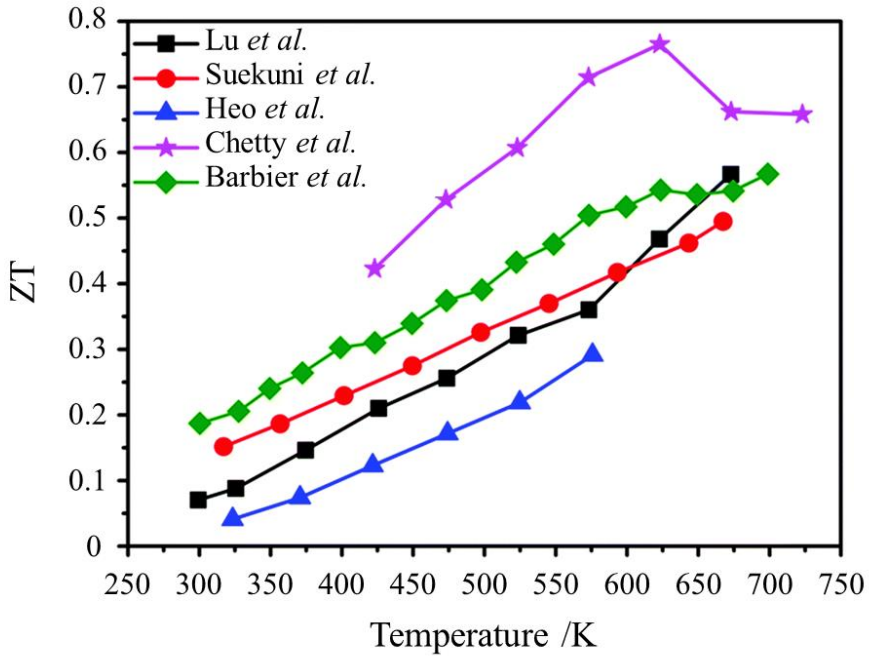

Figure H.1 Summary of the thermoelectric figure of merit, ZT, for $Cu_{12}Sb_4S_{13}$, adapted from the work of Chetty *et al.*,[254] containing data from Lu *et al.*,[255] Suekuni *et al.*,[271] Heo *et al.*,[258] Chetty *et al.*,[259] and Barbier *et al.*[270]

Appendix I Additional thermal properties of $Cu_5Fe_{1-x}Mn_xS_4$ ($0 \leq x \leq 0.10$).

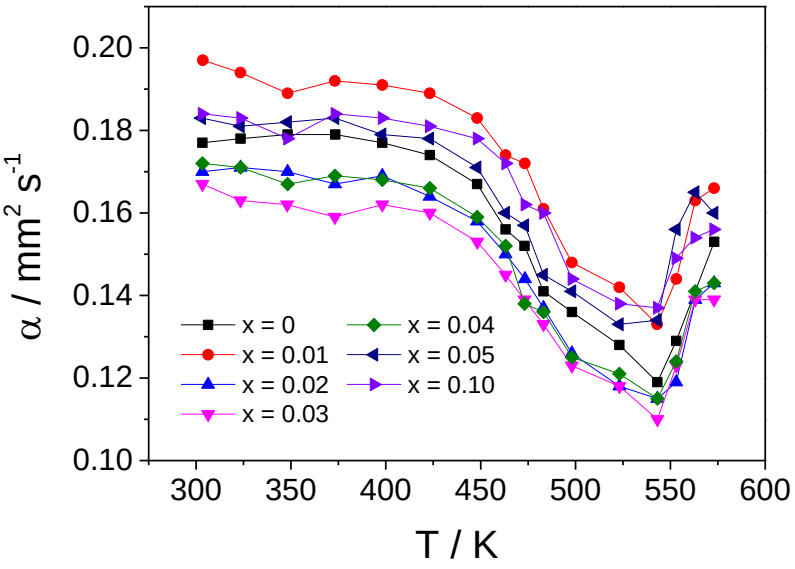

Figure I.1 Temperature dependence of the thermal diffusivity of $Cu_5Fe_{1-x}Mn_xS_4$.

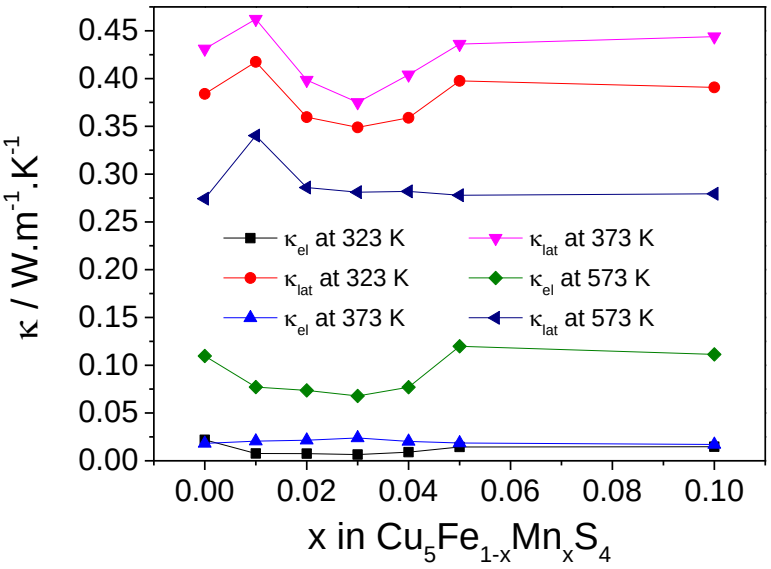

Figure I.2 Estimated lattice and electronic components of the thermal conductivity of $Cu_5Fe_{1-x}Mn_xS_4$ as a function of x, calculated using the Wiedemann-Franz law.

Appendix J Repeated measurements of the electrical properties of $Cu_5Fe_{1-x}Mn_xS_4$ (x = 0 and 0.04) and XRD data on temperature-damaged bornite sample.

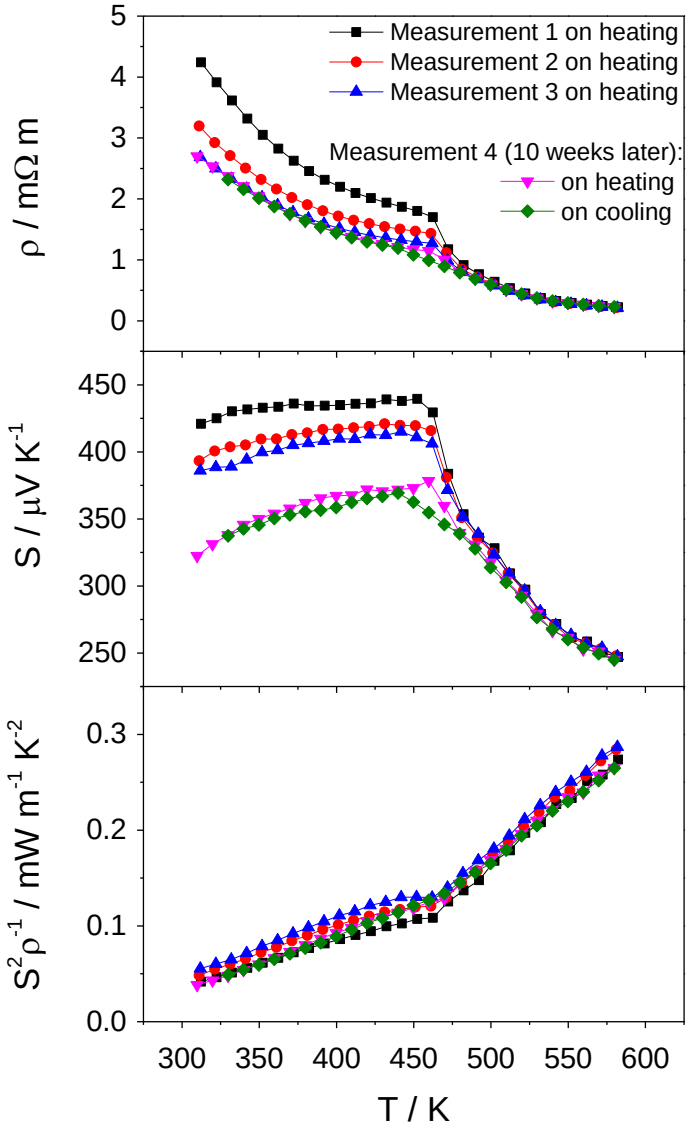

Figure J.1 Repeated measurements on heating and cooling of the electrical resistivity (top), Seebeck coefficient (middle) and power factor (bottom) as a function of temperature for Cu_5FeS_4.

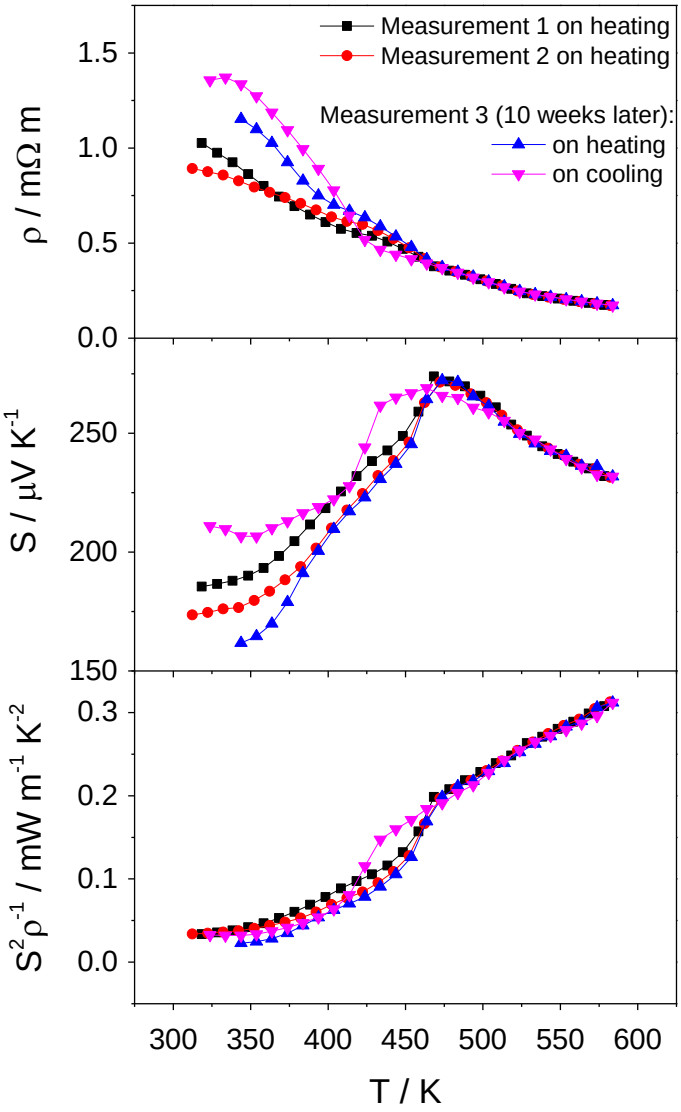

Figure J.2 Repeated measurements on heating and cooling of the electrical resistivity (top), Seebeck coefficient (middle) and power factor (bottom) as a function of temperature for $Cu_5Fe_{0.96}Mn_{0.04}S_4$.

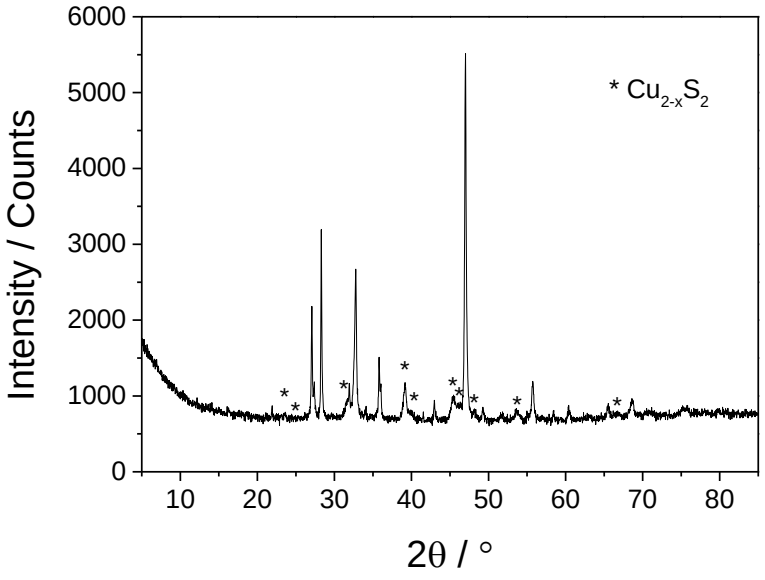

Figure J.3 Powder X-ray diffraction data of Cu_5FeS_4 after measurements of electrical transport properties up to 890 K. The impurity peaks corresponding to $Cu_{2-x}S$ are marked.